Thermal and structural performance of a new fiber-reinforced polymer thermal break for energy-efficient constructions

THÈSE N^{O} 7097 (2016)

PRÉSENTÉE LE 8 JUILLET 2016

À LA FACULTÉ DE L'ENVIRONNEMENT NATUREL, ARCHITECTURAL ET CONSTRUIT
LABORATOIRE DE CONSTRUCTION EN COMPOSITES
PROGRAMME DOCTORAL EN GÉNIE CIVIL ET ENVIRONNEMENT

ÉCOLE POLYTECHNIQUE FÉDÉRALE DE LAUSANNE

POUR L'OBTENTION DU GRADE DE DOCTEUR ÈS SCIENCES

PAR

Kyriaki GOULOUTI

acceptée sur proposition du jury:

Prof. M. Bierlaire, président du jury
Prof. T. Keller, Dr J. de Castro San Roman Fest, directeurs de thèse
Prof. J. R. Correia, rapporteur
Prof. A. Kenel, rapporteur
Prof. C.-A. Roulet, rapporteur

ÉCOLE POLYTECHNIQUE
FÉDÉRALE DE LAUSANNE
Suisse
2016

To all the people who supported me

«…γιά νά γυρίσει ὁ ἥλιος θέλει δουλειά πολλή…»

Οδυσσέας Ελύτης

Preface

In the context of the sustainable development of our society, the energy consumption of our building stock, which accounts for almost 40% of total energy consumption, must be significantly reduced. As an example, the European Directive 2010/31/EU accordingly prescribes that by the end of 2020 all new buildings have to be designed as net zero-energy buildings.

Against this background, this PhD thesis addresses a construction detail that can cause up to 30% of a building's heat losses, i.e. the structural connection of balconies, which penetrates the thermal insulation layer and may thus create significant thermal bridges.

Within a CTI project, and based on new structural materials emerging in the civil engineering domain such as glass (GFRP) and aramid (AFRP) fiber-reinforced polymer composites of very low thermal conductivity, a new balcony thermal break element with high insulation capacity has been developed and its thermal and structural performances have been experimentally and theoretically analyzed and optimized.

I would like to acknowledge the support for this research project provided by the Commission for Technology and Innovation CTI (Project-No. 13435.1 PFFLR-IW) and industry partner F.J. Aschwanden AG, and the collaboration with Prof. Dr. Albin Kenel of the Lucerne University of Applied Sciences and Arts.

Prof. Dr. Thomas Keller

EPFL-CCLab

Acknowledgments

This research was conducted within four years in Composite Construction Laboratory under the supervision of Prof. Dr. T. Keller and Dr. J.de Castro. During this period, a lot of challenges had to be overcome, both scientifically and personally. Undoubtedly, the benefits of this fruitful experience are priceless. Above all, I would like to express my gratitude to Prof. Keller. It is because of him that this project was finally successful. I will always remember his support as a professor and as a father, and I will always be grateful for that. My special thanks also to J. de Castro, for her support and friendship, during the doctoral studies.

In addition, I would like to express my appreciation to the jury members of the thesis comitee, Prof. J.R. Correia, Prof. A. Kenel, Prof. C.-A. Roulet and the president of the jury, Prof. M. Bierlaire. Their comments and feedback have been appreciated during these four years and during the thesis defense.

The mechanical experiments that I carried out could not have been possible without the group of the technicians in Structural Engineering Institute. I would like to acknowledge Sylvain, Gérald, Gilles, Patrice, Frédérique and Armin for their collaboration and friendship. I will always remember the good moments that we had during the experiments in the laboratory. My sincere thanks also to Ioannis for his collaboration and support of my research, since the knowledge gained from this cooperation opened new scientific horizons.

I would like to thank all my colleagues - friends in CCLab for the moments that we shared during all these years. I would like to acknowledge specially Carlos, Haifeng, Sonia and Vahid for their support and sincere friendship. Many special thanks to Hadi and Chrysanthi for their friendship all these years.

My thesis could not have been possible without the support and prayers of my family. I would like to express my gratitude to all that they have given to me.

Kyriaki Goulouti, 22.06.2016

Abstract

The thermal bridges constitute critical regions in building envelopes and they are created due to the interruption of the insulation layer. One of the many structural thermal bridges in building envelopes is created in balcony junctions because of the required structural continuity of the concrete slab. The detrimental effects of such thermal bridges are minimized, by using thermal breaks that interrupt the heat flow towards the external environment by adding an intermediate insulation layer between the internal floor and the balcony slab. For the majority of these thermal breaks, the load transfer from the balcony's cantilever to the main structure occurs through stainless steel bars, which penetrate the insulation layer and still have a high thermal conductivity.

The current research proposes a new thermal break composed of fiber-reinforced polymer composite materials (FRP) that have much better thermal properties than the conventional materials and investigates its short- and long-term structural and thermal behavior. The tensile force from the cantilever moment is transmitted by an aramid-FRP (ARFP) loop, whose thermal conductivity is about 170 times smaller than that of stainless steel. The compression component of the moment is transferred by a short glass-FRP (GFRP) element while the shear compression diagonal is transmitted by a FRP-PU hexagonal foam sandwich. The insulation layer is composed of a thin layer of aerogel granulate. All the components are assembled in a polymer box.

The thermal performance of the above-mentioned thermal break was validated by estimating its impact on the energy balance of a traditional building, using three different building envelopes (a MINERGIE envelope, a MINERGIE-P envelope and an optimum envelope). Furthermore, 3d finite element steady-state thermal simulations were performed in order to define the true losses through the optimized thermal break. Finally, the thermal behavior of the thermal break was compared with that of traditional thermal breaks.

The structural validation of the FRP thermal break included the mechanical characterization of the components through static, long-term and durability experiments. The static experiments of the components comprised tensile experiments (AFRP loop) and compression experiments (FRP-PU hexagonal foam sandwich and GFRP bar). The long-term behavior was evaluated through tensile and compression creep experiments, while its simulation and prediction were achieved by applying traditional creep methods and two new proposed models that were able to predict the secondary creep stage (Gradient regression and Gradient regression with NHPP). The durability was evaluated by their immersion in alkaline environment, simulating that of the concrete. Finally, the total behavior of the balcony junction was examined through full scale beam experiments that led to the analytical modelling of the system.

Keywords

Thermal bridges, thermal break, balcony connection, linear thermal transmittance, mechanical experiments, beam experiments, power creep law, gradient regression, non-homogeneous Poisson process.

Résumé

Les ponts thermiques constituent des endroits critiques de l’enveloppe thermique des bâtiments et apparaissent lors de toute interruption de l’isolation thermique. Il existe plusieurs types des ponts thermiques dont celui crée par la continuité structurale des dalles de balcon. Afin de minimiser les effets négatifs de ces ponts thermiques (déperditions de chaleur ainsi que risques de condensation et donc le risque d’apparition de moisissures), des consoles isolantes sont employées, permettant d’interrompre la transmission thermique vers l’environnement extérieur ceci en insérant une couche d’isolation entre la dalle intérieure du bâtiment et la dalle du balcon. La plupart de ces consoles isolantes sont composées de barres en acier inoxydable permettant de transférer les efforts du porte-à-faux à la structure principale. Cependant, les barres en acier pénètrent l’isolation thermique avec une conductivité thermique importante.

Cette recherche propose une nouvelle console isolante, composée de matériaux composites renforcés par des fibres (FRP) dont les propriétés thermiques sont bien meilleures que celles des matériaux traditionnels, et étudie sa performance structurale et thermique à court et à long terme. La force de traction engendrée par le moment négatif du porte-à-faux est transmise par une boucle à base de fibres d’aramide (AFRP), dont la conductivité thermique est 170 fois inférieure à celle de l’acier inoxydable., Quant à la force de compression due au moment négatif, est transférée par une courte barre à base de fibres de verre (GFRP), puis l’effort tranchant est transféré par un élément en sandwich hexagonal en A/GFRP et mousse polyuréthane (PU). La couche d’isolation est composée d’une fine couche de granulé en aérogel. Tous les éléments sont montés dans une boîte en PVC.

La performance thermique de cette console isolante a été validée en évaluant son effet dans le bilan énergétique d’un bâtiment traditionnel, en utilisant trois types enveloppes thermiques différentes (une enveloppe MINERGIE, une enveloppe MINERGIE-P et une enveloppe optimisée). De plus, des simulations thermiques en 3D par éléments finis et sous régime stationnaire ont été réalisées afin de définir les pertes thermiques précises de cette console isolante optimisée. Finalement, son comportement thermique a été comparé à celui de consoles isolantes traditionnelles.

La performance structurelle de la console isolante en FRP comprenait tout d’abord la caractérisation mécanique de chaque composant par des essais statiques, des essais à long terme et des essais de durabilité. Des essais de traction (boucle en AFRP) et des essais de compression (sandwich hexagonal en A/GFRP-PU et barre en GFRP) ont été menés. Le comportement à long terme a été validé par des essais de fluage en traction et compression. En ce qui concerne la simulation et la prédiction du comportement à long terme, des méthodes de fluage traditionnelles ont été utilisées et deux nouvelles méthodes proposées, permettant de simuler le fluage secondaire (Gradient regression and Gradient regression with NHPP). La durabilité des éléments a été évaluée en les immergeant dans une solution alcaline. Enfin, le comportement global de la console isolante intégrée dans une structure réelle a été examiné lors d’essais de flexion de poutres à grande échelle. Les résultats ont permis de valider le model analytique du système proposé.

Mots clés

Ponts thermiques, console isolante, connexion en porte-à-faux, transmittance thermique linéaire, essais mécaniques, essais de flexion, power creep law, gradient regression, non-homogeneous Poisson process.

Contents

Preface i

Acknowledgments iii

Abstract v

Résumé vii

1. Introduction 1

- **1.1.** Context and motivation 1
- **1.2.** Objectives 4
- **1.3.** Methodology 4
- **1.4.** Thesis organization 5
- **1.5.** References 8

2. Thermal performance evaluation 9

- **2.1.** Introduction 9
- **2.2.** Case study and general assumptions 12
- **2.3.** Specification of envelopes 15
  - **2.3.1.** MINERGIE and MINERGIE-P envelopes 15
  - **2.3.2.** Optimum envelope 16
    - **2.3.2.1.** Full factorial design 19
    - **2.3.2.2.** Optimum envelope specification 21
- **2.4.** Evaluation of optimized FRP thermal breaks 22
- **2.5.** Conclusions 26
- **2.6.** References 27

3. Structural and thermal performance 29
3.1. Introduction 29
3.2. Thermal and structural concept 31
  3.2.1. Overview 31
  3.2.2. Loop component 33
  3.2.3. Hexagon sandwich component 34
3.3. Thermal break performance 36
3.4. Structural performance 38
  3.4.1. Hexagon diagonal-compression experiments and results 38
    3.4.1.1. Experimental set-up 38
    3.4.1.2. Experimental results 42
  3.4.2. Hexagon bar-compression experiments and results 45
  3.4.3. Loop tensile experiments and results 46
    3.4.3.1. Experimental set-up 46
    3.4.3.2. Experimental results 46
3.5. Discussion 49
  3.5.1. Verification of concrete failure 49
    3.5.1.1. Loop 49
    3.5.1.2. Compression bar 49
    3.5.1.3. Hexagon diagonal 50
  3.5.2. Serviceability verification 50
3.6. Conclusions 52
3.7. References 53
4. Structural system performance 55
4.1. Introduction 55
4.2. Experimental set-up 56
  4.2.1. Thermal break components 56
  4.2.2. Experimental beams and program 57
  4.2.3. Instrumentation and measurements 60
4.3. Experimental results 61
  4.3.1. Load-deflection responses 61
  4.3.2. Failure modes 63
  4.3.3. Strain measurements 65

4.4. Discussion 66
    4.4.1. Design model and section forces 66
    4.4.2. AFRP loop responses and concrete anchoring 68
    4.4.3. GFRP bar responses and concrete support 69
    4.4.4. Hexagon diagonal responses and concrete support 69
    4.4.5. SLS and ULS verification 70
    4.4.6. Maximum balcony span 73
4.5. Conclusions 74
4.6. References 75
5. Creep prediction 77
5.1. Introduction 77
5.2. Experimental set-up 79
5.3. Modeling and results 82
    5.3.1. Findley's Law and General Power Law 82
    5.3.2. Gradient regression and non-homogeneous Poisson process 86
        5.3.2.1. Gradient regression 87
        5.3.2.2. Non-homogeneous Poisson process 92
5.4. Discussion 96
5.5. Conclusions 100
5.6. References 101
6. Conclusions and future work 103
6.1. Conclusions 103
6.2. Original contributions 105
6.3. Recommendations for future work 106
List of Figures 107
List of Tables 113
Annex A – Experimental design 115
Annex B – Preliminary cross-sandwich elements 125
Annex C – AFRP tensile loop component 135
Annex D – GFRP compression bar 147
Annex E – Hexagon sandwich component 151
Annex F – FE thermal simulation 161
Annex G – Full scale beam experiments 171
Annex H – Creep modeling and prediction 183
Curriculum Vitae 191

1 Introduction

1.1. Context and motivation

Over the last 30 years, the need for limiting the energy requirements in the building sector, which account for almost 40% of the energy consumption in the EU[1], has stimulated researchers to conceive new energy building policies and strategies. This has had a considerable influence on the way architects and engineers design energy-efficient constructions. Despite the fact that significant progress has already been made in this direction, the tendency towards achieving an increasingly effective energy performance is an endless procedure. Improving the energy efficiency of buildings constitutes and will continue to constitute one of the main cores of EU energy policy, not only to meet the EU's 2020 targets (Directive 2010/31/EU, EPBD recast), but also to meet the long-term objectives of the climate strategy, as established by the low-carbon economy roadmap 2050[2].

In the context of achieving the near-zero energy society, as required by the EPBD recast, new buildings nowadays are designed in such a way as to increasingly meet a variety of different requirements, i.e. they should be, as much as possible, sustainable, zero-net energy use, healthy and comfortable, grid-friendly and yet economical to build and maintain. However, one critical issue regarding the building energy design that remains to be adequately resolved is the thermal bridge location. A variety of different thermal bridges can be created in a building, see Fig.1.1., causing multidimensional heat loss, high condensation and mold growth risk, due to the low internal superficial temperature, with a negative impact on both the structure's life and indoor environmental quality[3].

One such thermal bridge that has been particularly studied and could be responsible for up to 30% of total heat losses in certain cases[4] is created in the interruption of the envelope insulation layer by a balcony cantilever, Fig. 1.2. The different energy policies implemented in Europe consider this and other thermal bridges in their requirements for energy-efficient buildings as shown for instance in Switzerland's energy policy, SIA[5] and MoPEC[6], and in the two most used energy lables in Europe, i.e. MINERGIE and Passivhaus[7,8].

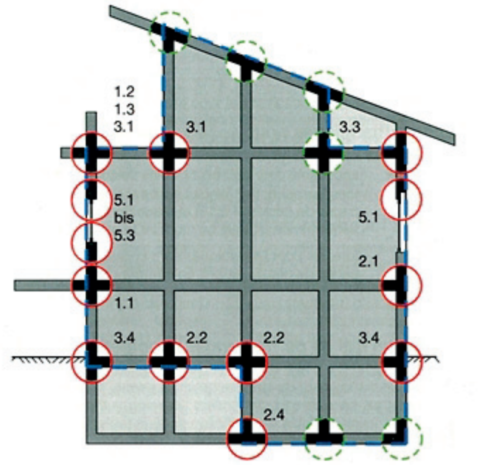

Figure 1.1. Different types of thermal bridges[9].

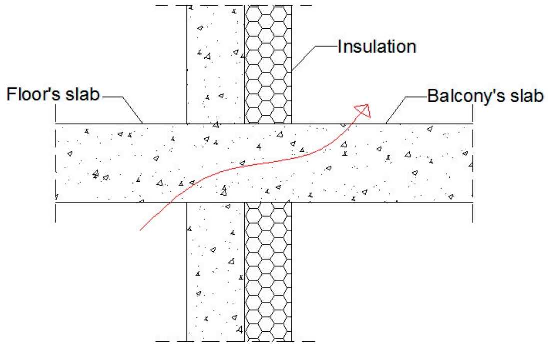

Figure 1.2. Balcony thermal bridge.

The Swiss building code SIA 380/1 proposes two methods for the evaluation and optimization of the envelope's energy performance; the global and the punctual methods. While the global method does not establish any requirement regarding thermal bridges, the punctual method prescribes limit values and target values for the thermal transmittance, ψ, of the envelope elements. In the case of balcony connections these values are ψ=0.30W/mK and ψ=0.15W/mK, respectively. Furthermore, the Swiss building code SIA 180[9] requires the evaluation of the critical superficial humidity and internal temperature in order to avoid condensation or mold growth risk. Finally, MoPEC requirements concerning thermal bridges are based on SIA 380/1. The MINERGIE energy standards in Switzerland apply requirements concerning thermal bridges similar to those of the SIA codes. In the basic MINERGIE standard the limit value (ψ=0.30W/mK) must be met if the punctual method is used. In MINERGIE-P and MINERGIE-A only the global method is applied and thus no requirements are prescribed for thermal bridges.

It is becoming evident that the only way to satisfy the limit or target values for thermal bridges with a view to achieving the zero-energy building objective is to further optimize the building's critical details by homogenizing the thermal resistance throughout the building envelope[10]. The current solution for dealing with thermal bridges is the use of thermal breaks that interrupt the heat flow towards the external environment by adding an intermediate insulation layer between the internal floor and the balcony slab, as shown in Fig. 1.3. Conventional thermal breaks that are composed of steel or stainless steel bars, to transmit the vertical loads from the cantilever to the main structure, are far from offering an optimized solution to the critical thermal bridge region. On the contrary, new materials like fiber-reinforced polymer composites (FRPs), which offer higher thermal resistance, could offer an alternative answer to the problem, see Table 1.1.

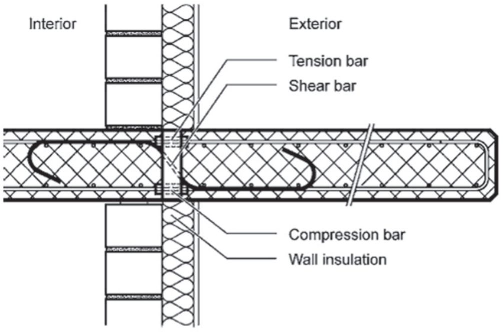

Figure 1.3. Typical thermal break with steel bars currently used for balcony connections[11].

Table 1.1. Thermal conductivity of commonly used materials in thermal breaks.

Material	***λ (W/mK)***
Reinforcing steel	50
Reinforcing stainless steel	17
EPS foam	0.032-0.040
XPS foam	0.025-0.040
Mineral wool	0.030-0.035
AFRP (aramid fiber composites)	0.04
GFRP (glass fiber composites)	1.0
Aerogel (insulation)	0.013

A new FRP thermal break is presented in Fig. 1.4. It is comprised by an AFRP upper loop, an A/GFRP sandwich hexagon and a lower GFRP bar, attached to the hexagon component. All thermal break components are assembled together in a PVC box, filled with aerogel insulating material. The structural concept of the thermal break is based on a simple N-shape truss system in which the AFRP loop and the GFRP bar transfer the bending moment, while the A/GFRP hexagon component transfers the shear forces, through the diagonal compression strut, Fig. 1.5.

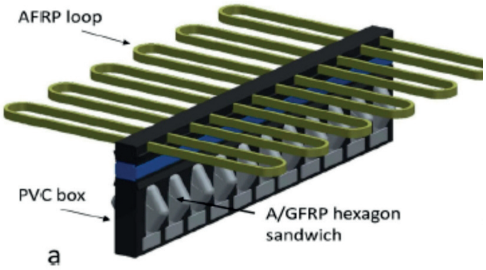

Figure 1.4. New FRP thermal break.

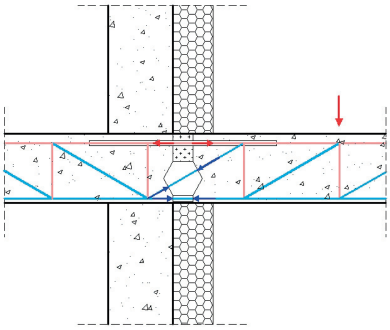

Figure 1.5. Structural system of new FRP thermal break.

1.2. Objectives

The general aim of this research is to investigate the short- and long-term thermal and structural performance of the above-mentioned new FRP thermal break for balcony connections. In order to achieve this aim the following objectives are defined:

a) evaluate the thermal performance of the FRP thermal break and its impact on the energy balance of a building.
b) investigate and model the structural performance of the individual FRP components that compose the thermal break.
c) investigate and model the structural system performance of the FRP thermal break embedded in the surrounding concrete slab.
d) investigate and model the long-term creep behavior of the individual FRP components in order to verify the balcony's long-term behavior.

1.3. Methodology

The aforementioned objectives are achieved via the following methods:

a) determination of a conventional building case study and its three envelope alternatives; MINERGIE, MINERGIE-P and an optimum envelope.
b) evaluation of the potential influence that heat losses through FRP thermal breaks have on the energy balance of the building case study and comparison with the heat losses through conventional thermal breaks, by means of building energy simulations (BES).

c) evaluation of the true heat losses through FRP thermal breaks by means of thermal numerical simulations.
d) experimental investigation of the structural behavior of the individual components. Static tensile and tension creep experiments on the AFRP loop component, static compression and compression creep experiments on the hexagon A/GFRP component, static compression experiments on the GFRP bar and durability experiments on all the components.
e) experimental investigation of the balcony system that incorporates the FRP thermal break, through full-scale beam experiments, simulating the real structure.
f) correlation of the experimental results from the individual components and the full-scale beam experiments for the derivation of a mechanical model. Analysis of the FRP connection in serviceability (SLS) and ultimate limit state (ULS).
g) numerical investigations of the time-dependent creep behavior of the individual components in order to develop new methodologies for predicting the long-term creep properties.

1.4. Thesis organization

The main core of the current research is organized in four chapters in order to elaborate on the four objectives defined in Section 1.2. The final chapter summarizes the conclusions of the research. A brief summary of the chapters is presented in the following and in Table 1.2:

- Chapter 2: The potential heat losses through an FRP thermal break are correlated to the total transmission losses, the losses through the opaque elements and the total heating needs requirements of the three different building envelopes calculated using building energy simulation (BES). The results are compared with those of traditional thermal breaks. The final energy gain from an FRP thermal break is estimated.
- Chapter 3: The new FRP thermal break is presented in detail. Its thermal performance is estimated and the true thermal losses are calculated. A three-dimensional model is built and the linear thermal transmittance (ψ) is calculated by numerically solving the energy balance balcony detail that includes the FRP thermal break. The structural behavior of the individual components (AFRP loop, A/GFRP hexagon, GFRP bar) is experimentally investigated. The strength and stiffness of every component are defined. Their sensitivity under sustained loads is examined as well as the influence of the alkaline concrete environment.
- Chapter 4: The structural system performance of the FRP thermal break embedded into the surrounding slab is experimentally investigated. Two different types of thermal breaks are

examined, which correspond to the basic FRP thermal break unit; a) one AFRP loop combined with two GFRP hexagon sandwiches and b) one AFRP loop combined with two AFRP hexagon sandwiches. Three different vertical load configurations are applied on the balcony side and the failure modes of the concrete beams are examined in detail. The feasibility of such a connection in SLS and ULS is verified and a final mechanical model of the balcony connection is derived. Based on this model, the maximum spans are calculated for the different load configurations.

- Chapter 5: The creep experimental results of the AFRP loop, the GFRP hexagons and a 25-year GFRP girder box experiment, are analyzed. Two new methodologies are proposed to predict long-term creep behavior and take probabilistically into account random incidents happening during the experiments. These methodologies are validated and the associated prediction errors calculated. Finally, the results are compared with those obtained using the traditional time-dependent approach of the general power law.
- Chapter 6: The conclusions of the research regarding the experimental, numerical and analytical results are presented and discussed. Indications of future work are also introduced.

The annexes present additional information and are linked to the main chapters, as shown in Table1.2. as follows:

a) Annex A: Experimental design of optimum envelope configuration.
b) Annex B: Preliminary cross sandwich.
c) Annex C: AFRP loop component.
d) Annex D: GFRP compression bar.
e) Annex E: A/GFRP hexagon sandwich.
f) Annex F: FE thermal simulation.
g) Annex G: Full-scale beams experiments.
h) Annex H: Creep prediction models.

The results of the thesis have been included in four journal papers – three of which have been published, and one in progress.

1. Goulouti K, de Castro J, Vassilopoulos P A, Keller T, Thermal performance evaluation of fiber-reinforced polymer thermal breaks for balcony connections, Energy and Buildings, 70 (2014), 365-371.
2. Goulouti K, de Castro J, Keller T, Aramid/glass fiber-reinforced thermal break – thermal and structural performance, Composite Structures, 136 (2016), 113-123.

3. Goulouti K, de Castro J, Keller T, Aramid/glass fiber-reinforced thermal break – structural system performance, Composite Structures, 152 (2016), 455-463.
4. Goulouti K, Lymperopoulos I, Creep modeling and prediction for fiber-reinforced polymers with Gradient regression and Non-Homogeneous Poisson Process, (in progress).

Table 1.2. Thesis organization.

Main Chapters	***Methodology***			***Annexes***
	Experimental	***Numerical***	***Analytical***	
2. Thermal performance evaluation		Thermal break impact on energy balance.		A
3. Structural and thermal performance of FRP components	Static, long-term and durability behavior of individual components.	Thermal performance of FRP thermal break.		B,C,D,E,F
4. Structural system performance	Full-scale beam experiments.		Mechanical model of balcony connection.	B,C,D,E,F,G
5. New methodology for creep prediction		Creep prediction models.		C,E,H

1.5. References

1. EPBD:2010. Directive 2010/31/EU of the European Parliament and of the Council of 19 May 2010 on the energy performance of buildings (recast).

2. Hamdy, M., Hasan, A., Siren, K., 2013. A multi-stage optimization method for cost-optimal and nearly-zero-energy building solutions in line with the EPBD-recast 2010. Energy and Buildings 56, 189–203.

3. G. Evola, G. Margani, and L. Marletta, Energy and cost evaluation of thermal bridge correction in Mediterranean climate, Energy and Buildings 43 (2011) 2385-2393.

4. Bericht Minergie 2013. Revisionsentwurf 2013 der Norm SIA 380/1 und mögliche Auswirkungen auf kantonale Vorschriften. Bericht zuhanden der Konferenz Kantonaler Energiefachstellen (EnFK), AG MuKEn, http://www.endk.ch/media/archive1/dokumentation/muken/Bericht-SIA380_1EnDK2013-12-12-def.pdf, (assessed 16.06.2015).

5. Swiss Standards Association, Swisscode SIA 380/1 L'énergie thermique dans les bâtiments, Swiss Society of Engineers and Architects, Zurich, Switzerland, 2009.

6. EnDK, Conférence des services cantonaux et d'énergie, Aide à l'application EN: "Part maximale d'énergies non renouvelable dans les bâtiments à construire", Berne, 2009.

7. MINERGIE, The MINERGIE-Standard for Buildings. Higher quality of life, lower energy consumption, Switzerland, October 2010.

8. Passivhaus Institut, Kriterien und Algorithmen für kühl-gemäßigte Klima, Zertifizierte Passivhaus Komponente-Balkonanschluss, Wärmebrückenarme Konstruktion-Balkonanschluss, 2013.

9. Justification energitique, Check-list des ponts thermiques, EnFK, December 2010.

10. F. Branco, A. Tadeu, and N. Simoes, Heat conduction across double brick walls via BEM, Building and Environment 39 (2004) 51-58.10. EN ISO 10211 Thermal Bridges in Building Construction: Heat Flows and Surface Temperatures. Detailed Calculations, 2007.

11.T. Keller, F. Riebel, A. Zhou, Multifunctional Hybrid GFRP/Steel Joint for Concrete Slab Structures, Journal of Composites for Construction 10 (2006) 550-560.

2

Thermal performance evaluation

2.1. Introduction

Since July 2012, the EU requires that member states (including Croatia, Norway and Switzerland) implement the amended version of the Energy Performance Building Directive (EPBD), so that by 31 December 2020, all new buildings are nearly zero-energy buildings (NZEB)[1]. The EPBD describes the nearly net-zero energy building as a building that has a very high energy performance[2], which signifies buildings with minimized heating needs, but not at the expense of indoor comfort. Therefore special attention should be paid to the optimization of every building element, so that good internal comfort is guaranteed and energy waste due to poor design is avoided.

Critical regions of the building envelope constitute the thermal bridges, created by every interruption of the insulation layer and generally in zones with reduced thermal resistance[3], which affect both energy consumption and indoor comfort. Multidimensional heat flows are generated at these locations, in addition to the heat flow normally transmitted through the building envelope. Furthermore, a high risk of condensation and mold growth exists in thermal bridge regions due to the low internal superficial temperature, with a negative impact on the structure and indoor environmental quality[4]. Since thermal bridges are such a critical issue, the different energy policies implemented in Europe consider them in their requirements for energy-efficient buildings as shown for instance in Switzerland's energy policy, SIA[5] and MoPEC[6], and in two of the most prevalent European energy standards, MINERGIE[7] and Passivhaus[8].

Authors: Kyriaki Goulouti, Julia de Castro, Anastasios P. Vassilopoulos, Thomas Keller
Composite Construction Laboratory CCLab, Ecole Polytechnique Fédérale de Lausanne EPFL.

Contribution: The main core of the paper was conceived and conducted by Kyriaki Goulouti (energy simulations, experimental design). The analysis was developed in collaboration with Prof. T. Keller.

The building codes and standards primarily focus on requirements concerning the performance of the building envelope, of which thermal bridges are a part. The Swiss code SIA 380/1 proposes two methods for the evaluation and optimization of the envelope's energy performance; the global and the punctual methods. While the global method does not establish any requirement regarding thermal bridges, the punctual method prescribes limit values and target values for the thermal transmittance, ψ, of the envelope elements. In the case of balcony connections these values are ψ=0.30W/mK and ψ=0.15W/mK, respectively. Furthermore, the Swiss building code SIA 180[9] requires the evaluation of the critical superficial humidity and internal temperature in order to avoid condensation or mould growth risk. Finally, MoPEC requirements concerning thermal bridges are based on SIA 380/1.

The energy standards in Switzerland, MINERGIE, apply similar requirements concerning thermal bridges to the SIA codes. In the basic MINERGIE standard the limit value (ψ=0.30W/mK) must be met if the punctual method is used. In MINERGIE-P and MINERGIE-A only the global method is applied and thus no requirements are prescribed for thermal bridges. The German Passivhaus standard has stricter requirements concerning thermal bridges. The evaluation of the thermal transmittance through the thermal bridges according to EN ISO 10211[10] and/or EN ISO 10077[11] is required. Concerning thermal bridges created in balcony connections, the thermal bridge correction factor is limited to ΔU=0.025W/m^{2}K while, if a value of ΔU=0.01W/m^{2}K is complied with, the balcony connection is considered as 'thermal bridge free'. In addition, the temperature factor, f_{rsi}, should not exceed the minimum value for mold growth risk[12].

The only way to satisfy the limit or target values for thermal bridges is to homogenize the thermal resistance throughout the building envelope[13]. With regard to thermal bridges created in balcony connections in concrete or masonry structures, the industrial sector proposes a variety of balcony thermal breaks, which interrupt the heat flow towards the external environment by adding an intermediate insulation layer between the internal floor and the balcony slab, as shown in Fig. 2.1. For the majority of thermal breaks, the load transfer from the balcony's cantilever to the main structure occurs through stainless steel bars, which penetrate the insulation layer and still have a high thermal conductivity. Table 2.1 summarizes the thermal conductivity of the most commonly used materials in such connections (according to EN ISO 10456:2007[14]). Depending on a variety of parameters (wall thermal transmittance, diameter of bars, number and distance of elements, etc.), the thermal performance of these elements, evaluated by the linear thermal transmittance, ψ, varies between 0.11 and 0.35 W/mK (according to manufacturer data sheets). However, the lowest values can only be achieved for very small overhangs (if U-values of the walls of 0.10W/m^{2}K according to MINERGIE-P or NZEB are aimed at). ψ-values for typically used balconies (projections of 1.2-1.5m) are then around 0.25-0.30 W/mK and therefore meet the Swiss limit value, but not the target value.

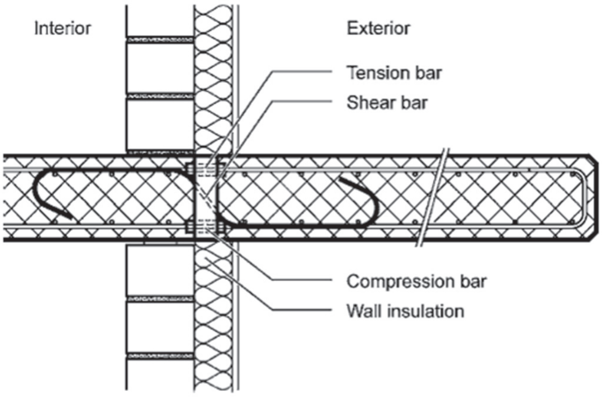

Figure 2.1. Typical thermal break with steel bars currently used for balcony connections[15].

Table 2.1. Thermal conductivity of commonly used materials in thermal breaks.

Material	*λ (W/mK)*
Reinforcing steel	50
Reinforcing stainless steel	17
EPS foam	0.032-0.040
XPS foam	0.025-0.040
Mineral wool	0.030-0.035

New materials exist nowadays with much improved thermal properties, see Table 2.2, which could replace existing conventional ones and improve the performance of thermal breaks. Keller et al.[15] studied a new hybrid element, in which the lower stainless steel reinforcement was replaced by a compression-shear glass-fiber reinforced polymer (GFRP) element, which improved the thermal performance by 26% compared to the pure steel solution[16]. However, the remaining tension steel bars were still leading to significant losses. Even better thermal properties than those of glass fibers are offered by aramid fibers, see Table 2.2, and combined with high-performance insulation materials e.g. aerogels, thermal transmittances of ψ=0.10W/mK, far below the SIA target value, can be achieved.

Table 2.2. Thermal conductivity of aramid, glass fibers and aerogel materials.

Material	*λ (W/mK)*
AFRP (aramid fiber composites)	0.04[a]
GFRP (glass fiber composites)	1.0[a]
Aerogel (insulation)	0.013[b]

a values from Swiss-Composite[28], **b** values from Cabot[29]

The objective of this work is to evaluate the possible impact of such an improved and optimized thermal break on the energy balance of a typical residential building in Switzerland's environmental conditions. In a case study the thermal losses through the balcony connections are estimated and compared to the total transmission losses and the heating needs. Three different thermal transmittances are taken into account, ψ=0.30, 0.15 and 0.10 W/mK, corresponding to the SIA limit and target values and to an optimized FRP thermal break, respectively. For each value, three different envelopes are considered, corresponding to the MINERGIE and MINERGIE-P standards as well as to an optimized envelope according to NZEB requirements. In a MINERGIE or MINERGIE-P envelope, the losses through thermal bridges can always be compensated by optimizing other building elements e.g. using more efficient glazing types or thicker insulation. However, when the envelope cannot be optimized any further and all the elements exhibit the best currently attainable performance, the real impact of thermal bridges on the building's energy consumption can be estimated. The impact of thermal losses through balcony connections will thus be quantified for optimally performing thermal breaks and building envelopes as well.

2.2. Case study and general assumptions

A typical two-story residential building was selected for the analysis, as shown in Fig. 2.2. The building was assumed as being situated in Pully, one of the eastern suburbs of Lausanne, located on the shores of Lake Geneva. The altitude was selected as being 461m where data were available from a meteorological station. On the ground floor were a kitchen, a living room and subsidiary rooms, while on the first floor were four rooms and a bathroom, see Figs. 2.3 and 2.4. A balcony and a projecting roof were designed around the first floor, which served as protection against weather conditions. The energy reference area (ERA) according to SIA 380/1 was 180m^2 and the total building height was 7.1m (external dimensions, see Fig. 2.5). The ERA is defined as the total sum of the horizontal surfaces (external dimensions) that are included inside the thermal envelope. The orientation of the building and the balcony and roof projection dimensions were parameters included in the study.

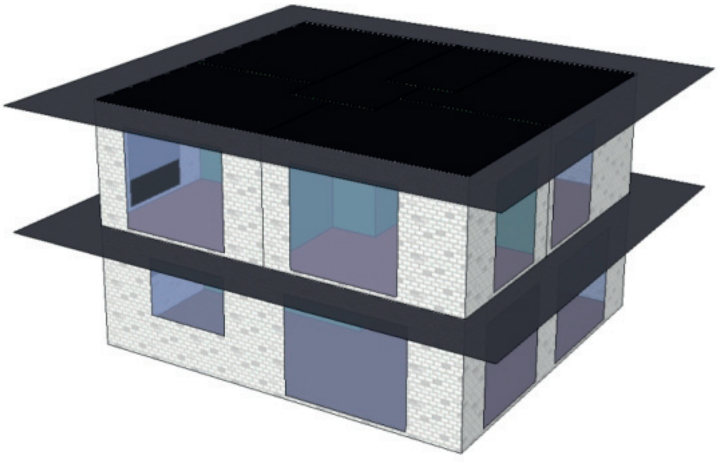

Figure 2.2. 3D visualization of case study building.

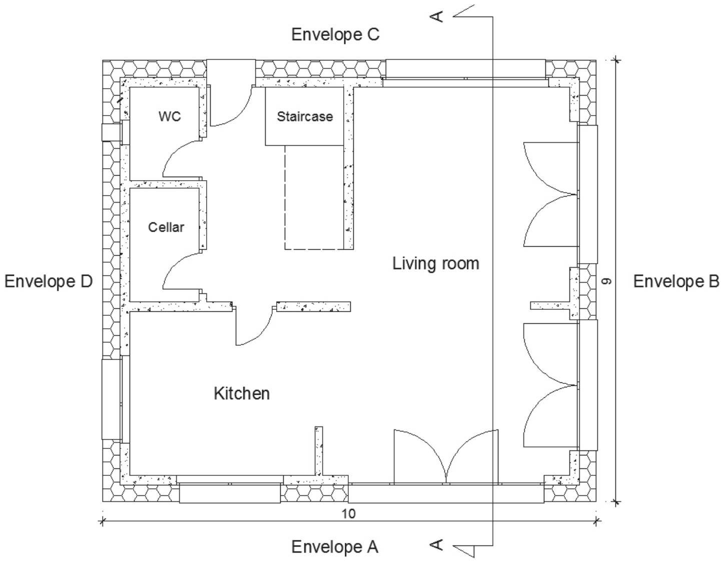
A
Envelope C
WC
Staircase
Cellar
Living room
Envelope D
9
Envelope B
Kitchen
10
Envelope A
A

Figure 2.3. Plan of ground floor (dimensions in (m)).

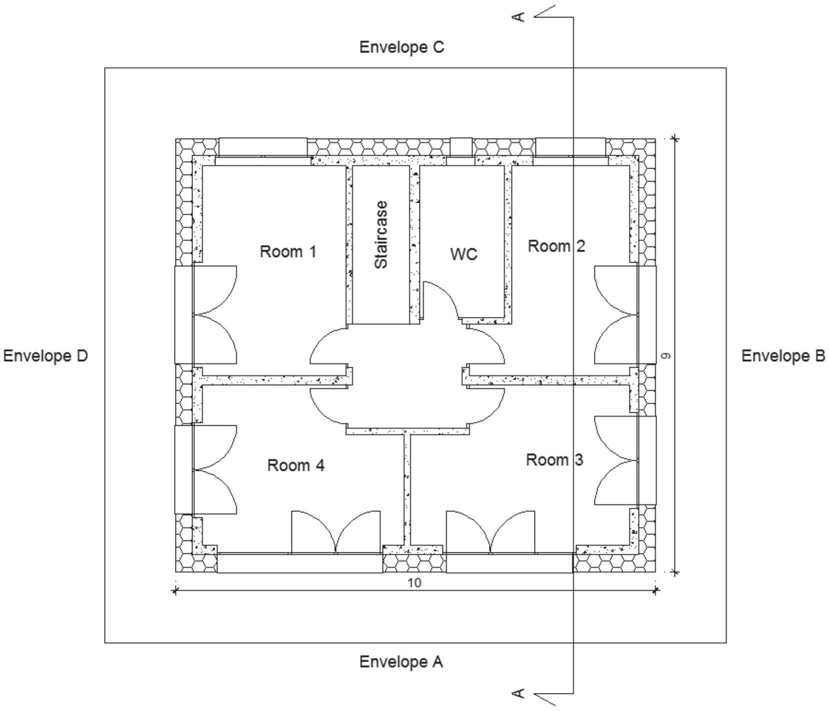
A
Envelope C
Staircase
Room 1
WC
Room 2
Envelope D
9
Envelope B
Room 4
Room 3
10
Envelope A
A

Figure 2.4. Plan of first floor (dimensions in (m)).

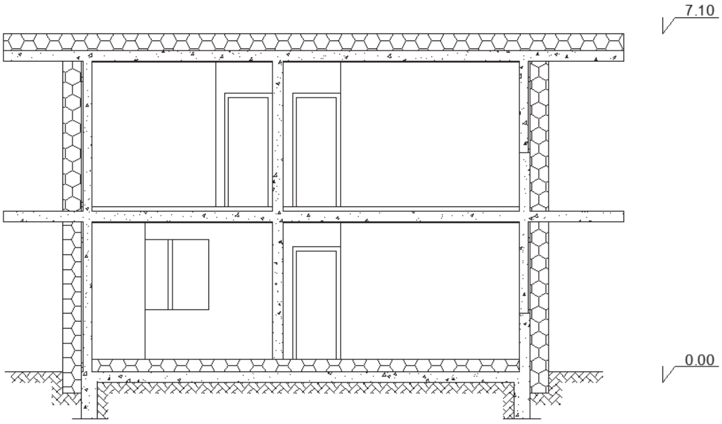

Figure 2.5. Section A-A with envelope (insulation layers).

The energy simulations were performed using LESOSAI, a software for the certification, thermal balance calculation and life cycle analysis of buildings[17]. The analysis was performed according to SIA 380/1 requirements on an annual basis, using a monthly calculation step. The heating period was defined as being from October until April. The monthly mean values used for the analysis corresponded to a reference year, obtained from SIA 2028[18], which is implemented in LESOSAI. The average external temperature was 11°C and the minimum -4.3°C, on an annual basis. Since the case study refers to a residential building, a homogeneous internal temperature of 20°C was prescribed. Natural ventilation and an air change rate of $0.7 m^3/hm^2$ were assumed, according to SIA 380/1. The internal gains depended on the ERA, according to SIA 380/1.

2.3. Specification of envelopes

2.3.1. MINERGIE and MINERGIE-P envelopes

The primary requirement concerning a MINERGIE building is the envelope performance and since the study is focused on the evaluation of thermal bridges, which are part of the building envelope, no other MINERGIE requirement has been examined. The MINERGIE envelope is defined as an envelope for which the heating needs, *Qh*, are less than 90% of the limit value, *Qh,li*, of SIA 380/1: $Qh \leq 0.9 \cdot Qh,li$. The SIA limit value, calculated for the case study, was Qh,li=49.1kWh/m^2. This value is valid for the three different envelopes, since it is based only on the building category and geometry of the building, i.e. the surface of the thermal envelope, A_{th} (439.2m^2 in this case) and the ERA (180m^2)[5]. The thermal envelope includes all the building elements that totally enclose the heated or cooled spaces.

The MINERGIE limit value for the heating needs was thus Q_h=44.2kWh/m^2 and the building elements were chosen in such a way that this value was achieved. The thermal insulation was assumed to be on the external side of the wall, see Fig. 2.5, with a wall thermal transmittance of U=0.25W/m^{2}K. Concerning the roof and the ground slab, the thermal transmittance was selected as being U=0.20W/m^{2}K. The balcony and the roof projections were calculated to be 1.5m, according to the position of the sun for the longest and shortest days of the year, 21st June and 21st December, for the latitude of Pully[19], see Fig. 2.5. In addition, movable shading devices were considered (blinds, curtains, etc.) and the shading factor was selected as being 0.1. Concerning the orientation of the building, envelope A was orientated towards the South, see Figs. 2.3 and 2.4.

The total transparent surface represented 40% of the ERA[20]. A triple glazing was used with a thermal transmittance of U=0.70W/m^{2}K and a solar heat gain coefficient of *SHGC*=60%, while a PVC frame was selected with U=1.10W/m^{2}K. The frame corresponded to 30% of the total window surface[5] and a linear thermal transmittance, ψ=0.07 W/mK, was used for the spacers[17]. The thermal bridges around the windows were taken into account and a constant value for the linear thermal transmittance, corresponding to the target value of SIA 380/1, ψ=0.05W/mK, was assumed. The thermal bridges created at the junction between the ground floor and the external walls were considered as having a linear thermal transmittance of ψ=0.10W/mK (again the target value of SIA 380/1). Based on all these selections, the resulting heating needs met the limits established by MINERGIE, see Table 2.3.

As far as MINERGIE-P is concerned, the heating needs are restricted to 60% of the limit value of SIA 380/1, i.e. Q_h=29.9kWh/m^2. Again, the building elements were selected in order to reach this value. The thermal transmittance of the walls and roof were U=0.15W/m^{2}K, while for the ground slab U=0.10W/m^{2}K resulted. The total transparent surface again represented 40% of the ERA, but more efficient windows were chosen. A triple glazing was used with U=0.60W/m^{2}K and a solar coefficient of *SHGC*=60%. A similar frame was assumed as for the MINERGIE envelope, which represented 30% of the total window surface. However, a high-performance spacer was selected with ψ=0.032W/mK. For the other thermal bridges, the same assumptions were made as before (target values of SIA 380/1). The fixed and movable shading factors remained the same as for the MINERGIE envelope. Resulting heating needs are summarized in Table 2.3.

Table 2.3. Heating needs for examined envelopes and linear thermal transmittances of thermal breaks.

Envelopes	***Linear thermal transmittance, (W/mK)***		
	ψ=0.30	ψ=0.15	ψ=0.10
MINERGIE (kWh/m^2)	42.8	38.7	37.3
MINERGIE-P (kWh/m^2)	29.1	25.2	24.0
OPTIMUM (kWh/m^2)	13.1	10.5	9.6

2.3.2. Optimum envelope

The optimum envelope is that which presents the lowest possible heating needs, Q_h, as defined in SIA 380/1 and Eq. (1)[5]:

$$Q_h = \sum_{1}^{12} \left[(Q_T + Q_V) - n_g (Q_i + Q_s) \right] \tag{1}$$

where Q_T is the transmission losses, Q_V the losses due to air change, n_g the factor of internal gains (depending on the thermal inertia of the building and the relationship between the total gains and losses), Q_i the internal gains and Q_s the solar gains. Minimizing the heating needs thus signifies defining and optimizing all the parameters that minimize the transmission losses of the opaque and transparent elements and also increase the solar gains, taking into account that the ventilation losses and internal gains are values established by the standards.

Although building energy design is a multifactorial problem, Mechri et al. [21] retained the following as the most important design parameters: shape, orientation, transparent envelope surface, external solar shading, outer color and mass distribution. They proved that the variance of the energy needs for heating is mainly influenced by the transparent envelope surface ratio, which is defined as the window-to-wall surface ratio, *WWR*. Furthermore, the thermal transmittance of the windows is normally almost five times greater than that of the other elements of the envelope and large amounts of energy are lost through the transparent elements[22]. Consequently, one of the most important parameters in designing energy-efficient buildings is the design and selection of an appropriate window system[23]. Therefore, the optimization of the transparent envelope surface determines the optimum envelope as well, provided that the other building elements exhibit the best currently attainable performance.

The transparent envelope surface ratio, *WWR,* is the parameter that should be optimized for each of the four envelope sides. However, the *WWR* is directly linked to other parameters, e.g. the orientation of the building, balcony or roof projection and the thermal transmittance *U* of the glazing, and therefore cannot be optimized independently. Hence, the optimum combination of these parameters, resulting in the lowest heating needs, should be determined. To achieve this, a parametric analysis was performed taking seven parameters into account: four *WWRs* for envelopes A, B, C, D (see Fig. 2.3), thermal transmittance of windows *U*, balcony and roof projection *P* and orientation *O,* with four levels for each parameter, as shown in Table 2.4.

Table 2.4. Optimum envelope: seven examined parameters with assumed value ranges.

Parameters	*1st level*	*2nd level*	*3rd level*	*4th level*
WWRA (%)	20	30	40	50
WWRB (%)	20	30	40	50
WWRC (%)	15	20	25	30
WWRD (%)	20	25	30	35
Thermal transmittance of windows, *U* (W/m^{2}K)	0.4	0.5	0.6	0.7
Balcony and roof projections, *P* (m)	0.75	1	1.25	1.5
Orientation, *O* (°)	0	45	90	315

Shaded are lower and upper levels used for full factorial design.

As it can be seen in this table, for the main envelopes A and B the *WWR* was varied from 20% to 50% with 10% increments. Since these envelopes are rotated according to the orientation parameter from East to West, values above 50% become critical for overheating and values below 20% are not justified, since maximum solar gains are sought. Concerning envelope C, rotated from NW to NE, the *WWR* started at 15%, which is the lowest value for appropriate daylight[24], and increased to 30%, in increments of 5%, since higher *WWRs* are not justified at these orientations due to limited solar radiation. For envelope D, rotated from SW to NW, the lowest value of *WWR* was 20%, since in the W position solar radiation is almost the same as in the E, but the highest value was 35%, since the subsidiary spaces are placed on this side. Concerning the thermal transmittance of the windows, *U*, a corresponding *SHGC*-value was selected for each value, based on window types already existing on the market. Triple-glazed windows were chosen starting from U=0.40W/m^{2}K with *SHGC*=56% and U=0.50W/m^{2}K with *SHGC*=60%. The third value corresponded to U=0.60W/m^{2}K and *SHGC*=60%, while the last one was U=0.70W/m^{2}K and *SHGC*=62%. The two intermediate values have the same *SHGC* and therefore the window with the lower thermal transmittance (U=0.50W/m^{2}K) was more efficient. However, it was decided to include the U=0.60W/m^{2}K value since it is the one most commonly used and represents today's standard for MINERGIE buildings. The balcony and roof projection was varied between 0.75m and 1.5m, in increments of 0.25m. The highest value represented the one calculated from the position of the sun for the longest and shortest days and overhangs smaller than 0.75m were excluded. As far as orientation is concerned the values were varied between 0° and 315°. The 0° orientation means that there is no deviation from the North and envelopes A and B were orientated to the south and east. An angle of 45° means that they were orientated to the SW and SE, an angle of 90° rotating them to the W and S, while the 315° rotation means that they were orientated to the SE and NE. In this way, the effect of W and E was taken into account and the most favorable orientation could thus be determined.

Performing this parametric analysis with seven parameters and four levels and taking all the possible interactions into account would lead to 4^7=16384 simulations for the determination of the optimum combination in terms of heating needs. To avoid this large number of simulations, an experimental design method was applied[25]. In this way, with a minimum number of simulations, adequate information concerning parameter effects and the interactions among them were deduced[26], see next section.

Regarding all the other building elements not included in the optimization analysis, their selected performances corresponded to the best currently attainable. The thermal transmittance of the opaque elements was selected as being U=0.10W/m^{2}K, since in practice a value U=0.12W/m^{2}K can be achieved[27]. For the window frames the best value was used, which corresponded to a frame of PVC–XL, with U=1.0W/m^{2}K. The percentage of the frame in relation to the overall window surface was varied for each window between 18–22%, according to the specific configurations. The best available spacer was used, made of composite materials, with ψ=0.032 W/mK. Finally, the linear thermal transmittance of all thermal bridges (around windows, ground slab, balcony and roof projection) was selected to correspond to the target values set by the SIA (ψ=0.05 / 0.20 / 0.15 / 0.15W/mK).

2.3.2.1. Full factorial design

The aim of this experimental design was to identify, from the seven parameters, the dominant ones and thus reduce their number and consequently the number of simulations. The best method to approach a problem with several factors is the factorial analysis[25]. To determine the most significant parameters and their interactions, a 2^7 full factorial analysis was conducted, taking into account the seven parameters selecting only the maximum and minimum levels for each one, see Table 2.4. For this analysis all the interactions up to the 7th order were taken into account and 2^7 =128 simulations were conducted using LESOSAI. The maximum and minimum levels were coded as -1 and +1 respectively and a linear random coefficient model (or linear regression model) was fitted according to Eq. (2):

$$\begin{aligned}
&Q_h = a_0 + a_1 \cdot WWRA + a_2 \cdot WWRB + a_3 \cdot WWRC + a_4 \cdot WWRD + a_5 \cdot U + a_6 \cdot P + a_7 \cdot O \\
&a_{12} \cdot WWRA \cdot WWRB + a_{13} \cdot WWRA \cdot WWRC + a_{14} \cdot WWRA \cdot WWRD + \\
&a_{15} \cdot WWRA \cdot U + a_{16} \cdot WWRA \cdot P + a_{16} \cdot WWRA \cdot P + a_{17} \cdot WWRA \cdot O + a_{25} \cdot WWRB \cdot U + \\
&a_{27} \cdot WWRB \cdot O + a_{47} \cdot WWRD \cdot O
\end{aligned} \tag{2}$$

The outcomes of the analysis were the model coefficients (a_0, a_1, a_2, etc.) of the regression model as follows:

$$\begin{aligned}
&Q_h = 17.729 - 1.876 \cdot WWRA + 0.35 \cdot WWRB + 0.349 \cdot WWRC - 0.257 \cdot WWRD + 1.696 \cdot U + \\
&1.599 \cdot P + 1.346 \cdot O + 0.0805 \cdot WWRA \cdot WWRB + 0.0039 \cdot WWRA \cdot WWRC + \\
&0.0914 \cdot WWRA \cdot WWRD + 0.138 \cdot WWRA \cdot U + 0.22 \cdot WWRA \cdot P + 0.722 \cdot WWRA \cdot O + \\
&0.196 \cdot WWRB \cdot U + 0.193 \cdot WWRB \cdot O - 0.249 \cdot WWRD \cdot O
\end{aligned} \tag{3}$$

The significance of the individual parameters and interactions on heating needs are demonstrated by the relative effects, which were calculated by dividing each resulting coefficient by the a_0-value. The resulting dominant parameters and interactions, with the greatest influence on heating needs, were *WWRA*, *U*, *P*, *O* and the interaction $WWRA \times O$, respectively, see Fig. 2.6. The parameter *WWRA* had the highest effect of 10.6% on heating needs. The thermal transmittance of the windows *U* (9.6%) and balcony projection *P* (9.0%) followed, while the orientation, *O*, influenced heating needs by 7.6%.

Comparing envelope A to the others, the result was coherent, since at the first level (0°), it was totally orientated towards the South, where solar radiation was the highest during the winter. The *U* parameter had a high effect on heating needs too, since it is related to thermal losses to the external environment and solar gains, while the *P* and *O* parameters are related to solar gains inside the building. The interaction with the most significant effect was *WWRA* ×*O*, which was even higher than the effect of the other *WWR*-parameters. This result can be explained by the fact that envelope A, at the first level, was totally orientated towards the south and was therefore sensitive to possible deviations from this orientation.

Furthermore, a half normal plot was used to represent all the 127 results, see Fig.2.7. This plot shows the absolute value of the effects of the parameters and interactions estimated against their cumulative normal probabilities[25]. The results show that *WWRA*, *U*, *P* and *O* have the highest probability and thus represent the four parameters with which the further analysis will be continued.

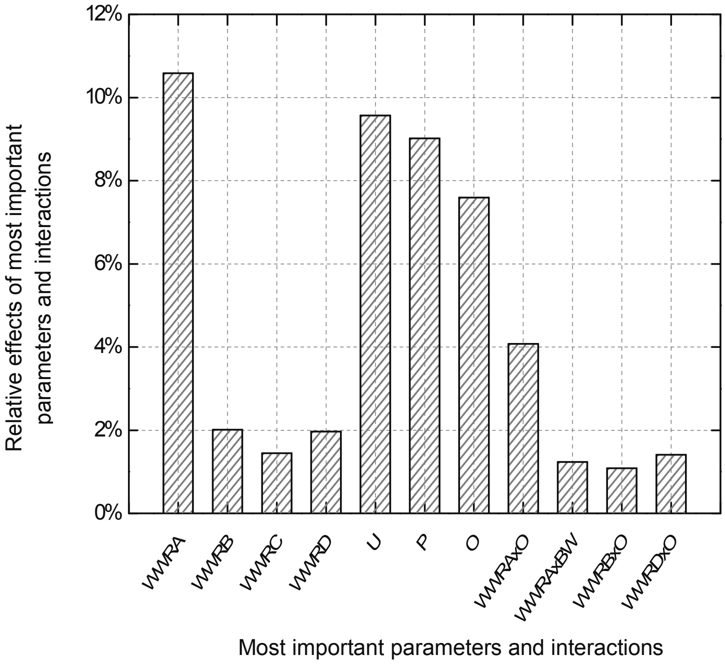

Figure 2.6. Relative effects of most important parameters and interactions on heating requirements.

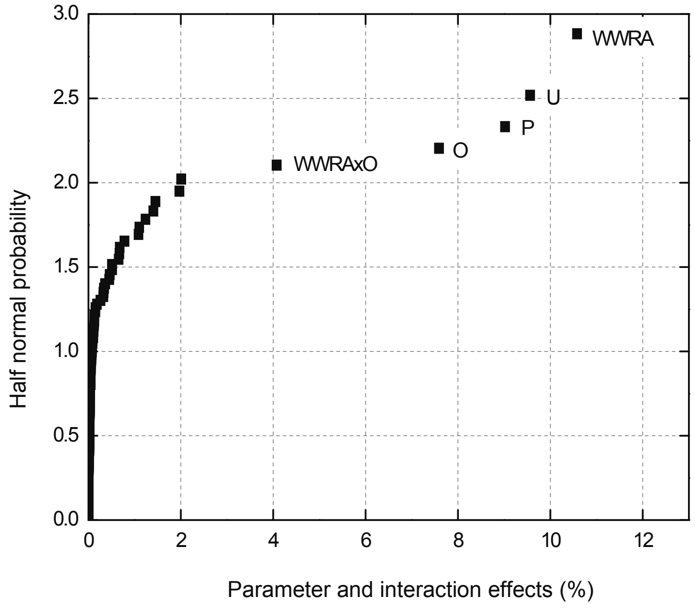

Figure 2.7. Half normal plot of parameters and all interactions.

2.3.2.2. Optimum envelope specification

The optimum envelope was derived from a parametric analysis that was performed with the four identified dominant parameters, selecting all four levels for each one, see Table 2.5. All the possible interactions were taken into account and therefore 4^4=256 simulations were performed. Specific values were chosen for the three omitted parameters (*WWRB, WWRC and WWRD*). Since envelope B is one of the main envelopes of the building, rotated from Northeast to South, the selected value for *WWR* was 50%, for better exploitation of solar gains. For the other two envelopes C and D, 30% was selected. For a 90° rotation, envelope C was orientated towards the East, so the maximum level of envelope C was adopted. Regarding envelope D, the 90° rotation orientated it towards the North, hence the *WWR* for this orientation should not exceed the maximum value used in the factorial design (30%), for envelope C.

Table 2.5. Optimum envelope: examined parameters with corresponding four levels.

Parameters	*1st level*	*2nd level*	*3rd level*	*4th level*
WWRA (%)	20	30	40	50
Thermal transmittance of windows, *U* (W/m²K)	0.4	0.5	0.6	0.7
Balcony and roof projections, *P* (m)	0.75	1	1.25	1.5
Orientation, *O* (°)	0	45	90	315

The results of the simulations are presented in Table 2.6, which shows the combinations with the five lowest and two highest (colored rows) heating needs. The best combination, which led to the lowest heating needs of Q_h= 10.50kWh/m^2, was *WWRA*=50%, *U*=0.4W/m^{2}K, *P*=0.75m and *O*=0°. The combination for which envelopes A and B were orientated towards the south and east (*O*=0°) therefore exhibited the lowest heating needs. Their orientation towards the south and west (*O*=90°) gave a slightly higher value (Q_h= 11.1kWh/m^2). Furthermore, windows with higher thermal transmittance but also higher solar gains (*U*=0.50W/m^{2}K with *SHGC*= 60%) also led to low heating needs. The depth of the balcony and roof projections should be as small as possible, provided that overheating problems are being overcome. The highest heating needs however resulted from low (20%) and medium (40%) values of *WWRA*, high values for the window thermal transmittance and balcony projection, while the rotation angle was 315°.

Table 2.6. Combinations with the lowest heating needs Q_h.

WWRA (%)	*U (W/m²K)*	*P (m)*	*O (°)*	Q_h *(kWh/m²)*
50	0.4	0.75	0	10.5
50	0.5	0.75	0	11.0
50	0.4	0.75	90	11.1
40	0.4	0.75	90	11.5
40	0.4	0.75	90	11.6
40	0.7	1.5	315	23.3
20	0.7	1.5	315	24.0

2.4. Evaluation of optimized FRP thermal breaks

Based on the obtained optimum envelope and the other two MINERGIE envelopes, the effect of the optimized FRP thermal breaks on transmission losses and heating needs can be evaluated. The resulting heating needs for the three examined envelopes and thermal transmittances of the assumed thermal breaks (ψ=0.10, 0.15, 0.30W/mK) are presented in Table 2.3. Thermal breaks include both those of the balcony and roof connections around the whole building.

The percentage of thermal losses through thermal bridges in relation to total transmission losses, as a function of their linear thermal transmittance, ψ, and envelope type, are shown in Fig. 2.8. The total transmission losses include losses through the opaque and transparent elements, ventilation losses and losses through the thermal bridges. It is obvious that the percentage of transmission losses through the thermal bridges significantly decreased, by a factor of approximately 3, with lower thermal transmittance of the latter. Within one constant ψ-value, the percentages of thermal losses through the thermal bridges increased with improved envelopes because the total transmission losses decreased when the envelope was improved. However, the possible gains due to improving the thermal bridges were still modest compared to the total transmission losses – in the order of 3-5% of the latter.

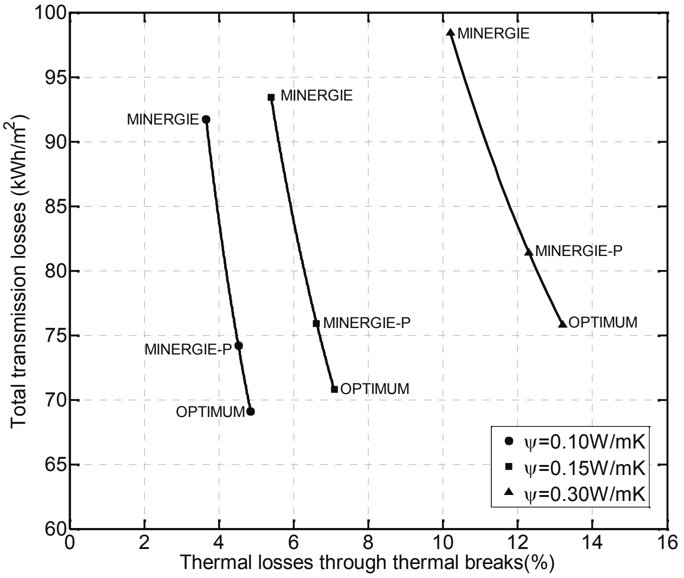

Figure 2.8. Losses through thermal breaks as percentage of total transmission losses and function of envelope type and thermal transmittance of thermal breaks.

The total transmission losses through the MINERGIE-P and the optimum envelopes were not very different either for the case of ψ=0.30 W/mK, or for ψ=0.10 W/mK. This was because the optimization of the envelope led to greater window surfaces and thus higher losses through the transparent elements than in a MINERGIE-P envelope. On the other hand, the optimization permitted greater solar gains, resulting in lower heating needs. Window losses are compensated by window solar gains and the significance of their losses thus cannot be estimated independently of the solar gains. Disregarding the small solar gains through the opaque elements, the losses through the thermal bridges should therefore be related to the losses through the opaque envelope elements only – thus the net losses, as shown in Fig. 2.9. The ventilation losses were also omitted from this calculation, since thermal bridges are part of the building envelope and hence the opaque elements. In this case, the transmission losses of the optimum envelope were clearly lower than those of MINERGIE-P. The percentages of the losses through the thermal bridges became very significant – up to 32% of those through the opaque elements, compared to

13.2% through the total transmission losses. The losses through the opaque elements were reduced through improved thermal breaks by 12 % for MINERGIE or 18% for the optimum envelope.

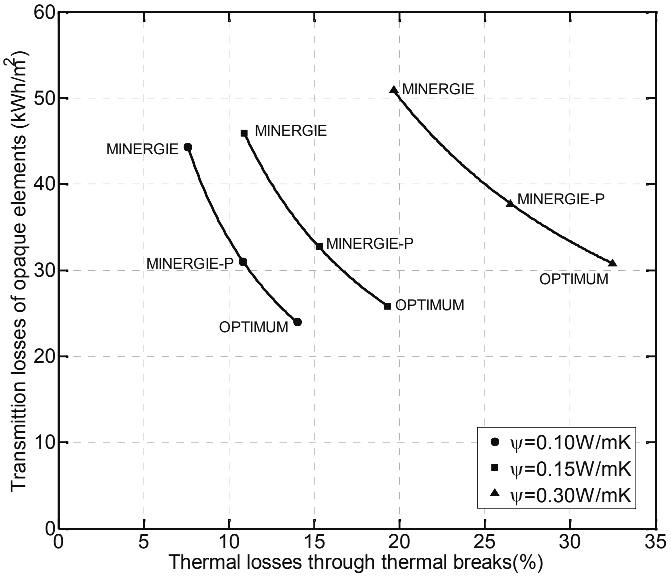

Figure 2.9. Losses through thermal breaks as percentage of those through opaque elements and function of envelope type and thermal transmittance of thermal breaks.

Since the performance of a building envelope is not only characterized by its thermal losses, but also by its capability to accumulate solar gains, the losses through thermal bridges can also be related to the heating needs. Figure 2.10 shows the percentages of the losses through the three thermal bridge types related to the total heating needs of the three different envelopes. This percentage shows the importance of the losses through thermal bridges in relation to heating needs. Even if in the end these losses are compensated by the gains, they still exist and represent one aspect of the envelope's performance. In the case of the optimum envelope, between 35% (for ψ=0.10W/mK) and 76% (ψ=0.30W/mK) of the heating needs originated from the thermal bridges.

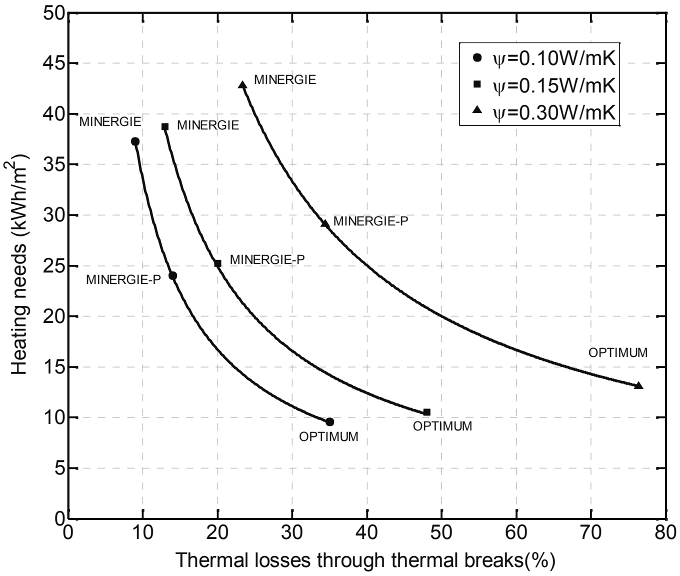

Figure 2.10. Losses through thermal breaks as percentage of heating requirements and function of envelope type and thermal transmittance of thermal breaks.

2.5. Conclusions

In this study the potential effects of high-performance fiber-reinforced polymer thermal breaks for balconies or roof projections on the thermal losses through the envelopes and on the heating needs of typical residential buildings in Switzerland were investigated and quantified. The new thermal breaks have linear thermal transmittance values $\psi \leq 0.1$W/mK, which are therefore far below the limit or target values of SIA 380/1 (0.30 or 0.15W/mK respectively). The effects were evaluated for three types of envelopes: MINERGIE, MINERGIE-P and a further optimized envelope. The following conclusions were drawn:

1) The losses through the thermal bridges in relation to the total transmission losses decrease by a factor of approximately three if ψ is decreased from 0.30 to 0.10W/mK. However, this reduction, if related to the total transmission losses of the building, remains modest in the order of 3-5% of the total losses.

2) If however the losses through the thermal bridges are related to those through the opaque elements of the building envelope only, the latter are reduced by 12% for the MINERGIE or 18% for the optimum envelope if ψ is decreased from 0.3 to 0.1W/mK. These reductions now become significant.

The relation to the opaque elements only is justified by the fact that losses and gains through the transparent elements more or less compensate each other and because thermal bridges are part of the opaque elements.

3) If finally the losses through the thermal bridges are related to the heating needs of a building with an optimized envelope, the percentage of the losses on the needs is reduced by 41% if ψ is decreased from 0.30 to 0.10W/mK.

In the attempt to approach zero-energy buildings with zero heating needs, thermal losses though thermal breaks can thus have a very significant effect, which therefore justifies the investment in the development of new thermal breaks optimized in terms of thermal transmittance.

2.6. References

1. H. Erhorn and H. Erhorn-Kluttig, The Path towards 2020: Nearly Zero-Energy Buildings, The REHVA European HVAC Journal 49 (2012) 12-15.

2. J. Kurnitski, F. Allard, D. Braham, et al., How to define nearly net zero energy buildings nZEB - REHVA proposal for uniformed national implementation of EPBD recast, The REHVA European HVAC Journal 48 (2011) 6-12.

3. C.-A. Roulet, Santé et qualité de l'environnement intérieur dans les bâtiments, second ed, Presses Polytechniques et Universitaires Romandes, Lausanne, 2010.

4. G. Evola, G. Margani, and L. Marletta, Energy and cost evaluation of thermal bridge correction in Mediterranean climate, Energy and Buildings 43 (2011) 2385-2393.

5. Swiss Standards Association, Swisscode SIA 380/1 L'énergie thermique dans les bâtiments, Swiss Society of Engineers and Architects, Zurich, Switzerland, 2009.

6. EnDK, Conférence des services cantonaux et d'énergie, Aide à l'application EN: "Part maximale d'énergies non renouvelable dans les bâtiments à construire", Berne, 2009.

7. MINERGIE, The MINERGIE-Standard for Buildings. Higher quality of life, lower energy consumption, Switzerland, October 2010.

8. Passivhaus Institut, Kriterien und Algorithmen für kühl-gemäßigte Klima, Zertifizierte Passivhaus Komponente-Balkonanschluss, Wärmebrückenarme Konstruktion-Balkonanschluss, 2013.

9. Swiss Standards Association, Swisscode SIA 180 Isolation thermique et protection contre l'humidité dans les bâtiments, Swiss Society of Engineers and Architects, 1999.

10. EN ISO 10211 Thermal Bridges in Building Construction: Heat Flows and Surface Temperatures. Detailed Calculations, 2007.

11. EN ISO 10077, Thermal Performance of windows, doors and shutters. Calculation of thermal transmittance, 2012.

12. IBO-Austrian Institute for Healthy and Ecological Building, Passivhaus-Bauteilkatalog, 3rd ed., SpringerWienNewYork.

13. F. Branco, A. Tadeu, and N. Simoes, Heat conduction across double brick walls via BEM, Building and Environment 39 (2004) 51-58.

14. EN ISO 10456, Building materials and products -- Hygrothermal properties -- Tabulated design values and procedures for determining declared and design thermal values.

15. T. Keller, F. Riebel, A. Zhou, Multifunctional Hybrid GFRP/Steel Joint for Concrete Slab Structures, Journal of Composites for Construction 10 (2006) 550-560.

16. K. Ghazi Wakili, H. Simmler, T. Frank, Experimental and numerical thermal analysis of a balcony board with integrated glass fiber reinforced polymer GFRP elements, Energy and Buildings 39, (2007) 76-81.
17. LESOSAI 7.2: Certification and thermal balance calculation for buildings, http://www.lesosai.com/en/index.cfm, 2013.
18. Swiss Standards Association, Cahier Technique SIA 2028 Données climatiques pour la physique du bâtiment, l'énergie et les installations du bâtiment, Swiss Society of Engineers and Architects, Zurich, Switzerland, 2008.
19. Website of http://www.sunearthtools.com/dp/tools/pos_sun.php?lang=fr (accessed 04.04.13).
20. R. Fraefel, La maison d'habitation MINERGIE, Aide à la planification destinée aux professionnels du bâtiment, MINERGIE 2004.
21. H. E. Mechri, A. Capozzoli, and V. Corrado, Use of ANOVA approach for sensitive building energy design, Applied Energy 87 (2010) 3073-3083.
22. H. Bülow-Hübe, Energy efficient window system: Effects on the energy use and daylight in buildings, in Department of Construction and Architecture, Lund University, Division of Energy and Building Design, Lund 2001.
23. K. L. Haglund, Decision-making Methodology & Selection Tools for High-performance Window Systems in U.S. Climates in: Proceedings of the Best2 on Building Enclosure Science and Technology, in Portland OR, April 2010.
24. P. Lyons and Associates, Report to Australian Building Codes Board on Optimum Window Size for Energy Efficiency: BCA Volume One, December 2008.
25. D. C Montgomery, Design and analysis of experiments, seventh ed, John Wiley and Sons, US, 2008.
26. M. Badache, S. Hallé, and D. Rousse, A full 3^4 factorial experimental design for efficiency optimization of an unglazed transpired solar collector prototype, Solar Energy 86 (2012) 2802-2810.
27. M. Ragonesi, U.-P. Menti, A. Tschui, B. Zurfluh et Bureau EHE, MINERGIE-P, first ed, MINERGIE, Switzerland.
28. Website of http://www.swiss-composite.ch/scs4/html/index.shtml?lang=en (assessed 15.03.2013).
29. Website of http://www.cabot-corp.com/Aerogel/Building-Insulation (assessed 15.03.2013).

3 Structural and thermal performance

3.1. Introduction

Against a background of increasingly strict sustainability requirements in our society, the reduction of the energy consumption of building stock represents a major challenge. As building stock accounts for almost 40% of total energy consumption in the European Union, the aim is to design all new buildings as nearly zero-energy buildings (NZEB) by the end of 2020[1]. One major cause of energy losses in buildings is thermal bridges in the building envelope, created by any interruption of the insulation layer or locations with reduced thermal resistance[2]. Up to 30% of total heat losses of buildings can occur through thermal bridges in particular cases[3].

A typical and frequent thermal bridge in building envelopes is caused by the penetration of the envelope by an internal concrete slab in order to create an external cantilevered balcony, as shown in Fig. 3.1[4,5]. The insulation layer is interrupted and a thermal break element is usually installed between the inner slab and the balcony to provide additional thermal resistance. However, the thermal insulation capability of such elements is much reduced compared to that of the surrounding wall, since they comprise stainless steel bars to provide structural continuity, i.e. transfer of exterior balcony bending moments and shear forces to the interior slab. Stainless steel bars, however, exhibit much higher thermal conductivity than commonly used insulating materials, such as mineral wool or polyurethane (PU), see Table 3.1. Although the penetrating total bar cross section is normally small (depending on the balcony span), thermal losses may still be considerable.

Authors: Kyriaki Goulouti, Julia de Castro, Thomas Keller

Composite Construction Laboratory CCLab, Ecole Polytechnique Fédérale de Lausanne EPFL.

Contribution: The main core of the paper was conducted by Kyriaki Goulouti (thermal simulations, mechanical experiments). The analysis was developed in collaboration with Prof. T. Keller.

The thermal performance of such thermal breaks can be evaluated by the linear thermal transmittance, ψ, defined according to ISO 10211:2007[6]. The value represents the heat losses through the elements in addition to the losses through the surrounding wall. In Switzerland, Swiss Code SIA 380/1[7] specifies a corresponding limit value of $\psi \leq 0.30$W/mK and target value of $\psi \leq 0.15$W/mK, the former being obligatory for all products on the market. In order to approach the target value with traditional thermal breaks (stainless steel bars), the possible balcony span is, in most cases, significantly reduced.

In recent years, attempts have been made to replace stainless steel bars with glass fiber-reinforced polymer (GFRP) composite components, whose thermal conductivity is much lower, see Table 3.1, to thermally improve this construction detail[4,8,9]. However, the comparatively low stiffness of GFRP materials results in a stiffness-driven thermal break design, in order to meet the deflection limits of the balcony. The required amount of GFRP material is thus increased, leading to an increase in cost. Furthermore, no appropriate anchoring of the upper GFRP tensile component has been developed; the required anchoring length of straight pultruded GFRP bars, for instance, is much longer than that of steel bars, hindering the easy handling and transportation of the prefabricated thermal breaks. Bars with hooked ends cannot be used because the elements cannot be threaded from the top into the pre-installed slab steel reinforcement (see structural concept description below).

In this work, a new approach has been pursued and a new FRP thermal break was conceived with superior thermal and structural performance compared to existing steel and GFRP elements. The aim was to develop a thermal break that can meet the target value of Swiss code[7] ($\psi \leq 0.15$W/mK) and nevertheless enables significant cantilever spans of up to 4.0m. The main novelty is the use of aramid fibers, which exhibit much lower thermal conductivity and higher stiffness than glass fibers, see Table 3.1. Furthermore, the development of more FRP material-tailored (and thus economical) structural components was the aim rather than purely substituting steel by GFRP bars. This paper describes the concept of the new thermal break and evaluates its thermal and structural performance through experimental and numerical investigations. The long-term effects such as creep and exposure to alkaline environments of the parts embedded in the concrete are also addressed.

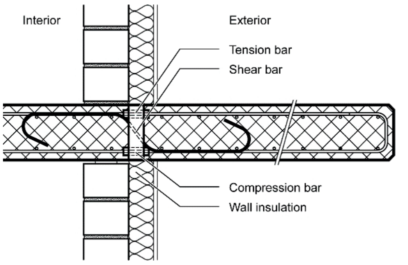

Figure 3.1. Traditional stainless steel thermal break for balconies[4].

3.2. Thermal and structural concept

3.2.1 Overview

The material selection for the new thermal break element was primarily driven by thermal performance criteria, i.e. the materials' thermal conductivity. In this respect, aramid fibers and aramid fiber-reinforced polymer (AFRP) composite laminates exhibit much better performance than glass fibers and GFRP laminates, see Table 3.1. However, aramid fibers have low compressive strength and their use for components subjected to high compressive stresses is limited[10], which is why glass fibers and GFRP laminates could not be completely excluded in the new design (see structural concept description below). However, GFRP materials still offer enhanced thermal behavior compared to stainless steel. An improvement of existing thermal breaks was also aimed at for the non-load-bearing insulation material of the element (between the adjacent concrete slabs) by selecting aerogel granulate[11], which offers a much better thermal performance than mineral wool or PU foam, see Table 3.1.

Table 3.1. Thermal conductivity of thermal break materials.

Material	*Thermal conductivity (W/mK)*
Stainless steel bars	15.0
Reinforced concrete	2.5
Glass fibers	1.0
Aramid fibers	0.04
Epoxy resin	0.52
GFRP laminate	0.70
Aramid laminate	0.10
Mineral wool	0.035
PU foam	0.028
Aerogel granulate	0.013

Aerogel data from[11], remaining data from[12]

The structural concept of the new thermal break is based on a simple N-shape truss system in which the load-bearing components of the element are incorporated and transfer the bending moments and shear forces from the balcony cantilever to the inner slab, as shown in Fig. 3.2. The negative bending moment is transferred by an upper tensile and lower compressive force (equal in magnitude), while the shear force is transferred by a diagonal compression strut. Based on this concept, an AFRP loop component was conceived to bear the upper tensile force. Furthermore, a combined A/GFRP hexagon component, consisting of an upper AFRP or GFRP sandwich and a lower short and compact GFRP bar, was developed to transfer the two compressive forces from shear and bending, as described in detail below and shown in Figs. 3.2 and 3.3a. Loop and hexagon components are assembled together in a prefabricated, 50mm-wide PVC box, which is subsequently filled with the aerogel granulate. The box is composed of three parts and the height of the middle part (which does not contain any component penetrations) can be adapted to the slab thickness. On the construction site, the prefabricated thermal break (aerogel-filled box with loops and hexagons) can then easily be inserted from the top into a prepared recess in the already installed concrete steel reinforcement, as shown in Fig. 3.3b. The spacing of the loops and hexagons, along the balcony length depends on the load level, i.e. the cantilever span of the balcony. The basic thermal break unit is 150mm wide, comprising one loop and two hexagon components; Fig. 3.3 shows the densest arrangement with the highest load-bearing capacity. The short GFRP bar of the hexagon can be arranged flush with the bottom side of the slab when no fire safety is required, i.e. in cases where the balcony does not represent an emergency exit (which is normally the case). Otherwise, the component can be raised by 10mm to provide space for a fire protection layer, as shown in Fig. 3.2.

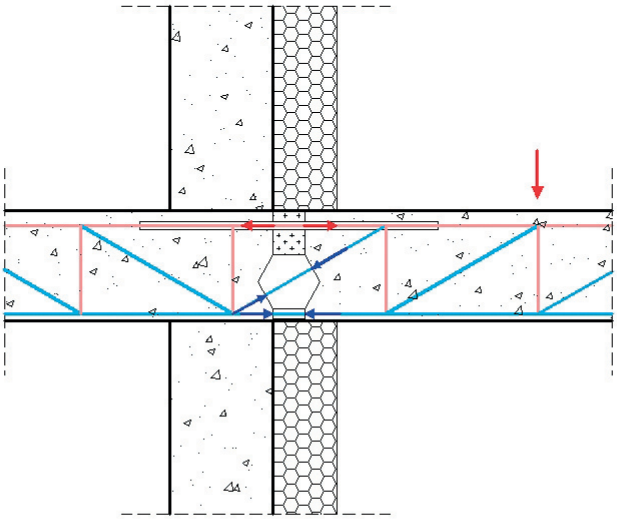

Figure 3.2. Structural concept of new A/GFRP thermal break.

In the pre-design phase, the dimensions of the A/GFRP components, i.e. the cross-sectional areas in particular, used in the following were derived from theory and manufacturer datasheets. Since AFRP and GFRP composites are brittle materials, the AFRP loop and A/GFRP hexagon components were designed in such a way that simultaneous ductile concrete failure occurs in the upper loop anchorage zone and lower compression contact zone of the short bar element. The corresponding concrete strength was estimated based on the experimental results obtained for a hybrid GFRP/steel thermal break which had a similar short GFRP compression element at the lower concrete edge[4]. A concrete confinement factor of k_c=1.70 was adopted in the pre-design phase, due to the similar local pressure exerted by the compression element on the concrete surfaces[4].

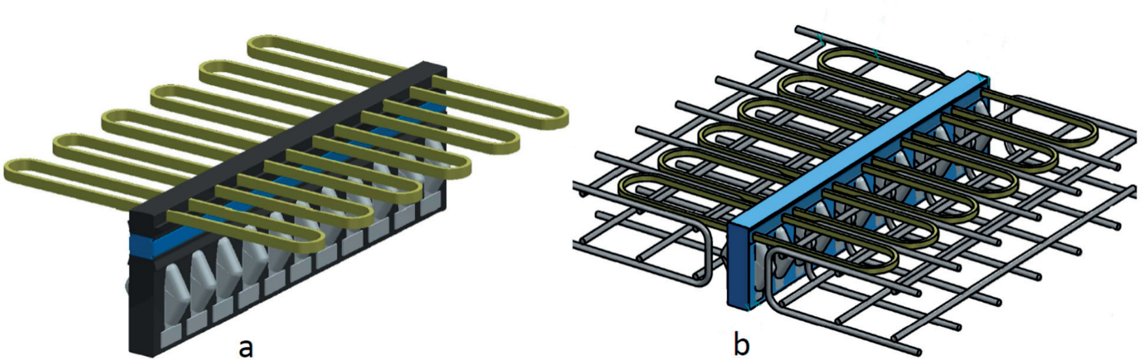

Figure 3.3. New thermally-insulated A/GFRP thermal break: a) prefabricated element, b) element placed from top into pre-installed concrete slab reinforcement.

3.2.2 Loop component

The AFRP loop shape was selected in order to have a self-anchored component with relatively short cantilevered length on both sides of the box for transportation and installation purposes; the loop dimensions are shown in Fig. 3.4. The loop width of 120mm allows the placing of the component between two parallel steel bars in the uppermost fourth concrete reinforcement layer, which normally have a spacing of 150mm, see Fig. 3.3b. The nominal cross section is 2x(10x15)mm^2 and consists of 110 loops of a Kevlar-49 roving of 805tex. The matrix is an Epikote epoxy resin, MGS RIM 235, with an Epikure curing agent RIMH 236. The resulting laminate has a nominal fiber volume fraction of 41%, a calculated elastic modulus of 43 GPa and a tensile strength of 790-900 MPa[12]. The loops were manufactured (at this project stage) by hand-wrapping the resin-wetted roving around a corresponding mold. In a later stage, the components will be produced by automated filament winding, the best solution according to an evaluation of potential manufacturing processes.

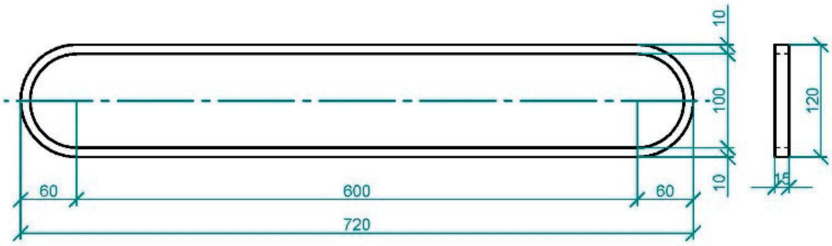

Figure 3.4. AFRP loop; dimensions in (mm).

3.2.3 Hexagon sandwich component

The selection of the hexagon shape to transfer the shear-compression diagonal force was mainly based on the required fully automated manufacturing process, in order to produce a large number of components rapidly and economically. As for the loop (filament winding), tape winding was shown by a corresponding evaluation to be the best solution.

The hexagon sandwich is composed of a hexagonally-shaped PU foam element around which three laminates are wound in three directions, each arranged at a 60° angle to the previous one and perpendicular to two adjacent parallel sides of the hexagon, see Fig. 3.5a. To assure the alignment of the layers and correct superposition, corresponding recesses are introduced into the foam, see Fig. 3.5b. Adhesively bonded to the lower hexagon side and wrapped into the outermost laminate is a short and compact GFRP bar of a 30x30mm^2 cross section, which transfers the compression force of the bending moment between the two opposite concrete faces.

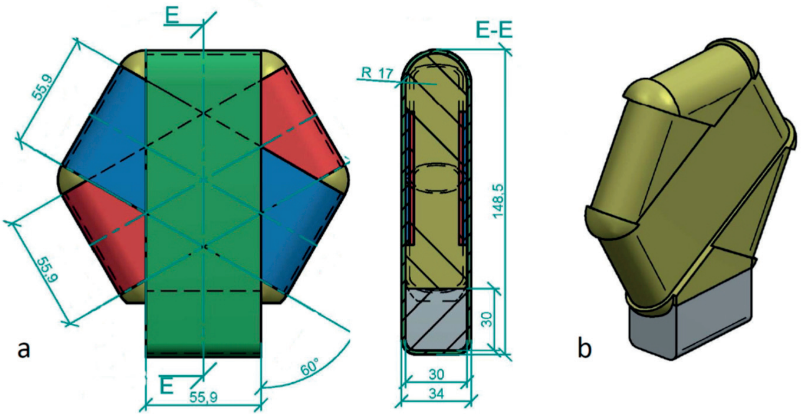

Figure 3.5. A/GFRP hexagon sandwich: a) tape layers, b) PU foam core and adhesively-bonded GFRP UD compression bar, dimensions in (mm).

The composition, dimensions and particular shape of the hexagon sandwich resulted from a multi-criteria optimization in the pre-design phase. The hexagon side length is identical to the box/thermal break width. The former is limited by the slab thickness (the hexagon axis should match the truss diagonal as in Fig. 3.2) and the latter by the required insulation thickness, in order to achieve adequate insulation capacity. The hexagon thickness of 30mm and sandwich composition resulted from the required width of the short compression bar (see below) and buckling stability of the sandwich in the direction of the compression diagonal. A semicircular shape was selected for the edges of the sandwich, which is easy to manufacture by the tape winding process and favorably responds to the hydrostatic pressure exerted by the concrete on the embedded ends of the compression diagonal region of the sandwich. The compression diagonal crossing of the two other laminates further contributes to the stabilization of the compressed laminates against wrinkling[13]. The cross-sectional dimensions of the short quadratic compression bar was a compromise between i) a minimum height, to avoid considerably reducing the bending lever arm, ii) a minimum width, to avoid significantly enlarging the sandwich element, iii) the requirement that ductile concrete failure should occur first, and iv) the requirement that the stresses due to the permanent load should not exceed 20% of the strength in order to prevent creep rupture.

Since the shear forces are much smaller than the compressive forces from the bending moments, the use of aramid fibers for the shear-compression diagonal still remained a feasible option and both aramid and glass fibers were thus considered for the winding of the hexagon in the experimental work. The nominal thickness of each of the three overlapping laminates is 2.0 mm. The GFRP laminates are composed of 12 layers of an E-glass UD-tape of 200g/m^2 weight each, while 12 layers of a Kevlar-49 UD-tape of 100 g/m^2 weight are used for the AFRP laminates; the epoxy resin was the same as that selected for the loops. The resulting fiber volume fractions are 47% (GFRP) and 41% (AFRP), the calculated elastic moduli 36 GPa (GFRP) and 43 GPa (AFRP), and the compression strengths 480-600 MPa (GFRP) and 180-190 MPa (AFRP)[12], respectively. The laminates were manually wound around the foam core at this stage and cured at ambient temperature. The complex foam shape was manufactured by fabricating a corresponding mold and filling it with expandable PU foam. Foam cores of three different densities were produced; the corresponding mechanical properties are summarized in Table 3.2.

Due to the high compressive forces resulting from the bending moments, glass fibers had to be selected for the short compression bar, thus excluding the use of aramid fibers. The element is composed of UD E-glass fiber rovings and the same epoxy resin is used as for the loop. The fiber volume fraction is 50% and the corresponding elastic modulus 38 GPa. A bar of around 1m length was produced by hand lay-up, from which the components were cut. In future the components will be produced by a fully automated pultrusion process.

Table 3.2. Hexagon sandwich: PU foam properties (manufacturer data).

Foam density (kg/m³)		***E-modulus (MPa)***	***G-Modulus (MPa)***	***Compressive strength (MPa)***	***Shear strength (MPa)***
H	**145±5**	55	21	1.40	0.70
M	**131±4**	48	18	1.22	0.63
L	**98±2**	33	13	0.84	0.45

3.3. Thermal break performance

The thermal performance of thermal breaks for balconies is evaluated by the linear thermal transmittance, ψ, obtained according to ISO 10211:2007[16] as follows:

$$\psi = L_{3D} - \sum_{j=1}^{N_j} U_j \cdot A_j\,, \quad L_{3D} = \frac{\Phi}{\theta_i - \theta_e} \quad (1)$$

where L_{3D} =thermal coupling coefficient from three-dimensional calculation, U_j = thermal transmittance of wall component j, A_j =area of wall component j, Φ =heat flow rate, θ_i =internal temperature, θ_e =external temperature. The L_{3D}-values are obtained from a three-dimensional numerical analysis under steady state conditions[6]. Accordingly, four numerical models were established[6] for a thermal break unit spacing of 150, 300 and 450mm, and a basic case without structural components (aerogel insulation only). Ansys Fluent 15 was used for the thermal simulation; symmetry conditions were applied and, based on a sensitivity analysis, a combined structured/unstructured mesh was selected, see Fig. 3.6. The concrete slab thickness was 0.20m. Depending on the fiber volume fraction, thermal conductivities of 0.1 and 0.6 W/mK were applied for the AFRP and GFRP laminates. Two different U-values were selected for the walls: U=0.10W/m^{2}K and 0.20W/m^{2}K (since the ψ-values depend on the U-values according to Eq. (1)). Convective boundary conditions h_{in}=7.7W/m^{2}K and h_{out}=25W/m^{2}K and a temperature difference θ_i -θ_e =30°C were applied (corresponding to θ_i=20°C and θ_e=-10°C).

The resulting linear thermal transmittance values, as a function of the fiber type in the hexagon component (A/GFRP or G/GFRP), unit spacing and U-value are shown in Fig. 3.7. The A/GFRP hexagon values are significantly below the G/GFRP hexagon values and meet the target value of $\psi \leq 0.15$W/mK according to Swiss Code SIA 380/1[7]. The curves of the pure aerogel insulation show the significant effect of the U-value on the results. Furthermore, Fig. 3.8 shows the temperature distribution across the wall. The internal superficial temperature remains high (close to 19°C or 292K), higher than the dew point critical temperature, thus avoiding possible condensation problems. These results prove the excellent thermal performance of the new A/GFRP thermal break.

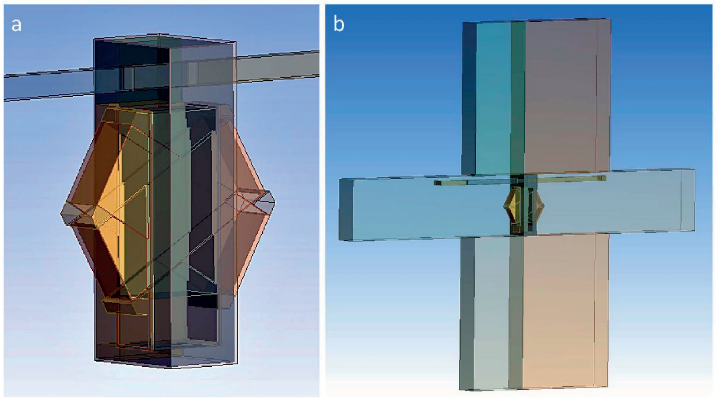

Figure 3.6. A/GFRP thermal break: FE-model for thermal performance evaluation (0.15m unit spacing), a) thermal break model (one half-unit), b) element integrated into slab-wall segment acc. to ISO 10211:2007[6]

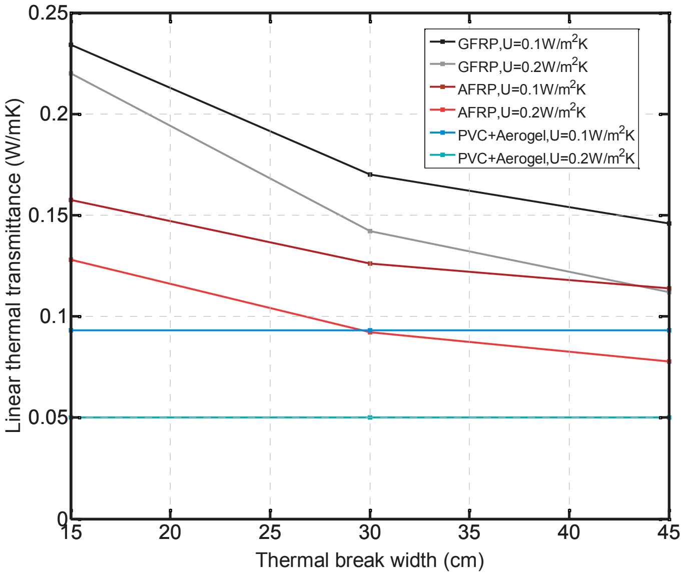

Figure 3.7. A/GFRP thermal break: linear thermal transmittance as function of element unit spacing (15, 30 and 45cm), hexagon fiber type and wall *U*-value.

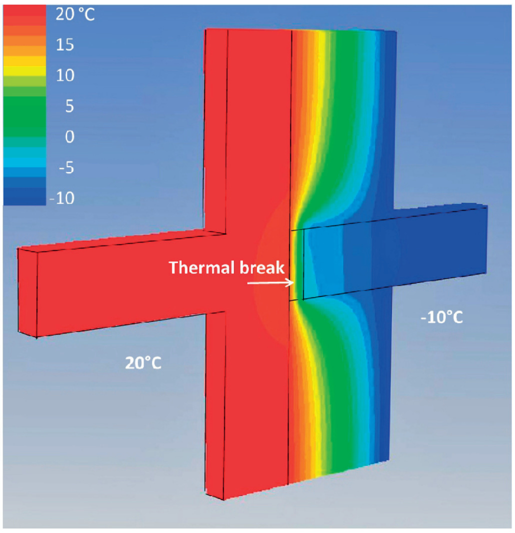

Figure 3.8. A/GFRP thermal break; temperature field (in °C) in connector zone.

3.4. Structural component performance

3.4.1. Hexagon diagonal-compression experiments and results

3.4.1.1. Experimental set-up

The short- and long-term load-bearing behaviors of the hexagon sandwich shear-compression diagonal were experimentally investigated. Quasi-static, creep and durability experiments were performed. In all experiments, the shear-compressive diagonal was subjected to axial compressive loading. A 15° deviation of the axis of the shear-compression strut from the hexagon diagonal (i.e. a flatter diagonal) was also considered, since the behavior might change from fiber-dominated to matrix-dominated due to the off-axis loading. The hexagon was always oriented in the most unfavorable way, i.e. the second/ intermediate (and not the innermost) laminate was loaded. Hexagons comprising AFRP and GFRP laminates and three different foam densities were investigated; a specimen with aramid fibers is shown in Fig. 3.9a.

Two different load introduction set-ups were used to simulate the hydrostatic pressure of the concrete on the embedded semicircular hexagon parts, see Fig. 3.10. In set-up S1 (Fig. 3.10a), the pressure was applied by two steel elements with semicircular recess of the same 55.9mm width as the laminate, while in set-up S2 (Fig. 3.10b) the steel elements were enlarged to cover the same hexagon parts as inside the concrete slab. Set-up S3 (Fig. 3.10c) corresponded to S2, but was turned by the aforementioned angle of 15°. To smoothly transfer the load from the steel elements to the hexagon laminates, intermediate epoxy adhesive layers (Sikadur-30 from Sika AG, Switzerland) of 4-5mm thickness were applied onto the embedded laminate parts, as shown in Fig. 3.9b for S1 and Fig. 3.9c for S2, respectively. Set-up S1 was initially used for the quasi-static experiments. Since the results exhibited large scatter in the case of the ultimate load, set-up S2 was developed, which also better represented the actual loading situation. However, for the creep and durability experiments, set-up S1 (with smaller epoxy layer area) was used to minimize the potentially negative effects of the epoxy layers (additional creep and water uptake) on the results.

The compressive load was applied by a W+B servohydraulic universal testing machine of 500kN load capacity. The experiments were performed under displacement control at a rate of 0.02mm/s in three to five cycles up to failure. The axial deformation of the diagonal was measured using two linear voltage displacement transducers (HBM LVDTs, gage length 20mm), one on each specimen side, see Fig. 3.10.

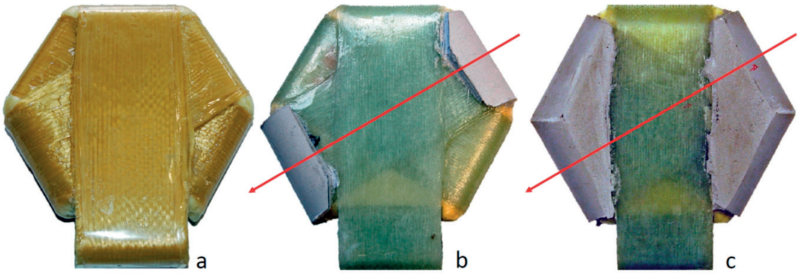

Figure 3.9. A/GFRP hexagon sandwich a) AFRP specimen, b) GFRP specimen with additional epoxy layers on embedded laminate parts for set-up S1, c) for set-ups S2 and S3.

Three creep experiments were performed in a conditioned room (20°C, 70%RH). Set-up S1 was installed in a cage allowing the application of a tensile force to the system, see Fig. 3.11. Three different loads were applied, 15, 20 and 25kN, during 30 days each. The experiments at 15kN and 25kN were performed using high foam density specimens while the intermediate 20kN load was applied on an intermediate foam density specimen. The selected load range corresponded to approximately 20% of the ultimate load of the quasi-static experiments (the creep rupture limit mentioned above). In a fourth creep experiment, the worst case was simulated by applying a 15kN load on a low foam density specimen at the deviated angle of 15° (using fixture S3), thus simulating a more matrix-dominated behavior. Furthermore, in view of the sensitivity of GFRP materials to the alkaline concrete environment, four specimens (two composed of high and two of low foam density) were preconditioned in alkaline water of 30°C and pH=13.5 for up to eight months. After the creep exposure and durability preconditioning, all specimens were loaded to failure as in the above-described quasi-static experiments using the corresponding set-ups S1, S2 or S3.

The experimental matrix, indicating all parameter combinations and numbers of specimens, is shown in Table 3.3. The specimen code, e.g. 'HGH1-1', is comprised as follows: 'H'=hexagon, 'G'=GFRP wrapping, ‘H’=high foam density (145kg/m^3, see Table 3.2), ‘1’=S1, ‘-1’=specimen no. 1 of this parameter combination (the latter may be extended by ‘C’=creep or ‘W’=water).

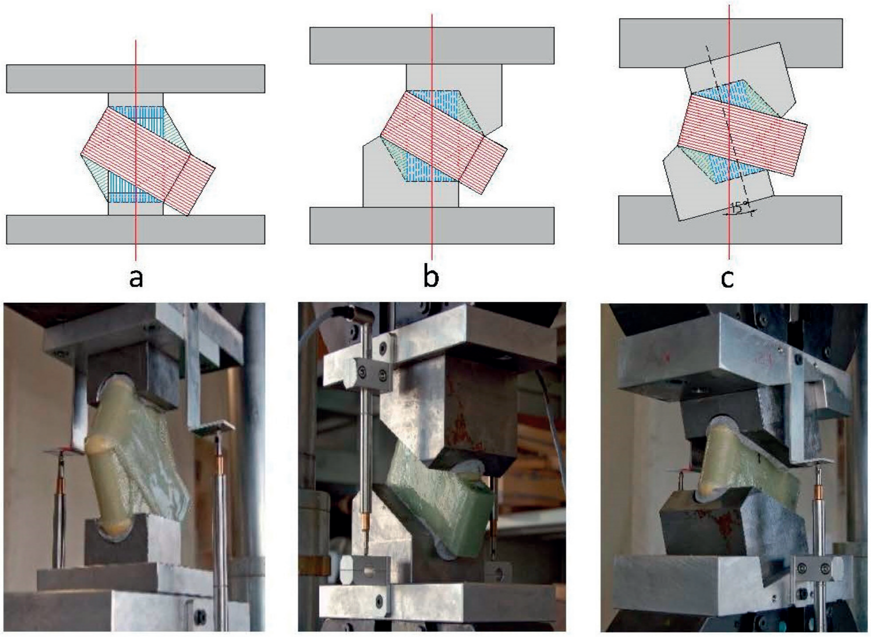

Figure 3.10. A/GFRP hexagon sandwich: compression experiment set-up, a) S1, b) S2, c) S3 (red line indicates machine load axis).

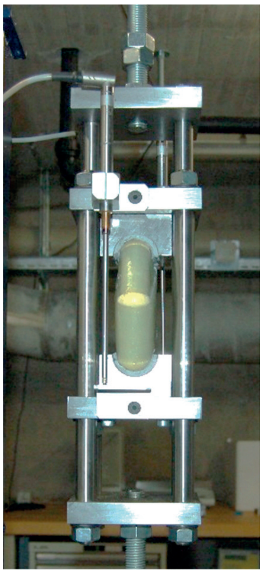

Figure 3.11. A/GFRP hexagon sandwich: creep experiment, set-up S1.

Table 3.3. A/GFRP hexagon sandwich: overview of set-ups and experimental results.

Specimen	*Fiber type*	*Foam density (kg/m^3)*	*Set-up*	*Stiffness (kN/mm)*	*Ultimate load (kN)*	*Deformation at ultimate load (mm)*
HGH1-1	Glass	145	S1	100	82	0.90
HGH1-2	Glass	145	S1	99	61	5.76
HGH1-3C*	Glass	145	S1	80	58	0.73
HGH1-4C*	Glass	145	S1	55	70	1.27
HGH1-5W**	Glass	145	S1	49	57	1.36
HGM1-1C*	Glass	131	S1	63	64	1.39
HGL1-1W**	Glass	98	S1	31	46	1.47
HAL1-1	Aramid	98	S1	72	44	0.97
HGH2-1	Glass	145	S2	88	115	1.50
HGH2-2	Glass	145	S2	91	104	1.63
HGH2-3W**	Glass	145	S2	66	86	1.24
HGM2-1	Glass	131	S2	70	72	1.04
HAM2-1	Aramid	131	S2	82	66	1.23
HGL2-1	Glass	98	S2	68	71	1.62
HGL2-2	Glass	98	S2	48	58	1.15
HGL2-3W**	Glass	98	S2	28	41	1.47
HAL2-1	Aramid	98	S2	55	56	1.68
HAL2-2	Aramid	98	S2	84	65	1.19
HGH3-1	Glass	145	S3	81	147	2.28
HGL3-1	Glass	98	S3	79	105	1.73
HGL3-2C*	Glass	98	S3	70	73	1.38

* Subsequent to creep experiment

** Subsequent to alkaline water exposure

3.4.1.2. Experimental results

The load-displacement responses of the quasi-static experiments are shown in Fig. 3.12. Only the curves of the S2 set-up are shown since, as mentioned above, the S1 set-up produced a large scatter in the case of ultimate loads. The S3 set-up curves were similar to those of the S2 set-up. The stiffnesses of the initially linear curve segments, ultimate loads and deformations at ultimate loads for all set-ups are listed in Table 3.3.

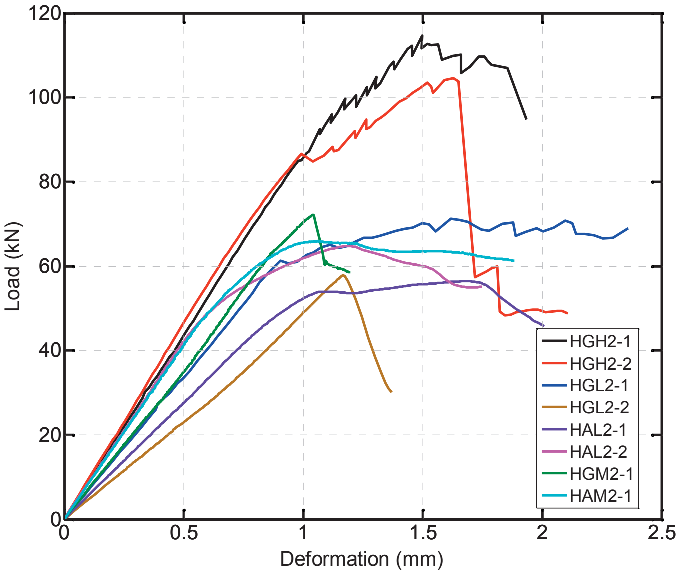

Figure 3.12. A/GFRP hexagon sandwich: load-deformation responses in S2 experiments.

The S2 responses were initially linear and started to become non-linear in the 0.6-0.8mm range of deformation (Fig. 3.12). Subsequently, in most cases, the specimens exhibited significant deformations until reaching the ultimate load. Stiffness and ultimate load values were correlated with the core foam density, as shown in Fig. 3.13; both show a non-linear increase with increasing density. Due to the higher laminate stiffness, AFRP specimens had a slightly stiffer response than GFRP specimens of the same density. However, the AFRP ultimate loads were slightly lower than the corresponding GFRP ultimate loads. The S3 off-axis specimens exhibited significantly higher ultimate loads than the S2 specimens of the same density, see Table 3.3. This can be explained by the fact that the loaded laminate width was larger in the S3 than in the S1 and S2 set-ups, see Fig. 3.10. The experimental results exhibited significant scatter, which was mainly attributed to the hand-layup fabrication of the complex hexagon specimens. Nevertheless, the results were consistent, i.e. the AFRP specimens exhibited higher stiffness but lower compression strength than the GFRP specimens. The differences, however, were small and thus indicated that aramid could also be used for the shear-compression diagonal.

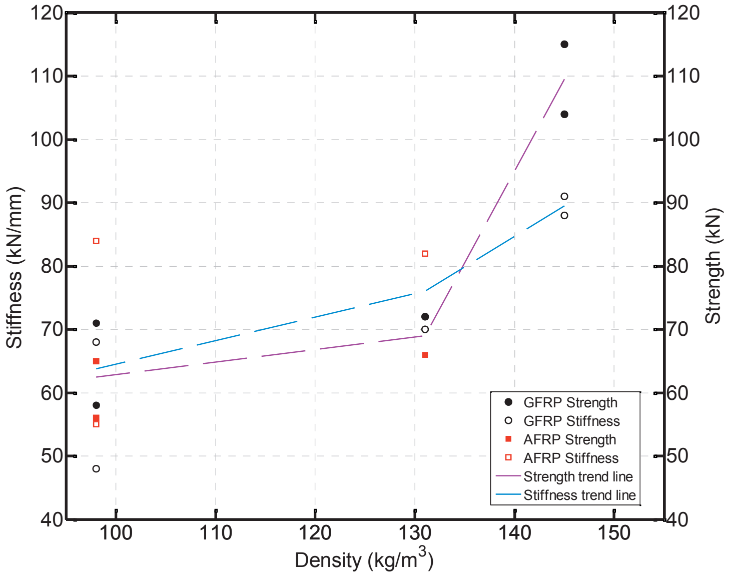

Figure 3.13. A/GFRP hexagon sandwich: stiffness and ultimate load vs. density relationships of S2 experiments.

The failure mode was identical in all three set-ups, independent of fiber type and foam density, see Fig. 3.14. In all specimens, failure occurred along the transition lines from the semicircular to the straight laminate parts (transverse to the fiber direction) on both ends of the diagonal. Along these transition lines, the total laminate thickness doubled due to the superposition of the inner and intermediate (loaded) laminate on one side and of the intermediate and outer laminate on the other side. Depending on the degree of confinement by the steel fixture, two slightly different failure modes occurred. At partial confinement, a type of laminate kinking was observed at the step from the single to the double laminate thickness, see Fig. 3.14a. At full confinement, the failure mode consisted of wrinkling in the curved part, see Fig. 3.14b. Partial confinement was always present at one edge of the transition line, independent of the set-up type, and failure may thus have always initiated at this location.

The experimental creep results for the three axially loaded hexagons during the 30 days are shown in Fig. 3.15a. The density effect is clearly visible in the logarithmic plot of the creep deformation (without the elastic part) in Fig. 3.15b. The HGM1-1C specimen, loaded at 20kN, (intermediate foam density) exhibited a higher creep rate than specimens HGH1-3C/4C (high foam density), loaded at 15/25kN, which exhibited a similar creep rate. Furthermore, the results for set-up S3 at 15° are shown (specimen HGL3-2C). Although the specimen was loaded in the off-axis direction and thus a higher creep rate was expected, its response was similar to that of HG1H-3C loaded at 0°. The unconfined length of the off-axis specimen, however, was shorter and the creep fostering factors (matrix-dominated behavior and low foam density) seemed to have been compensated by the creep reducing factors (shorter unconfined length).

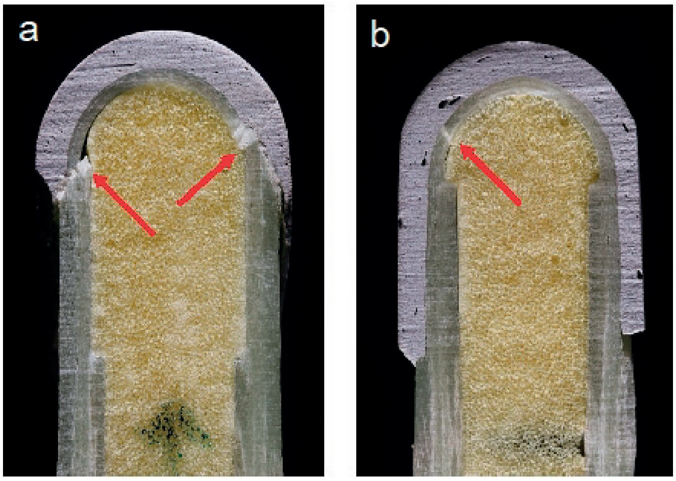

Figure 3.14. A/GFRP hexagon sandwich: failure mode a) partly confined; b) fully confined.

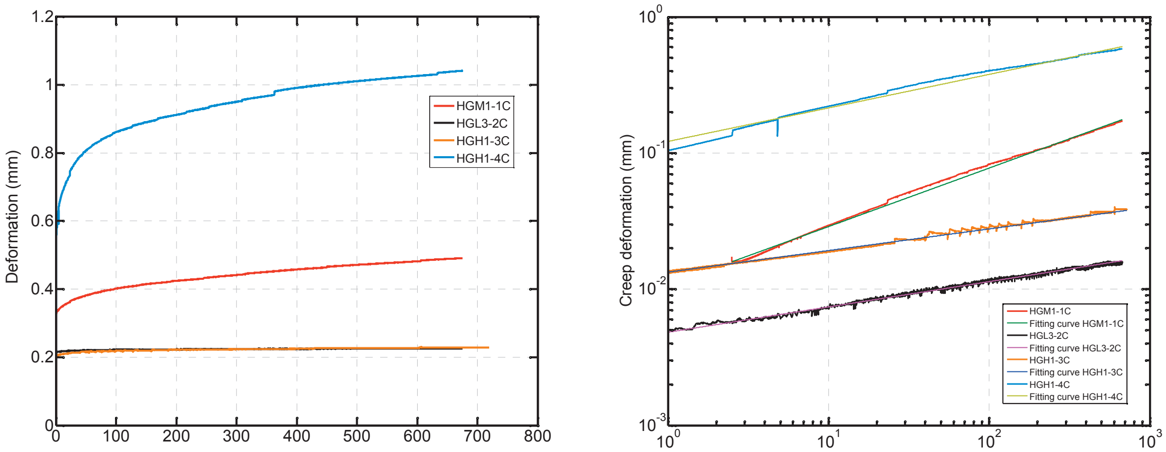

a **b**

Figure 3.15. A/GFRP hexagon sandwich: experimental creep results at different load levels, a) total deformations on linear scale, b) creep deformations on log scale and model.

General power laws according to Eq. (2) were fitted to the experimental data in order to extrapolate the measured creep deformations up to the operating life in building construction, i.e. 50 years in most cases:

$$\delta = \delta_0 + m \cdot t^n \quad (2)$$

where δ = total deformation after time, t; δ_0 = elastic deformation; m and n = fitting parameters. The modeling results are also shown in Table 3.4 and Fig. 3.15b and matched the experimental results reasonably well. The resulting long-term (50 year) creep deformations were small. After the creep experiments, the specimens were loaded to failure. The resulting stiffness and strength were not affected by the creep loading; the results were within the scatter range of the quasi-static results, see Table 3.3.

Table 3.4. Creep parameters and results according to Eq. (2).

Specimen	*Load (kN)*	*m*	*n*	δ_0 *(mm)*	δ_{50} *(mm)*
HGH1-3C	15	0.013	0.16	0.19	0.30
HGH1-4C	25	0.120	0.25	0.46	3.55
HGM1-1C	20	0.010	0.43	0.32	3.00
HGL3-2C	15	0.005	0.19	0.21	0.26
LA-9C	20	0.040	0.14	1.18	1.42

The preconditioning in alkaline water had a significant effect on stiffness and strength. The high foam density specimens (HGH1-5W, HGH2-3W) exhibited average stiffness and strength losses of 34% and 19% respectively, compared to the corresponding unconditioned specimens. The effect on the low foam density specimens (HGL1-1W, HGL2-3W) was more significant; the average losses were 52% (stiffness) and 36% (strength). It should however be considered that these components will never be fully immersed in alkaline water and are subjected to direct alkaline water contact only during the pouring and setting of the concrete.

3.4.2. Hexagon bar-compression experiments and results

Quasi-static experiments were performed to evaluate the stiffness of the GFRP compression bar, which is required for the serviceability verification. No other investigations were performed since the axial compressive stresses in the component are small at concrete failure, and thus the sensitivity to creep and alkaline pore water effects is also small – see the results for a similar GFRP component[14]. Four prismatic specimens of $12x12x50mm^3$ were cut from the UD GFRP compression bar and axially loaded to failure under displacement control at a rate of 0.02mm/s. The axial strains were measured by two strain gages (HBM, 120LY61). The load-strain responses were linear up to failure and the resulting elastic modulus and nominal axial strength were 44±6.5GPa and 350±66MPa, respectively.

3.4.3 Loop tensile experiments and results

3.4.3.1. Experimental set-up

As for the hexagon components, quasi-static, creep and durability experiments were performed on the AFRP loops. They were subjected to an axial tensile load in all cases, either without preconditioning, during creep or after preconditioning in the same alkaline bath as described above. The experimental set-up of the tensile experiments is shown in Fig. 3.16a. The tension load was applied through two steel sheaves with an Amsler or a Zwick servohydraulic universal testing machine of 1000kN load capacity, at a loading rate of 500N/s in two to four cycles up to failure. The axial deformations were measured with two LVDTs (HBM, gage length 50mm, one on each specimen side), and axial strains were recorded via four strain gages (HBM 120LY61), applied at mid-height on each specimen.

One creep experiment was performed under the same climatic conditions as for the hexagon components. A load of 20kN was applied during 176 days. Furthermore, one loop was immersed in the same alkaline bath as the hexagon components during 230 days and subsequently loaded to failure.

3.4.3.2. Experimental results

The load-displacement responses of selected AFRP loops are shown in Fig. 3.17. The behavior was linear up to a brittle failure. The stiffnesses, ultimate loads and ultimate strains of all specimens are listed in Table 3.5. The results present a certain scatter, attributable to the manual winding of the roving across the 15mm cross section width, which led to small roving angle deviations from the loop axis. Failure was always initiated at the transition point from the semicircular to the straight part of the loop and occurred suddenly through fiber failure and delamination, see Fig. 3.16b.

The creep results during the period of 176 days are shown in Fig. 3.18. The same general power law as shown in Eq. (2) was fitted to the experimental data. The modeling results, shown in Table 3.4 and Fig. 3.18, matched the experimental results reasonably well. The extrapolation up to 50 years resulted in insignificant long-term creep deformations. Post-creep stiffness and strength were not influenced by the creep loading, see Table 3.5 (specimen LA-9C); they were within the scatter range of the quasi-static results.

The alkaline water exposure during 230 days caused no discernible decrease in stiffness and strength, see Table 3.5 (specimen LA-10W), and the results were again within the scatter range of the unconditioned specimens.

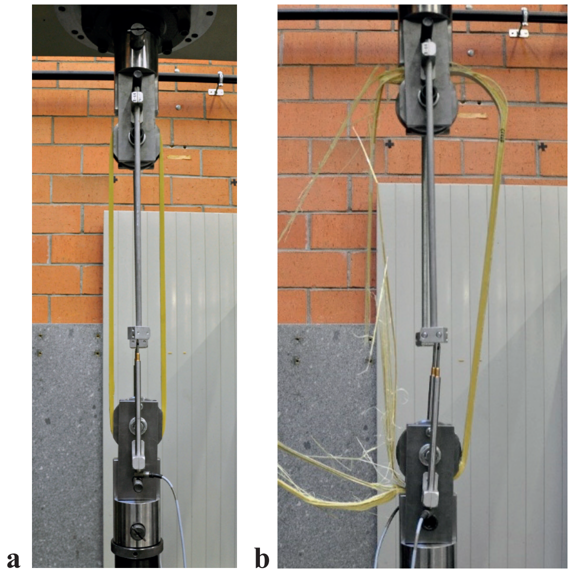

Figure 3.16. AFRP loop: a) tension experiment set-up and b) failure mode.

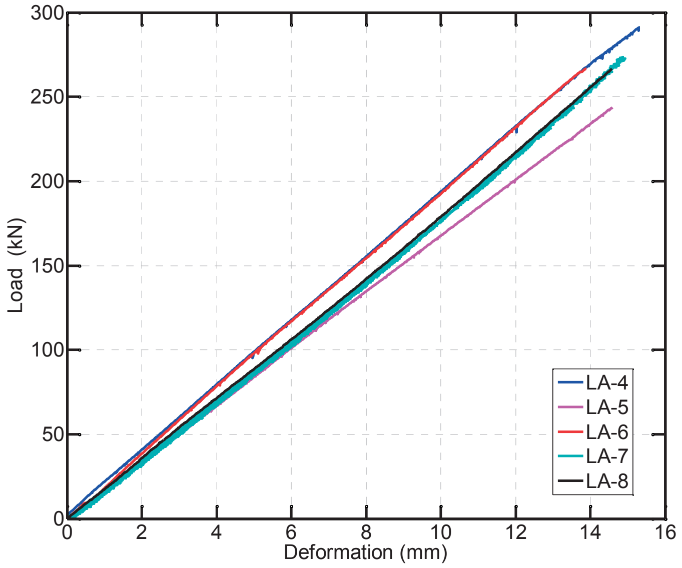

Figure 3.17. AFRP loop: load-deformation responses.

Table 3.5. AFRP loop: overview of experimental results.

Specimen	*Stiffness (kN/mm)*	*Ultimate load (kN)*	*Ultimate strain (%)*
LA-1	n/a	261	1.63
LA-2	n/a	315	1.72
LA-3	n/a	271	1.95
LA-4	20.0	291	1.72
LA-5	16.9	244	1.85
LA-6	20.0	267	1.68
LA-7	17.2	273	1.81
LA-8	17.2	267	n/a
Average LA1-8	18.3±3.2	274±42	1.77±0.22
LA-9C*	19.4	304	n/a
LA-10W**	18.1	251	n/a

* Subsequent to creep experiment

**Subsequent to alkaline water exposure

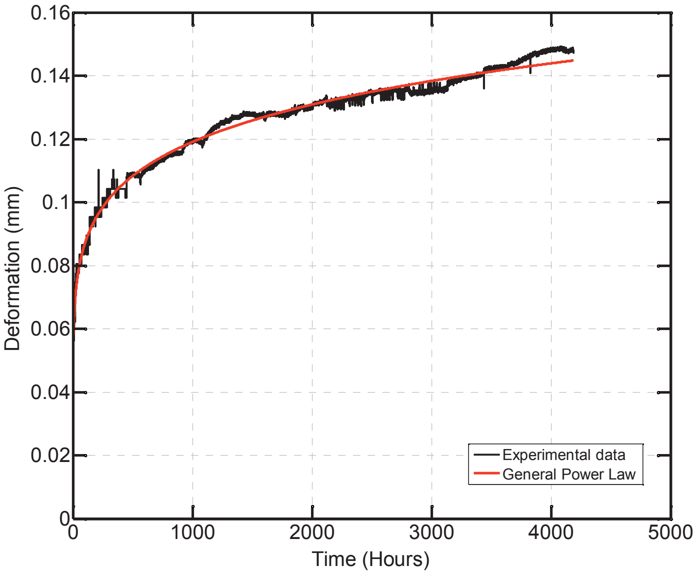

Figure 3.18. AFRP loop: experimental elastic and creep deformations and model (m=0.040, n=0.14).

3.5. Discussion

The design of such thermal breaks includes the verification of the ultimate limit state (structural safety) and serviceability limit state[15]. In the pre-design, the dimensions of the AFRP loop and the short GFRP bar of the hexagon were derived based on the intention to produce a ductile concrete failure, as described above. In the following, it is demonstrated that the intended ductile failure occurs and the serviceability requirements for the targeted 4.0m balcony are met, if the aforementioned k_c-factor (1.70) and a typical concrete prism strength of f_c=40MPa[4] are adopted.

3.5.1 Verification of concrete failure

3.5.1.1 Loop

The concrete resistance at the curved loop-anchor interface, F_{cL}, can be estimated based on Barlow's formula:

$$F_{cL} = f_c \cdot k_c \cdot \frac{d_m}{2 \cdot t} \cdot A \tag{3}$$

where d_m=average loop diameter (110mm), t=loop thickness (10mm), A=loop cross section (300mm^2). The resulting value of 112kN is 59% lower than the average loop ultimate load of 274kN (Table 3.4), which confirms that the targeted concrete failure will occur.

3.5.1.2 Compression bar

The concrete resistance at the interface to the compression bar, F_{cB}, is:

$$F_{cB} = f_c \cdot k_c \cdot A \tag{4}$$

where A=bar cross section (900mm^2). The resulting concrete resistance of 61kN is only 17% of the average bar ultimate load of 315 kN, which confirms the targeted concrete failure. The bar cross section seems overdesigned, but it could not be significantly reduced due to the creep rupture limit (see above). The concrete resistance at the bar interface is approximately half of the concrete resistance at the loop anchorage (112kN), which is why one loop and two hexagons are combined in one thermal break unit to transfer the bending moment.

3.5.1.3 Hexagon diagonal

Based on the same Eq. (3), the concrete resistance at the hexagon-diagonal interface, F_{cD}, can be obtained. Using d_m=28mm, t=2mm, and A=2·55.9·2=223.6mm^2 results in F_{cD}=106kN, which is approximately 40% higher than the average experimental ultimate loads, see Table 3. The hexagon diagonal will thus fail before concrete failure occurs. This has to be taken into account in the thermal break and balcony design, i.e. ductile concrete bending failure has to occur before brittle A/GFRP shear failure.

3.5.2 Serviceability verification

The verification of the serviceability limit state comprises, in particular, verification of the balcony deflection. In the following, the maximum span, L, is estimated based on the deflection limit of $2L/350$ for such balconies[15]. This limit has to be met for short-term loads; deflections due to permanent loads (including creep) are normally cambered.

The maximum balcony deflection at the cantilevering edge, δ, is composed of the reinforced concrete slab deflection, δ_S, and the deflection due to the rotation, φ_C, in the thermal break:

$$\delta = \delta_S + \varphi_C \cdot L \leq \frac{2L}{350} \tag{5}$$

The concrete slab deflection caused by a uniformly distributed load, q (assumed as being 1.5kN/m^2 according to SIA261:2003[16]), and a concentrated load, Q (1kN[16]), at the free edge, is:

$$\delta_S = \frac{L^3}{E_S \cdot I_S} \cdot \left(\frac{q \cdot L}{8} + \frac{Q}{3} \right) \tag{6}$$

where E_S=concrete elastic modulus (assumed as being 20GPa and thus taking cracking into account), I_S=h^3/12 (for a 1.0m width), h=slab thickness (assumed as being 0.30m).

The rotation in the thermal break is primarily caused by the elongation of the loop, which occurs along the entire length of the loop due to the absence of any significant bond between the straight smooth loop surface and the concrete. The shortening of the short compression bar and the compression diagonal (the latter producing only a small vertical offset of the slab) are negligible compared to the loop elongation, Δl_L, which is:

$$\Delta l_L = \frac{q \cdot L^2 + 2 \cdot Q \cdot L}{2 \cdot 0.85h} \cdot \frac{l_L}{A_L \cdot E_L / s} \tag{7}$$

where the first term represents the tensile force in the loop assuming a lever arm of $0.85h$, and l_L=loop length (720mm), A_L=loop cross section (300mm^2), E_L=loop elastic modulus (43GPa), s=unit width (150mm). The rotation in the thermal break is then approximately:

$$\varphi_C = \frac{\Delta l_L}{0.85h} \tag{8}$$

Eq. (5) is fulfilled for a maximum span of 6.1m, which is much greater than the targeted span of 4.0m. However, 78% of the deflection results from the rotation in the thermal break.

3.6. Conclusions

The thermal and structural concept of a new highly insulated balcony thermal break is presented, together with the short- and long-term experimental evaluation of the load-bearing prototype components. The following conclusions were drawn:

1) The use of i) AFRP composites in the tension and moderately loaded compression components, ii) GFRP in the highly loaded compression components, and iii) aerogel granulate between the components, leads to an excellent thermal performance; a linear thermal transmittance of less than 0.15 W/mK can be achieved.

2) Compared to pure GFRP thermal breaks, the use of AFRP improves the stiffness and thus reduces balcony deformations and enables the cantilever span to be increased. Creep deformations are small and can be cambered.

3) The experimental prototype investigations confirmed the targeted ductile failure mode through concrete crushing in the component-concrete interfaces of the bending moment-transferring components. The serviceability limit state conditions are met for the targeted balcony cantilever span of 4.0m.

4) In contrast to AFRP components, GFRP components exhibited sensitivity to the alkaline concrete environment.

5) The material-tailored component design enables the use of fully automated processes such as filament and tape winding and pultrusion to economically manufacture large quantities within a short time.

3.7. References

1. EPBD:2010. Directive 2010/31/EU of the European Parliament and of the Council of 19 May 2010 on the energy performance of buildings (recast).

2. Goulouti K, de Castro J, Vassilopoulos AP, Keller T. Thermal performance evaluation of fiber-reinforced polymer thermal breaks for balcony connections. Energy and Buildings 2014; 70: 365-371.

3. Bericht Minergie 2013. Revisionsentwurf 2013 der Norm SIA 380/1 und mögliche Auswirkungen auf kantonale Vorschriften. Bericht zuhanden der Konferenz Kantonaler Energiefachstellen (EnFK), AG MuKEn, http://www.endk.ch/media/archive1/dokumentation/muken/Bericht-SIA380_1EnDK2013-12-12-def.pdf, (assessed 16.06.2015)

4. Keller T, Riebel F, Zhou A. Multifunctional hybrid GFRP/steel joint for concrete slab structures. Journal of Composites for Construction 2006; 10/6: 550-560.

5. Aschwanden: http://aschwanden.com/de/produkte.29/arbo.34/arbo-400.75.html (assessed 05.06.2015).

6. ISO 10211. Thermal bridges in building construction: heat flows and surface temperatures – detailed calculations. International Organization for Standardization, Geneva, Switzerland, 2007.

7. SIA 380/1. Thermische Energie im Hochbau. Schweizerischer Ingenieur- und Architektenverein, Zürich, Switzerland, 2009.

8. Keller T, Riebel F. Structural behavior of multifunctional GFRP joints for concrete structures. Construction and Building Materials 2009; 23: 1620-1627.

9. K. Ghazi Wakili, H. Simmler, T. Frank, Experimental and numerical thermal analysis of a balcony board with integrated glass fiber reinforced polymer GFRP elements, Energy and Buildings 2007; 39: 76–81.

10. Dobb MG, Johnson DJ, Saville BP. Compressional behaviour of Kevlar fibres. Polymer 1981; 22: 960-965.

11. Cabot: http://www.cabot-corp.com/Aerogel/Building-Insulation (assessed 05.06.2015).

12. Swiss-Composite: http://www.swiss-composite.ch/scs4/html/index.shtml?lang=en (assessed 05.06.2015).

13. Manshadi BD, Vassilopoulos AP, de Castro J, Keller T. Contribution to shear wrinkling of GFRP webs in cell-core sandwiches. Journal of Composites for Construction 15(5) (2011) 833-840.

14. Riebel F, Keller T. Long-term compression performance of a pultruded GFRP element exposed to concrete pore water solution. Journal of Composites for Construction 2007; 11/4: 437-447.

15. SIA260:2003. Basis of structural design. Swiss Society of Engineers and Architects, Zurich, 2003.

16. SIA261:2003. Actions on Structures. Swiss Society of Engineers and Architects, Zurich, 2003.

4 Structural system performance

4.1. Introduction

In the context of sustainable development, the reduction of the energy consumption of the overall building stock represents a major challenge. Developments towards construction designs with high thermal insulation capacity are increased and new standards are set, e.g. the European Directive 2010/31/EU (EPBD recast)[1], which prescribes that all new buildings must be conceived as 'nearly zero-energy buildings' by the end of 2020. One construction detail that can cause up to 30% of the heat losses of a building is the thermal insulation-penetrating connection of building exterior balconies to interior concrete slabs[2,3]. Thermal break elements are used for these connections that partially interrupt the heat flow towards the external environment. However, they still comprise insulation-penetrating stainless steel bars with high thermal conductivity. On the other hand, fiber-reinforced polymer materials (FRPs) – composed of glass (GFRP) or, even much more insulating, aramid fibers (AFRPs) – have an up to 170 times lower thermal conductivity than stainless steel and are therefore much more appropriate for this specific application[3,4]. Several attempts had already been made to replace the stainless steel bars by GFRP components[5,6] but none of them was successful on the market for various reasons[7].

A new concept for a highly insulating, combined AFRP/GFRP thermal break was recently developed and its excellent thermal insulation capacity has been proven[7]. The new thermal break is shown in Fig. 4.1a and is able to transfer negative bending moments and shear forces from the exterior balcony to the interior

---

Authors: Kyriaki Goulouti, Julia de Castro, Thomas Keller

Composite Construction Laboratory CCLab, Ecole Polytechnique Fédérale de Lausanne EPFL.

Contribution: The main core of the paper was conducted by Kyriaki Goulouti (mechanical experiments). The structural analysis was developed in collaboration with Prof. T. Keller.

concrete slab. The concrete slab is interrupted in the envelope's insulation layer by a 55-mm- wide PVC box, which is filled with a highly insulating aerogel granulate material and can be adapted to slab height. The upper tension forces, caused by the balcony's negative bending moments, are transferred through the PVC box and anchored in the adjacent concrete slabs by 720-mm-long AFRP loops, spaced at 150 mm. The lower compression forces, also resulting from the bending moment, are transferred by 55.9-mm-long GFRP compression bars. Glass fibers had to be chosen in this case due to the relatively low compression strength of the (thermally much better) aramid fibers[8]. The GFRP bars are integrated into a hexagonal sandwich component, which provides a compression diagonal through the PVC box to transfer the shear forces, see Fig. 4.1b. The three directions of the hexagon are either wrapped with AFRP or GFRP laminates and polyurethane (PU)-foams of different densities are used as core materials. The details of the material selection and component composition are described in Chapter 3.

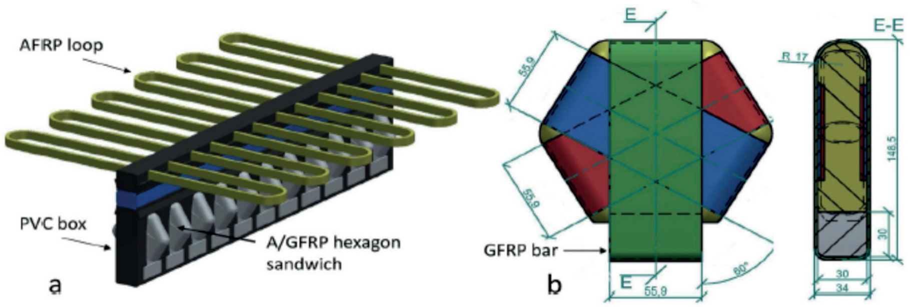

Figure 4.1. New A/GFRP thermal break: a) components assembled, b) A/GFRP hexagon sandwich component with integrated compression bar, (dimensions in (mm).

The structural behavior of the individual AFRP/GFRP components has already been experimentally investigated and characterized. The corresponding results were presented in Chapter 3 and form the basis for this work. In the following, the behavior of the whole system, the new thermal break embedded in the adjacent concrete slabs, is investigated. The behavior in the serviceability and ultimate limit states is analyzed and the maximum balcony span derived.

4.2. Experimental set-up

4.2.1. Thermal break components

The dimensions and mechanical properties of the thermal break components (AFRP tension loop, A/GFRP hexagon diagonal, GFRP compression bar), which are relevant for describing the system behavior, i.e. the interaction between the thermal break components and the surrounding concrete, are summarized in

Table 4.1. The mechanical properties are average experimental values, resulting from the component evaluation described in Chapter 3. The cross-sectional area values, *A*, refer to both the components' FRP cross-sections and the concrete contact areas of the components. E-Modulus, *E*, and strength, f_u, values refer to the FRP cross sections, while stiffness, *S*, and ultimate load, F_u, values are attributed to the components' performance. Two different PU foam densities (98 and 131 kg/m^3) and fiber types (AFRP and GFRP) were used in the hexagon components.

Table 4.1. Cross sections and mechanical properties of components (average experimental values[7]).

Component	*Length L (mm)*	*Area A (mm^2)*	*Stiffness S (kN/mm)*	*E-modulus E (GPa)*	*Ult. Load F_u (kN)*	*Strength f_u (MPa)*
AFRP tension loop	720	300[1] 1500[2]	18	47	274	913
A/GFRP hexagon compression diagonal, PU 98kg/m^3	125	224[3] 1677[4]	65	36	59	264
A/GFRP hexagon compression diagonal, PU 131kg/m^3	125	224[3] 1677[4]	76	42	69	309
GFRP compression bar	55	900[5]	792	44	315	350

[1] AFRP (2·15·10 mm^2), [2]concrete contact (projection, 15·100 mm^2)
[3] A/GFRP (2·2·55.9 mm^2), [4]concrete contact (projection, 30·55.9 mm^2)
[5] GFRP (30·30 mm^2) = concrete contact (30·30 mm^2)

4.2.2. Experimental beams and program

Since balconies are normally subjected to uniformly distributed loads and thus represent one-way cantilevering slab structures, their structural behavior can be experimentally simulated using a beam configuration. Accordingly, six experimental beams of full-scale dimensions, comprising, with one exception, one thermal break unit each – i.e. one loop combined with two hexagons with integrated compression bars[7]– were investigated. In one beam, however, one loop was combined with only one hexagon/bar component, see Table 4.2. Hexagons with higher foam density (and thus wrinkling resistance) were selected in the cases where higher shear loads were expected.

The slab inside the building was represented by a beam of 1000-mm length, 220-mm height and 300-mm width (denominated 'interior' beam in the following), to which a 700-mm-long cantilevering ('exterior') beam of the same cross section, representing the balcony, was connected through the thermal break unit, see Figs. 4.2 and 4.3. The gap of 55-mm length between the two beams, normally containing the PVC box filled with aerogel insulation, was kept open in order to observe the components' behavior. The 100-mm-long steel plate of the cantilever support was moved 110 mm back from the gap edge in order to simulate the most unfavorable case[5] and not create a favorable confinement of the concrete at the support of the GFRP compression bars. The beams were reinforced with two longitudinal steel bars B500[9] of ϕ 14 mm on the top and two bars of ϕ 10 mm on the bottom side and stirrups of ϕ 10 mm spaced at 150 mm. They were manufactured in two series; the average cylinder compression strengths, f_{cm}, measured on the day of the experiments, are listed in Table 4.2.

Table 4.2. Parameter overview and main results.

Beam	*Loop AFRP*	*Hexagon (PU foam density,* kg/m^3*)*	*Bar GFRP*	*Concrete strength f_{cm} (MPa)*	*Load distance e (mm)*	*SLS load F_{SLS} (kN)*	*Ult. Load F_u(kN)*	F_u / F_{SLS}	*Failure mode*
G600	1	2 GFRP (98 kg/m^3)	2	34.7	600	5.7	26.4	4.6	Concrete top crushing
G400	1	2 GFRP (98 kg/m^3)	2	34.5	400	11.3	40.7	3.6	Concrete top crushing
G200	1	2 GFRP (131kg/m^3)	2	30.1	200	20.4	48.1	2.4	Concrete top tearing, bottom spalling
G400-1	1	1 GFRP (131kg/m^3)	1	29.9	400	12.1	25.8	2.1	GFRP wrinkling
A400	1	2 GFRP (98 kg/m^3)	2	34.3	400	9.3	39.2	4.2	Concrete top crushing AFRP wrinkling
A200	1	2 GFRP (131kg/m^3)	2	30.1	200	22.4	43.2	1.9	Concrete top tearing, bottom spalling, AFRP wrinkling

The cantilever (exterior) beam was loaded by a single concentrated load via a hydraulic jack, whose distance from the support (lever arm, e+110 mm) was varied in order to create different moment-to-shear force, *M*/*F*, ratios, see Table 4.3. The beams were loaded in three to six cycles up to failure under displacement control at a rate of 4.0 mm/min. The first cycle was below the concrete cracking displacement. The dead load of the cantilever beams was negligible compared to the sustained ultimate loads (3-5% of the latter). The beam designation indicates the fiber type of the hexagon wrapping (A=aramid, G=glass) and the load distance (e=200/400/600 mm), see Table 4.2.

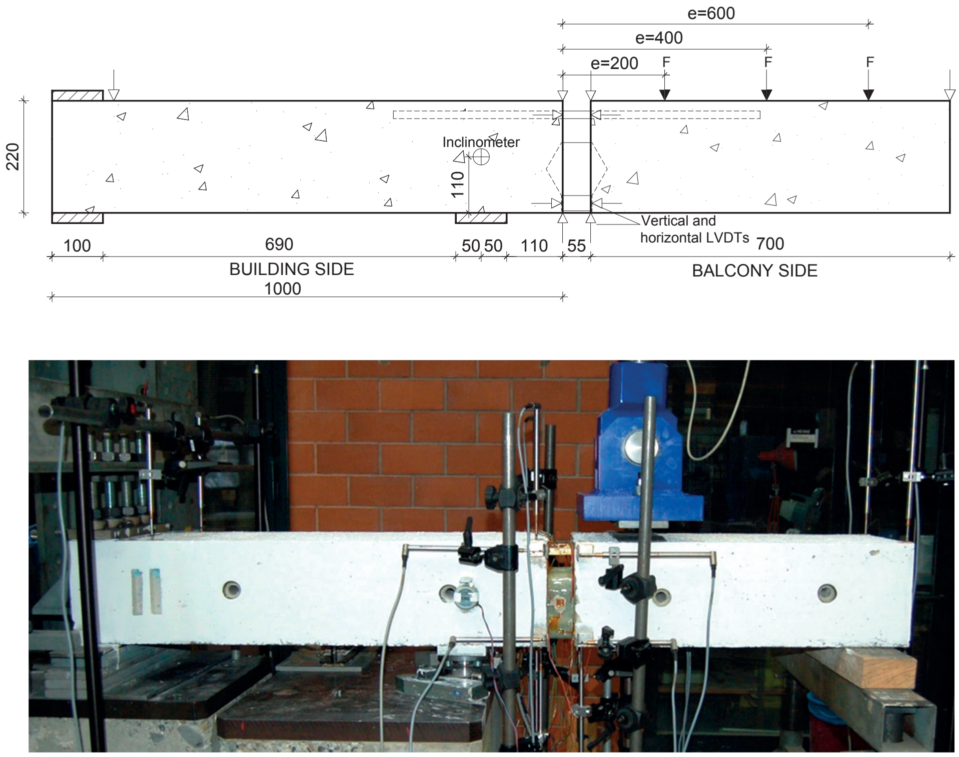
e=600
e=400
e=200
F
F
F
220
Inclinometer
110
Vertical and
horizontal LVDTs
100
690
50 50
110
55
700
BUILDING SIDE
1000
BALCONY SIDE

Figure 4.2. Experimental set-up with instrumentation and loading positions, dimensions in (mm), (timber block removed prior to loading).

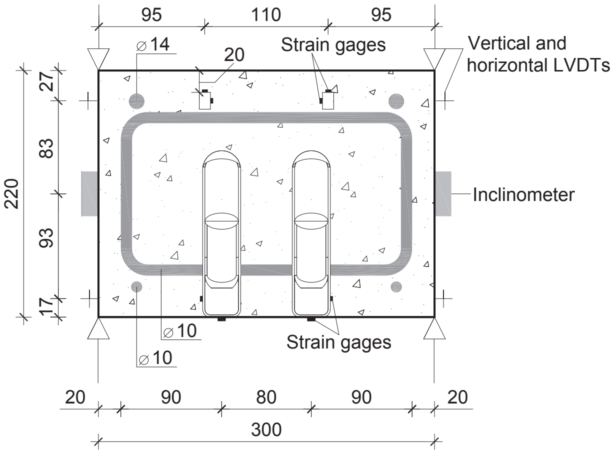
95
110
95
⌀14
20
Strain gages
Vertical and
horizontal LVDTs
27
83
220
93
17
Inclinometer
⌀10
⌀10
Strain gages
20
90
80
90
20
300

Figure 4.3. Cross section of experimental beam with one thermal break unit, concrete reinforcement and instrumentation, dimensions in (mm).

Table 4.3. AFRP loop tension and GFRP bar compression forces at ultimate load and concrete stresses and confinement factors.

Beam	*Concrete strength f_{cm} (MPa)*	*Ult. loads and moments*			*Loop anchorage*			*Bar compression*		
		F_u (kN)	*e+0.11 (m)*	*M_u (kNm)*	*T_u (kN)*	*$f_{cu,L}$ (MPa)*	*$k_{c,L}$ (-)*	*$C_{u,B}$ (kN)*	*$f_{cu,B}$ (MPa)*	*$k_{c,B}$ (-)*
G600	34.7	26.4	0.71	18.7	106.8	71.2	2.05[1]	30.5	33.9	0.98
G400	34.5	40.7	0.51	20.8	118.3	78.8	2.29[1]	23.9	26.6	0.77
G200	30.1	48.1	0.31	14.9	85.0	56.6	1.88	0.8	0.9	0.03
G400-1	29.9	25.8	0.51	13.2	75.0	50.0	1.67	30.3[2]	31.9	1.07
A400	34.3	39.2	0.51	20.0	113.9	75.9	2.21[1]	23.0	25.6	0.75
A200	30.1	43.2	0.31	13.4	76.3	50.9	1.78	0.7	0.8	0.03

[1] top concrete failure, [2]only one hexagon considered

4.2.3. Instrumentation and measurements

At each of the four corners of the cross sections on each side of the insulation gap, the vertical and horizontal (in beam direction) displacements were measured by displacement transducers (LVDTs), see Figs. 4.2 and 4.3. Analogously, the vertical deflection of the two upper corners of the cross section at the cantilever end was measured. Furthermore, on each lateral beam side, inclinometers fixed at mid-height on the vertical support axis measured the rotation at this location caused by the upward deformation and cracking of the interior beam.

Four strain gages were applied on the AFRP loop at the center of the insulation gap, in the loop direction, one of them laterally at mid-height and one on the top side of each loop arm. Similarly, four strain gages were installed on the two GFRP compression bars at the center of the gap, one gage laterally at mid-height and one on the bottom side of each bar. Further gages were applied laterally on the hexagons' diagonals in the diagonal direction. However, since the outermost wrapping direction was vertical, no reliable strains could be measured in the diagonal direction. Furthermore, the concrete crack formation and propagation and crack lengths and widths were mapped at the displacement steps before unloading and reloading for the further cycles.

4.3. Experimental results

4.3.1. Load-deflection responses

All six beams exhibited a nonlinear load-deflection response, the latter indicating the average value of the two LVDTs at the cantilever end, see Fig. 4.4 (only the failure cycles are shown). With decreasing load distance, *e*, the initial stiffness and ultimate load increased, while the ultimate displacement decreased (e.g. from G200 to G600). As the ultimate load was approached, the stiffness of all beams further decreased and the load then gradually decreased (in half of the cases) with increasing displacement. The two beams with the same lever arm exhibited a similar response; the different wrapping of the hexagons (AFRP or GFRP) thus did not significantly influence the behavior – in particular not at the serviceability load, F_{SLS}, which was determined at a cantilever end deformation of 2L/350=4.9mm, with L= 700+55+110 = 865mm[7,10] .The ultimate load of the beam with only one hexagon (G400-1) was significantly lower than that of the same beam with two hexagons (G400). The ultimate loads, F_u, and serviceability loads, F_{SLS}, of all beams are summarized in Table 4.2. Their ratio F_u/F_{SLS} varied according to the lever arm length between 1.9 (shortest lever arm) and 4.6 (longest lever arm).

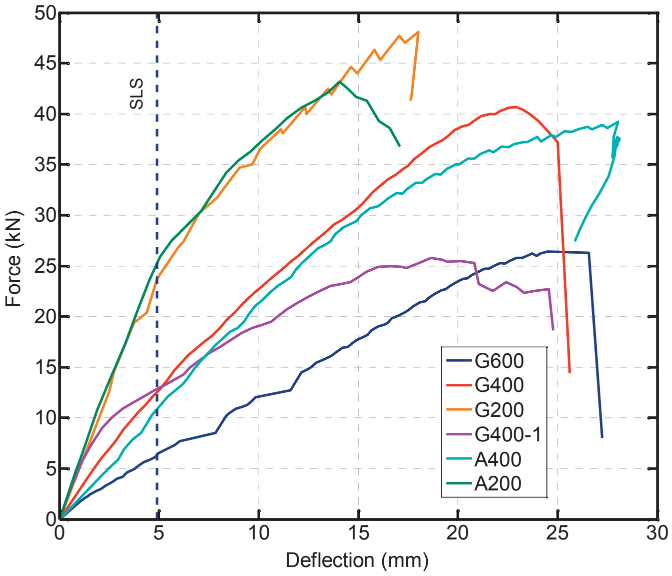

Figure 4.4. Load-deflection responses of all beams (deflections at cantilever end of failure cycle).

The load-displacement responses of beams G200 and G600, during all the cycles, are compared in Fig. 4.5. Some permanent deformations were obviously accumulated during concrete cracking, which occurred on top of the interior span due to the negative bending moments. However, concrete cracking was limited to only one to three cracks, see Fig. 4.6. The curves also show significant load decreases while displacements were maintained before unloading from the top of the individual cycles. These decreases were much more pronounced in the case of shorter lever arms, i.e. higher loads in the hexagons' compression diagonal, and thus could be attributed to the viscoelastic behavior of this component.

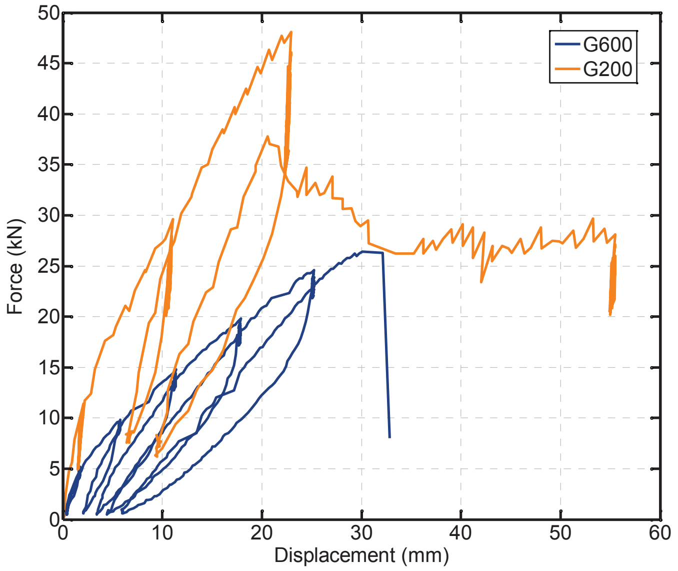

Figure 4.5. Load-deflection responses of beams G200 and G600 during all cycles.

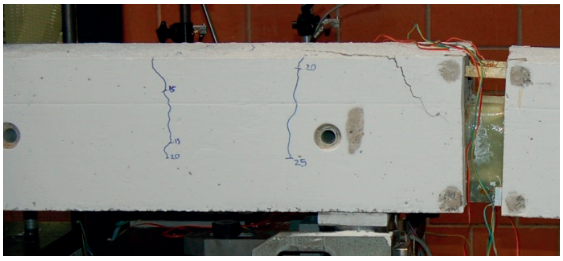

Figure 4.6. Crack formation and propagation in beam G600 during 15-, 20-, 25-kN cycles.

4.3.2. Failure modes

The failure modes depended primarily on the lever arm length and fiber type of the hexagon wrapping, see Table 4.2. With longer lever arms (G600, G400 and A400), the concrete in the AFRP loop anchorage zone of the interior span failed through crushing and a diagonal crack plane formed through the whole beam width from the upper loop anchorage zone down to the two hexagon compression diagonal supports, see Fig. 4.7a. Small cracks formed at the supports of the GFRP bars, but this zone did not fail, see Fig. 4.7b. The hexagons with GFRP wrapping remained undamaged (in G600 and G400), while those with AFRP wrapping (in A400) exhibited wrinkling in the compression diagonal. The beams exhibited a clear rotation in the gap; the two adjacent concrete planes remained not parallel, as shown in Fig. 4.8.

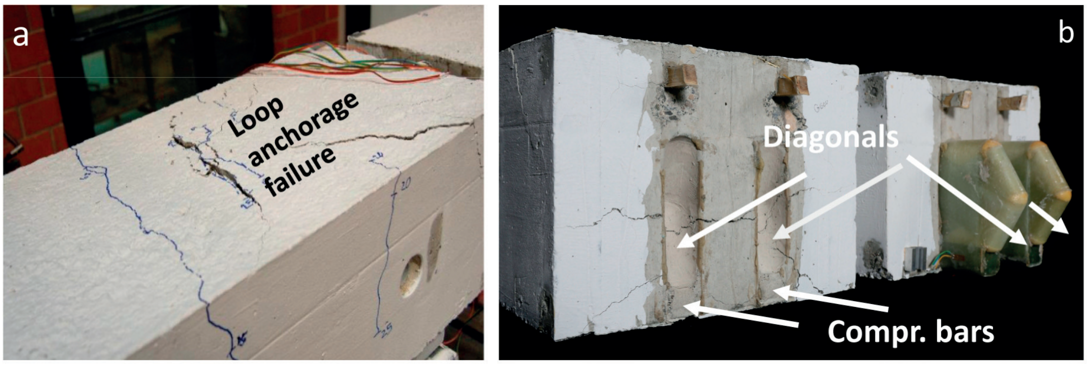

Figure 4.7. Failure mode of beam G600: a) top concrete failure in loop anchorage zone, b) cracks through the hexagon diagonals' support area of interior (left) beam, undamaged hexagons in cantilever (right) beam.

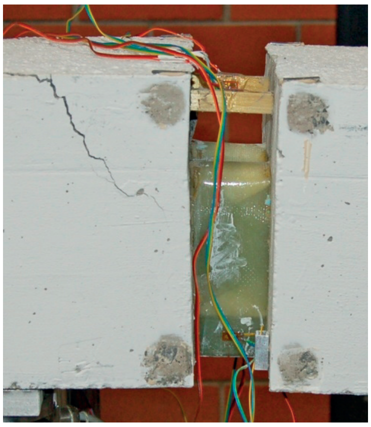

Figure 4.8. Beam G600 at ultimate load: concentrated rotation in insulation gap.

The beams with the shortest lever arm (G200 and A200) failed differently. The bottom part of the concrete on the supported part failed, i.e. the part below the prolongation of the hexagon compression diagonals spalled, see Fig. 4.9a. The loop deformed into an S-shape, see Fig. 4.10, and was thus torn off from the concrete on the loading side. The hexagons with GFRP wrapping (in G200) remained undamaged (with the exception of minor crushing at one edge in one of them) while those with AFRP wrapping (in A200) were crushed in the upper part of the compression diagonal, see Fig. 4.9b. In addition to the rotation in the gap, a clear vertical offset was visible, see Fig. 4.10 (and compare to Fig. 4.8). Beam G400-1, which had only one hexagon with GFRP wrapping, again failed differently. No significant damage could be observed in the concrete, see Fig. 4.11a, while the hexagon's GFRP diagonals failed through wrinkling on one side, see Fig. 4.11b. Overall, all beams exhibited a ductile failure mode caused, in all cases but one, by progressive concrete failure and in one case by GFRP wrinkling.

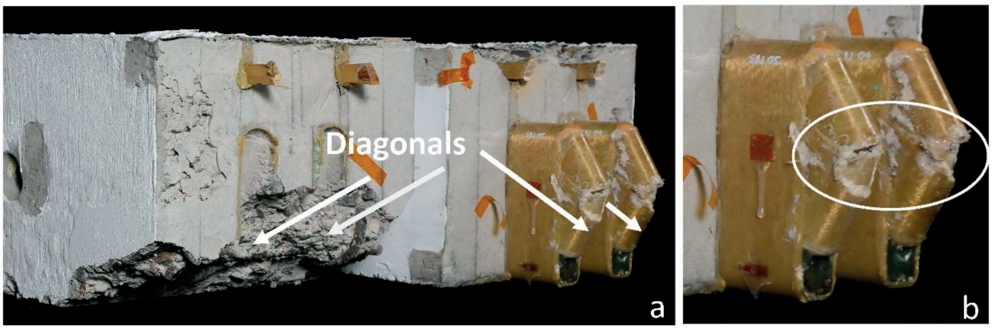

Figure 4.9. Failure mode of beam A200: a) bottom concrete spalling in interior (left) beam, b) wrinkling/crushing of AFRP hexagon diagonal.

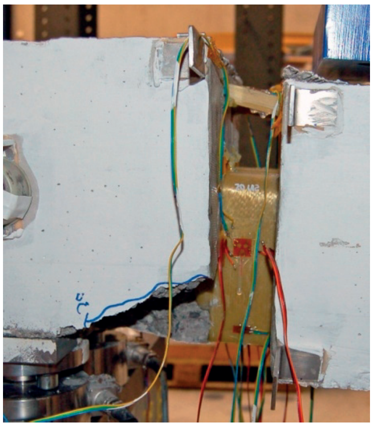

Figure 4.10. Beam A200 at ultimate load: rotation and vertical offset in insulation gap.

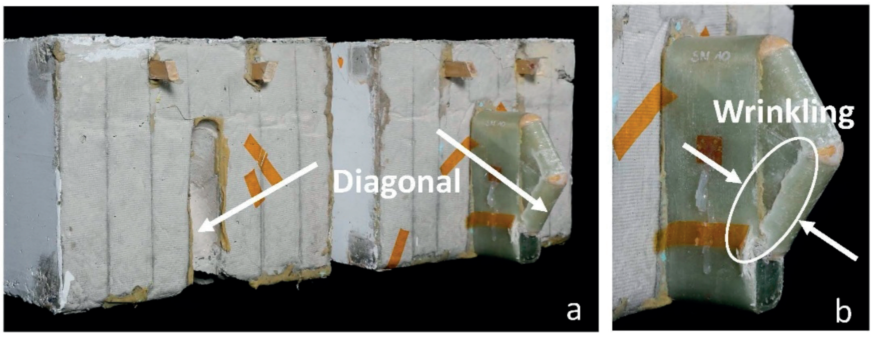

Figure 4.11. Failure mode of beam G400-1: a) undamaged concrete in interior (left) beam, b) wrinkling of GFRP hexagon diagonal.

4.3.3 Strain measurements

The load-axial strain responses of all beams, measured on the lateral sides of the AFRP loops (tension strains) and GFRP bars (compression strains), at the center of the insulation gap in the failure cycle, are shown in Figs. 4.12 and 4.13 (average values from the two gages). In both cases, the curves exhibited the same dependence on the lever arm length as the load-deflection curves shown in Fig. 4.4 and discussed above, i.e. the shorter the lever arm, the stiffer the behavior – with one exception, the compression strains in the GFRP bars of beams G200/A200 were almost zero and are not shown in Fig. 4.13. In general, the compression strains in the GFRP bars were small compared to the tension strains in the AFRP loop.

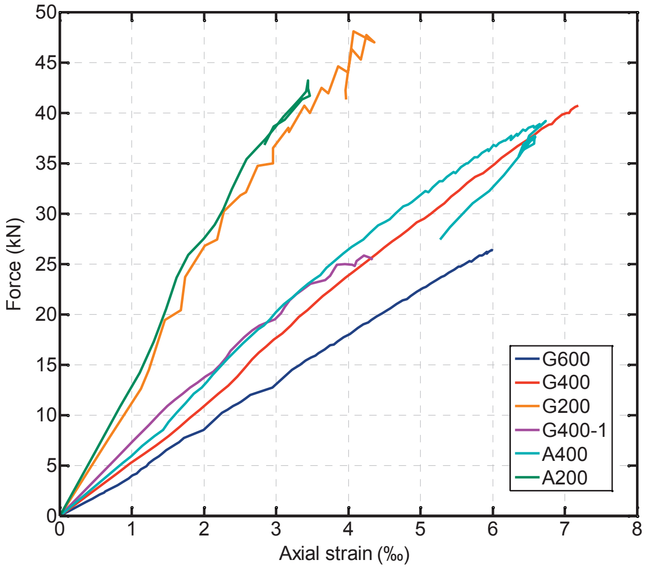

Figure 4.12. Load-strain responses (tension) of AFRP loop at mid-height and mid-gap of all beams (failure cycle).

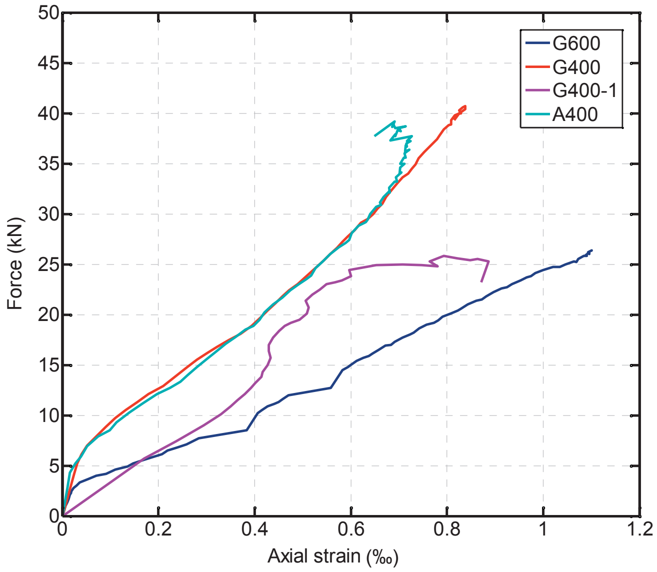

Figure 4.13. Load-strain responses (compression) of GFRP bar at mid-height and mid-gap of longer lever arm beams (failure cycle).

4.4. Discussion

4.4.1. Design model and section forces

The design model, on which the conception of the A/GFRP components is based[7] and which can serve for the verification of the ultimate and serviceability limit states (ULS and SLS), is shown in Fig. 4.14. The (exterior) balcony loads are transferred via a truss structure across the insulation gap to the (interior) support. The edge of the 100-mm-wide support plate was selected as the actual support in this case, taking the beam's negative curvature into account. The continuity of the tensioned top chord of the truss across the insulation gap is formed by the AFRP loop, which is overlapped with the fourth layer of the layer steel reinforcement on both gap sides in the anchoring zones (see Fig. 4.3). The continuity of the compressed bottom chord is assured by the short GFRP bars in the gap that transfer the forces by contact. The diagonals are in compression, inclined at 45° in the concrete and at φ=30° through the gap, i.e. parallel to the diagonal hexagon wrapping, while the vertical tension members are formed by the steel stirrups in the concrete. The loop and bars transfer the bending moment while the diagonals and vertical tension members transfer the shear force, i.e. the exterior vertical load in this case.

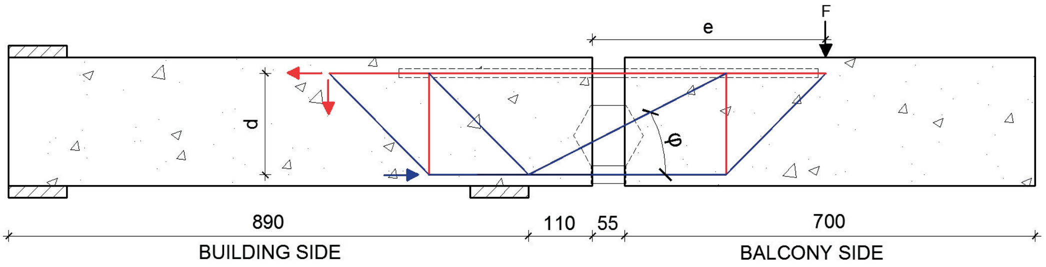

Figure 4.14. Free-body diagram of thermal break region as basis for design (tension forces in red, compression forces in blue, dimensions in (mm)).

The top tension force in the AFRP loop, at ultimate load, T_u, can be derived from the bending moment at the support point, M_u, as follows:

$$T_u = M_u / d = F_u \cdot (e + 110) / d \tag{1}$$

with d = 220-(15+2)-20-15/2 = 176mm (static height). The bottom compression force in one GFRP bar (there are two in one unit), at ultimate load, $C_{u,B}$, results from horizontal equilibrium as follows:

$$C_{u,B} = T_u / 2 - F_u / (2 \cdot \tan \varphi) \tag{2}$$

where the second term on the right side is the horizontal component of one hexagon diagonal with $\varphi = 30°$ (diagonal inclination). The compression force in one hexagon diagonal at ultimate load, $C_{u,D}$, can be calculated as:

$$C_{u,D} = F_u / (2 \cdot \sin \varphi) \tag{3}$$

The ultimate loads, F_u, and moments, M_u, and resulting values of T_u, $C_{u,B}$, and $C_{u,D}$, are given in Tables 4.3 and 4.4 for all beams and will be discussed in the following. The corresponding forces in the serviceability limit state (SLS) can be determined analogously, based on F_{SLS} (instead of F_u), listed in Table 4.2.

Table 4.4. Compression diagonal forces at ultimate load and concrete stresses and confinement factors.

Beam	$C_{u,D}$ (kN)	$F_{u,D}$ (kN)	$C_{u,D}/F_{u,D}$	$f_{cu,D}$ (MPa)	$k_{c,D}$
G600	26.4	59	0.45	12	0.35
G400	40.7	59	0.69	18.2	0.53
G200	48.1	69	0.70	22.6	0.752
G400-1	51.63	69	0.751	24.3	0.81
A400	39.2	59	0.661	17.5	0.51
A200	43.2	69	0.631	20.3	0.672

[1] Wrinkling failure, [2]concrete spalling failure, [3] only one hexagon considered

4.4.2. AFRP loop responses and concrete anchoring

In the previous work on the component behavior[7] it has already been demonstrated how the SLS verification, i.e. verification of the balcony deflections, can be done. It was assumed that the loop extension would occur along the whole loop length due to the absence of any significant bond between the straight smooth loop surface and the concrete. The measurements of the beams now confirmed this assumption, as demonstrated in Table 4.5. Based on the axial strain measurements on the loop axis level at mid-gap, ε_L, the loop extensions were estimated as $\Delta_{h,L} = \varepsilon_L \cdot L_L$, with L_L = 720mm (loop length, see Table 4.1). The resulting values matched well the values of the insulation gap openings on the loop level, measured by the LVDTs, $\Delta_{h,gap}$, the average deviation being only 2%. The differences can be partially attributed to the widths of the small number of loop-crossing interior cracks, which are not taken into account in this comparison.

Based on the concrete contact areas between the loop ends and the surrounding concrete, $A_{c,L}$ = 1500 mm^2 (see Table 4.1), the corresponding concrete compression stresses at ultimate load were calculated as $f_{cu,L} = T_u / A_{c,L}$, and compared to the concrete strength, f_{cm}, using the concrete confinement factor $k_{c,L} = f_{cu,L}/f_{cm}$[9]; the resulting values are listed in Table 4.3. The comparison of the confinement factors with the observed failure modes (see Table 4.2) showed that loop anchorage failure (i.e. concrete crushing) occurred for $k_{c,L} > 2.0$ – thus in beams with the longest lever arms and therefore highest moments and loop forces (G600, G400, A400).

Table 4.5. Horizontal deformations on loop level at ultimate load (failure cycle only).

Beam	$\varepsilon_L{}^1$ (‰)	$\Delta_{h,L}$ (mm)	$\Delta_{h,gap}{}^1$ (mm)	$\Delta_{h,L}/\Delta_{h,gap}$
G600	6.0	4.3	4.3	1.00
G400	7.2	5.2	4.6	1.12
G200	4.2	3.0	3.4	0.89
G400-1	4.2	3.0	2.7	1.12
A400	6.7	4.9	5.4	0.90
A200	3.4	2.5	2.3	1.08
Average				1.02±0.20

[1] average from two strain gages or two LVDTs

4.4.3. GFRP bar responses and concrete support

As shown above, the axial compression strains in the GFRP bars were much smaller than those in the AFRP loop. Accordingly, the compression forces at ultimate load, $C_{u,B}$, were also small, see Table 4.3. In the cases with the shortest lever arms (G200, A200), the load was even directly transferred through the hexagon compression diagonals, the compression bars thus remaining unloaded, as confirmed by the strain measurements (see above). The concrete stresses in the contact areas, calculated as $f_{cu,B} = C_{u,B} / A_{c,B}$, with $A_{c,B}$ = 900mm^2 (concrete contact area, see Table 4.1), were also small. The corresponding confinement factors $k_{c,B} = f_{cu,B} / f_{cm}$ remained below 1.0. In a comparable case, concrete failure occurred at factors of k_c = 1.72[5]– it can thus be concluded that the concrete contact zones of the GFRP bars never failed.

4.4.4. Hexagon diagonal responses and concrete support

The compression forces in the hexagon diagonals, $C_{u,D}$ (see Table 4.4, values at ultimate loads) led to a shortening of the latter, which resulted in a vertical offset of the exterior compared to the interior beams, $\Delta_{v,gap}$. The corresponding differences measured by the vertical LVDTs between the loaded and supported gap sides are listed in Table 4.6 (values in failure cycle) – they remained small, between 2.1 and 4.3 mm, and are further discussed in the following.

The forces in the hexagon compression diagonals at ultimate load are further compared to the hexagon diagonal compression (wrinkling) resistances, $F_{u,D}$, resulting from the component evaluation, see

Tables 4.1 and 4.4. It can be concluded that in the beams where wrinkling occurred (G400-1, A400, A200), the component wrinkling resistance was not reached. The main reason was that the wrinkling failure mode was not always uniformly distributed across the diagonal width, as was the case in the component evaluation[7]– see beam A200 in Fig. 4.9b as example. It seems that the compression force was less inclined in this case than the diagonal direction and shifted to the upper diagonal part where thus a localized, combined wrinkling/crushing failure occurred. In the G400-1 case, wrinkling occurred uniformly distributed across the diagonal width, see Fig. 4.11b, however only on one side. In this case the compression force came closest to the component resistance under ideal conditions.

The concrete stresses in the hexagon diagonal contact areas, $f_{cu,D}$ = $C_{u,D}$ /$A_{c,D}$, with $A_{c,D}$ = 1677mm^2 (concrete contact area, see Table 4.1), were much lower than the concrete strength, and the corresponding $k_{c,D}$-values were thus below 1.0, see Table 4.4. Nevertheless, concrete spalling failure occurred in beams G200 and A200, which, however, cannot have been induced by the not-loaded GFRP bars in these cases, as shown above. The only explanation is that again the diagonal stresses in the concrete contact area were not as uniformly distributed as assumed in the above calculation and thus led to the observed spalling (see Fig. 4.9a).

4.4.5. SLS and ULS verification

The verification of the serviceability limit state (SLS) is primarily a verification of the deflections, as explained above. There are three main contributors to the deflection of the cantilever end: 1) the deflection caused by the rotation of the interior beam mainly due to concrete cracking, $\Delta_{v,cr}$, the latter was measured by the inclinometers above the support, 2) the deflection caused by the diagonal shortening, $\Delta_{v,gap}$, which is identical to the vertical offset in the gap as mentioned above, 3) the deflection resulting from a concentrated rotation in the gap, $\Delta_{v,gap\text{-}rot} = (\Delta_{h,L}+\Delta_{h,B})\cdot L/d$, with $\Delta_{h,L}$ = loop extension (see Table 4.5); $\Delta_{h,B} = \varepsilon_B \cdot L_B$ (compression bar shortening), with ε_B = axial compression strain on bar axis level at mid-gap (see Fig. 4.13) and L_B = 55mm (compression bar length); L=727.2mm (distance mid-gap to cantilever end); d = 176mm (see above). The measurement-based values of these three contributors are listed in Table 4.6, together with their sum, $\Delta_{v,tot} = \Delta_{v,cr} + \Delta_{v,gap}+\Delta_{v,gap\text{-}rot}$, and compared to the deflection at the cantilever end measured by the LVDTs, $\Delta_{v,end}$. On average, the sums of the contributors matched well the measured deflections at the cantilever end, the average deviation being only 2%.

Table 4.6. Vertical deformations at cantilever end at ultimate load (failure cycle).

Beams	$\Delta_{v,cr}$[1] *(mm)*	$\Delta_{v,gap}$[1] *(mm)*	$\Delta_{h,L}$ *(mm)*	ε_B[1] *(‰)*	$\Delta_{h,B}$ *(mm)*	$\Delta_{v,gap\text{-}rot}$[1] *(mm)*	$\Delta_{v,tot}$ *(mm)*	$\Delta_{v,end}$[1] *(mm)*	$\Delta_{v,tot}/\Delta_{v,end}$	$\Delta_{v,gap}/\Delta_{v,end}$
G600	2.9	3.8	4.3	1.1	0.06	18.0	24.7	25.0	0.99	0.15
G400	3.4	3.1	5.2	0.8	0.04	21.6	28.1	23.2	1.21	0.13
G200	2.6	2.1	3.0	0	0.00	12.4	17.1	18.0	0.95	0.12
G400-1	2.0	2.7	3.0	0.85	0.05	12.6	17.3	18.8	0.92	0.14
A400	4.0	4.3	4.9	0.7	0.04	20.4	28.7	27.8	1.03	0.15
A200	1.9	2.1	2.5	0	0.00	10.3	14.3	14.2	1.01	0.15
Average									1.02±0.2	0.14±0.02

[1] averages from two inclinometers or strain gages or LVDTs

The development of all these values during the failure cycle of beam G600 is also shown in Fig. 4.15. From these results it could be concluded that the contributions of concrete cracking and diagonal shortening (i.e. shear) were small compared to that of the (moment) rotation in the gap. The latter mainly occurred due to the extension of the AFRP loop, which was much larger than the small shortening of the GFRP compression bars. In particular, the vertical offset due to the diagonal shortening (shear), $\Delta_{v,gap}$, was only 14% (on average) of the total deflection for this short cantilever length (see Table 4.6). Since this offset is independent of the cantilever length, this percentage will decrease for longer (more realistic) balcony spans where the contribution from the moment rotation in the gap will thus clearly prevail – the deformation caused by shear can therefore be disregarded. In the SLS verification, the deflection can thus be calculated as the deflection of a continuous, possibly cracked concrete beam, plus the deflection from the moment rotation in the gap, caused by the extension of the AFRP loop and disregarding the shortening of the GFRP bars, as assumed (but not yet proven) in Chapter 3.

Concerning the ultimate limit state (ULS), the moment transfer capacity of the thermal break is limited by the resistance of the AFRP loop anchoring in the concrete cover, see Fig. 4.16. The shear capacity is primarily limited by the concrete spalling of the hexagon diagonal supports while damage to the hexagons may also occur in the case of AFRP wrapping. Within these two limits, the moment/shear combinations can be selected, as shown in Fig. 4.16. Also shown is beam G400-1 with only one hexagon, which should not be considered in this respect. These limits however have to be refined by further experiments and material safety factors have to be derived in order to establish reliable ULS design diagrams for practical applications.

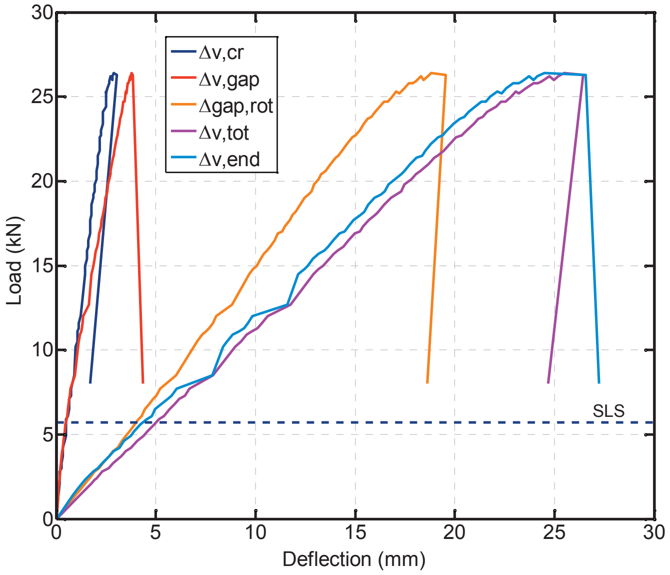

Figure 4.15. Contributors to deflection at cantilever end of beam G600 (failure cycle).

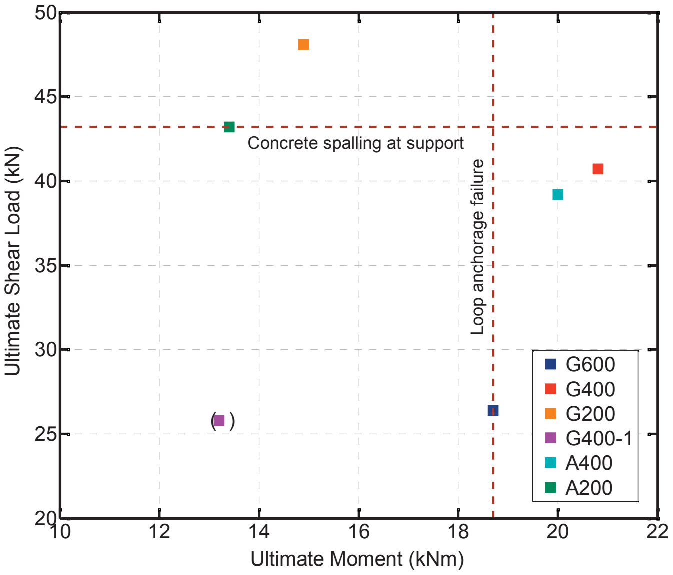

Figure 4.16. Ultimate shear load-moment interaction and performance limits.

4.4.6. Maximum balcony span

In the previous work[7], it has been shown that a targeted maximum span of 4.0 m for balconies using this new thermal break could be met by considering only the SLS criterion. In the following, the maximum span for which the ULS condition is also fulfilled will be derived. For this purpose, the experimental F_u and M_u values obtained in Table 4.3 will firstly be transformed into design values f_{Rd} and m_{Rd} as follows:

$$f_{Rd} = \frac{0.8 \cdot F_u}{a \cdot \gamma_c}, \quad m_{Rd} = \frac{0.8 \cdot M_u}{a \cdot \gamma_c}$$

with a = 0.3m (beam width), γ_c = 1.5 (material safety factor for concrete[9], since failure occurs in the concrete), factor 0.8 to transform the experimental values into characteristic (95%-fractile) values[10] – the corresponding results are shown in Table 4.7.

A balcony of 0.20-m thickness with a uniformly distributed variable load of q = 3.0 kN/m^2 is further assumed[11]. Using load factors of 1.35 for the permanent load and 1.50 for the variable load and assuming f_{Rd} = 70 kN/m and m_{Rd} = 36 kNm/m according to Table 4.7 results in maximum spans of 6.2 m for the shear and 2.5 m for the moment criterion, the latter being below the targeted 4.0 m. It is thus confirmed that the limiting factor of the system is the anchoring of the AFRP loop in the concrete cover.

Table 4.7. Design resistance values for ULS verification.

Beam	***F_u (kN)***	***M_u (kNm)***	***f_{Rd} (kN/m)***	***m_{Rd} (kNm/m)***
G600	26.4	18.7	47.0	33.3
G400	40.7	20.8	72.4	37.0
G200	48.1	14.9	85.6	26.5
A400	39.2	20.0	69.8	35.6
A200	43.2	13.4	77.8	23.9

4.5. Conclusions

A new highly insulating balcony thermal break has been developed which consists of combined AFRP/GFRP loop and sandwich components. In a previous work, the excellent thermal performance has been demonstrated and the load-bearing behavior of the components characterized. In the current work, the system behavior, i.e. the behavior of the thermal break embedded at the interface between a building interior and an exterior balcony concrete slab, has been investigated. The following conclusions were drawn:

1) A simple statically determined truss model can be used to calculate the section forces in the thermal break components, i.e. the tension force in the AFRP loops and the compression forces in the A/GFRP hexagon diagonals and the GFRP compression bars.

2) The balcony deflections can be estimated by adding the deflections caused by a concentrated rotation in the thermal break to those of a continuous concrete slab (without thermal break). The former can be obtained from the extension of the AFRP loop that is uniform over its whole length.

3) The failure modes are ductile due to prevailing concrete failures and, in the cases of AFRP hexagons, simultaneous wrinkling of the sandwich faces. However, the ultimate loads using GFRP hexagons (which did not wrinkle) were not significantly higher than those using AFRP hexagons. The much better thermal performance of AFRP hexagons can thus be exploited.

4) The maximum balcony span of the current system is approximately 2.50 m and is limited by the anchoring resistance of the AFRP loops in the concrete cover.

To further increase the balcony span, the loop ends could be slightly bent downwards to activate more concrete resistance. A further improvement might be a covering of the curved hexagon diagonal ends by small Teflon sheets in order to eliminate friction and thus better assure that the compression forces do not deviate from the diagonal direction.

4.6. References

1. EPBD:2010. Directive 2010/31/EU of the European Parliament and of the Council of 19 May 2010 on the energy performance of buildings (recast).

2. Bericht Minergie 2013. Revisionsentwurf 2013 der Norm SIA 380/1 und mögliche Auswirkungen auf kantonale Vorschriften. Bericht zuhanden der Konferenz Kantonaler Energiefachstellen (EnFK), AG MuKEn, http://www.endk.ch/media/archive1/dokumentation/muken/Bericht-SIA380_1EnDK2013-12-12-def.pdf, (assessed 16.06.2015).

3. Goulouti K, de Castro J, Vassilopoulos AP, Keller T. Thermal performance evaluation of fiber-reinforced polymer thermal breaks for balcony connections. Energy and Buildings 2014; 70: 365-371.

4. K. Ghazi Wakili, H. Simmler, T. Frank, Experimental and numerical thermal analysis of a balcony board with integrated glass fiber reinforced polymer GFRP elements, Energy and Buildings 2007; 39: 76–81.

5. Keller T, Riebel F, Zhou A. Multifunctional hybrid GFRP/steel joint for concrete slab structures. Journal of Composites for Construction 2006; 10/6: 550-560.

6. Keller T, Riebel F, Zhou A. Multifunctional all-GFRP joint for concrete slab structures. Journal of Composites for Construction 2007; 21: 1206-1217.

7. Goulouti K, de Castro J, Keller T. Aramid/glass fiber-reinforced thermal break – thermal and structural performance. Composite Structures 2016; 136: 113-123.

8. Dobb MG, Johnson DJ, Saville BP. Compressional behavior of Kevlar fibers. Polymer 1981; 22: 960-965.

9. SIA262:2003. Concrete Structures. Swiss Society of Engineers and Architects, Zurich, 2003.

10. SIA260:2003. Basis of Structural Design. Swiss Society of Engineers and Architects, Zurich, 2003.

11. SIA261:2003. Actions on Structures. Swiss Society of Engineers and Architects, Zurich, 2003.

5

Creep modeling and prediction

5.1. Introduction

The need for limiting energy consumption in buildings heralded a new era in the research field, resulting in new materials, and new building concepts and strategies. Within this context a new fiber- reinforced polymer (FRP) thermal break was conceived for the thermal bridge created in the balcony projection, which offers enhanced thermal and structural performance[1,2].

For the structural validation of this thermal break, the creep behavior of the FRP components was also studied[1], since creep phenomena affect the long-term mechanical properties of FRPs and their durability[2] and thus the serviceability[4] of the structures. The analysis of the experimental creep data of these FRP components raised questions regarding two different aspects: a) the suitability and validity of the most frequently used methodologies for the simulation of creep behavior and long-term prediction of the mechanical properties of FRP elements in general and b) the sudden and irregular increase of creep deformation, designated as 'jumps', exhibited by the studied FRP components, see Fig.5.1.

There are three characteristic stages of the creep response: primary, secondary and tertiary creep, Fig. 5.2. The primary stage is characterized by a diminishing creep rate, the secondary or stationary creep by a steady creep rate and in the tertiary stage the creep strain accelerates rapidly. The secondary creep is the most significant stage since it is the most long-lasting creep period, and thus structural elements are designed taking into account a secondary creep response.

Authors: Kyriaki Goulouti[1], Ioannis Lymperopoulos[2].

Composite Construction Laboratory CCLab[1], Department of Mechanical Engineering, Automatic Control Laboratory, EPFL[2].

Contribution: The main core of the paper was conceived and conducted by Kyriaki Goulouti (mechanical experiments, computational methodology). The numerical analysis was developed in collaboration with Ioannis Lymperopoulos.

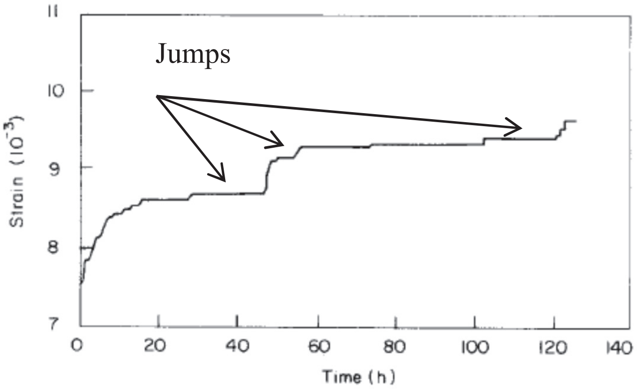

Figure 5.1. Compression creep of GFRP[5].

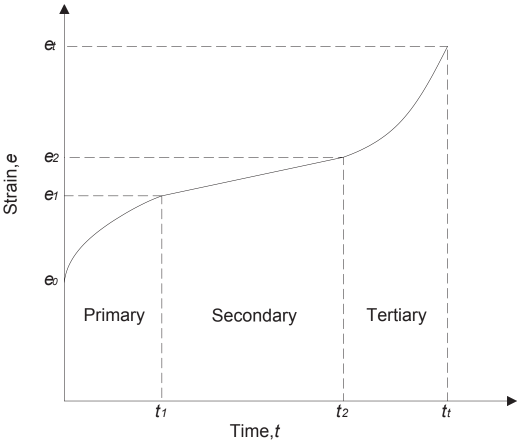

Figure 5.2. Typical creep curve.

The existing methodologies for the analysis of the long-term creep behavior of materials include theoretical and phenomenological models (spring-dashpot models), empirical models (power law models), superposition principles and the Prony series. The most frequently used techniques in the literature are Findley's formulation and the general power law[6]. Focusing on the studies using these methods, there are cases in which the application of a specific model and the fitting of a predefined equation proved to be inappropriate to capture the real trend of the material's behavior; [7,8,9,10] are examples in which the model overestimates or underestimates the actual deformation. This can also be attributed to the fact that these methods are able to describe only the primary creep stage, characterized by a rapid increase in creep deformation. The secondary creep however exhibits a smooth and steady deformation increase, a trend that cannot be described by a power formulation[7]. It should be noted though, that in cases of a high creep rate these methods perform well in predicting the deformation[11]. Furthermore, these fitting methodologies are applied to the whole experimental data series without validating the model or providing a specific measure of the accuracy and associated error[7-16]. Likewise, no indications regarding the reliability of the long-term prediction are given, resulting in possible misinterpretation of the material's behavior.

With regard to the second question and the irregular stepwise creep deformation, in all the aforementioned studies the experimental results show such a stepwise response and in [7,8,12,14] this phenomenon is more pronounced. These sudden steps or jumps are randomly distributed along the timeline of the experiment and should be differentiated from the measurement noise[5] resulting from temperature variation or the inaccuracy of the measurement device. Similar steps have also been reported for other materials, e.g. steel, copper, aluminum, nickel-based alloys, amorphous polymers, and nanocomposites[17-25.] The explanations of the non-uniform increasing deformation for these materials refer to the structure of the materials and more precisely to the « non-uniform distribution of the creep-strengthening material », « dislocation by interaction with a series of defects, resulting from dynamic ageing in creep », «dislocation-disclination », and «interfacial diffusion and sliding». The fact that a physical reason underlies the formation of the steps in metals could imply that such behavior is also linked to the material structure of FRPs. To the authors' knowledge, no study has ever discussed the possible existence of a physical reason concerning the stepwise creep behavior of FRPs.

The current study deals with the two aforementioned topics. First, a new methodology is proposed to explain and predict creep deformation, which is more appropriate to the experimental creep data. The new model is derived by identifying the creep rate in order to capture the trend of the creep deformation. For validation reasons, different training lengths of the experimental data are taken into account. Moreover, a probabilistic approach was also employed, namely the Non-homogeneous Poisson Process (NHPP), in order to treat the stepwise response of the creep deformation. Finally, the results of the two methods are compared with the general power law, in terms of predictability for a period up to 25 years.

5.2. Experimental set-up

Four experimental data series were used for the analysis of the new methodologies concerning the creep phenomenon. Three of the four creep experiments were performed within the framework of the structural validation of a new FRP thermal break. The thermal break has been described in detail in Chapter 3 and its structural concept is presented schematically in Fig. 5.3. The creep experiments concerned the compression creep of the glass fiber reinforced polymer (GFRP) hexagon sandwich component, responsible for transmitting the shear forces under the vertical load on the balcony cantilever and the tension creep of the aramid fiber-reinforced polymer (AFRP) loop component, responsible for transmitting the tensile forces of the bending moments.

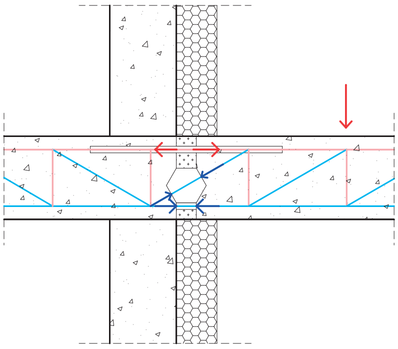

Figure 5.3. Structural concept of new A/GFRP thermal break.

The GFRP hexagon sandwich is composed of a hexagonal shaped PU foam around which three laminates are wound in three directions. The nominal thickness of each one of the three overlapping laminates is 2.0 mm. The GFRP laminates are each composed of 12 layers of an E-glass UD-tape each, resulting in a fiber volume fractions of 47%. The AFRP loop component has a 15x10mm cross section and consists of 110 loops of a Kevlar-49 roving. The resulting laminate has a nominal fiber volume fraction of 41%. All the dimensions and details concerning these specimens can be found in Chapter 3.

Two compression creep experiments were performed under two load levels; 20kN and 25kN, for a period of one month and one tensile creep experiment was performed under a sustained load at 20kN, for a period of six months. The experiments were performed in a conditioned room under steady, controlled temperature (20°) and humidity (RH=70%). The set-up for the creep experiments, is presented in Fig. 5.4 for both specimens. The creep frame is a hydraulic drive system and it is designed for the application of a tensile load. Special creep cages were used, in order to transform the tensile load into a compressive load for of the creep compression experiments. Load cells were used, in order to control the stability of the applied load. As far as the measuring system is concerned, two LVDTs , (HBM LVDTS 10mm, 80 mV/V ± 1%), were used on both sides of the specimen, to measure the total deformation of the specimen. An HBM QuantumX data logger was used. During loading, the frequency of the measurements was 20Hz and it was reduced to 1Hz for the first hour. The frequency was further reduced to 0.02Hz and was maintained at this level until the end of the experiments. The experimental results for the creep deformation are presented in Fig. 5.5a for the compression creep (elastic deformation e_{25C}=0.46mm and e_{20C}=0.32mm) and 5.5b for the tension creep (elastic deformation e_{20T}=1.175mm).

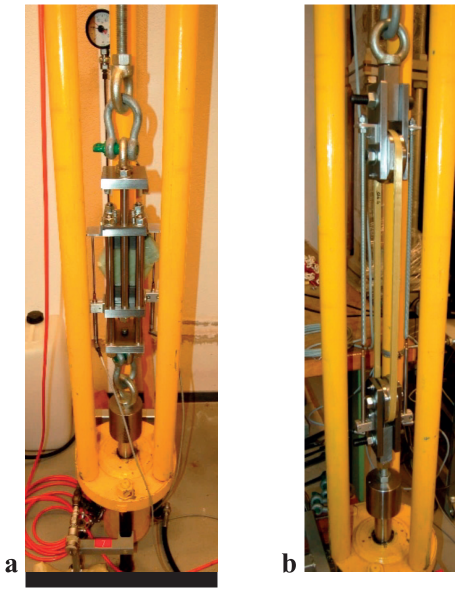

Figure 5.4. Creep set-up of a) GFRP hexagon sandwich component and b) AFRP loop component.

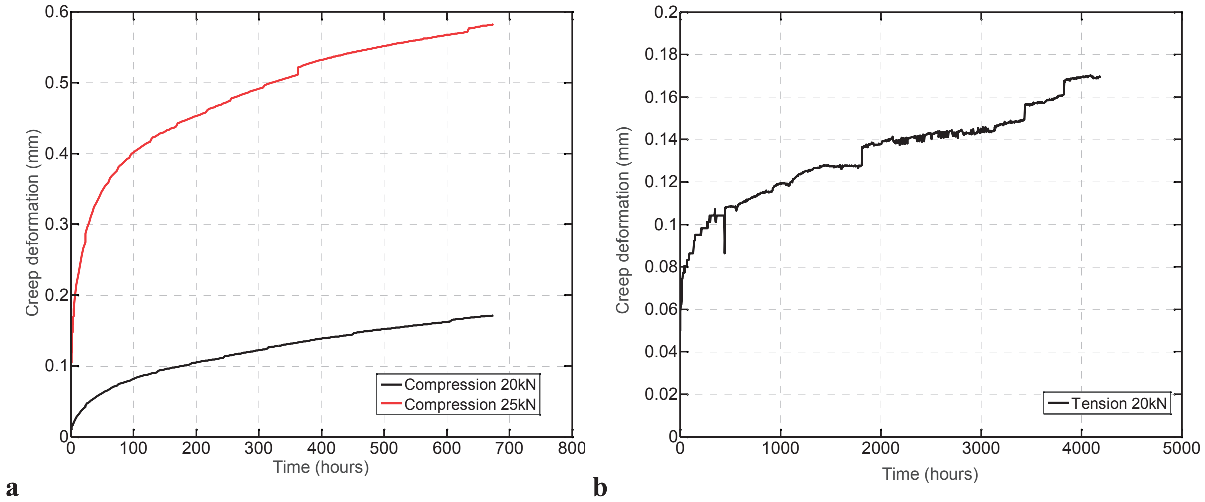

Figure 5.5. Creep deformation of a) compression creep of GFRP hexagonal sandwich components and b) tension creep of AFRP loop.

A fourth experiment concerned the long-term four-point bending creep investigation of a GFRP box-girder for a testing period of 25 years[25]. The flanges were fabricated of unidirectional profiles and the webs of ±45° filament-wound laminates, of a nominal thickness of 3mm. The creep load was 60kN and the creep deflection was measured ‘in the center of the girder in the region of the constant bending moment’[25]. The experimental results for the creep deflection (e_{60B}= 11.40mm) are presented in Fig. 5.6.

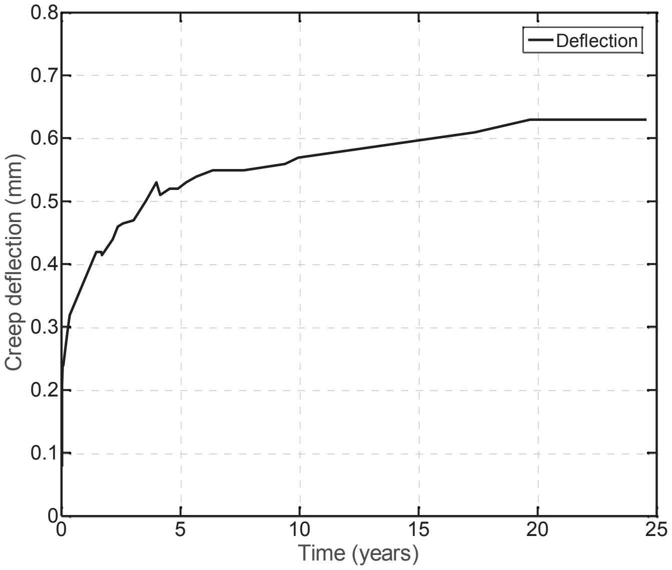

Figure 5.6. Creep deflection of GFRP box girder[26].

5.3. Modeling and results

5.3.1. Findley's Law and General Power Law

Among the most frequently used methodologies for analyzing the creep behavior are the general power law and Findley's power law, as expressed in Eq. (1) and (2), respectively. The general power law assumes a two terms form as follows

$$\varepsilon = \varepsilon_0 + \varepsilon_c = \varepsilon_0 + m\left(\frac{t}{t_0}\right)^{n_F} \tag{1}$$

where ε is the total strain at time t , ε_0 is the instantaneous elastic strain at time t_0, ε_c is the time-dependent creep strain, and m and n_F are dimensionless material parameters which can be graphically determined, by fitting the experimental creep data. Findley assumed specific hyperbolic relationships between ε_0 and m, which were derived from the rheological behavior of polymeric materials. Findley's formulation is expressed by Eq. (2), which gives the time-dependent strain, (ε), under a specific stress level, (σ)

$$\varepsilon = \varepsilon'_{0_F} \sin h\left(\frac{\sigma}{\sigma_{e_F}}\right) + m'_F \sin h\left(\frac{\sigma}{\sigma_{m_F}}\right)\left(\frac{t}{t_0}\right)^{n_F} \tag{2}$$

where ε'_{0_F} , σ_{e_F} , m'_F, σ_{m_F}, n_F are material parameters which can be graphically determined from the fitting of at least three experimental data series from three different stress levels.

Findley’s law was not applied to these experimental results, either because there were not at least three load levels available (in the case of AFRP tension creep and GFRP box-girder bending creep experiments), or because the available experimental data did not exhibit the required linearity, due to the sligthly different material properties (GFRP compression creep), as described in Chapter 3.

The general power law was applied for the time dependent deformation, δ_c, and a linear regression model, Eq. (3), was fitted to the measured creep deformation

$$\delta_c = at^b + c \tag{3}$$

where a, b, c are regression coefficients and t is the time. The procedure was programmed with Matlab, by fitting the equation directly to the data, using the least squares optimisation procedure for the determination of the model parameters and without transforming the data to loglog scale. This led to slightly different results, compared to Chapter 3.

Validation

In order to validate the prediction capability of the methods described here, different portions of the data were used for regression (training the model) and for model validation. Defining the critical point in the timeline that separates which measurements shall be used for training and which for validation is generally difficult, since no particular defining point exists by default. Thus, a study was performed by taking different training lengths, to examine the sensitivity of the model, and measure its predictability at the end of the experiment. We consider here that for all methods examined, their short-term predictability (i.e. after one month), also provides an indication regarding their long-term predictability (e.g. prediction after 25 years).

Different training lengths were used; 50%, 60%, 70% and 80% of the total available data and the remaining part, respectively, for validation. The different fittings were evaluated in terms of goodness of fit by the coefficient of determination (R^2) and the root mean square error (RMSE). The average of these coefficients for the different training lengths, 50%-80%, is presented in Table 5.1. The coefficients of determination for all the experiments are close to 1, with standard deviations approaching zero, while the RMSEs are insignificant with small standard deviations.

Table 5.1. Average of goodness of fit for different training lengths of the power law.

Creep experiments	R^2	*RMSE*
Compression creep 20 kN	0.999±0	0.00105±0
Compression creep 25 kN	0.998±0.0009	0.0045±0.001
Tension creep 20 kN	0.9796±0.008	0.00245±0.0002
Bending creep 60 kN	0.996±0.0010	0.0107±0.0018

Fig. 5.7 shows the results of the 25kN compression creep for two different training lengths 50% and 80%. The power law accurately predicted the deformation for the 80% training length, since the difference between the measured and the predicted deformation was approximately 0.2%, while for the 50% this difference was around 3%. Furthermore, Fig. 5.8 shows the results of the tension experiment. The traditional power law was not accurate in simulating the creep deformation, since the predicted deformation was always approximately 10% lower than the measured one, independently of the training length. During the first 140 days, the power law modeled and predicted well the deformation, however, after this time point time, significant deformation jumps occurred that changed the trend of the creep deformation and led to inconsistencies between the data and the model.

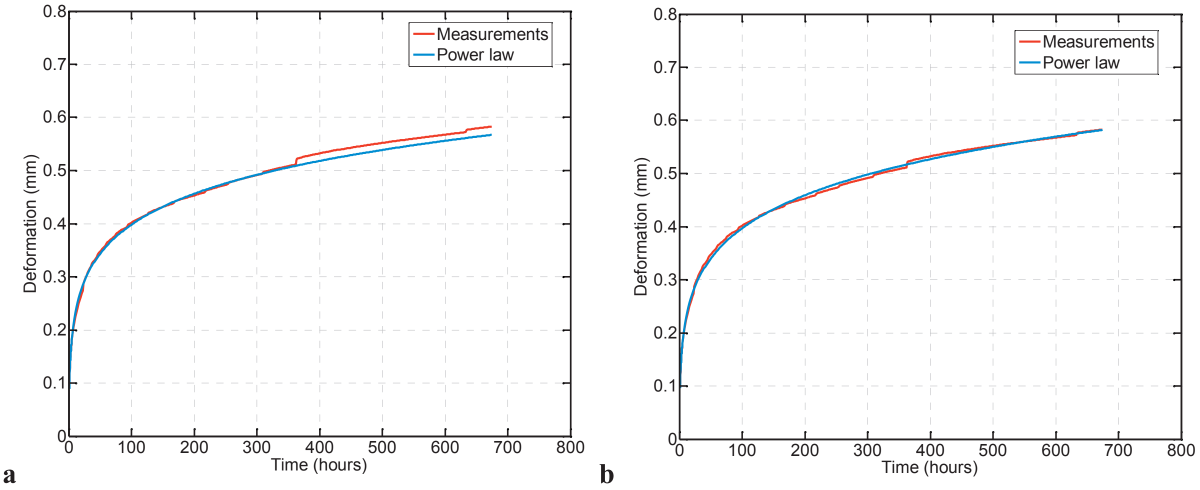

Figure 5.7. Power law models. Compression creep at 25kN: a) 50% for fitting and 50% for validation, b) 80% for fitting and 20% for validation.

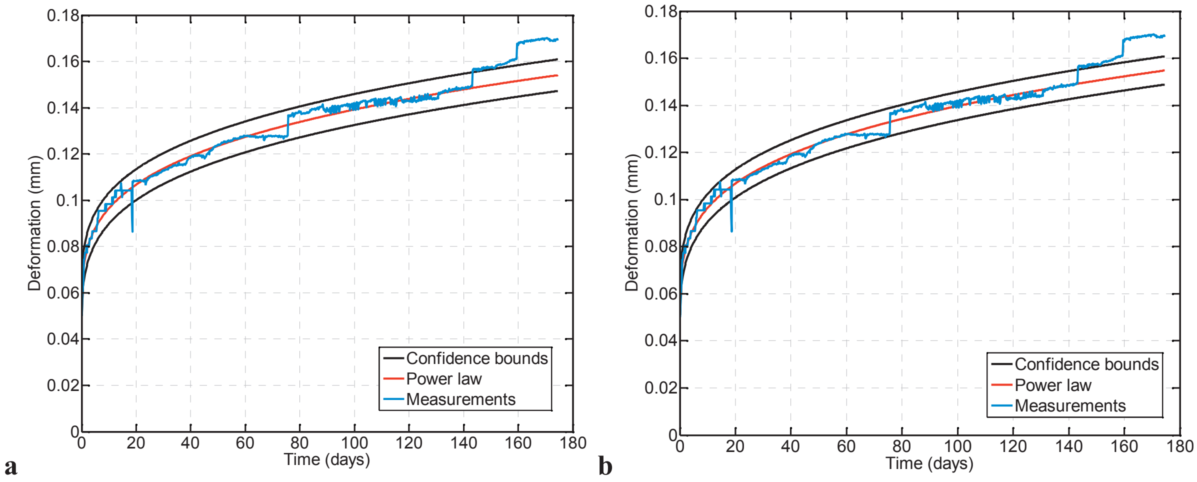

Figure 5.8. Power law models. Tension creep of 20kN: a) 50% for fitting and 50% for validation, b) 80% for fitting and 20% for validation.

Fig. 5.9 shows the results of the same approach for the 25-year long-term beam experiment and in this case the differences were more pronounced. The power law model does not follow the trend of the system's response and it always overestimates the deformation, after approximately 5 years. From this time point, when the specimen probably enters the secondary creep stage, there exists a slower increase of the deformation with a steadier slope. This behavior cannot be captured by the power law model, which continues to increase without changing its trend.

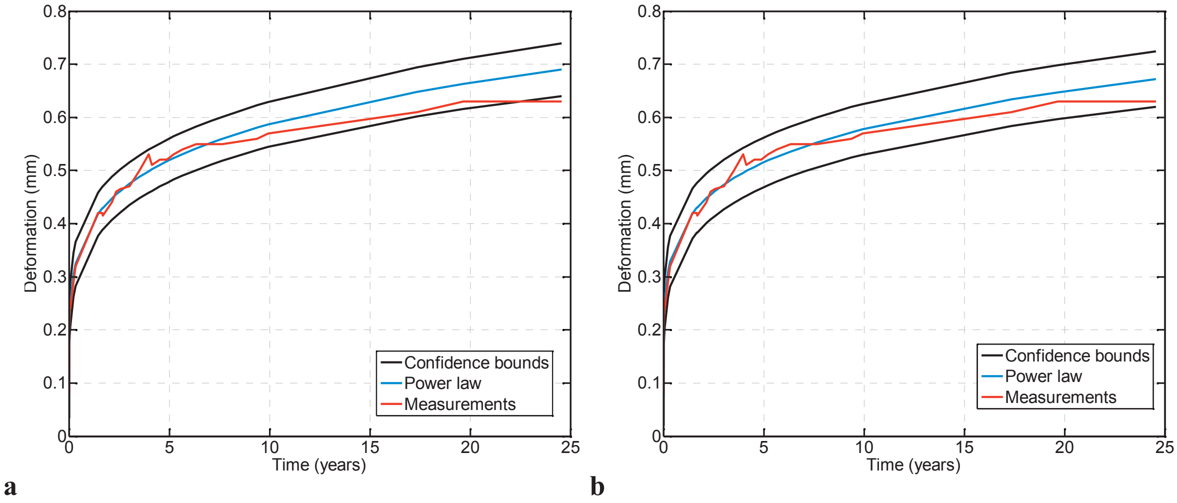

Figure 5.9. Power law models. Bending creep of 61kN: a) 40% for fitting and 60% for validation, b) 80% for fitting and 20% for validation.

Table 5.2 shows the Root Mean Square Error (RMSE) of the prediction and the error of the final deformation for all the experiments and training lengths. For the compression creep experiments the power law predictions are sensitive to the different training lengths. By increasing the data from 50% to 80%, the RMSE is reduced by a factor of approximately 8 e.g. for the 25kN compression creep, while the final deformation by a factor of 3. The tension creep exhibited similar behavior for all the training lengths, because of the deformation jumps that changed its trend, in the end of the experiment. As far as the bending creep is concerned, the RMSE and the error of the final deformation were also similar for all the training lengths, resulting from the secondary creep phenomena.

Table 5.2. Power law model validation for all the creep experiments.

Training lenghts	***Comp. Creep 20kN***		***Comp. creep 25kN***		***Tension creep 20kN***		***Bend. creep 60kN***	
	RMSE (‰)	**Error (%)**	**RMSE (‰)**	**Error (%)**	**RMSE (‰)**	**Error (%)**	**RMSE (‰)**	**Error (%)**
50%	4.38	4.07	12.85	2.74	7.72	9.41	30.6[1]	5.00
60%	3.13	2.91	6.96	1.20	7.06	7.64	----	----
70%	2.40	1.97	2.11	0.34	8.67	8.23	25.6	3.46
80%	1.71	1.74	1.50	0.17	11.36	8.82	17.36	2.70
Average	2.76±1		4.54±4.6		8.19±1.64		30.6±2.82	

[1] 40% for the bending creep, due to the available data.

5.3.2. Gradient Regression and Non-Homogeneous Poisson Process

In this work, two complementary methodologies are presented for the modeling and prediction of the creep deformation. With regard to the first one (gradient regression), a creep model is extracted by identifying the creep rate; i.e. the gradient of the creep deformation. This procedure allows both capturing the rapid increase of the creep deformation, which occurs during the first stage, and the subsequent identification of the creep trend of the secondary creep stage, which is characterized by a steady creep rate. The second method takes advantage of the information derived from the creep rate, and uses a stochastic approach to predict the future creep deformation, by taking into account deformation jumps. This probabilistic part is simulated using a NHPP (Non-Homogeneous Poisson Process) method.

The experimental data measure the creep deformation, excluding the instantaneous elastic deformation, ε_0, and constitute measurements of time (t_O in seconds) and the corresponding creep deformation (Y_O in mm), $D_i = \{t_O(i), Y_O(i)\}_{i=1}^{N_s}$, where O denotes for original data and N_s is the total number of the collected samples. In order to avoid and reduce possible measurement artifacts, facilitate the computational procedure and reduce calculation time, the sampling rate was decreased by down sampling the data. For this reason, data were selected every N_d step from the original dataset.

Due to the higher frequency at the beginning of the experiment (see next section), the time measurement differences were not constant. To simplify the regression problem, a constant time-step was used and the data were linearly interpolated. The final data series had the form, $D_f = \{t(i), Yi)\}_{i=1}^{N_s/N_d}$, Fig. 5.10.

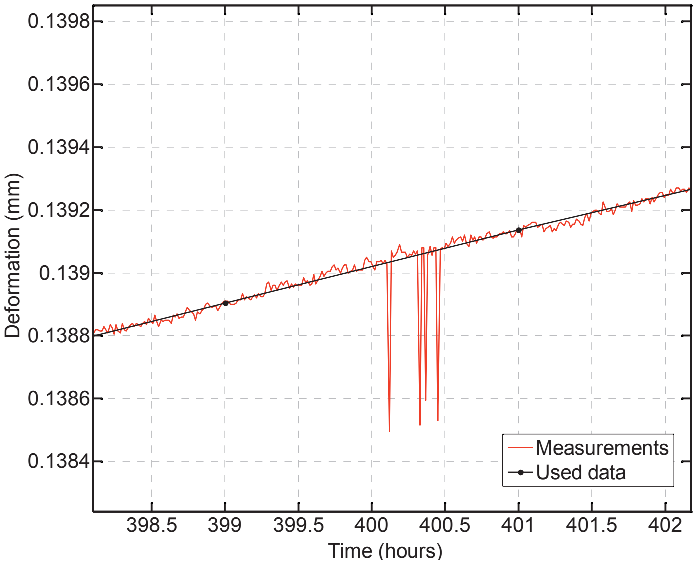

Figure 5.10. Data cleaning, for simplification of regression problem, for compression creep 20kN.

5.3.2.1. Gradient Regression

The reason for choosing the gradient regression, instead of the absolute value regression, lies in the physical process underlying the creep deformation. The creep phenomenon is described by a natural monotonicity, since the deformation increases during the experiment and never diminishes. However, the growth rate of the creep deformation decreases with time, as it approaches and throughout the secondary creep stage. It becomes steady at a future time point, t_s, and reaches a lower threshold at the beginning of the tertiary creep stage. Computationally, this trend is described by the gradient, which becomes smaller, towards zero, as time passes.

The gradient of the creep deformation was approximated through forward finite differences as described by Eq. (4).

$$\Delta Y(k) = \frac{Y(t(k+1)-Y(t(k-1))}{t(k+1)-t(k-1)}, \qquad k = 1\!:\!N\ \ /N\ \ -1 \tag{4}$$

A preliminary study was conducted and a number of possible models were evaluated in terms of goodness of fit by statistical measures (RMSE, R^2). The derived creep gradient model is a decaying rational functions, Eq.5, (x variable denotes the time).

$$g(\theta) = \frac{p_1 x + p_2}{x^2 + q_1 x + q_2}, \tag{5}$$

The parameters $\theta = \{p_1, p_2, q_1, q_2,\}$, were estimated using the least squares optimization procedure, against the interpolated dataset. The optimization procedure was naturally non-convex and multiple start events were used, to prevent it from becoming in local-minima. After determination of the optimal parameters, the actual creep curve, can be calculated, by integrating the estimated creep gradient. It is important to note that for this method, all data were included, including the random jumps of the creep deformation.

Fig. 5.11 shows the gradient of the compression creep at 20kN, with the fitted Eq. (5), and the 99% confidence intervals, as well. The final model of the creep deformation after integration of the gradient has the form of Eq. 6,

$$\delta_c = \int_0^t g(\theta)d \tag{6}$$

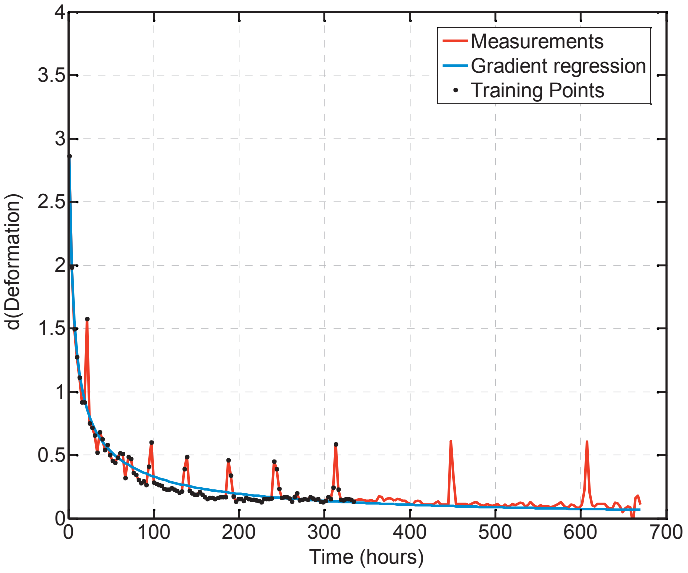

Figure 5.11. Gradient and fitted model, with training length 50%, for the compression creep 20kN.

The same procedure, concerning the training lengths was followed in the case of the gradient regression. The average of goodness of fit is shown in Table 5.3 for all the experiments and different training lengths. It should be noted that the measures inTable 5.3, refer to the fitting of the gradient and they are thus not directly comparable with the corresponding measures of the general power law, which refer to the fitting of the absolute values of the creep deformation. The worst case was the tension creep, which exhibited an irregular behavior.

Table 5.3. Average of goodness of fit for different training lengths of the gradient regression.

Creep experiments	R^2	*RMSE*
Compression creep 20 kN	0.92+0.008	0.1+0.008
Compression creep 25 kN	0.97+0.005	0.33+0.02
Tension creep 20 kN	0.13±0.018	0.27±0.022
Bending creep 61 kN	0.95±0	0.016±0.0054

Fig. 5.12 shows the fitting and the model validation of the 25kN compression creep. The 50% training length almost concured with a deformation jump and thus leading to high RMSE, while for the case of 80% training length, the latter diminished by a factor of approximately 7. For the case of tension creep the results are shown in Fig.5.13. The gradient regression doesn't perform well, in both cases, because of the deformation jumps, occured in the end of the experiment. However, this was not the case for the 80% training length, since the 80% almost concured with the deformation jumps. Furthermore, the results for the long-term beam experiment are shown in Fig. 5.14. These results were more promising, since independently of the training lengths used, the deformation up to the end of the experiment and the final deformation were accurately predicted. For the former the final deformation was overestimated by only 0.63% and for the latter it was overestimated by 2.5%. The good results obtained from the long-term data showed that with the gradient regression the effects of the secondary stage of the creep deformation could be modeled, since the diminishing creep rate was simulated by the decaying function.

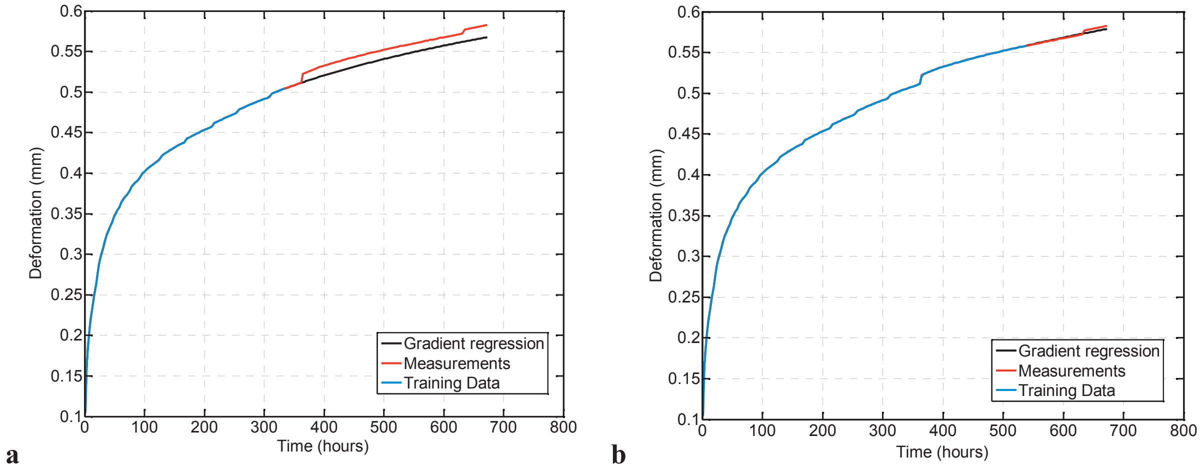

Figure 5.12. Compression creep at 25kN – Gradient regression, a) 50% and b) 80%.

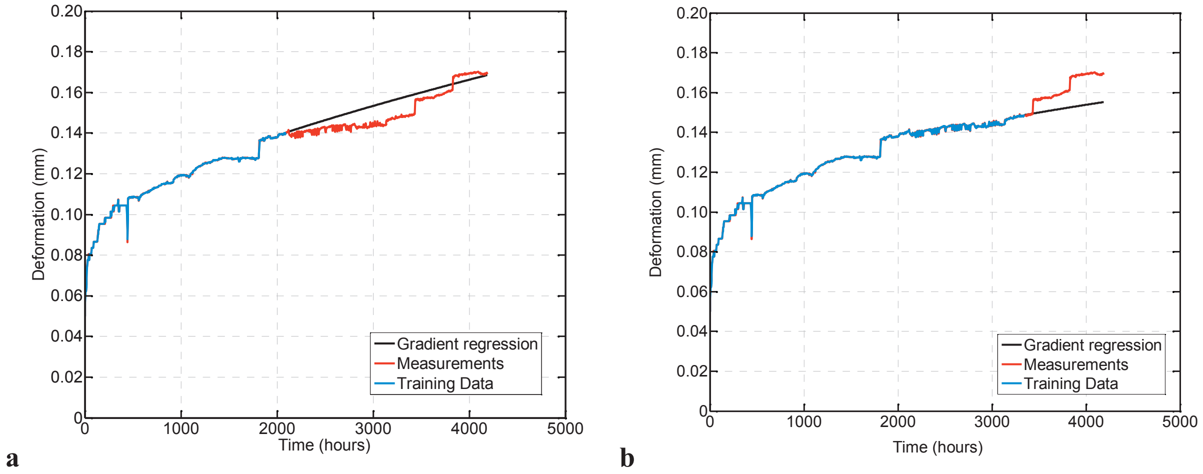

Figure 5.13. Tension creep at 20kN – Gradient regression, a) 50% and b) 80%.

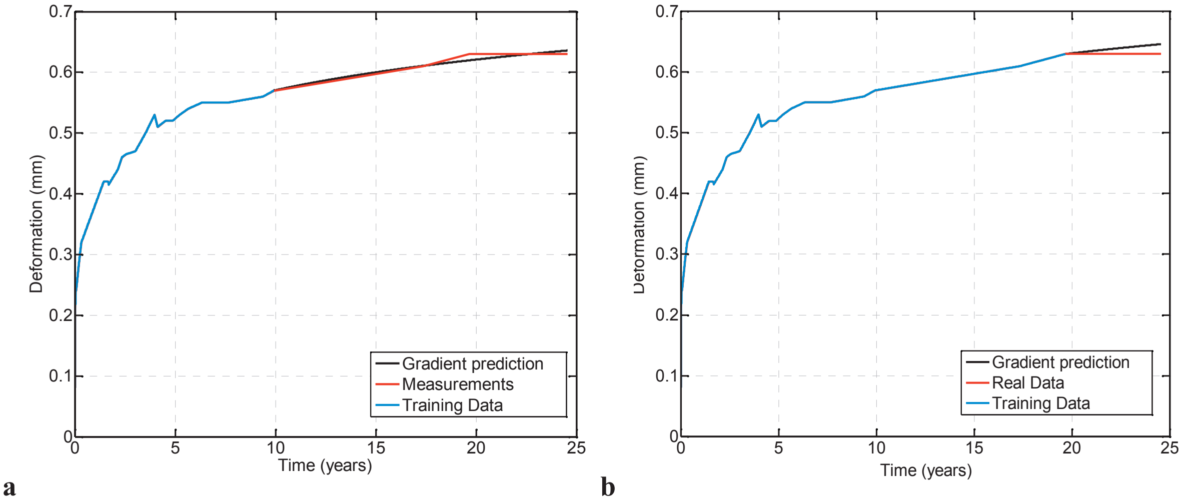

Figure 5.14. Long-term bending creep for 50% and 80% training lengths of gradient regression.

In Table 5.4 the model validation is presented for all the experiments. All the experiments could be accurately described and predicted by the gradient model, with small prediction errors. Concerning the compression experiments, as from the 60% training length, the errors remained at the same level. This shows that from this time point (60% corresponds to 18 days) the specimens exhibit a steadier behavior, probably entering the secondary stage. The tension creep experiment, exhibited better performance for small number of training lengths, due to deformation jumps in the end of the experiment. Finally, the long-term creep experiment showed a very good behavior, independently of the training length, signifying that once the specimen has entered the secondary creep stage the gradient regression can indeed model accurately the creep deformation.

Table 5.4. Gradient regression validation for all the creep experiments.

Training lenghts	***Comp. Creep 20kN***		***Comp. creep 25kN***		***Tension creep 20kN***		***Bend. creep 60kN***	
	RMSE (‰)	**Error (%)**	**RMSE (‰)**	**Error (%)**	**RMSE (‰)**	**Error (%)**	**RMSE (‰)**	**Error (%)**
50%	6.60	6.97	11.15	2.47	6.05	0.85	4.00	0.94
60%	2.95	3.00	1.55	0.25	6.00	6.00	---	---
70%	1.58	1.60	1.53	0.35	12.21	11.65	5.70	0.84
80%	0.97	0.57	1.80	0.54	11.06	8.80	9.70	2.60
Average	2.28±4		1.70±8		8.8±5.5		5±7	

[1] 40% for the bending creep, due to the available data.

5.3.2.2. Non-Homogeneous Poisson Process (NHPP)

The study continued with the separate treatment of the jumps appearing randomly in the data. A data-driven approach was followed, since independently of the underlying mechanism that creates them, their presence affects the long-term prediction accuracy of the creep deformation. The creep deformation is underestimated if they are not taken into account, since each jump results in an increase and this will also irregularly continue in the future. In order to consider the potential influence of these steps and assimilate it in the prediction of the creep deformation, a probabilistic approach and in particular a Poisson process was used to describe the stochasticity of their replication.

The first step of the method is the identification of the stepwise response (random jumps) as they occur in the data. Jumps were defined as all the deformation events in the creep-rate that did not follow the monotonically decreasing trend, but they had an opposite (increasing) effect on the gradient. To avoid including measurement jitter, a lower threshold was defined as to what constitutes a jump (this was adjusted to the different experimental data behavior).

During the analysis of the data, it was observed that most of the jumps exhibited a similar magnitude of deformation see Fig. 5.15. For this reason and to simplify the stochastic analysis, a constant magnitude for all identified jumps was assumed and was defined as the average of the magnitudes observed. For the isolated cases where the magnitude of the jump was significantly different, it was assumed that several jump-events occurred almost simultaneously. These values were identified separately for each experimental data set.

The Poisson process is a probabilistic model used in queuing theory. The process describes the probability of independent events (e.g. jumps in the creep deformation) that occur during a finite time interval. The Poisson process is used when the rate of the events, $\Lambda(t) = \Lambda$, occurring in a time interval, t, is constant and known. The process does not assume information concerning the magnitude and the exact timing of the events within the interval. In this case, the number of events, $N(t)$, occurring in a finite time interval is a random variable and is defined by the Poisson distribution, Eq.(7):

$$P\{N(t) = n\} = \frac{(\Lambda)^n}{n!} e^{-\Lambda} \tag{7}$$

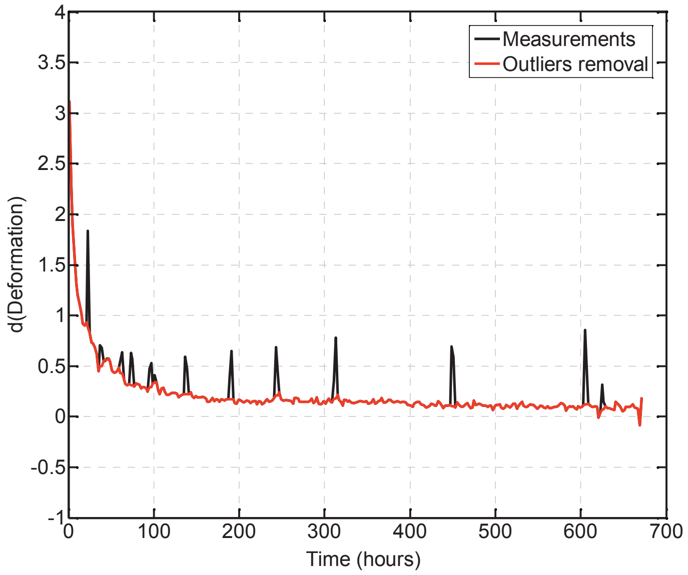

Figure 5.15. Jump identification for 20kN compression creep.

When the rate of the events, *Λ(t)*, does not remain constant but varies in time the process is designated non-homogeneous. In this case the rate of the Poisson process, *Λ (t),* is a deterministic function of time, $\lambda(t)$, and has to be identified from the experimental data. Consequently, the expected number of the random events is described by Eq.(8):

$$E[N(0,t)] = \int_0^t \lambda(u)d \tag{8}$$

To define the Poisson distribution for the specific problem of the jumps in the creep deformation, the number of jumps, *N(t)*, was counted during a defined time interval, $[t(n), t(n+1)]$, in the gradient of the deformation. The frequency of the occurrence of the jumps was not constant, and as time elapsed fewer and fewer jumps occurred, see Fig.5.15. Hence a decaying function of time was fitted to the number of the events, Eq. (9), according to the non-homogeneous Poisson process methodology[27]. The heterogeneous with time rate of Poisson events, was set as *Λ (t) = N(t)*, Since this process has a random stochastic character, multiple scenarios *S* (e.g. S = 300, 400, verifying the consistency of the results) were used for the simulation in order to collect statistics. The Poisson random draw was repeated, for each scenario, at each time interval according to its respective *Λ (t)* as in Eq. (10), (*x* variable denotes the time).

$$h(x) = \frac{d_1x+d_2}{x^2+b_1x+b_2}, \tag{9}$$

$$O_t^s \sim P \qquad (\Lambda(t)), \quad s = 1,2,\dots S, \quad t = 1,2,\dots N_t \tag{10}$$

Where d_1, d_2, b_1, b_2 e are regression coefficients. The rest of the data, without the jumps, were treated with the same models, $g(\theta)$, as before. The expected creep deformation was finally modeled by the integration of $g(\theta)$ and the addition of the jumps, Eq. 11:

$$E[\delta_c] = \int_0^t g(\theta)d \ + \int_0^t \lambda(u)d \qquad (11)$$

The model was validated by taking into account different training lengths, as before. Table 5.5 shows the goodness of fit for all the analyzed experiments. The tension creep showed the worst performance, as before, for the same reasons. Furthermore, the 25-year experiment was not considered for the NHPP, since no obvious jumps occured during the duration of the experiment, possibly due to the low frequency of the measurements.

Table 5.5. Average of goodness of fit for different training lengths of the NHPP.

Creep experiments	***R^2***	***RMSE***
Compression creep 20 kN	0.92+0.008	0+0.01
Compression creep 25 kN	0.972+0.008	0.31+0.046
Tension creep 20 kN	0.126+0.02	0.265+0.022

Fig. 5.16 shows the results of the 25kN creep compression for 50% and 80% training lengths. In both cases, the final deformation could be accurately predicted, while the change in the creep trend due to the jumps was captured with the probabilistic approach and the final real deformation was within the scenario deformation range. Fig. 5.17 shows the tension creep experiment. Independently of the training length, the final deformation was within the probabilistic scenarios. The 80% case was more interesting, since the NHPP could accurately predict the final deformation even if there were significant jumps at the end of the experiment.

Finally, Table 5.6 presents the prediction errors of all the experiments. The same conclusions concerning the different training lengths can be drawn as for the gradient method. For the compression experiments after 60% training length the errors stabilized, showing the smoother creep behavior. As for the tension creep, independently of the relative high errors, the final deformation was within the probabilistic scenario range. The good results exhibited by the NHPP prove that the stochastic approach is the only way to deal with the random deformation jumps.

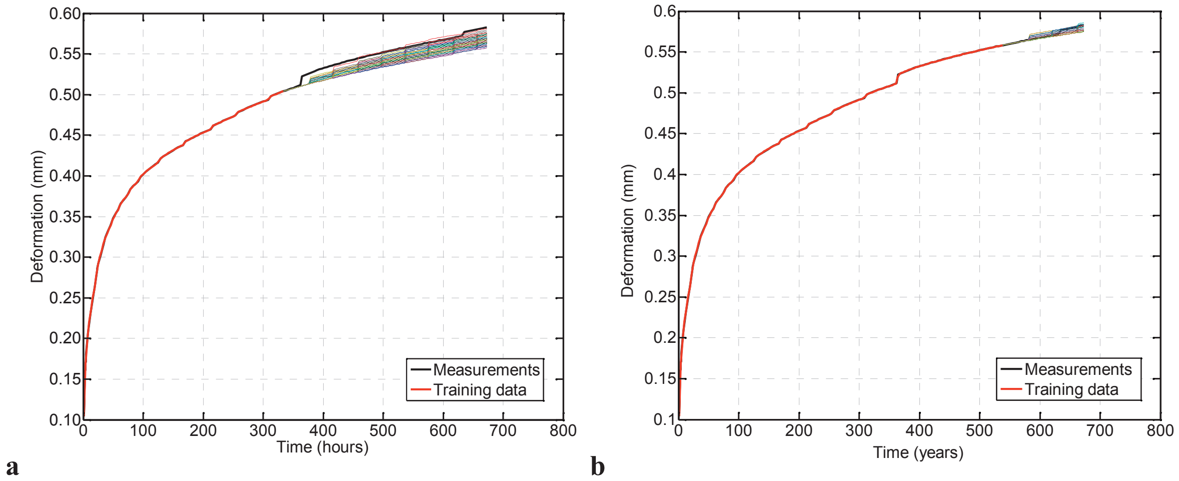

Figure 5.16. Compression creep at 25kN – NHPP, a) 50% and b) 80%.

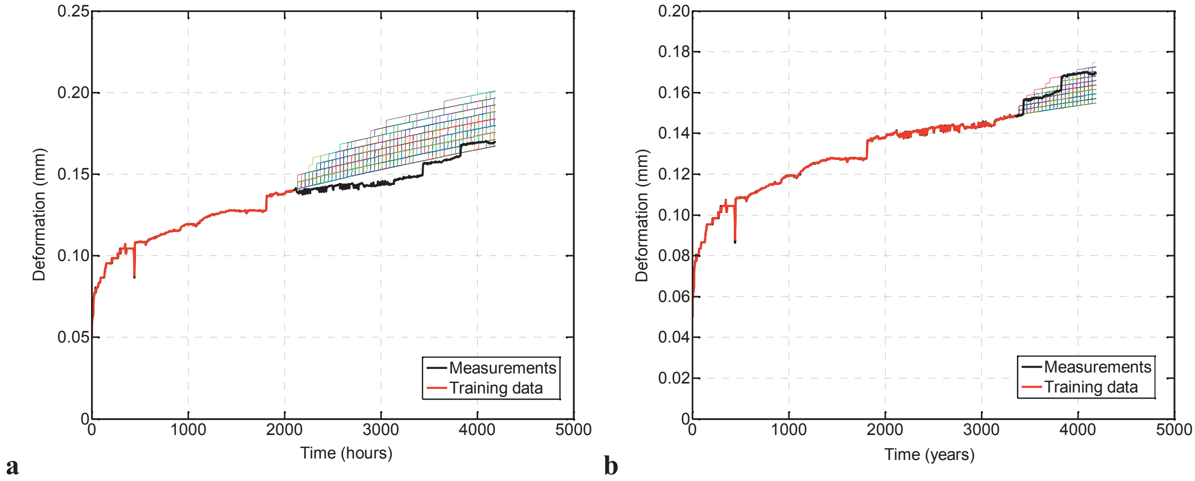

Figure 5.17. Creep deformation prediction with NHPP for the 20kN tension creep, a) 50% and b) 80% training lengths.

Table 5.6. Gradient regression validation for all the creep experiments.

Training lenghts	***Comp. Creep 20kN***	***Comp. creep 25kN***	***Tension creep 20kN***
	RMSE (‰)	**RMSE (‰)**	**RMSE (‰)**
50%	5.70	12.50	12.40
60%	1.30	5.3.0	5.00
70%	1.00	2.15	8.50
80%	1.00	2.00	6.80
Average	1.15±4	3±8	7.7±5

5.4. Discussion

The results of the three methodologies show a better performance of the gradient regression and the NHPP compared to that of the power law. The calculated prediction errors (still modest for all the methodologies) were on average higher for the power law model for all the different training lengths, see Fig. 5.18a. Furthermore, comparing the gradient and the power law model, the final deformation predicted by the gradient method was closer to the real value, Fig.5.18b. There were only a few cases where the gradient regression performed less well than or similarly to the power law, mainly for the tension creep. The fact that the short-term prediction error was smaller for the gradient and the NHPP indicates that these models could be more reliable for the long-term predictions, not only for the final future deformation but also for the specimen's overall future creep behavior.

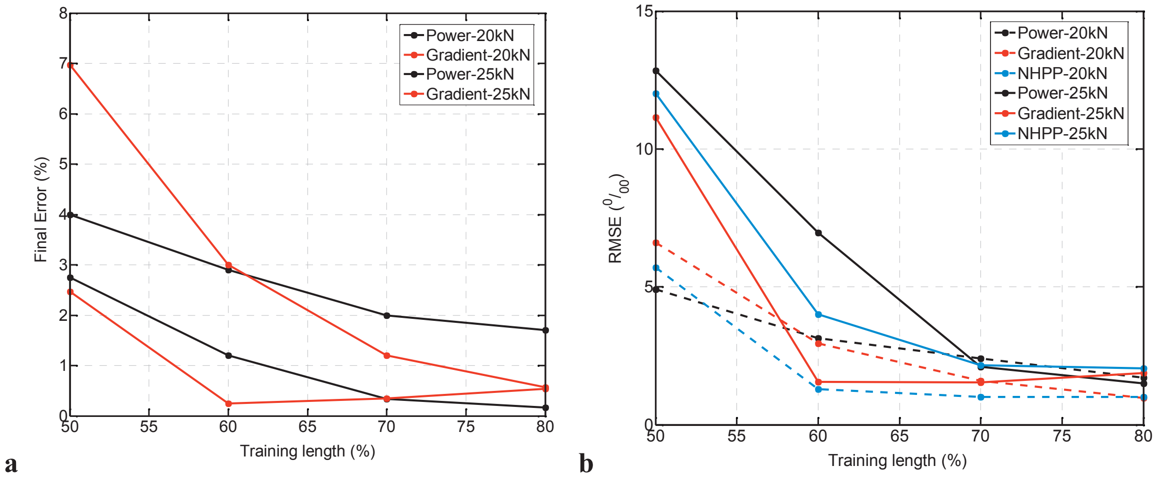

Figure 5.18. a) RMSE for different methods and different training lengths for compression experiments. b) difference of final predicted deformation.

Furthermore, the gradient and the NHPP were less sensitive than the power law to the training length, as shown by Tables 5.2, 5.4 and 5.6. After 60% training length (for the compression and tension creep experiments), these methods were more stable and data-independent than the power law. This shows that from this time point, the new methods captured a change in the creep rate, resulting from the secondary creep phenomenon. The gradient regression can thus identify the time point at which the secondary creep stage begins, along the experiment.

In addition, once the specimen enters the secondary creep stage, the gradient regression is more reliable for future predictions as shown from the long-term (25-year) bending creep experiment, in which the gradient regression captured the asymptotic secondary creep trend. Fig. 5.19a summarizes the RMSEs computed for different training lengths and Fig. 5.19b shows the final predicted deformation for the gradient regression and the power law. Apart from two peaks in the errors, the rest of the results show the better performance of the gradient regression. The power law prediction errors always remained at the same levels, independently of the training lengths used, overestimating the final real deformation by a maximum of 9%.

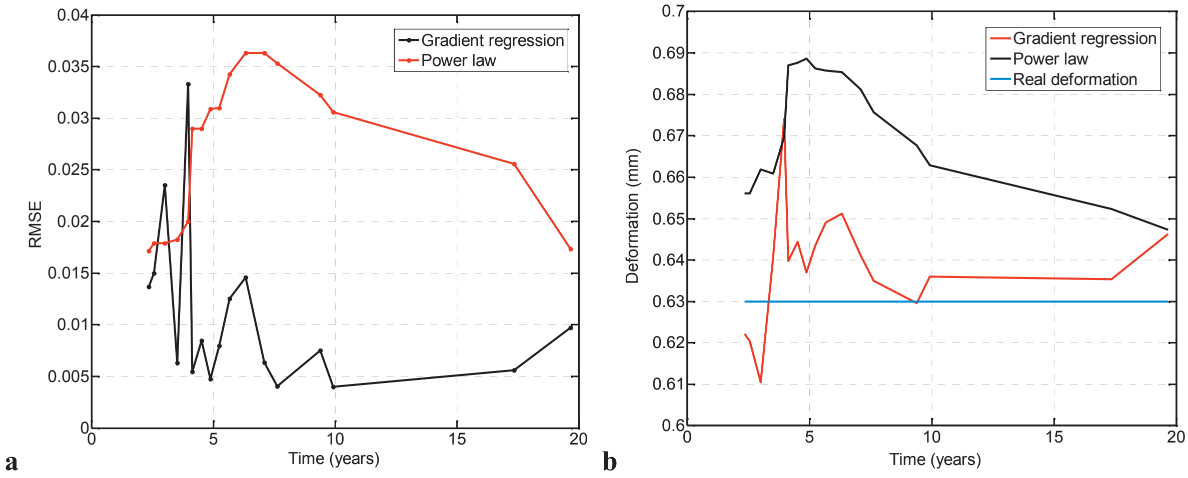

Figure 5.19. Gradient regression and power law prediction for 25 years bending creep, a) RMSE and b) Deformation, starting from 2.4 years training length.

Since the aforementioned thermal break will be used for balcony connections in new constructions, its long-term behavior is crucial throughout the building's service life; 50 years, according to the building codes. In this study, the deformation was extrapolated in future time steps and specifically after half of the building's life, i.e. 25 years, using the three methods, see Figures 5.20-22. Without experiments to validate these future extrapolations, the long-term prediction can give only indications regarding the system's future response. The power law predictions were always higher than those of the new methods, regarding the compression creep experiments. On the contrary, for the tension creep the power law exhibited lower response, resulting from the fact that the power law could not model the deformation jumps in the end of the experiment, as presented in Fig. 5.8. Furthermore, the shape of the gradient regression model during the 25-year extrapolation shows the high creep rate of the primary creep during the first years and the steady creep rate of the secondary stage. Finally, the difference between the gradient and the NHPP predictions depends on the number and magnitude of jumps that occurred during the experiment. Hence, disregarding the jumps may lead to a high degree of inaccuracy of the future deformation, as is for the case for 20kN compression and tension creep. If no significant jumps are present, both methods exhibit a similar performance, as for the 25kN compression creep.

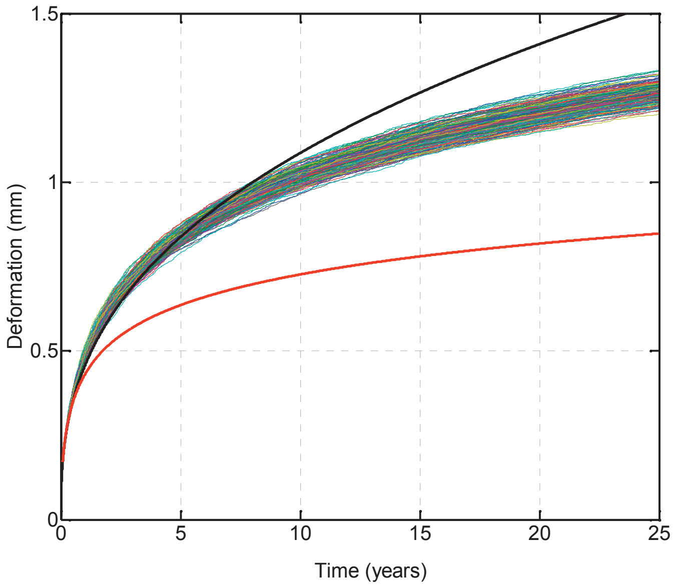

Figure 5.20. 20kN compression creep 25 years prediction, NHPP scenarios (varicolored lines), Power law (black line), Gradient regression (red line).

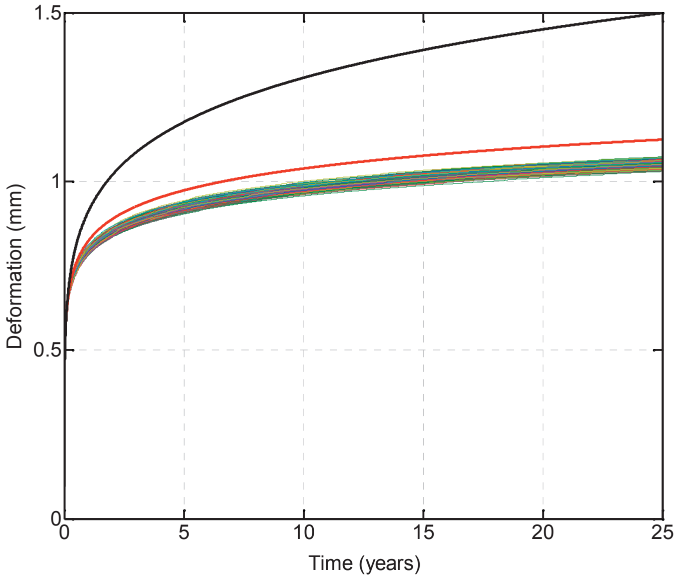

Figure 5.21. 25kN compression creep 25 years prediction, NHPP scenarios (varicolored lines), Power law (black line), Gradient regression (red line).

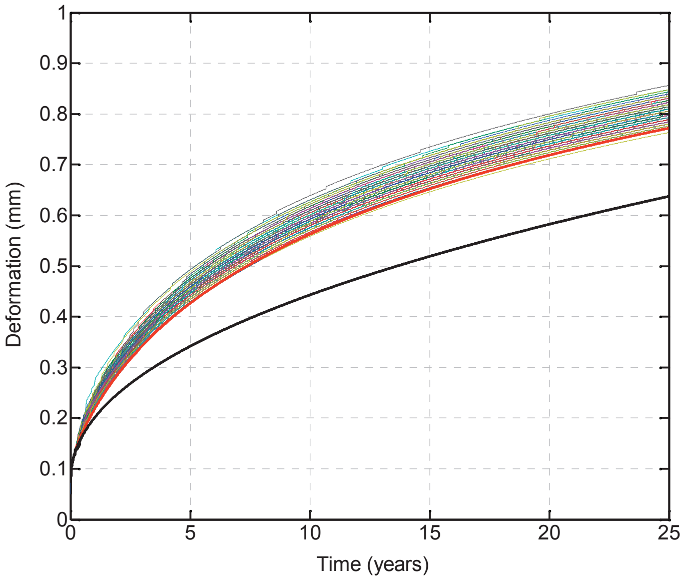

Figure 5.22. Loop tension creep 25 years prediction, NHPP scenarios (varicolored lines), Power law (black line), Gradient regression (red line).

5.5. Conclusions

Based on the creep experimental results, a comparative study was presented in this paper. The power law model was compared with two new proposed methods, the gradient regression and the NHPP. The following conclusions were drawn:

1) The gradient regression when compared to the original data regression enables the identification of the decreasing creep rate at the beginning and during the secondary creep stage.

2) The errors of the gradient and the NHPP models for predictions up to the end of the experiment were smaller than the errors of the power law model except for a few specific cases.

3) An appropriate way to consider the effect of the deformation jumps, which could be substantial in future predictions, is to use a probabilistic approach. In this study the NHPP was employed and it demonstrated a high degree of prediction accuracy.

4) The methods are promising for simulating time-dependent phenomena and creep prediction.

5.6. References

1. Goulouti K, de Castro J, Keller T, Aramid/glass fiber-reinforced thermal break –thermal and structural performance, Composite Structures, 136, 2016.

2. Goulouti K, de Castro J, Keller T, Aramid/glass fiber-reinforced thermal break – system structura performance, Composite Structures, 136, 2016.

3. Ascione F, Berardi V P , Leo F, Giordano A, An experimental study on the long-term behavior of CFRP pultruded laminates suitable to concrete structures rehabilitation, Composites Part B: Engineering, 39, (7-8), 2008.

4. Ascione L, Berardi V P, D'Aponte A, Creep phenomena in FRP materials, Mechanics Research Communications, 43, 2012.

5. Irion M N, Adams D F, Compression creep testing of unidirectional composite materials, 12, (2), 1981.

6. Lee L S, Creep and time-dependent response of composites, Louisiana Tech University, USA.

7. Scott D W, Zureick A-H, Compression creep of a pultruded E-glass/Vinylester composite, Composites Science and Technology, 58, (8), 1998.

8. Huang J-S, Gibson L J, Creep of sandwich beams with polymers foam cores, Journal of Materials in Civil Engineering, 2, 1990.

9. Garrido M, Correia J R, Branco F A, Keller T, Creep behavior of sandwich panels with rigid polyurethane foam core and glass-fibre reinforced polymer faces: Experimental tests and analytical modelling, Journal of Composite Materials, 48, (18), 2014.

10. Shao Y, Shanmugam J, Deflection of pultruded composite sheet piling, Journal of Composites for Construction, 8, 2004.

11. Findley N W, 26-Year creep and recovery of Poly(Vinyl Chloride) and Polyethylene, Polymer engineering and science, 27, 1987.

12. Bank LC, Mosallam A S, Creep and failure of a full-sized fiber reinforced plastic pultruded frame, Composites Engineering, 2, (3), 1992.

13. Bottoni M, Mazzotti C, Savoia M, Creep tests on GFRP pultruded elements subjected to traction or shear, Composite Structures, 108,2014.

14. Choi Y, Yuan R L, Time-Dependent Deformation of Pultruded Fiber Reinforced Polymer Composite Columns, Journal of Composites for Construction, 7, 2003.

15. Holmes H, Rahman T A, Creep behavior of glass reinforced plastic box beams, Composites 11,(2), 1980.

16. McClure G, Mahammadi Y, Compression creep of pultruded E-glass-reinforced-plastic angles, Journal of Materials in Civil Engineering, 7, 1995.

17. Sikka V K, David S A, Discontinuous creep deformation in a Type 316 Stainless steel casting, Metallurgical Transactions A, 12, 1981.

18. Monteiro S N, Luiz T da S, Le May U, On the nature of strain perturbations in the creep curves of austentic stainless steel, Scripta Metallurgica, 15, 1981.

19. Klueh R L, King J F, Unusual creep behavior in a commercial nickel-chromium alloy, Scripta Metallurgica, 13, 1979.

20. Lubahn J D, Felgar R P, Plasticity and Creep of Metals, J. Willey and Sons, 1961.

21. Andrade E N da C, On the viscous flow in metals and allied phenomena, Proceedings of the Royal Society Mathematical Physical and Engineering Sciences, 84-A, 1910.

22. Mori T, Nakasone Y, Taya M, Wakashima K, Steady-state creep rate of a composite: Two dimensional analysis, 75, (6), 1997.

23. Bershtein V A, Yakushev P N, Laser-Interferometric Creep Rate Spectroscopy of Polymers in Polymer Characterization, Advances in Polymer Science, 230, 2010.

24. Peschanskaya N. N, Step Deformation of Solid Amorphous Polymers, Physics of the solid state, 43 (8), 2000.

25. Peschanskaya N. N., Shpeizman V. V., Sinani A. B., Smirnov B. I., Micrometer-Scale Deformation Jumps at Different Stages of Creep in Solids, 46. (11), 2004.

26. Meier U, Müller R, Barbezat M, Terrasi G P, Box Girders under Extreme Long-Time Static and Fatigue Loading, CICE 2010- The 5th International Conference on FRP Composites in Civil Engineering, Beijing, China.

27. Leemis L, Estimating and Simulating Nonhomogeneous Poisson Process, Department of Mathematics, The College of William&Mary, 2003.

6 Conclusions and future work

6.1. Conclusions

The current research presented a new concept for an innovative, high-performance FRP thermal break for the balcony connections of concrete structures. The thermal break was thermally and structurally validated and its time-dependent behavior studied. The main conclusions of this research are discussed in the following.

The impact of the potential thermal losses through FRP and conventional thermal breaks was computed over the total transmission losses, the losses through opaque elements and the heating requirements of three building envelopes; a MINERGIE, a MINERGIE-P and an optimum envelope, defined via a parametric analysis. The losses through thermal bridges represent 5% of the total transmission losses of an optimum envelope if an FRP thermal break is used. Furthermore, FRP thermal break losses represent 14% of the transmission losses through the opaque elements for an optimum envelope, while thermal bridge losses through conventional thermal breaks represent 34% of the losses through opaque elements. Finally, the losses through thermal bridges are reduced by 41% for an optimum envelope if an FRP thermal break is used instead of a conventional one. The thermal performance evaluation showed that the more optimized the building envelope, the greater the importance of the thermal bridge losses in relation to the building energy losses.

The three-dimensional thermal simulation of the FRP thermal break revealed that linear thermal transmittances of less than the SIA target value (ψ=0.15W/mK) and even close to ψ=0.10W/mK could be achieved in specific cases. The highest thermal transmittances (ψ=0.23W/mK) are still below the SIA limit value (ψ=0.30 W/mK). It is important to note that these values are exhibited in cases where the maximum load capacity of the thermal break is exploited. In energy terms, the best FPR thermal break configuration consists of an AFRP loop combined with two AFRP hexagon sandwiches. Finally, the FRP thermal break combined with the highly insulating aerogel material leads to high internal superficial temperatures and high internal comfort for the user.

AFRP and GFRP hexagon sandwich specimens were subjected to compression loads, applied in the intermediate laminate, using different load introduction set-ups. As expected, the GFRP specimens exhibited higher strength and the AFRP specimens higher stiffness. The differences, however, were not significant, indicating that the AFRP specimens can also be used for the shear-compression diagonal. The correlation of the results with the foam density shows that the lowest strength and stiffness were exhibited by the specimens with the lowest foam density. The failure mode was similar for all the specimens, independently of fiber type and foam density, and it always occurred along the transition lines from the semicircular to the straight laminate parts (transverse to the fiber direction) on both ends of the diagonal. Finally, the specimens were not sensitive to compression creep phenomena. Their stiffness and strength were considerably affected by the alkaline environment however. Nonetheless, the durability experiments represented an unrealistic simulation that is highly unlikely to occur.

The AFRP loop component exhibited high strength and stiffness, with a certain scatter resulting from the manual fabrication of the specimens. The failure mode was consistent for all specimens and was always initiated at the transition from the semicircular to the straight part of the loop. The mechanical properties of the AFRP loop remained unaffected by the tension creep phenomena and the alkalinity environment, being within the scatter of the specimens.

The structural performance of the FRP thermal break was verified by six full-scale beam experiments and five of these included the basic FRP thermal module (one AFRP loop combined with two A/GFRP hexagons). Three different load configurations were applied, affecting the initial stiffness and ultimate load of the beams; the highest values were exhibited for the shortest lever arm, i.e. for higher shear forces and smaller moments. Furthermore, the different fiber type of the hexagons did not affect the beams' response, confirming that the aramid fibers can be also used, taking advantage of their enhanced thermal performance. The failure modes confirmed the ductile concrete failure and in the case of AFRP hexagons a simultaneous wrinkling of the sandwich faces occurred. The structural system's behavior can be adequately described by a simple statically determined truss model, while the beam deflection can be estimated by adding the deflections caused by a concentrated rotation in the thermal break to those of a continuous concrete slab. Finally, the maximum balcony span that could be achieved with the current system is approximately 2.50 m.

The time-dependent mechanical behavior of the GFRP hexagons, the AFRP loop and a GFRP box girder documented in literature was additionally studied, using numerical methods. Two new approaches were proposed for the long-term prediction of the creep deformation. The first one, based on the gradient regression of the creep data, enables the identification of the decreasing creep rate, with the potential simulation of the secondary creep stage. This was clearly proven by the successful prediction of the 25-year creep deformation of the GFRP box girder, in which the associated error was always far below that of the power law method for all the different training data (50%-80%). As far as the second method is concerned, the probabilistic consideration of the random jumps, normally occurring during creep experiment, became possible thanks to the non-homogeneous Poisson process. This method proved that the jumps can significantly influence the long-term creep prediction and in cases where they are disregarded, the predicted deformation can be underestimated, as shown in the case of the AFRP loop component.

6.2. Original contributions

The original contributions of the current thesis to the topic are introduced in this section.

a) Quantification of the thermal losses through FRP and conventional thermal breaks in relation to the overall energy balance of different building envelopes and also the optimized building envelope for Switzerland's climatic conditions.
b) Determination of the optimum envelope by parametric analysis, using a second-order degree model, for cold climatic conditions and its visual depiction with the response surface method.
c) Development of a new FRP thermal break for the balcony connections of concrete structures, with enhanced thermal and structural performance.
d) Development of two new approaches for the prediction of long-term creep deformation. The gradient regression is able to predict the secondary creep stage, while the NHPP can successfully describe the random jumps occurring in the creep deformation.

6.3. Recommendations for future work

In this section the potential continuation of this research topic is listed.

a) The thermal performance of the FRP thermal break should be further evaluated through thermal simulation under transient temperature conditions in order to study the effect of the thermal capacity of the FRP thermal break in the critical thermal bridge location.
b) Full-scale steady-state and transient-state experiments for the FRP balcony connection to validate the simulation results, calibrate the simulation model and achieve more accurate results, closer to reality.
c) Development of new models for the transient-state thermal bridge losses, derived by statistical methods.
d) Hygrothermal phenomena should also be studied as well as the hygrothermal performance of the FRP materials in this critical balcony connection.
e) Development of new models for the steady-state thermal bridge losses, which take into account the effective thermal bridge region.
f) Study of the seismic behavior of the FRP thermal break and structural enhancement, in order to permit its application in highly seismic zones.
g) Multi-objective optimization of the hexagon sandwich component, in terms of its thermal and structural response.
h) Enhancement of the system's performance in Momend Mode, by bending downwards the AFRP loop, in order to avoid the concrete top crushing failure.
i) Vibration control of the FRP thermal break and comparison with the steel thermal break.
j) Gradient regression of creep deformation to take into account the different load levels.
k) Additional verification of new proposed creep methodologies with further experiments and different materials.

List of Figures

Figure 1.1.	*Different types of thermal bridges.*	2
Figure 1.2.	*Balcony thermal bridge.*	2
Figure 1.3.	*Typical thermal break with steel bars currently used for balcony connections.*	3
Figure 1.4.	*New FRP thermal break.*	4
Figure 1.5.	*Structural system of new FRP thermal break.*	4
Figure 2.1.	*Typical thermal break with steel bars currently used for balcony connections.*	11
Figure 2.2.	*3D visualization of case study building.*	13
Figure 2.3.	*Plan of ground floor (dimensions in [m]).*	13
Figure 2.4.	*Plan of first floor (dimensions in [m]).*	14
Figure 2.5.	*Section A-A with envelope (insulation layers).*	14
Figure 2.6.	*Relative effects of most important parameters and interactions on heating requirements.*	20
Figure 2.7.	*Half normal plot of parameters and all interactions.*	21
Figure 2.8.	*Losses through thermal breaks as percentage of total transmission losses and function of envelope type and thermal transmittance of thermal breaks.*	23

Figure 2.9. *Losses through thermal breaks as percentage of those through opaque elements and function of envelope type and thermal transmittance of thermal breaks.* 24

Figure 2.10. *Losses through thermal breaks as percentage of heating requirements and function of envelope type and thermal transmittance of thermal breaks.* 25

Figure 3.1. *Traditional stainless steel thermal break for balconies.* 30

Figure 3.2. *Structural concept of new A/GFRP thermal break.* 32

Figure 3.3. *New thermally-insulated A/GFRP thermal break: a) prefabricated element, b) element placed from top into pre-installed concrete slab reinforcement.* 33

Figure 3.4. *AFRP loop; dimensions in (mm).* 34

Figure 3.5. *A/GFRP hexagon sandwich: a) tape layers, b) PU foam core and adhesively-bonded GFRP UD compression bar, dimensions in (mm).* 34

Figure 3.6. *A/GFRP thermal break: FE-model for thermal performance evaluation (0.15m unit spacing), a) thermal break model (one half-unit), b) element integrated into slab-wall segment acc. to ISO 10211:2007.* 37

Figure 3.7. *A/GFRP thermal break: linear thermal transmittance as function of element unit spacing (15, 30 and 45cm), hexagon fiber type and wall U-value.* 37

Figure 3.8. *A/GFRP thermal break; temperature field (in C) in connector zone.* 38

Figure 3.9. *A/GFRP hexagon sandwich a) AFRP specimen, b) GFRP specimen with additional epoxy layers on embedded laminate parts for set-up S1, c) for set-ups S2 and S3.* 39

Figure 3.10. *A/GFRP hexagon sandwich: compression experiment set-up, a) S1, b) S2, c) S3 (red line indicates machine load axis).* 40

Figure 3.11. *A/GFRP hexagon sandwich: creep experiment, set-up S1.* 40

Figure 3.12. *A/GFRP hexagon sandwich: load-displacement responses in S2 experiments.* 41

Figure 3.13. *A/GFRP hexagon sandwich: stiffness and ultimate load vs. density relationships of S2 experiments.* 43

Figure 3.14. *A/GFRP hexagon sandwich: failure mode a) partly confined; b) fully confined.* 44

Figure 3.15. *A/GFRP hexagon sandwich: experimental creep results at different load levels, a) total deformations on linear scale, b) creep deformations on log scale and model.* 44

Figure 3.16. *AFRP loop: a) tension experiment set-up and b) failure mode.* 47

Figure 3.17. *AFRP loop: load-displacement responses.* 47

Figure 3.18. *AFRP loop: experimental elastic and creep deformations and model.* 48

Figure 4.1. *New G/AFRP thermal break: a) components assembled, b) A/GFRP hexagon sandwich component with integrated compression bar, (dimensions in mm).* 56

Figure 4.2. *Experimental set-up with instrumentation and loading positions, dimensions in (mm).* 59

Figure 4.3. *Cross section of experimental beam with one thermal break unit, concrete reinforcement and instrumentation, dimensions in (mm).* 59

Figure 4.4. *Load-deflection responses of all beams (deflections at cantilever end of failure cycle).* 61

Figure 4.5. *Load-deflection responses of beams G200 and G600 during all cycles.* 62

Figure 4.6. *Crack formation and propagation in beam G600 during 15-, 20-, 25-kN cycles.* 62

Figure 4.7. *Failure mode of beam G600: a) top concrete failure in loop anchorage zone, b) cracks through the hexagon diagonals' support area of interior (left) beam, undamaged hexagons in cantilever (right) beam.* 63

Figure 4.8. *Beam G600 at ultimate load: concentrated rotation in insulation gap.* 63

Figure 4.9. *Failure mode of beam A200: a) bottom concrete spalling in interior (left) beam, b) wrinkling/crushing of AFRP hexagon diagonal.* 64

Figure 4.10. *Beam A200 at ultimate load: rotation and vertical offset in insulation gap.* 64

Figure 4.11. *Failure mode of beam G400-1: a) undamaged concrete in interior (left) beam, b) wrinkling of GFRP hexagon diagonal.* 65

Figure 4.12. *Load-strain responses (tension) of AFRP loop at mid-height and mid-gap of all beams (failure cycle).* 65

Figure 4.13. *Load-strain responses (compression) of GFRP bar at mid-height and mid-gap of all beams (failure cycle).* 66

Figure 4.14. *Free-body diagram of thermal break region as basis for design (tension forces in red, compression forces in blue, dimensions in (mm)).* 67

Figure 4.15. *Contributors to deflection at cantilever end of beam G600 (failure cycle).* 72

Figure 4.16. *Ultimate shear load-moment interaction and performance limits.* 72

Figure 5.1. *Compression creep of GFRP.* 78

Figure 5.2. *Typical creep curve.* 78

Figure 5.3. *Structural concept of new A/GFRP thermal break.* 80

Figure 5.4. *Creep set-up of a) GFRP hexagon sandwich component and b) AFRP loop component.* 81

Figure 5.5. *Creep deformation of a) compression creep of GFRP hexagonal sandwich components and b) tension creep of AFRP loop.* 81

Figure 5.6. *Creep deflection of GFRP box girder.* 82

Figure 5.7. *Power law models. Compression creep at 25kN: a) 50% for fitting and 50% for validation, b) 80% for fitting and 20% for validation.* 84

Figure 5.8. *Power law models. Tension creep of 20kN: a) 50% for fitting and 50% for validation, b) 80% for fitting and 20% for validation.* 85

Figure 5.9. *Power law models. Bending creep of 61kN: a) 40% for fitting and 60%for validation, b) 80% for fitting and 20% for validation.* 85

Figure 5.10. *Data cleaning, for simplification of regression problem, for compression creep 20kN.* 87

Figure 5.11 *Gradient and fitted model, with training length 50%, for the compression creep 20kN.* 88

Figure 5.12. *Compression creep at 25kN – Gradient regression, a) 50% and b) 80%.* 90

Figure 5.13. *Tension creep at 20kN – Gradient regression, a) 50% and b) 80%.* 90

Figure 5.14. *Long-term bending creep for 50% and 80% training lengths of gradient regression.* 91

Figure 5.15. *Jump identification for 20kN compression creep.* 93

Figure 5.16. *Compression creep at 25kN – NHPP, a) 50% and b) 80%.* 95

Figure 5.17. *Creep deformation prediction with NHPP for the 20kN tension creep, a) 50% and b) 80% training lengths.* 95

Figure 5.18. *a) RMSE for different methods and different training lengths for compression experiments. b) difference of final predicted deformation.* 96

Figure 5.19. *Gradient regression and power law prediction for 25 years bending creep, a) RMSE and b) Deformation, starting from 2.4 years training length.* 97

Figure 5.20. *20kN compression creep 25 years prediction, NHPP scenarios (varicolored lines), Power law (black line), Gradient regression (red line).* 98

Figure 5.21. *25kN compression creep 25 years prediction, NHPP scenarios (varicolored lines), Power law (black line), Gradient regression (red line).* 98

Figure 5.22. *Loop tension creep 25 years prediction, NHPP scenarios (varicolored lines), Power law (black line), Gradient regression (red line).* 99

List of Tables

Table 1.1. *Thermal conductivity of commonly used materials in thermal breaks.* 3

Table 1.2. *Thesis organization.* 7

Table 2.1. *Thermal conductivity of commonly used materials in thermal breaks.* 11

Table 2.2. *Thermal conductivity of aramid, glass fibers and aerogel materials.* 12

Table 2.3. *Heating needs for examined envelopes and linear thermal transmittances of thermal breaks.* 16

Table 2.4. *Optimum envelope: seven examined parameters with assumed value ranges.* 17

Table 2.5. *Optimum envelope: examined parameters with corresponding four levels.* 21

Table 2.6. *Combinations with the lowest heating needs* Q_h. 22

Table 3.1. *Thermal conductivity of thermal break materials.* 31

Table 3.2. *Hexagon sandwich: PU foam properties (manufacturer data).* 36

Table 3.3. *A/GFRP hexagon sandwich: overview of set-ups and experimental results.* 41

Table 3.4. *Creep parameters and results according to Eq. (2).* 45

Table 3.5. *AFRP loop: overview of experimental results.* 48

Table 4.1. *Cross sections and mechanical properties of components (average experimental values[7]).* 57

Table 4.2. *Parameter overview and main results.* 58

Table 4.3. *AFRP loop tension and GFRP bar compression forces at ultimate load and concrete stresses and confinement factors.* 60

Table 4.4. *Compression diagonal forces at ultimate load and concrete stresses and confinement factors.* 68

Table 4.5. *Horizontal deformations on loop level at ultimate load (failure cycle only).* 69

Table 4.6. *Vertical deformations at cantilever end at ultimate load (failure cycle).* 71

Table 4.7. *Design resistance values for ULS verification.* 73

Table 5.1. *Average of goodness of fit for different training lengths of the power law.* 84

Table 5.2. *Power law model validation for all the creep experiments.* 86

Table 5.3. *Average of goodness of fit for different training lengths of the gradient regression.* 89

Table 5.4. *Gradient regression validation for all the creep experiments.* 91

Table 5.5. *Average of goodness of fit for different training lengths of the NHPP.* 94

Table 5.6. *Gradient regression validation for all the creep experiments.* 95

A

Experimental design

A.1. Introduction

Appendix A presents a further experimental design and analysis based on the four predominant parameters (*WWRA, P O, and U*), resulting from the full factorial design, as described in Chapter 2. The objective of this analysis was to investigate different ways of expressing the relationship between the heating requirements and the four parameters. The understanding of this relationship could lead to a simpler and more standardized way of defining the optimum or the desired envelope for each specific climatic condition.

For this experimental design, three different models were fitted and the results were discussed and compared. 4^4=256 simulations were performed (already used for the determination of the optimum envelope), taking into account four levels for each parameter as well as all the possible interactions. First a constant coefficient model was fitted and the procedure was continued with a linear random coefficient and a quadratic model using the least squares fitting technique.

A.2. Constant coefficient model

The constant coefficient model (Eq.1) was fitted to the response (Q_h), up until the second-order interactions and the outcome of the analysis is presented in Eq. (2):

$$Q_h = Mean + WWRA + P + U + O + WWRA \cdot U + WWRA \cdot P + WWRA \cdot O + U \cdot P + U \cdot O + P \cdot O \qquad (1)$$

$$Q_h = 16.939 + \begin{bmatrix} 0.983 \\ 0.572 \\ -0.295 \\ -1.259 \end{bmatrix} + \begin{bmatrix} -1.638 \\ -0.727 \\ 0.591 \\ 1.773 \end{bmatrix} + \begin{bmatrix} -1.597 \\ -1 \\ 0.308 \\ 2.29 \end{bmatrix} + \begin{bmatrix} -0.364 \\ 0.406 \\ -2.328 \\ 2.29 \end{bmatrix} + \begin{bmatrix} 0.012 & 0.091 & 0.014 & -0.117 \\ 0.161 & -0.042 & -0.038 & -0.081 \\ 0.078 & -0.063 & -0.008 & -0.008 \\ -0.252 & 0.014 & 0.01 & 0.206 \end{bmatrix}$$

$$+ \begin{bmatrix} 0.166 & 0.092 & -0.063 & -0.195 \\ 0.001 & 0.015 & 0.004 & -0.022 \\ -0.102 & -0.028 & 0.018 & 0.072 \\ -0.073 & 0.091 & 0.03 & 0.134 \end{bmatrix} + \begin{bmatrix} 1.286 & -0.059 & -1.113 & -0.114 \\ 0.440 & -0.030 & -0.399 & -0.009 \\ -0.423 & 0.038 & 0.34 & 0.051 \\ -1.359 & 0.058 & 1.230 & 0.072 \end{bmatrix}$$

$$+ \begin{bmatrix} 0.078 & 0.110 & -0.060 & -0.129 \\ 0.078 & -0.006 & -0.026 & -0.045 \\ -0.33 & -0.042 & 0.031 & 0.44 \\ -0.122 & -0.062 & 0.055 & 0.130 \end{bmatrix} - + \begin{bmatrix} 0.079 & 0.004 & 0.003 & -0.022 \\ 0.017 & -0.035 & 0.007 & 0.026 \\ 0.073 & 0.101 & -0.101 & 0.166 \\ -0.167 & -0.070 & 0.091 & 0.166 \end{bmatrix}$$

$$+ \begin{bmatrix} -0.078 & 0.004 & 0 & 0.074 \\ 0.003 & 0.031 & -0.098 & 0.064 \\ 0.048 & -0.017 & 0.009 & -0.040 \\ 0.028 & -0.019 & 0.089 & -0.098 \end{bmatrix} \tag{2}$$

Fig. A.1 shows a dot-plot of the results, from which it can be concluded that the four main parameters have more influence on the system response than their interactions, apart from the interaction *WWRA·O*. This means that the system can be adequately described by a model that does not take into account all the interactions of the involved parameters. The orientation and the window thermal transmittance are the most important influencing the system, having higher negative or positive impacts on the system than other factors i.e. a non-optimal building orientation could result in higher heating needs than a non-optimal *WWR*. According to this model, heating requirements can be minimized with the following combination, *WWRA*=50%, *P*=0.75m, *U*=0.4 kWh/m^2 and *O*=90°, signifying that the main envelope of the building, that with the highest *WWR* (in this case envelope B) should be oriented towards the south.

The constant coefficient model shows the importance of the levels for each specific factor. Hence, if the *WWRA* is increased from 30% to 40%, the impact on the heating requirements is modest, which means that such a decision should be taken after a cost-benefit and a life-cycle analysis of the building. Furthermore, the impact on the heating needs by the balcony projection is multiplied by a factor of two, when the width is increased by 0.25m from level to level. With regard to the window thermal transmittance, the heating requirements are positively influenced as from values of less than 0.6 (kWh/m^2) and combining the results of the latter with the *WWR,* it should be noted that even for a cold climate like Switzerland, it is preferable to combine a higher *WWR* with a lower-performance *U*, than to have a lower

WWR with a high-performance *U*. Finally, the interaction *WWRA·O* with the combinations 20%-50% and 0°-90°, produces the highest positive or negative impact on the system response.

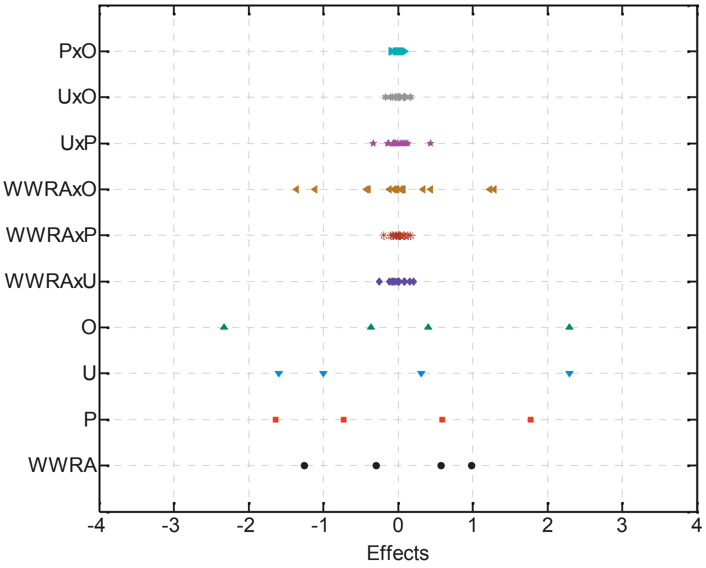

Figure A.1. Dot-plot of constant coefficient model.

The coefficient of determination was $R^2 = 0.99$. The accuracy of the model was verified by the Analysis of Variance of the residuals (ANOVA) and the results are presented in Table A.1. The zero *p-values* indicate that the hypothesis that these four factors have a high influence on the system's response is very probable. Furthermore, the ANOVA table reveals the most important factor, i.e. the orientation *O*, followed by the window thermal transmittance *U,* as already mentioned.

Table A.1. ANOVA table for constant coefficient model.

	SS	*DF*	*MS*	*F*	*p(%)*
Mean	73454.55	1	73454.55	-	-
WWR	189.78	3	63.26	121.07	0.00
U	568.62	3	189.54	362.76	0.00
P	428.70	3	142.90	273.49	0.00
O	700.33	3	233.44	446.78	0.00
Residual	5.51	243	0.02		

A.3. Linear random coefficient model

The analysis was continued by fitting a linear parametric model, using a least squares regression, according to Eq. 3. The regression coefficients are presented in Eq. 4. The parameter interactions were not taken into consideration in this model.

$$Q_h = a_0 + a_1 \cdot WWRA + a_2 \cdot U + a_3 \cdot P + a_4 \cdot O \qquad (3)$$

$$Q_h = 17.35 - 1.14 \cdot WWRA + 1.95 \cdot U + 1.73 \cdot P + 1.42 \cdot O \qquad (4)$$

The model shows that the most important factor regarding heating requirements is the window thermal transmittance, which has the highest regression estimate. It should be noted however that the coefficients of the four examined parameters have the same order of magnitude, meaning that they have a similar influence on the system response. The quality of the model was verified by the trace of the dispersion matrix, $(X^TX)^{-1}$, which is close to zero, Eq. 5. The coefficient of determination was $R^2 = 0.99$. Furthermore, the accuracy of the model was checked by the Analysis of Variance of the residuals (ANOVA) and the results are presented in Table A.2. The zero *p-values* indicate that the hypothesis that these four factors have a high influence on the system's response is very probable. Finally, the ANOVA table reveals the most important factor, i.e. the window thermal transmittance *U*.

$$tr(X^T X)^{-1} = \sum_{i=1}^{n} a_{ii} = 0.0325 \qquad (5)$$

Table A.2. ANOVA table for linear random model.

	SS	***DF***	***MS***	***F***	***p(%)***
Constant	77011.03	1	77011.03	34654.97	0.0
WWR	332.1506	1	332.1506	149.4678	0.0
U	968.2988	1	968.2988	435.7345	0.0
P	768.3984	1	768.3984	345.7793	0.0
O	514.9574	1	514.9574	231.7308	0.0
Residual	560	252	2.222222		

For this model, all the possible configurations are defined each time by keeping two of the parameters constant and plotting the heating requirements as a function of the other two, using a response surface. For example, if the orientation and window thermal transmittance of a building have been predefined as *O*=45° and *U*=0.5 kWh/m^2, the corresponding heating requirements for the different *WWRA* and *P* alternatives are presented in Fig. A.2.

In this graph the best combination is shown from the inclination of the response surface (*WWRA*=50% and *P*=0.75m). Furthermore, the different combinations of the two parameters leading to similar heating are also presented as shown by the straight lines on the *P*-*WWR* plane. As an example, it can be mentioned that similar heating are produced with the following two configurations: a) *WWRA*=35% and *P*=0.75m, b) *WWRA*=50% and *P*=0.95m. Fig. A.3 shows four more possible combinations of the four different factors.

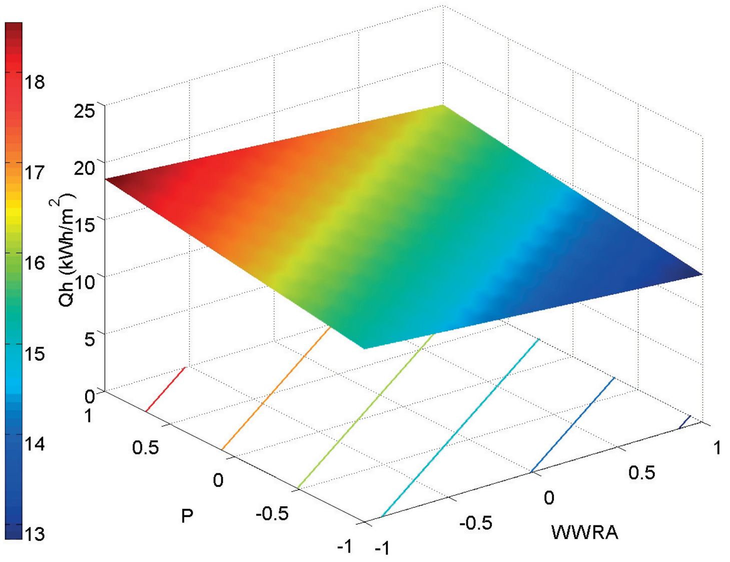

Figure A.2. Heating needs requirements (*Qh*) of linear model as function of *WWRA* and *P*.

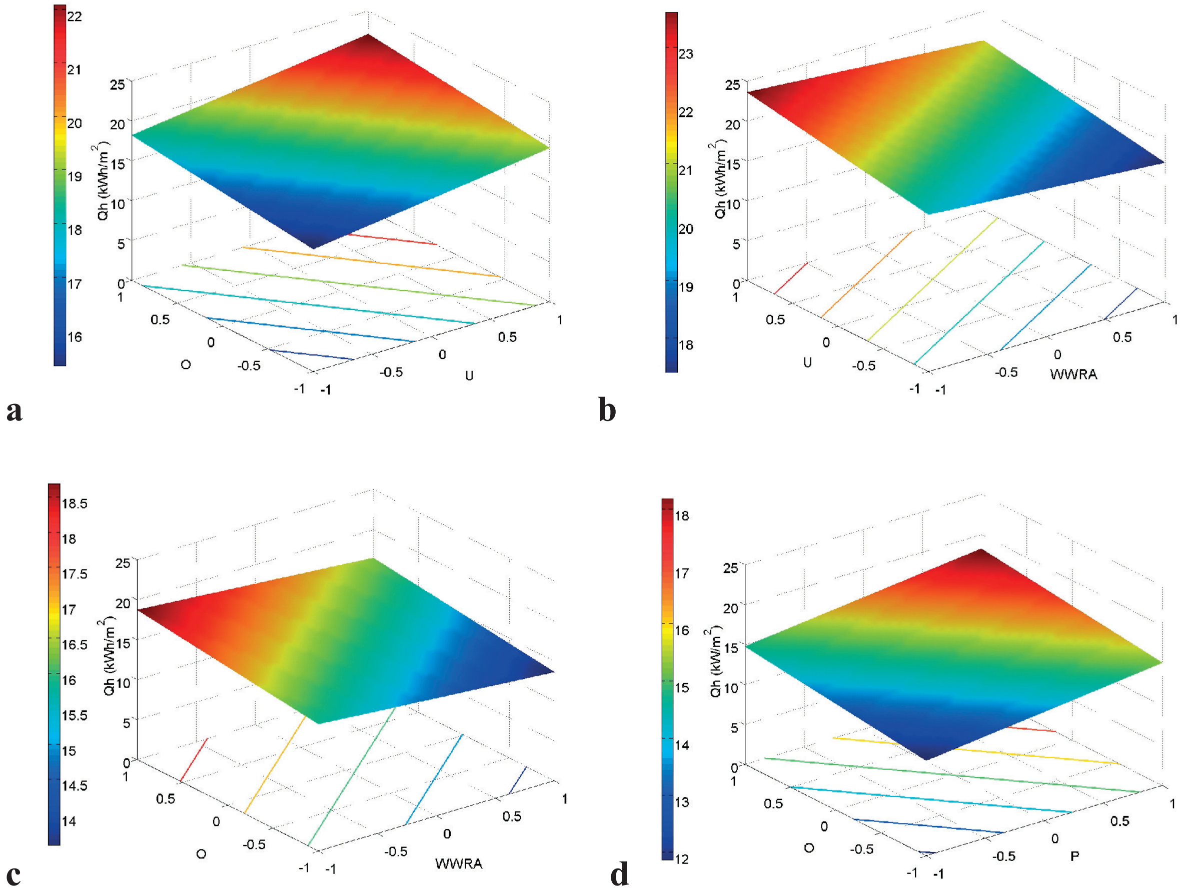

Figure A.3. Heating needs (*Qh*) for different combinations for linear model, a) *WWRA*=40%, *P*=1.25m, b) *O*=315°, *P*=1.25m, c) *P*=1.00m, *U*=0.5W/m^{2}K, d) *WWRA*=30%. *U*=0.4 W/m^{2}K.

A.4. Quadratic random coefficient model

A quadratic model was fitted, based on Eq. 6, using least squares fitting techniques. The interactions were included in the analysis. The model with the regression coefficients is presented in Eq. 7.

$$Q_h = a_0 + a_1 \cdot WWRA + a_2 \cdot U + a_3 \cdot P + a_4 \cdot O + a_{11} \cdot WWRA^2 + a_{22} \cdot U^2 + a_{33} \cdot P^2 + a_{44} \cdot O^2 + a_{12} \cdot WWRA \cdot U + a_{13} \cdot WWRA \cdot P + a_{14} \cdot WWRA \cdot O + a_{23} \cdot U \cdot O + a_{24} \cdot U \cdot P + a_{34} \cdot P \cdot O \tag{6}$$

$$Q_h = 14.97 - 1.04 \cdot WWRA + 1.98 \cdot U + 1.716 \cdot P + 1.03 \cdot O - 0.311 \cdot WWRA^2 + 0.78 \cdot U^2 + 0.153 \cdot P^2 + 2.85 \cdot O^2 + 0.137 \cdot WWRA \cdot U + 0.15 \cdot WWRA \cdot P + 0.37 \cdot WWRA \cdot O + 0.128 \cdot U \cdot O + 0.115 \cdot U \cdot P - 0.067 \cdot P \cdot O \tag{7}$$

This model reveals the higher value of the main effects compared to the interactions except for the second order interaction of *O*, which is the most important parameter concerning the heating needs for this model. Hence, a final version of a quadratic model could include only the main effects and the aforementioned interaction. The coefficient of determination was $R^2 = 0.99$. The quality of the model was verified by the trace of the dispersion matrix, $(X^TX)^{-1}$, which is close to zero, Eq. 8. Furthermore, the accuracy of the model was checked by the Analysis of Variance of the residuals (ANOVA) and the results are presented in Table A.3.

$$tr(X^T X)^{-1} = \sum_{i=1}^{n} a_{ii} = 0.24 \qquad (8)$$

Table A.3. ANOVA table for quadratic model.

	SS	*DF*	*MS*	*F*	*p(%)*
Linear	74926.14	11	6811.468	5848.368	0.00
Quadratic	262.5092	4	65.62729	56.34799	0.00
Residual	280.6875	241	1.164678		
Total	75469.34	256			

For the quadratic model, the most favorable configurations are defined each time by keeping two of the parameters constant and plotting the heating needs with the other two, as for the linear model. For example, if the orientation and window thermal transmittance of a building have been predefined as *O*=45° and *U*=0.5 kWh/m^2, the corresponding heating requirements for the different *WWRA* and *P* alternatives are presented in Fig. A.4. Fig. A.5 presents four different combinations, the same as those used for the linear model.

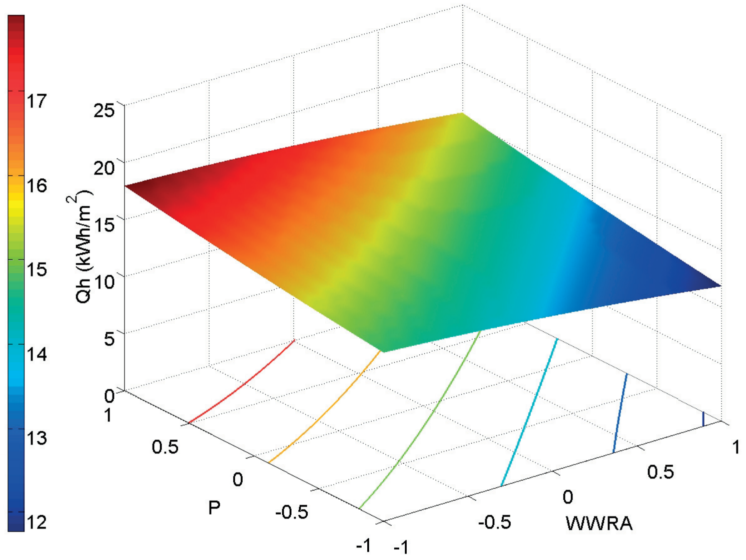

Figure A.4. Heating needs (*Qh*) of quadratic model as function of *WWRA* and *P*.

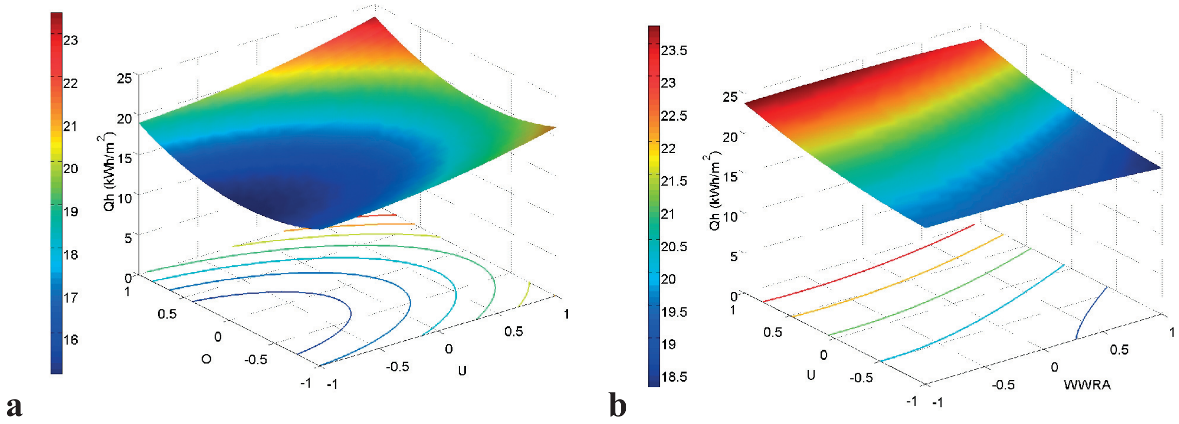

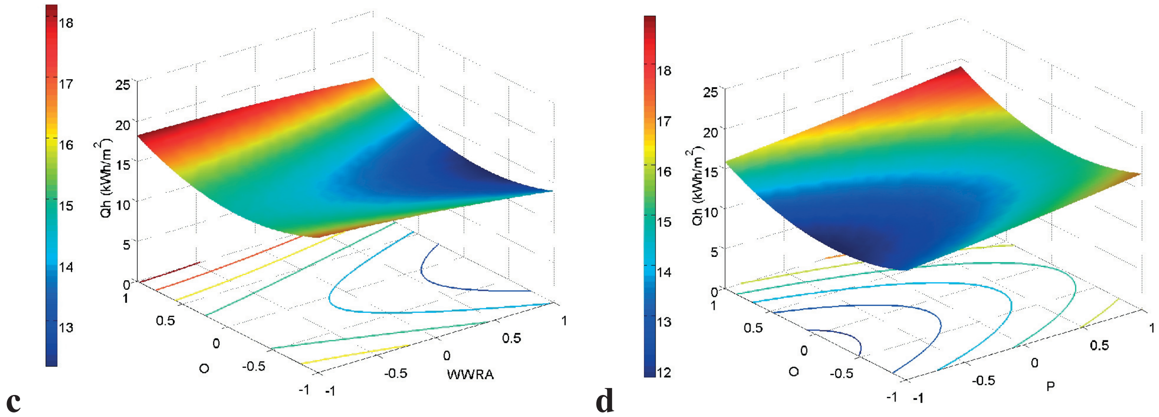

Figure A.5. Heating needs (*Qh*) for different combinations for quadratic model, a) *WWRA*=40%, *P*=1.25m, b) *O*=315°, *P*=1.25m, c) *P*=1.00m, *U*=0.5W/m^{2}K, d) *WWRA*=30%. *U*=0.4 W/m^{2}K.

A.5. Comparison of three models

The constant coefficient model was not accurate in predicting the optimum envelope, since the latter was slightly different from the one presented in Chapter 1, in which the orientation *O*=0° optimized the response. This results only from the chosen factor values and the explanation lies in examining what *O*=90° really means. A 90° turn of the envelope B, with a constant *WWRB*=50%, towards the south, always reduced the heating needs during the whole procedure. Hence, the constant coefficient model showed that the heating needs were more sensitive to a 90° turn than to a 0°, revealing the importance of this level and thus a significant regression coefficient.

As far as the linear and quadratic models are concerned, the regression coefficients of the main effects are of the same order of magnitude for both models, Fig. A.5. They cannot be directly compared, since the linear model is considered without interactions while the quadratic model was computed by taking into account interactions between the factors. It should be noted however that despite the fact that the second-order interactions of the quadratic model are small, they influence the optimum configuration, as can be seen in Figs. A.4 and A.5, creating minimums at intermediate points of the interval [-1,1]. Finally, the response surface constitutes an interesting and representative way to define the optimum configuration each time, according to the different constraints.

B Preliminary cross - sandwich elements

B.1. Introduction

The first step in the development of the balcony connection was the design of a preliminary cross - sandwich element, see Fig. B.1, in order to deal with the high complexity of the final hexagonal shear - compression sandwich element. With these trial specimens the feasibility of the fabrication procedure was examined as well as the mechanical behavior of the concept.

These cross-specimens have been designed to bear the compressive loads exerted by the compression struts in the final system in such a way that failure would occur in the concrete. They consist of a 25-mm-wide PU core, which is covered with a 2-mm inner UD (0°) FRP layer in the loading direction and a 2 - mm outer transverse UD (90°) layer. The outer UD (90°) layer should increase the stability, i.e. the buckling or wrinkling resistance.

B.2. Material properties

Two series of specimens were fabricated, which included GFRP and AFRP laminates and PUR701 foam, see Fig. B.2. The first series comprised two GFRP and two AFRP specimens, while the second comprised only AFRP specimens. The second series was produced because of the insufficient impregnation of the aramid fibers of the first series. The foam density of the second series was slightly lower (d_2=81.5±5.5 kg/m^3) than that of the first series, (d_1=106.3±1.4 kg/m^3). The GFRP specimens were composed of nine layers of E-glass UD-tape of 220 g/m^2. The AFRP specimens were composed of 14 layers of Kevlar-49

UD-tape of 100 g/m^2 weight. The matrix was an Epikote epoxy resin, MGS RIM 235, with an Epikure curing agent, RIMH 236. The resulting volume fraction was 40% for the GFRP and 50% for the AFRP specimens, the calculated elastic moduli were 31 GPa (GFRP) and 50 GPa (AFRP), and the compression strengths 480-600 MPa (GFRP) and 180-190 MPa (AFRP)[1].

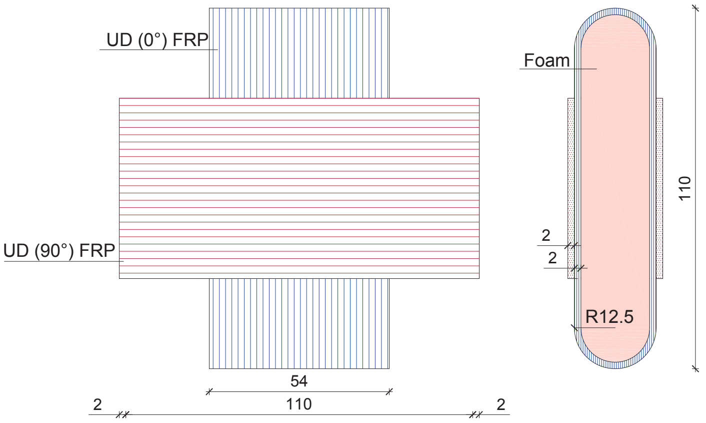

Figure B.1. Preliminary specimens, side view and cross section (dimensions in mm).

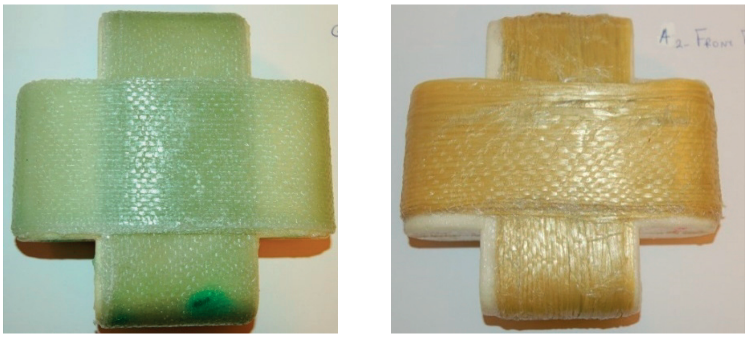

Figure B.2. GFRP specimen (left) and AFRP specimen - 2nd series (right).

B.3. Fabrication procedure

The fabrication of the specimens was performed manually, inducing potential imperfections. The procedure started with the fabrication of the PU foam, the core of the sandwich specimen. A cross -shape mold was fabricated in order to obtain the desirable form of the foam, see Fig. B.3a. The appropriate quantity of liquid PU was diffused into the mold to achieve the desirable density after expansion, see Fig. B.3b. The foam was removed from the mold with air pressure after its solidification (Fig. B.3c) and the application of the fiber fabrics followed, see Fig. B.4a. As can be seen more clearly from Fig. B.4a, the inner FRP layer was embedded 2mm deep inside the foam to avoid a concavity of the outer FRP layer. The fiber fabrics of the inner layer were impregnated with epoxy resin and wrapped around the foam in 9/14 loops, until the 2 - mm thick GFRP/AFRP layer was formed, see Fig. B.4a. Finally, the outer G(A)FRP layer was applied using the same procedure. After fabrication, the specimens were left for curing at ambient temperature, see Fig. B.4b.

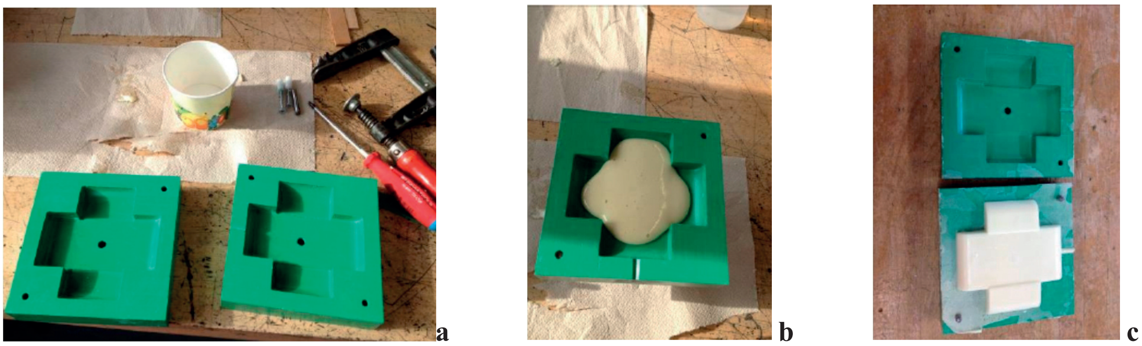

Figure B.3. Foam fabrication: a) Foam mold, b) Liquid PU, c) Solidified PU foam.

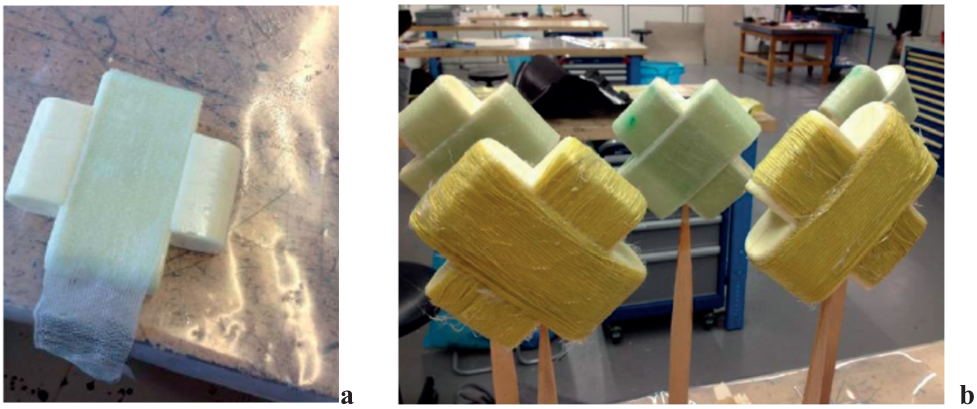

Figure B.4. a) Application of FRP layers, b) Curing of specimens - 1st series.

B.4. Set-up and instrumentation for static and creep experiments

The compressive load was applied to the internal FRP layer, as would happen in reality with the final hexagonal sandwiches. The specimens were positioned inside steel fixtures to achieve the three-axial stress state that occurs inside concrete. Due to irregularities of the FRP layers that would cause a non-uniform distribution of the load inside the fixtures, the curved specimen caps were covered with a 4-5-mm - thick adhesive layer (Sikadur-30), see Fig. B.5. Special care was taken to avoid misalignment of the specimens, with the help of a laser, which aligned the specimens vertically, according to the middle axis of the foam. Furthermore, a 5 - mm - thick band was left uncovered, see Fig. B.6, to force failure in this region of the specimen and study its behavior in the worst case, despite the fact that this scenario would not occur in reality, since this area is totally covered with concrete.

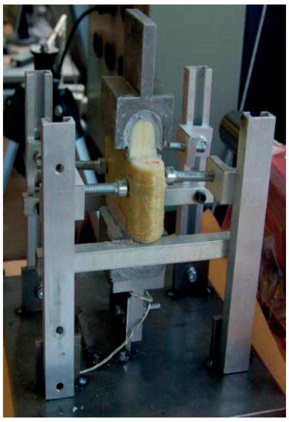

Figure B.5. Application of adhesive layer.

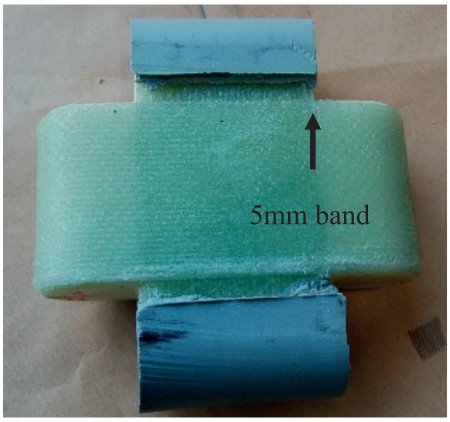

Figure B.6. Specimen with adhesive layer and 5-mm failure band.

The specimens were loaded using an INSTRON universal machine, of load capacity 300 kN. The static compressive experiments were performed under displacement control at a rate of 0.02mm/min in three to five cycles up to failure. The specimen deformations were measured with a video extensometer, with 0.1 - Hz frequency. The video extensometer recorded all the relative displacements among the targets, as shown in Fig. B.7. The deformation used for comparison of the specimens' behavior was that between the targets close to the poles of the specimen; the gage length was approximately 120 mm.

Five specimens were subjected to compression creep loads and temperature loads, using the INSTRON climatic chamber. The load levels were selected as 10kN and 15kN and the temperature loads were 20°C and 40°C, (one A-GFRP at 10 kN-20°C and 15 kN-20°C and one GFRP at 10 kN-40°C). The load levels were selected based on an estimation of the permanent load of a 4-m balcony span and the temperature levels according to the average ambient temperature (20°C) and 40°C, which is higher than the anticipated temperature, in the building envelope. The load levels corresponded to 23% and 35% of the (subsequent average) failure load of the GFRP specimens and were thus almost in line with the approximately 20-25% long-term strength of GFRP. Knowing that the most significant creep deformations already occur within the first days and in view of the aim of mainly checking the creep sensitivity at this project stage, the load duration was selected as being between four and nine days.

The creep deformation was measured with a displacement transducer (HBM LVDT 10mm) fixed at the two steel fixtures with a gage length of 120 mm, Fig. B.8. The frequency of the measurements was 20Hz until the target load was reached. This was subsequently reduced to 0.02Hz until the end of the experiment.

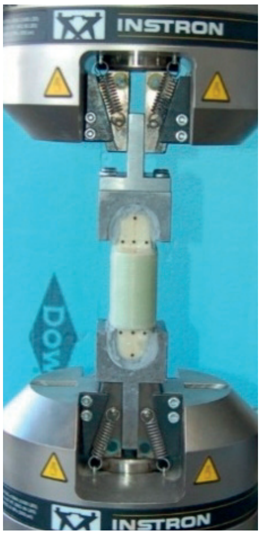

Figure B.7. Set-up for static experiments and VE targets.

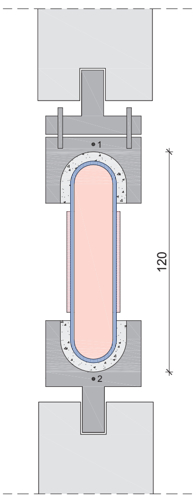

Figure B.8. Set-up for creep experiments.

B.5. Static behavior – results and discussion

Figure 9 presents the results of the static experiments. The GFRP and AFRP 1&2 specimens belong to the 1st series (high density), while the AFRP 3&4 specimens belong to the 2nd series (low density). For each group of specimens the results are consistent, in terms of load capacity and stiffness. The sudden drop in the load capacity of the GFRP specimens is explained by the nature of glass fibers, which have a tendency to crush once the stress limit is exceeded in the failure area. The smooth decrease of the load capacity exhibited by the AFRP specimens however derives from the fact that the aramid fibers bend rather than break in the failure area[2].

The lower stiffness of the GFRP specimens compared to the AFRP 1&2 can be explained by the lower calculated E-modulus of the GFRP specimens, resulting primarily from their smaller volume fraction, V_f. Between the two series of the AFRP specimens, the 1st series (AFRP 1&2) exhibited higher stiffness than the AFRP 3&4, as a result of the lower foam density of the latter. In terms of failure load the GFRP specimens exhibited better behavior, due to the higher compressive strength of the glass fibers (3.40 GPa), compared to the aramid fibers (0.70 GPa)[3].

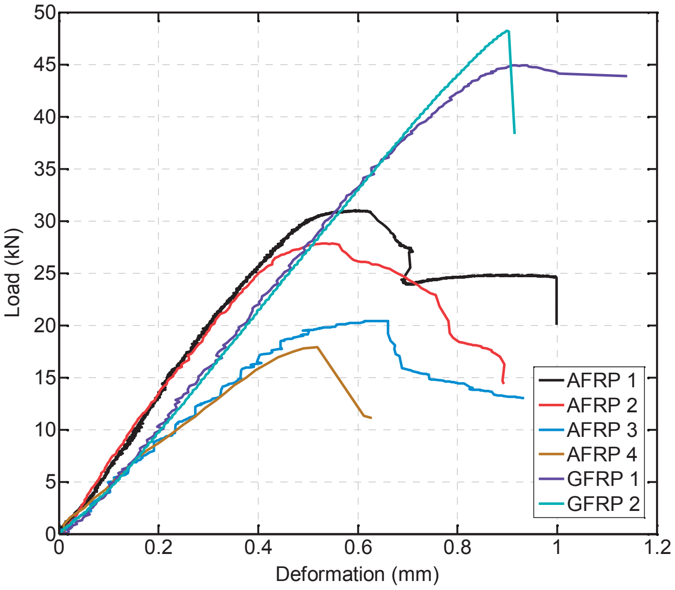

Figure 9. Load-displacement curves of A/GFRP specimens.

The failure in the GFRP specimens occurred in the 5 - mm failure band due to face sheet wrinkling, see Fig. B.10a. On the opposite side of the specimen, in addition to the damage at the failure band, delamination started from the failure band and extended to the inner part of the specimen, see Fig. B.10b.

Three of the four AFRP specimens failed through shear crimping. The failure mode of these specimens is shown in Fig. B.11 and can be explained by the nature of aramid fibers. According to Kulkarni et al.[4] when aramid fibers are subjected to compressive loads, if they buckle in phase, the shear strains in the matrix become predominant and cause shear instability.

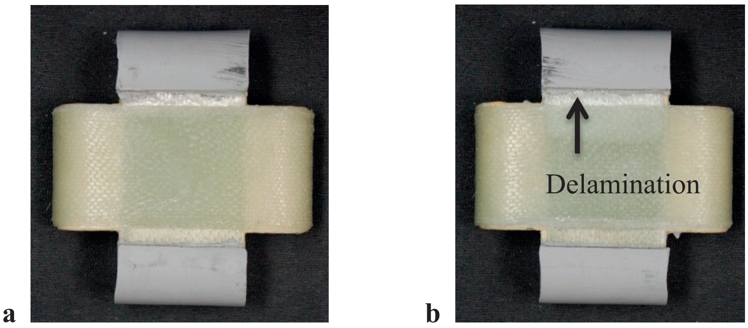

Figure B.10. GFRP1 specimen. a) Side 1 - Failure at the 5 - mm - thick failure band, b) Side 2 - Failure at the 5 - mm - thick failure band and delamination.

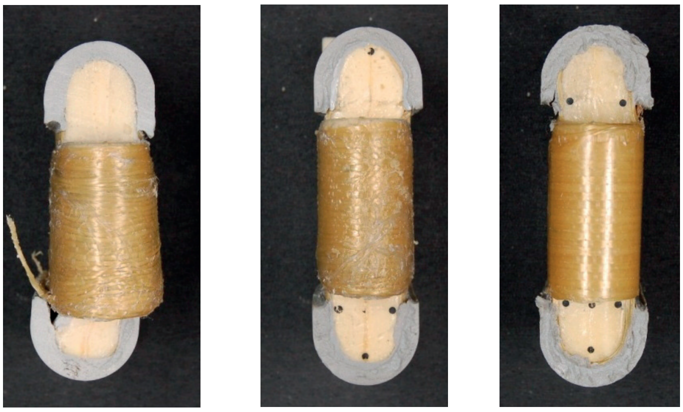

Figure B.11. AFRP specimens 1, 2 and 3.

B.6. Creep behavior – results and discussion

The total time - dependent deformations resulting from the creep experiments are shown in Fig. B.12. The GFRPT specimen subjected to 40°C and the other specimens were tested at ambient temperature, 20°C. During the first hours the deformation increased at a higher rate, while 24h after the beginning of the experiment, the creep rate diminished, maintaining a constant value. During the experiments, random jumps in the deformation were reported. There is no physical explanation for this phenomenon, as already noted in Chapter 5.

The experiments showed that the cross - sandwich specimens were not susceptible to creep phenomena. At the end of the creep experiment the maximum increase was exhibited by the AFRP specimen at 15kN, which corresponded to a 0.04 - mm deformation. The AFRP specimens presented higher creep deformation than the GFRP specimens, at both load levels. After three days, the creep deformation of the

AFRPs had increased 13%, while the GFRP specimens exhibited an increase of only 7% for both load levels. Concerning the GFRPT, the creep deformation was higher than that at ambient temperature at the same load level, due to the additional temperature load. Finally, between the same specimens at different loads, the creep deformation exhibited a linear behavior, a characteristic attributed to the low creep load applied (less than 40% of the failure load).

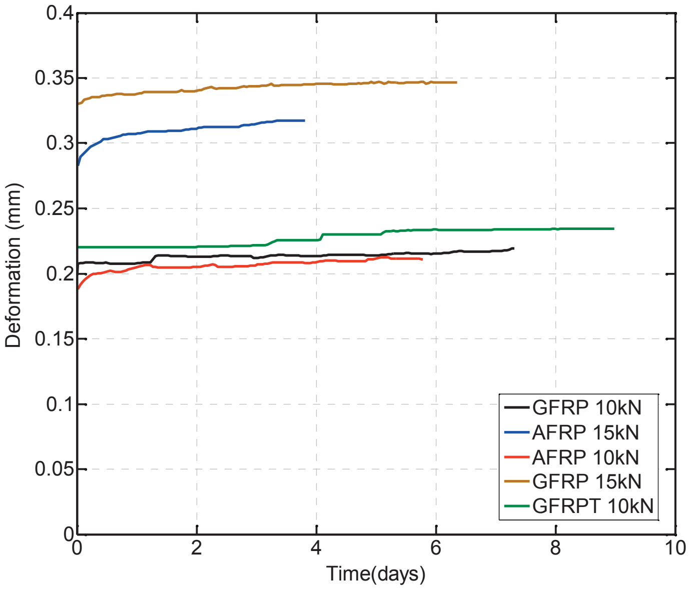

Figure B.12. Creep deformation of cross-specimens.

B.7. Conclusions

This preliminary study of the cross compression sandwich elements led to the following conclusions:

a) The complex sandwich structure is feasible from the manufacturing point of view.

b) The results of the static experiments are promising and an estimation concerning the load capacity of the final hexagon specimens could be achieved.

c) The long-term deformation of the specimens remains at low levels and will not be an obstacle to the final design of the hexagonal specimens and the balcony connection.

d) No decision can be made concerning the best option between aramid and glass fibers, due to the different foam densities. This aspect will be examined in the final hexagonal specimens in detail.

B.8. Compression curves

In this section the AFRP and GFRP static compression experimental curves are shown.

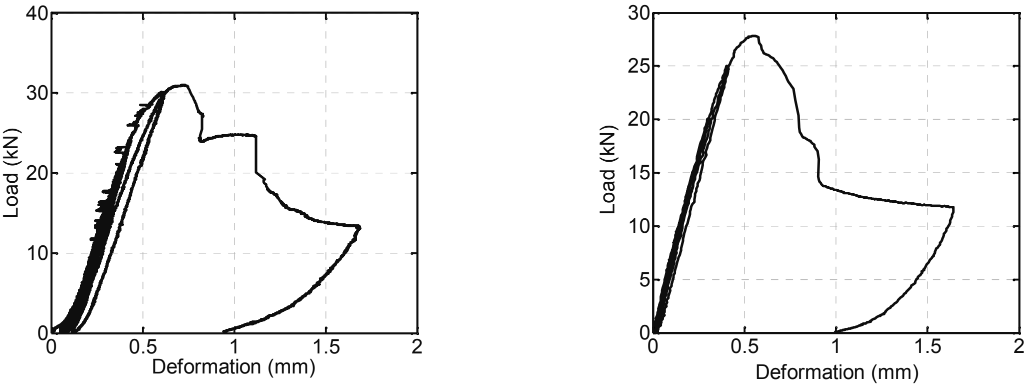

Figure B.23. AFRP 1 and AFRP 2 sandwich specimens.

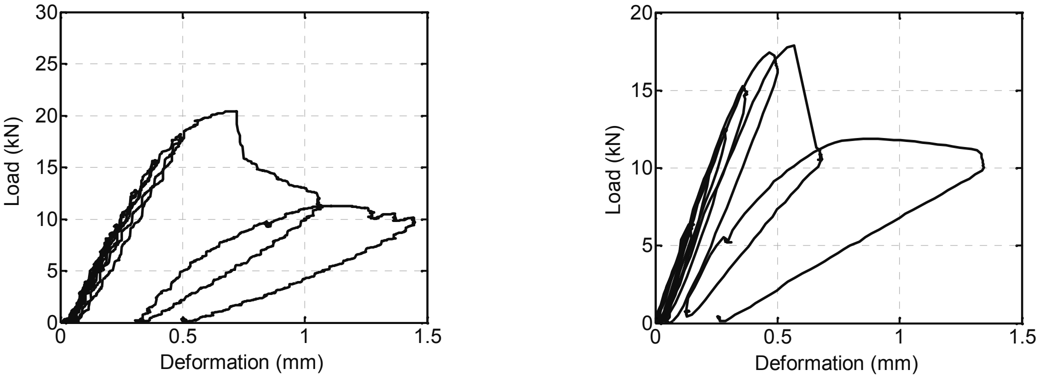

Figure B.34. AFRP 3 and AFRP 4 sandwich specimens.

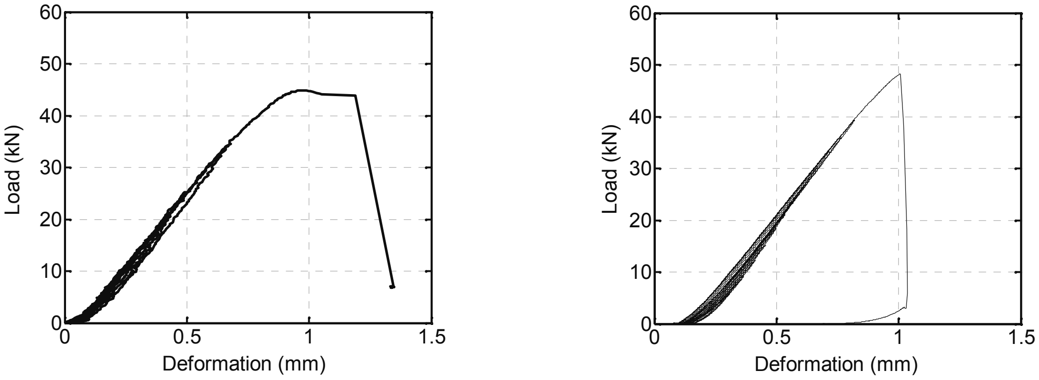

Figure B.45. GFRP 1 and GFRP 2 sandwich specimens.

B.9. References

1. Swiss-Composite: http://www.swiss-composite.ch/scs4/html/index.shtml?lang=en (assessed in 05.06.2015).

2. Greenwood J.H. , Rose P.G., Compressive behavior of Kevlar49 and composites. Journal of Materials Science, 1974. 9: p. 1809-1814

3. Barbero E J, Introduction to composite materials. Second ed. 2011, Taylor & Francis Group.

4. Kulkarni S.V., Rice J.S., Rosen B.W. , An investigation of the compressive strength of Kevlar 49/epoxy composites. Composites, 1975. 6(5): p. 217-225.

C

AFRP tensile loop component

C.1. Introduction

Appendix C presents additional information concerning the mechanical characterization of the AFRP loop component. At the beginning, the manual fabrication procedure is described, and additional information on the set-up of the static, long-term and durability experiments is given. At the end, the results of the different experiments are presented.

C.2. Fabrication procedure

The entire configuration for the loop fabrication is shown in Fig. C.1. The aramid fibers were impregnated with epoxy resin, inside the blue box, Fig. C.2. The impregnated aramid fibers were applied around an aluminum mold, which was being turned and the procedure was continued until the desirable cross section was achieved, Fig. C.3. Finally, the specimen was covered with a blue tape, to accomplish a plane and smoother cross section, Fig. C.4, and was placed in the oven at 27° C for six hours, Fig. C.5.

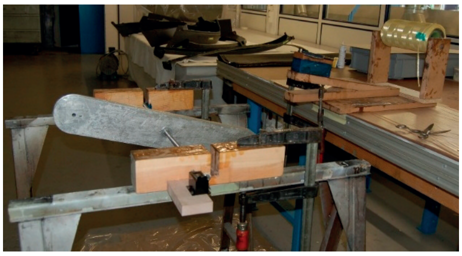

Figure C.1. Configuration for loop fabrication.

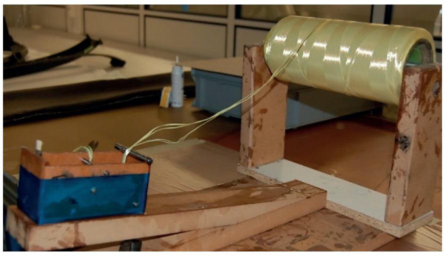

Figure C.2. Impregnation of aramid fibers.

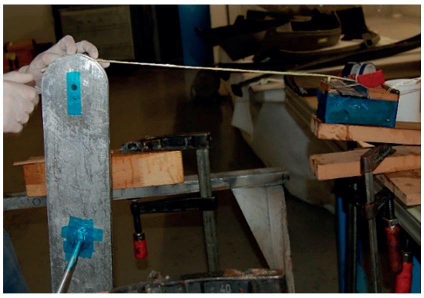

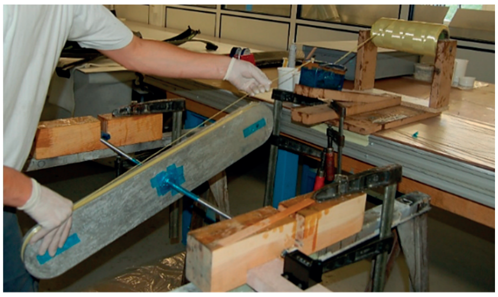

Figure C.3. Application of aramid fibers around mold (left), progression of specimen (right).

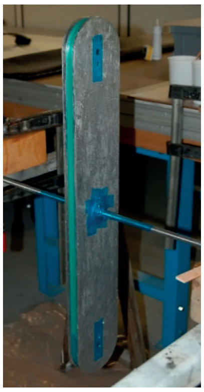

Figure C.4. Application of blue tape for plane section.

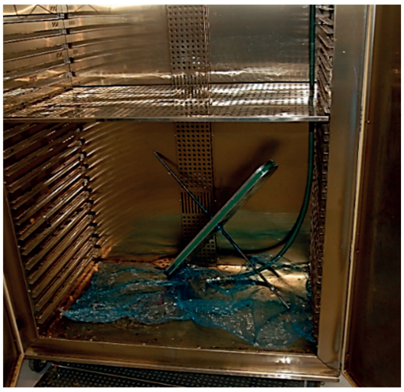

Figure C.5. Specimen inside oven at 27°.

C.3. Set-up and instrumentation

a) Static experiments

The specimens were subjected to axial tensile loading, using the set-up shown in Figs. C.6 and C.7. Two circular steel sheaves are positioned at the two edges of the specimen, Fig. C.8. The sheaves have the same dimensions as the loops and they provide lateral support to the specimen during the experiment, Fig. C.9. Each sheave is connected with two plates, which are connected via a bolt, with the plate used for gripping the specimen on the machine. This final connection offers an additional degree of freedom to the system, which is in fact a self-alignment system. At the beginning of the experiment and low load levels, the bolts allow the specimen to move freely, avoiding the development of bending moments during the experiment, which would cause premature failure of the specimen[1].

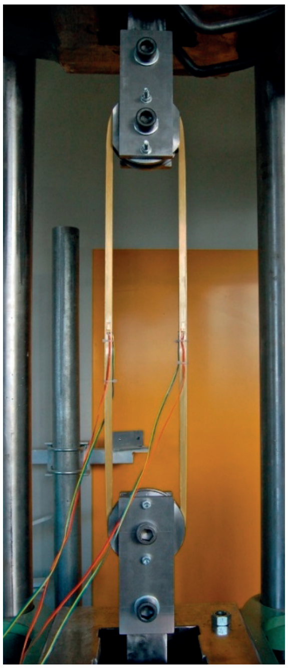

Figure C.6. Set-up for tensile experiments. Front-view.

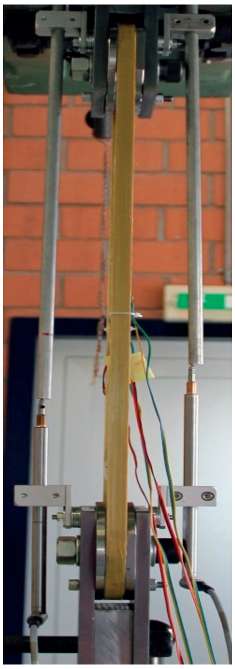

Figure C.7. Set-up for tensile experiments. Side-view.

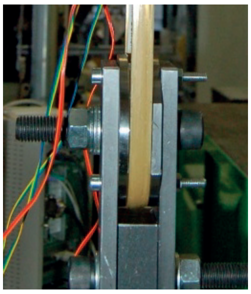

Figure C.8. Detail of specimen in supports.

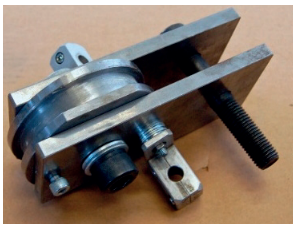

Figure C.9. Sheave used for tensile experiment.

In total, eight specimens were subjected to static tension loads. Experiments were conducted on a 1000 - KN AMSLER machine and were load controlled with a loading rate of 500N/s. For all three series, the strain was measured with strain gages (HBM 1-LY61-6/120). Four strain gages were glued in the middle of the specimen. The four gages were positioned on the top and lateral sides of the loop. The strain was measured at a frequency of 2Hz. Additionally, two displacement transducers (LVDTs HBM 50mm) were used for the last two series, and were placed on each side of the specimen to record its total elongation, Fig. C.7.

b) Creep experiments

A tensile creep experimental program was performed for the loop with a load duration of up to six months. After this period the loop was subjected to static load until failure. The purpose of this study was to analyze the long-term tensile behavior of the loop under constant load and the effect of the creep load on stiffness and strength.

The experiment was carried out in a special underground room, with temperature and humidity controlled by an air-conditioning unit. The temperature was set to 20°C and the relative humidity (RH) to 70%. The temperature and the RH were monitored by a hygrothermograph.

The set-up for the creep experiment is presented in Fig. C.10a. The creep frame is designed for the application of constant tensile loads and is a hydraulic drive system. It consists of a hydrostatic oil pressure pump, valves, pipes, a hydraulic cylinder and a hydraulic accumulator. The hydraulic cylinder is positioned at the bottom of the frame and consists of a piston and a cylinder head.

There was only one load level examined. The applied load corresponded to 7% of the load capacity of the loop. Two LVDTs were used at both sides of the specimen, Fig. C.10b, measuring its total elongation. An HBM QuantumX data logger was used. During the loading, the frequency of the measurements was 20Hz and this was reduced to 1Hz during the first hour. The frequency was further reduced to 0.02Hz and was kept at this level until the end of the experiment, which lasted 176 days.

The specimen was subsequently removed from the creep frame and its static behavior was examined by means of a short-term tensile failure experiment. The set-up is presented in Fig. C.11. Due to unexpected hydraulic problems with the AMSLER, a 500 - kN capacity Zwick machine was used. Apart from the different machine used, the set-up was kept the same as for the previous static experiments. Two LVDTs were used to measure the total elongation of the specimen. The load rate was the same as before, 500N/s.

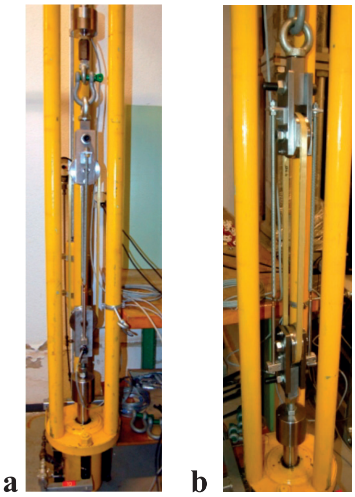

Figure C.10. Set-up for creep experiment.

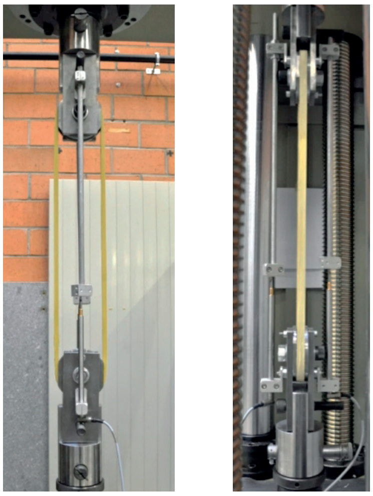

Figure C.11. Set-up for static experiments.

c) Durability experiments

The FRP thermal break is installed inside the concrete, where it is subjected to moisture uptake (during pouring and curing) and alkalinity. Therefore, the impact of alkaline moisture and additional temperature effects on the mechanical properties of the loop component were studied by means of a long-term durability experiment[2]. A bath with dimensions 60.7cm x 30.5cm x 30.5cm was used in order to simulate the aforementioned conditions, Fig. C.12. The alkaline solution was composed of 0.25mol/L KOH, 0.14mol/L NAOH and 0.06mol/L $Ca(OH)_2$[3]. The pH of the solution was approximately 13.5 and was controlled regularly with a pH meter instrument and a pH meter paper. The temperature was set to 30°C and was constantly controlled by a thermocouple (TP100), which was emerged in the solution.

The experiment lasted 230 days. During this period the stiffness was checked every two weeks for the first month and subsequently the measurements were taken over a period of 50-100 days. The water uptake was checked every week for the first 50 days and subsequently measurements were taken every 40 days.

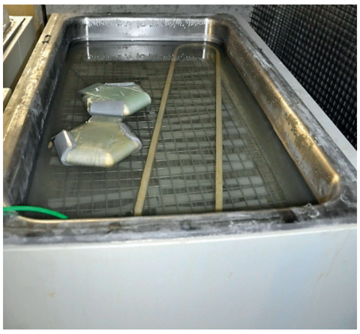

Figure C.12. Heated bath with alkaline solution.

C.4. Results and discussion

a) Creep experiments

The results obtained for the creep AFRP specimen under tensile static load are shown in Fig. C.13. No particular change in the stiffness, strength and failure mode was reported after creep exposure. These properties remained within the scatter limits, as noted in Chapter 2.

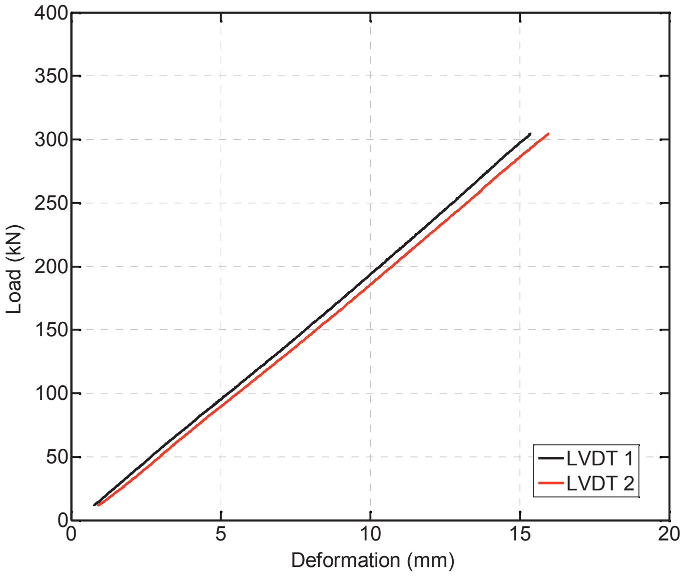

Figure C.13. Static experiment after creep exposure, specimen LA-9C.

b) Durability experiments

The results of the stiffness and the water uptake are shown in Figs. C.14 and C.15. The stiffness of the loop component, after a small increase most probably resulting from the post-curing of the specimen at 30°C, remained almost constant. The water uptake was very small, almost 1% after 233 days.

A visual inspection of the conditioned specimen revealed a change in the resin surface (less smooth) and a color degradation of the fibers, due to the alkaline solution, Fig. C.16. Fig. C.17 presents the results of the static experiments and demonstrates that the load capacity of the loop component was not influenced by the alkaline environment and was within the scatter of the experiments. The failure mode of the specimen was in accordance with all the previously tested specimens.

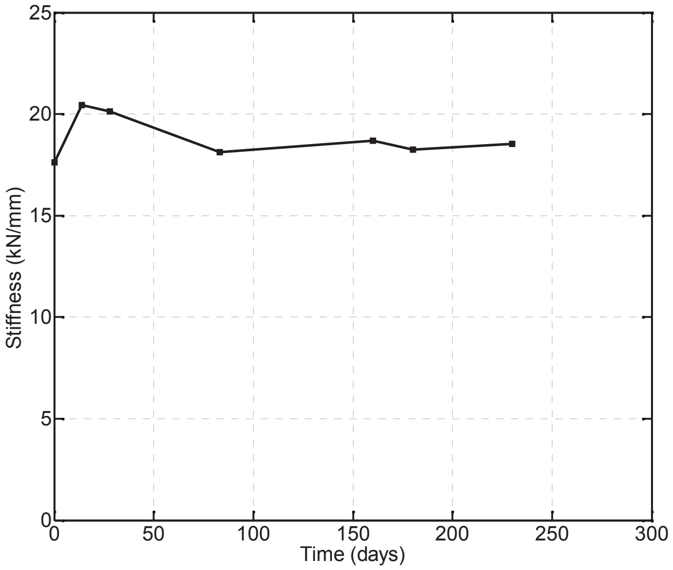

Figure C.14. Stiffness development of AFRP loop specimen LA-10W.

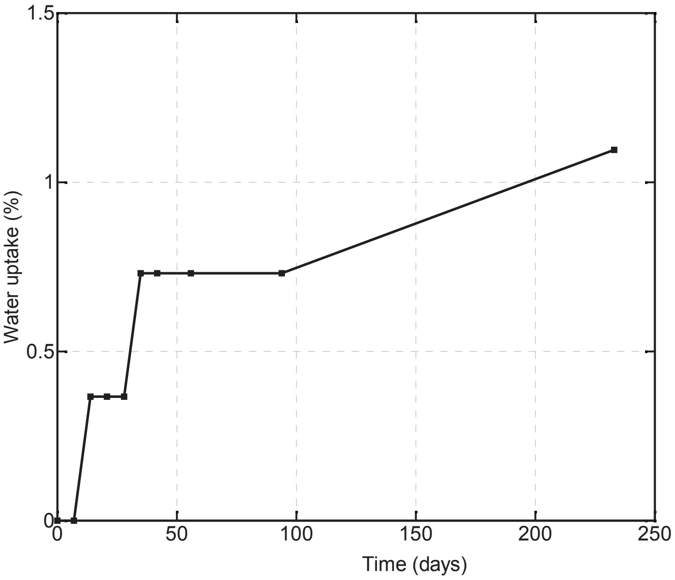

Figure C.15. Water uptake of AFRP loop specimen LA-10W.

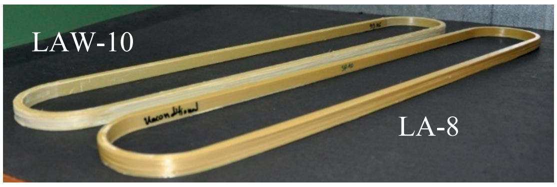

Figure C.16. Conditioned specimen, LAW-10 (left) and unconditioned specimen, LA-8 (right).

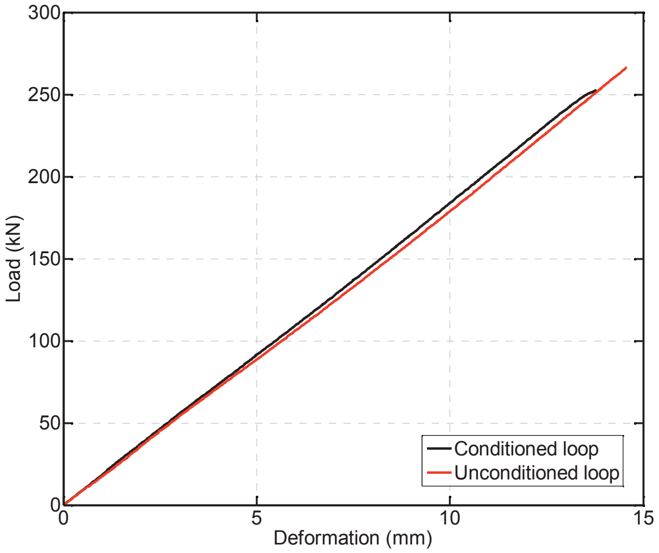

Figure C.17. Static behavior of conditioned (LAW-10) and unconditioned specimens (LA-8).

C.5. Load-strain and deformation curves

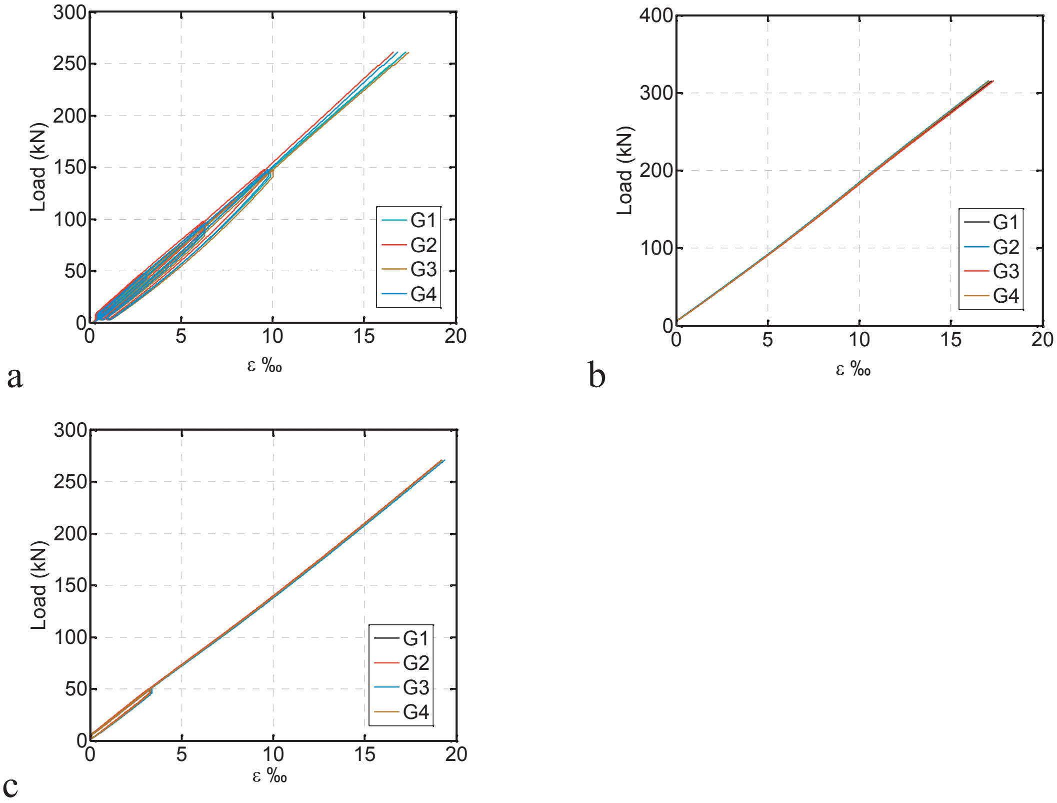

Figure C.18. Strain measurements of a) LA-1, b) LA-2, c) LA-3 loop specimens.

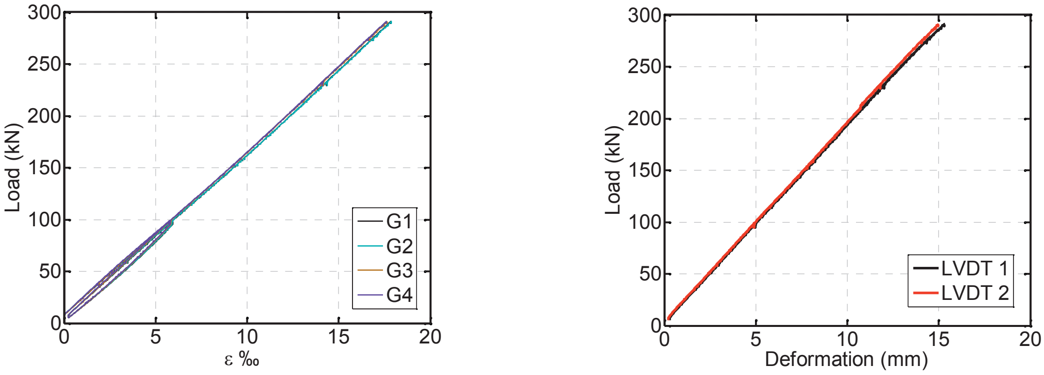
Load (kN)
300
250
200
150
100
50
0
0
5
10
15
20
ε ‰
G1
G2
G3
G4
Load (kN)
Deformation (mm)
LVDT 1
LVDT 2

a

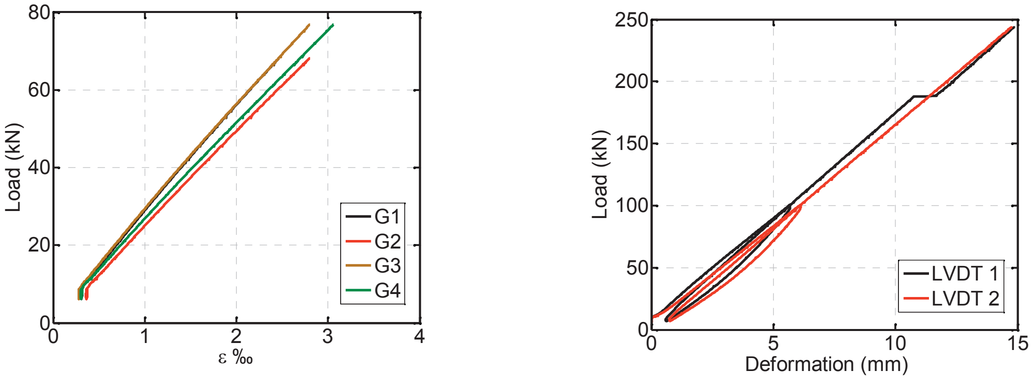
Load (kN)
80
60
40
20
0
0
1
2
3
4
ε ‰
G1
G2
G3
G4
Load (kN)
250
200
150
100
50
0
0
5
10
15
Deformation (mm)
LVDT 1
LVDT 2

b

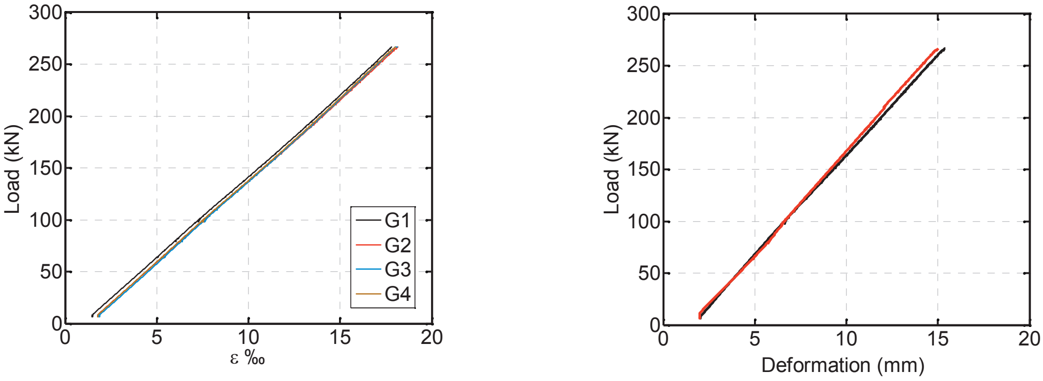
Load (kN)
300
250
200
150
100
50
0
0
5
10
15
20
ε ‰
G1
G2
G3
G4
Load (kN)
Deformation (mm)
LVDT 1
LVDT 2

c

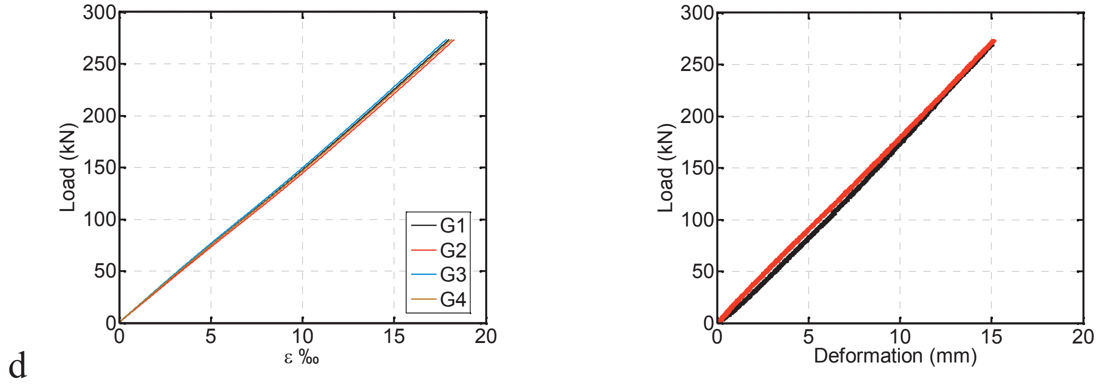

Figure C.19. Strain and LVDT measurements of a) LA- 4, b) LA- 5, c) LA- 6, d) LA-7 specimens.

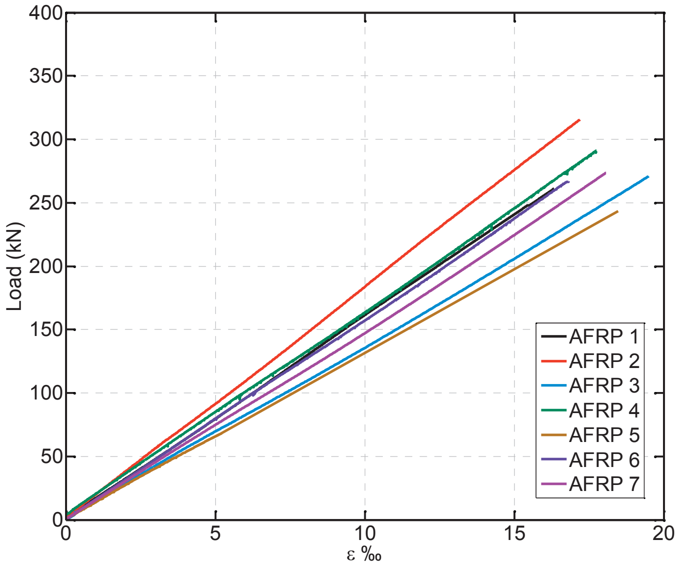

Figure C.20. Load-strain measurements for seven AFRP specimens.

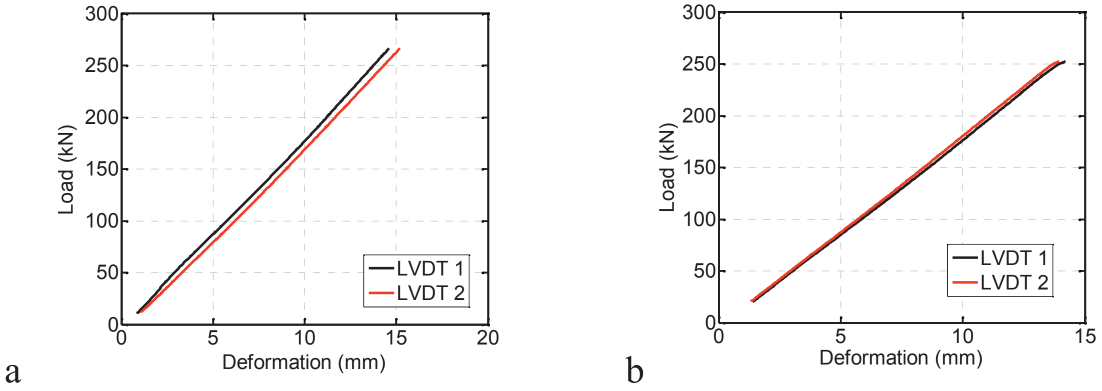

Figure C.21. LVDTs measurements of a) unconditioned, LA-8 and b) conditioned specimen, LAW-10.

C.6. References

1. ASTM Standard D3039/D3039M-08, Standard Test Method for Tensile Properties of Polymer Matrix Composite Materials, ASTM International, West Conshohocken, PA, 2008.

2. Riebel F, Structural behavior and durability of multifunctional fiber-reinforced polymer components, PhD Thesis N^{o} 3695 (2006), EPFL.

3. Chin J W, Aouadi K, Haight M R, Hughes W L, Nguyen T, Effects of water, salt solution and simulated concrete pore solution on the properties of composite matrix resins used in civil engineering applications, Polymer Composites, 22, 2001.

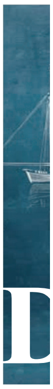

GFRP compression bar

D.1. Introduction

Appendix D presents the experiments conducted on the GFRP compression bar, bonded with the sandwich hexagon component. First, the set-up and instrumentation are described in detail and at the end the load-strain responses are presented as well as the failure mode.

D.2. Set-up and instrumentation

As described in Chapter 3, four prismatic specimens of 12x12x50mm^3, as described in the ASTM Standard[1], were cut from a UD GFRP compression bar, in order to evaluate their stiffness, required for the serviceability verification. No other experiment was conducted for the GFRP bars, since the compressive stresses created in the bar, at concrete failure, are small and thus there is no influence of creep phenomena or alkaline pore water. The specimens were axially loaded up to failure under displacement control at a rate of 0.02mm/s. The axial compressive strains were measured by four strain gages (HBM, 120LY61) in the first specimen and two gages (parallel and perpendicular to the GFRP layers) in the other three specimens. A W+B servohydraulic universal testing machine of 500-kN load capacity was used for the experiments. The set-up comprised steel plates, providing fixed end support to the specimen, as shown in Fig. D.1.

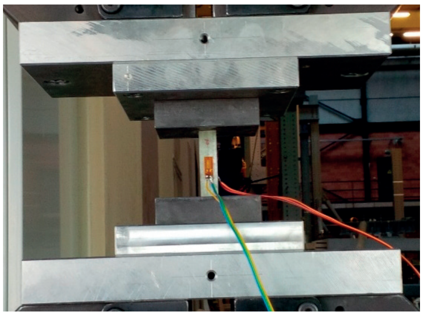

Figure D.1. Set-up for GFRP compression bar.

D.3. Results and discussion

The load-strain curves of the four specimens are shown in Fig. D.2. The load-strain responses were linear up to failure and the resulting elastic modulus and nominal axial strength were 44±6.5GPa and 350±66MPa, respectively.

Regarding the failure mode of the specimens, the first one, specimen CG-1, buckled towards the sides 3&4, leading to the development of shear forces in the matrix and a kinking failure, which started near the boundary, Fig. D.3. As far as the other specimens are concerned (CG-2-CG-4), kinking failure occurred simultaneously with splitting between the laminae along the specimen length[2], see Fig. D.3.

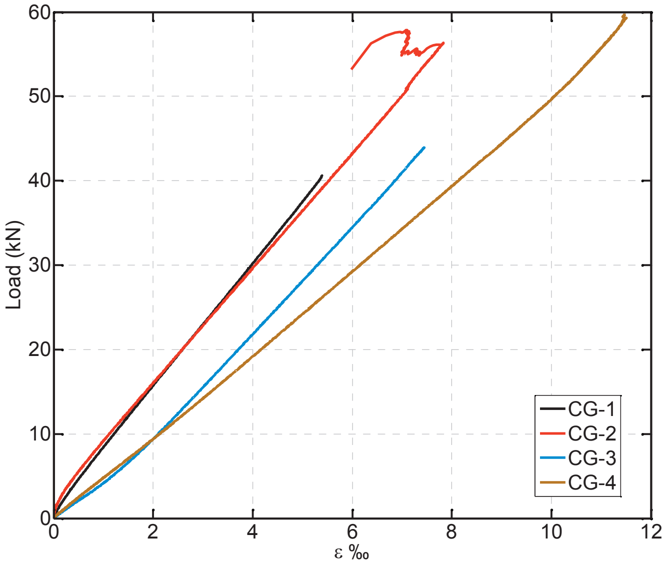

Figure D.2. Load-strain responses of four bar specimens.

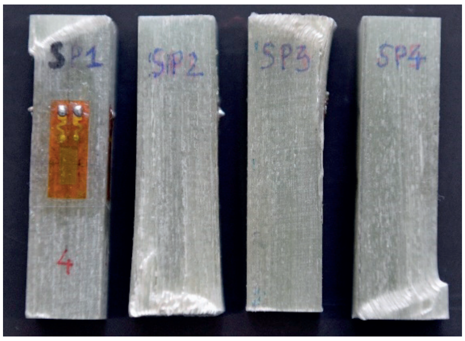

Figure D.3. Failure image of GFRP compression bars, CG-1 to CG-4, from left to right.

D.4. Load-strain curves

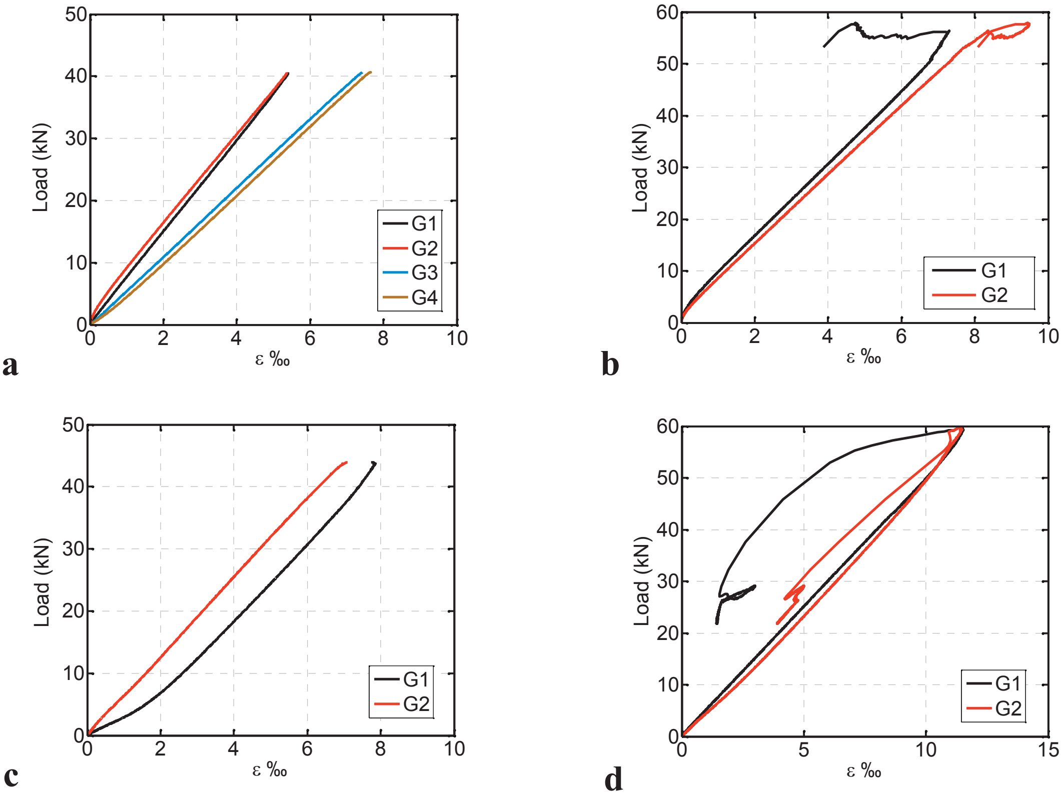

Figure D.4. Individual load-strain responses of four bar specimens; a)CG-1, b)CG-2, c)CG-3, d) CG-4.

D.5. References

1. ASTM Standard D695-10, Standard Test Method for Compressive Properties of Rigid Plastics, ASTM International, West Conshohocken, PA, 2010.
2. Sun W, Temperature effects on material properties and structural response od polymer matrix composites, PhD Thesis N° 6674 (2015).

E Hexagon sandwich component

E.1.Introduction

Appendix E presents additional information concerning the mechanical characterization of the hexagon sandwich component. First, the fabrication procedure is described. Furthermore, the static, creep and durability experiments are presented as well as the corresponding results. Three series of specimens were produced, which included GFRP and AFRP specimens, and 21 specimens were tested in total.

E.2. Fabrication procedure

The fabrication of the hexagon specimens (GFRP and AFRP) was manually controlled and the same principles were followed as in the cross specimens. At the beginning, the PU foam was fabricated by diffusing a certain quantity of liquid PU in a mold, in order to achieve the desirable foam density. The foam was removed with air pressure from the mold and the rectangular compression GFRP element was then glued to the bottom of the foam specimen. Fig. E.1 shows the foam specimens and the position of the layers that were embedded in the foam at 0°, -60° and +60° in order to avoid the concavity due to the 2-mm thickness of the layers. The application of the layers at the three different orientations (0°, -60° and +60°) proceeded from the inner (+60°) to the outer side (0°). Epoxy resin was applied to the glass fiber fabric (Fig. E.2), wrapping the foam around 12 times, thus forming a thickness of 2mm (Fig. E.3). This procedure was continued until the three layers were applied, Fig. E.4. Finally, the hexagon specimens were covered with a blue plastic tape to avoid possible misalignments of the outer layer and enhance its smoothness. The specimens were left for curing in ambient temperature.

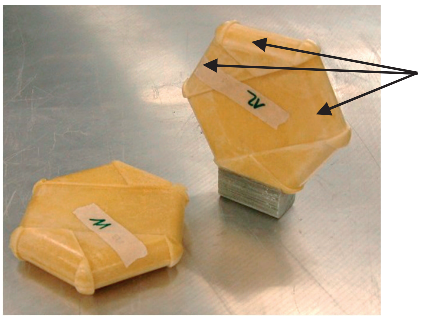

Recesses of FRP layers in the foam at 0°, -60° and +60°.

Figure E.1. Foam specimens and position of layers

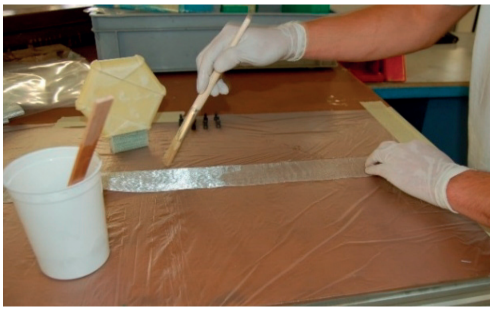

Figure E.2. Application of resin to fabric.

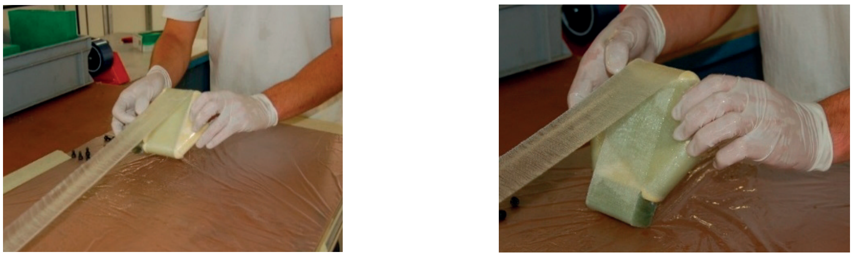

Figure E.3. Wrapping of foam specimen, inner layer (left), intermediate layer (right).

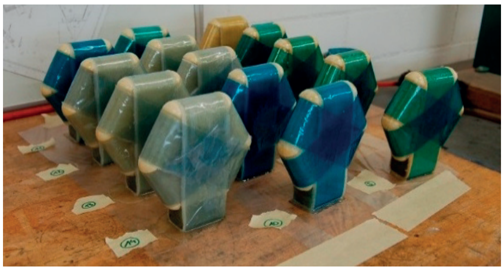

Figure E.4. Curing of GFRP and AFRP specimens.

E.3. Set-up and instrumentation

a) Static experiments

For the three different fixture types an adhesive layer (4-5mm) was applied at the ends of the specimens, in order to overcome the possible irregularities of the GFRP surface and better simulate the three-axial pressure occurring inside concrete. For this reason, a multi-step procedure was conceived for the application of the adhesive layer to avoid any misalignment of the specimens during the experiment, which would cause a premature failure under compressive loading. In the first step, the specimen was positioned in a ‘cage’. Using a cylinder, the specimen was aligned along its middle axis, Fig. E.5. In the second step, the cage was positioned on an aluminum frame, where the epoxy adhesive was applied to the lower aluminum part, Fig. E.6. The specimen was embedded into the latter, until the 4-5-mm layer was formed. After the curing of the adhesive (one day) the other edge of the specimen was fabricated, using the same procedure. After one day, the specimen was removed from the frame and put inside a climatic chamber for 24h at 40° in order to achieve a high curing degree.

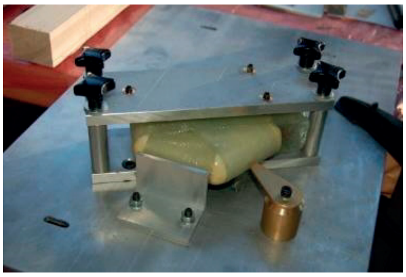

Figure E.5. Alignment of hexagon specimen

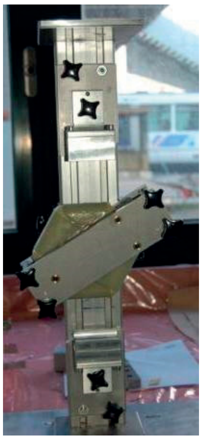

Figure E.6. Application of adhesive layer.

b) Long-term experiments

The creep experiments conducted on the hexagons were described in Chapter 3 and carried out in the same conditioned room as the loop component, see Appendix B. Figs. E.7 & E.8 show the set-up and creep fixture used to transform the tensile load to a compressive load. As to instrumentation, two LVDTs (HBM 10mm) were used on both sides of the specimen, measuring the total deformation. In every specimen load cells were placed on the top of the creep frame in order to verify the stability of the load at the selected levels. An HBM QuantumX data logger was used. During the loading, the frequency of the measurements was 20Hz and this was reduced to 1Hz during the first hour. The frequency was further reduced to 0.02Hz and was kept at this level until the end of the experiments, which lasted 30 days.

As far as specimen HGL3-2C is concerned, a different configuration was applied for the application of the creep load. The massive S3 fixture could not fit inside the creep frame so therefore the Walter + Bai Creep Testing Machine (compressive capacity 350kN) was employed, Fig. E.9. The system works with a hydro-pneumatic loading device, which is integrated in the base of the machine. The specimen is adjusted to the machine and a hand-driven pump places the specimen under pressure. The pump, besides producing the pressure corresponding to the required force, also serves to control the force during the test. Due to the relatively small dimensions of the specimen, a steel tube was fitted at the bottom of the S3 fixtures, in order to adjust the specimen on the machine. As for instrumentation, two LVDTs (HBM 20mm) were placed on both sides of the specimen and a load cell controlled the load stability. The measuring system and pattern were kept similar, as before.

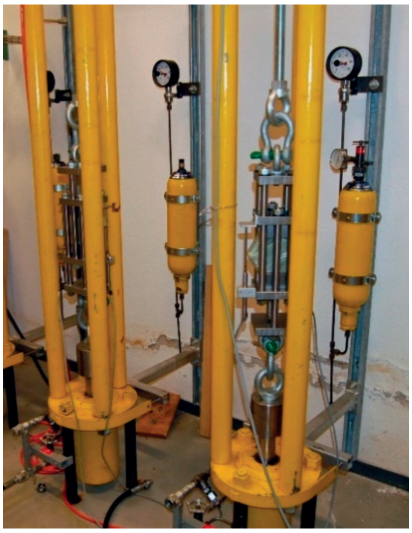

Figure E.7. Set-up for compression creep experiment.

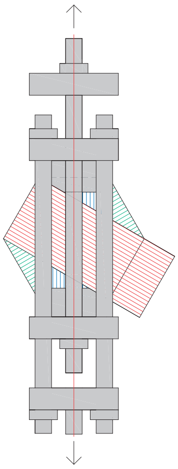

Figure E.8. Compression creep fixture.

Figure E.9. Set-up for HGL3-2C.

c) Durability experiments

As already described in Appendix B, the components were subjected to durability experiments inside an alkaline environment that simulated that of the concrete. The experimental program for the hexagons comprised two phases. During the first one, specimens HGH2-3W and HGL2-3W were immerged in the alkaline solution and after a period of five months, they were subjected to static compression loading using the S2 set-up. The closed form of the S2 fixture was causing misplacements of the specimens and thus the stiffness experiments, during the five-month conditioning period, were not reliable for these specimens and fixtures. This was the reason for the second part of the experimental program, which included the conditioning of HGH1-5W and HGL1-1W. The specimens were periodically subjected to stiffness experiments, using the S1 set-up that had a simpler form. Their stiffness was checked three times with static compression stiffness experiments; before immersion in the alkaline water, and 15 days and 30 days after immersion. They were finally subjected to a static compressive load until failure after 130 days. The set-up for the stiffness and failure experiments were the same as the corresponding compression ones, described in Chapter 3.

E.4. Results and discussion for durability experiments

No obvious damage was reported for the four conditioned specimens. Figure E.10 shows the water uptake of the HGH1-5W and HGL1-1W and Fig. E.11 shows the stiffness degradation. The water uptake was small for both specimens. Regarding the stiffness reduction, for both specimens it was approximately 50% after 130 days, independently of the foam density (see Table 3, Chapter 3). The results show the high influence that the alkalinity in combination with the temperature and moisture uptake can have on the mechanical properties of the specimens. However, it should be noted that the experiments simulated a far too harsh scenario and such values are not expected in reality. Finally, Fig. E.12 shows the failure compression experiments for the four conditioned specimens, immediately after removal from the alkaline water. The highest strength degradation was 29% in the case of HGL2-3W.

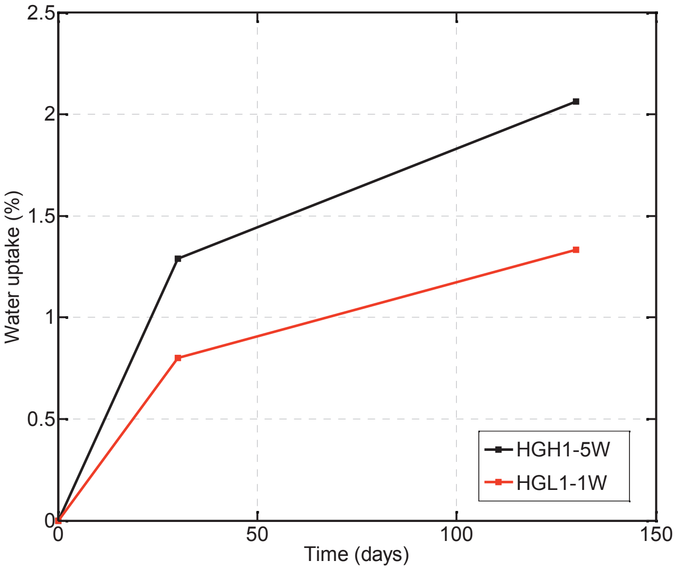

Figure E.10. Water uptake of GFRP hexagon specimens.

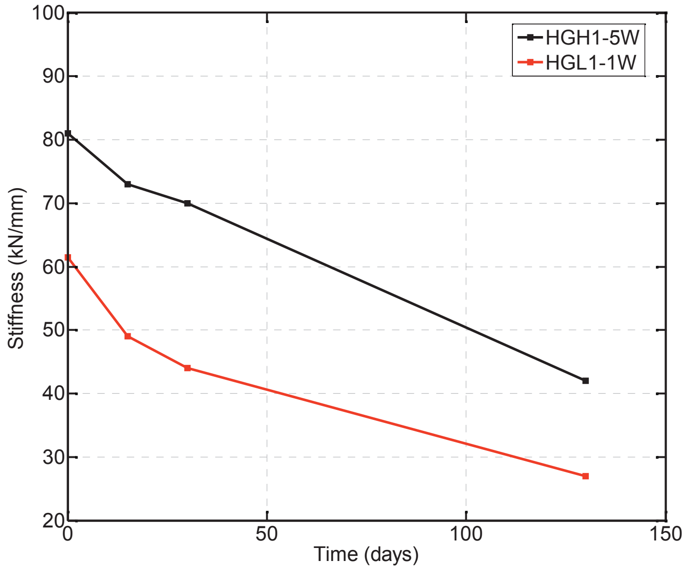

Figure E.11. Stiffness degradation of GFRP hexagon specimens.

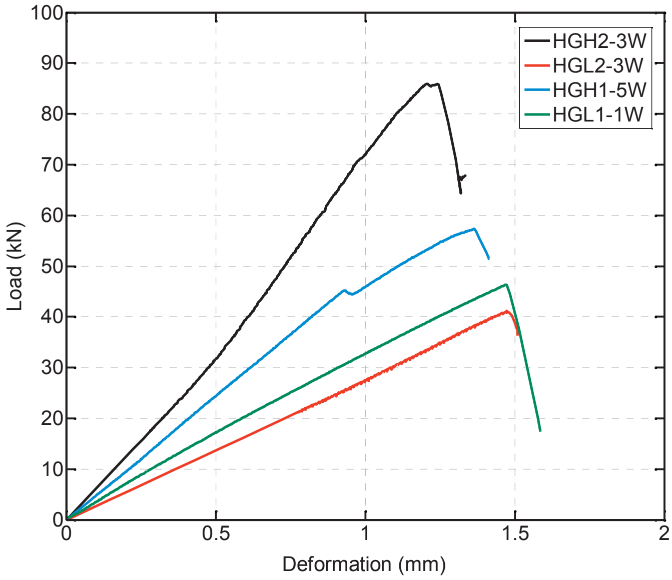

Figure E.12. Static compression results of GFRP hexagon specimens after alkaline water exposure.

E.5. Load-deformation curves

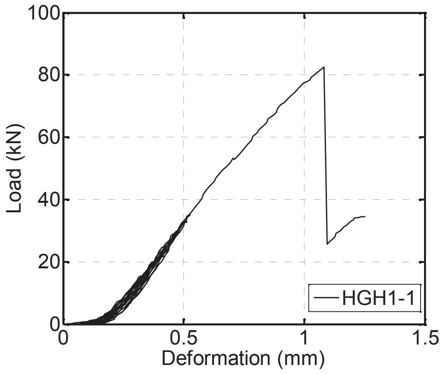

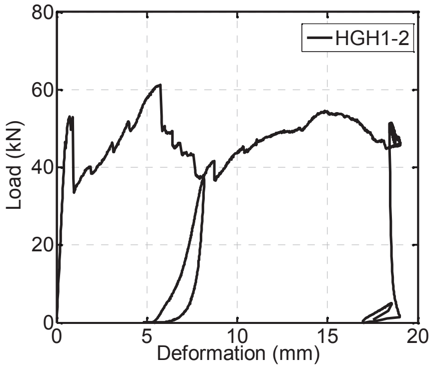

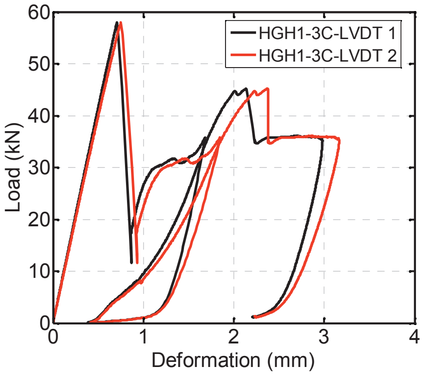

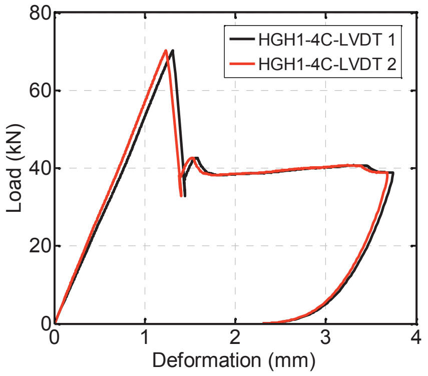

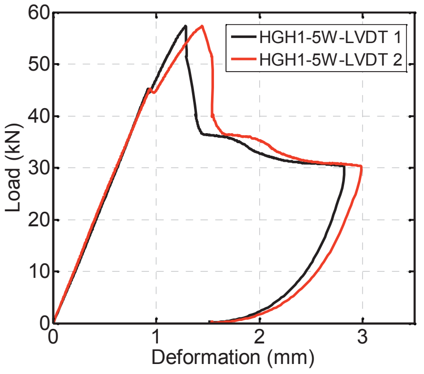

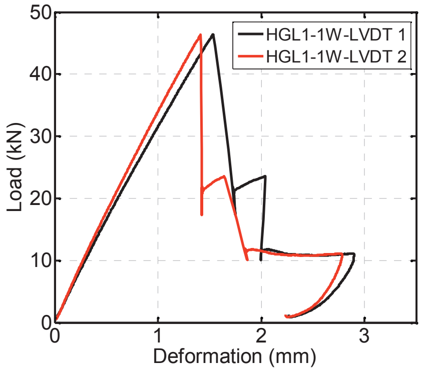

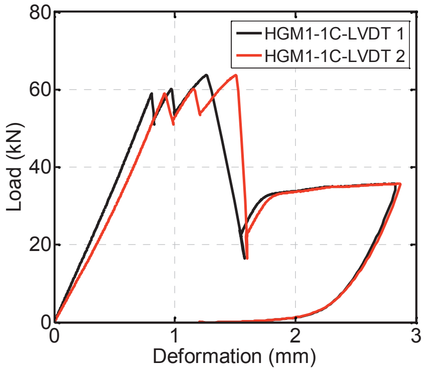
HGM1-1C-LVDT 1
HGM1-1C-LVDT 2
Load (kN)
Deformation (mm)
0
20
40
60
80
0
1
2
3

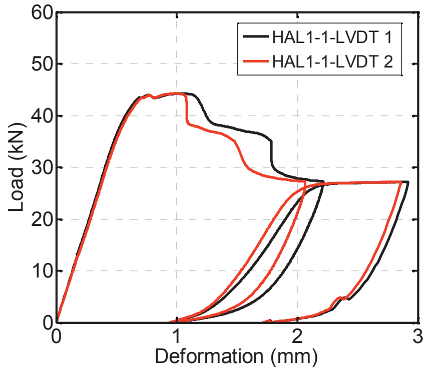
HAL1-1-LVDT 1
HAL1-1-LVDT 2
Load (kN)
Deformation (mm)
0
10
20
30
40
50
60
0
1
2
3

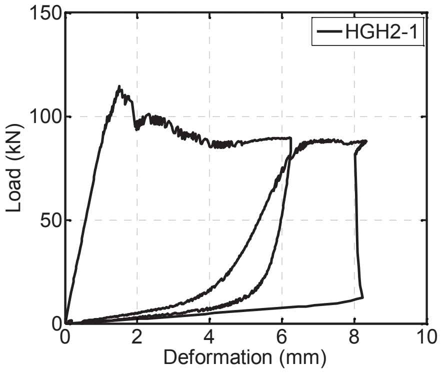
HGH2-1
Load (kN)
Deformation (mm)
0
50
100
150
0
2
4
6
8
10

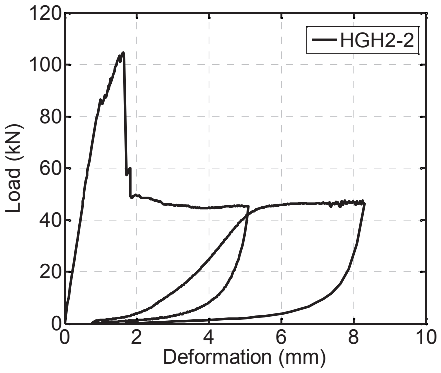
HGH2-2
Load (kN)
Deformation (mm)
0
20
40
60
80
100
120
0
2
4
6
8
10

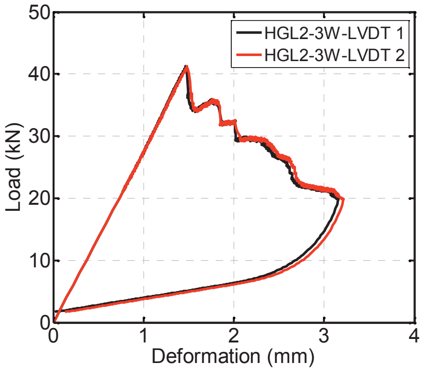
HGL2-3W-LVDT 1
HGL2-3W-LVDT 2
Load (kN)
Deformation (mm)
0
10
20
30
40
50
0
1
2
3
4

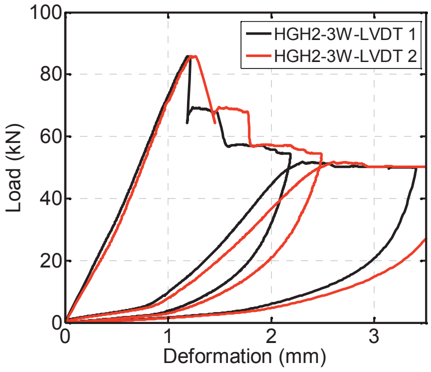
HGH2-3W-LVDT 1
HGH2-3W-LVDT 2
Load (kN)
Deformation (mm)
0
20
40
60
80
100
0
1
2
3

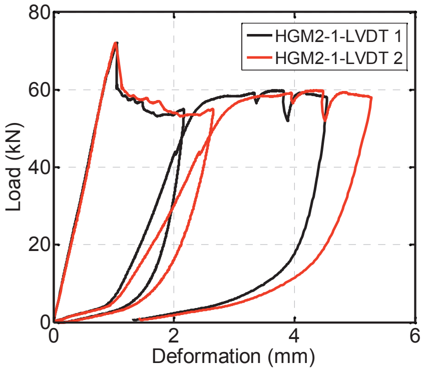
HGM2-1-LVDT 1
HGM2-1-LVDT 2
Load (kN)
Deformation (mm)
0
20
40
60
80
0
2
4
6

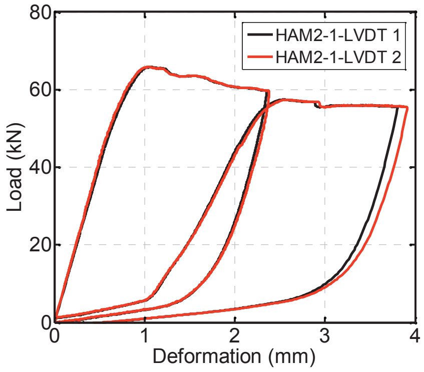
HAM2-1-LVDT 1
HAM2-1-LVDT 2
Load (kN)
Deformation (mm)
0
20
40
60
80
0
1
2
3
4

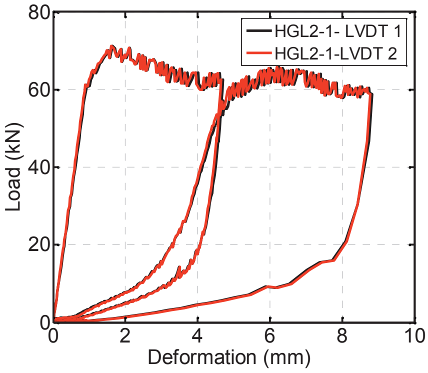
HGL2-1- LVDT 1
HGL2-1-LVDT 2
Load (kN)
Deformation (mm)
0
20
40
60
80
0
2
4
6
8
10

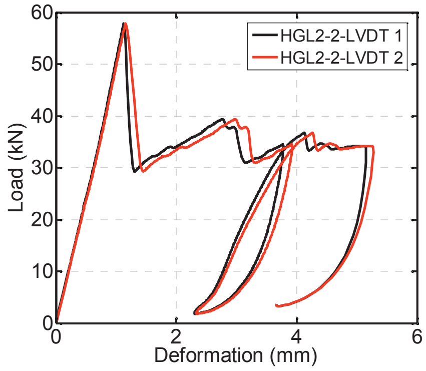
HGL2-2-LVDT 1
HGL2-2-LVDT 2
Load (kN)
Deformation (mm)
0
10
20
30
40
50
60
0
2
4
6

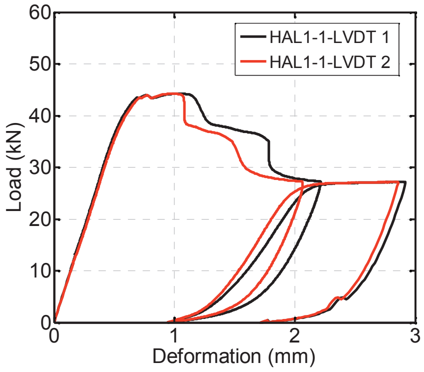
HAL1-1-LVDT 1
HAL1-1-LVDT 2
Load (kN)
Deformation (mm)
0
10
20
30
40
50
60
0
1
2
3

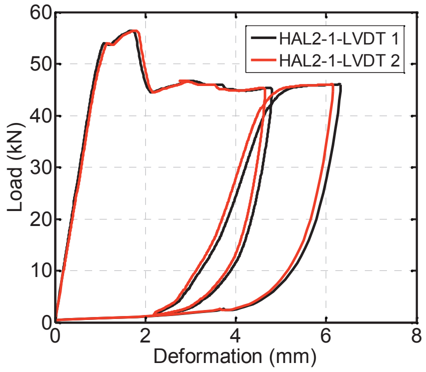
HAL2-1-LVDT 1
HAL2-1-LVDT 2
Load (kN)
Deformation (mm)
0
10
20
30
40
50
60
0
2
4
6
8

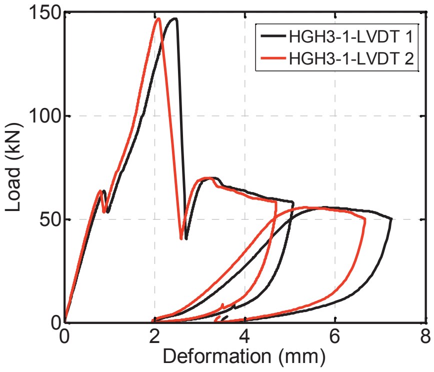
HGH3-1-LVDT 1
HGH3-1-LVDT 2
Load (kN)
Deformation (mm)
0
50
100
150
0
2
4
6
8

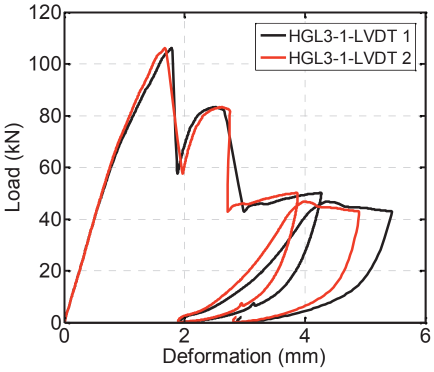
HGL3-1-LVDT 1
HGL3-1-LVDT 2
Load (kN)
Deformation (mm)
0
20
40
60
80
100
120
0
2
4
6

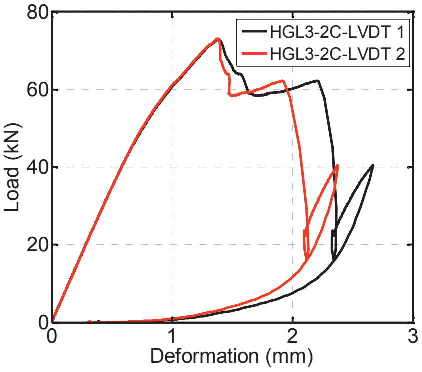
HGL3-2C-LVDT 1
HGL3-2C-LVDT 2
Load (kN)
Deformation (mm)
0
20
40
60
80
0
1
2
3

F

FE thermal simulation

F.1. Introduction

Appendix F presents additional information concerning the estimation and validation of the finite element thermal simulation of the FRP thermal break, first described in Chapter 3.

F.2. Geometry and mesh

a) FRP thermal break

The thermal models were generated in Ansys Fluent 15. They depicted a balcony detail that was composed of concrete structural members (wall and slab thickness of 200mm) and an external EPS insulation layer of variable width, in order to each time attain the two examined wall thermal transmittances (U=0.1 W/m^{2}K and U=0.2 W/m^{2}K). Half of the thermal bridge was simulated, taking advantage of the symmetry plane in the middle of the thermal bridge construction detail, Fig. F.1. The wall height of the final models was smaller than the ones prescribed by the standard (ISO 10211:2007), for the sake of rapid calculation. It was chosen (h=1200mm) from the temperature profile as recommended in the standard model (h=3500mm) and corresponded to the height, as from which the contour lines were already straight and parallel along the wall, Fig. F.2a. Furthermore, all the curved parts of the thermal break were simplified to the equivalent straight forms to avoid possible complications when generating the mesh for the thermal analysis, see Chapter 3.

Three different model types were generated, 15 cm, 30 cm and 45 cm, according to the three FRP thermal break configurations. The validation of the results regarding their mesh- and geometry-independence was done by generating different model types for the 15cm and 30cm thermal bridge cases. The results obtained from the final models and the corresponding validation models were consistent. Table F.1 presents the mesh properties of the final and the validation models.

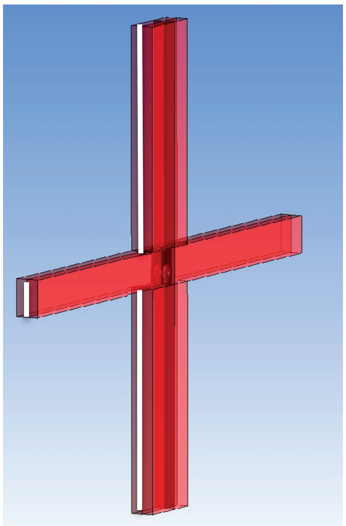

Figure F.1. Balcony construction detail and symmetry plane

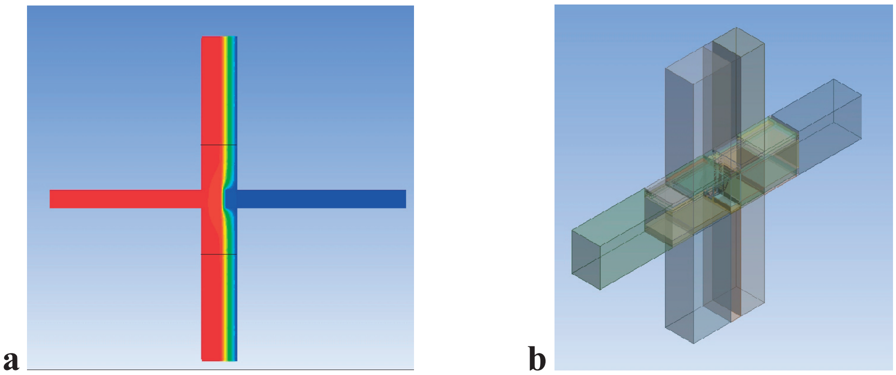

Figure F.2. a) Temperature profile of standard based model (*h*=3.50 m, 30 cm, *U*=0.2W/m^{2}K), b) final model with smaller dimensions

Table F.1. Mesh properties of thermal and validation models

Thermal bridge width		*Type of model*							
		Thermal model				*Validation*			
		$U=0.1(W/m^2k)$		*$U=0.2(W/m^2k)$*		*$U=0.1(W/m^2k)$*		*$U=0.2(W/m^2k)$*	
		Type of mesh	*Number of elements*	*Type of mesh*	*Number of elements*	*Type of mesh*	*Number of elements*	*Type of mesh*	*Number of elements*
15cm	*H=1.2m*	Unstr.[1]	11’100’928	Unstr.[1]	3’460’558				
	H=0.6m							Combined	5’829’503
30cm	*H=1.2m*	Unstr.[1]	6’260’557	Combined	9’305’732	Combined	18’306’754		
	H=3.5m							Unstr.[1]	2’855’858
45cm		Unstr.[1]	9’626’905	Unstr.[1]	4’765’020				

[1] Unstructured mesh.

b) Additional thermal models

Additional thermal models were developed to evaluate the thermal efficiency of the FRP thermal break and validate the simulation procedure. The first model concerned a balcony detail with a conventional steel thermal break. The next two thermal models represented ideal cases, in which no penetration of structural elements existed and the balcony connection included only aerogel and PU insulation. The procedure was validated by a model including a balcony detail with continuous slab and no thermal break. The results were compared with tabulated values recommended by OFEN (Office federal de l'énergie, Suisse).

The conventional thermal break model is presented in Fig. F.3a&b. This thermal break consists of two steel tension bars and two steel compression rods, while two steel plates transfer the shear forces. The insulation material of the connection consists of an upper rockwool foam and a lower PU foam. The dimensions of the model were chosen as prescribed by the standard ISO 10211:2007 (model width 250mm, wall height 1140mm, slab height 200mm). The dimensions of the other three thermal models were h=1200m, slab height=200mm; the model’s width does not influence the results (constant thermal properties throughout the width), Fig. F.3c. As far as the mesh is concerned, structured mesh was used.

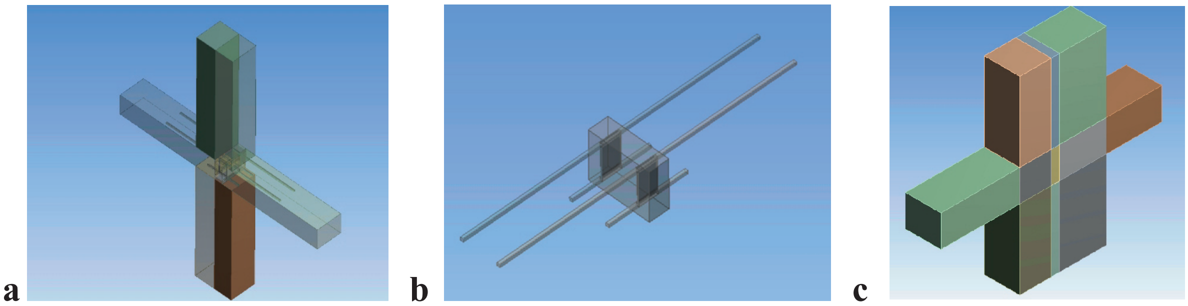

Figure F.3. a) Balcony detail of conventional thermal break, b) detail of conventional thermal break, c) balcony detail with aerogel insulation between slabs (yellow box).

F.3. Parameters of thermal analysis

The thermal properties of the materials used for all the different thermal analyses are presented in Table F.2. For the FRP materials the rule of mixtures was applied, according to the volume fraction of each material.

Table F.2. Material properties of thermal models

Materials	*Density (kg/m^3)*	*Thermal capacity (j/kgK)*	*Thermal conductivity (W/mK)*
EPS	15	1130	0.038
PU	100	1500	0.028
Rockwool	120	850	0.036
Aerogel	130	2	0.013
Forex	700	900	0.081
PVC	1420	900	0.19
Concrete	2000	750	2.5
Pultruded	1800	1200	0.30
GFRP	1940	887	0.70
AFRP	1300	1153.8	0.10
Steel	7900	50	15.0

Concerning the thermal model in FLUENT, double precision and a pressure-based steady state solver type were used. Convective surface boundary conditions with a steady temperature were applied to the external and internal environments. Adiabatic conditions were applied to the cut-off and symmetry planes. A PISO scheme was used for the solution method and the THIRD ORDER-MUSCL for solving the energy equation. No convergence criterion was used and the convergence was verified each time according to the balance of the total surface heat flux. The number of iterations until convergence varied for the different models, depending on the mesh, the number of elements and the dimensions of the model.

F.4. Results

The output of the thermal analysis consisted of the thermal transmittance values, ψ, see Chapter 3, and the temperature profile of the balcony detail, which indicates the temperature distribution along the internal wall and the possibility of a condensation risk, see Fig. F.4. These results concern the thermal break with the AFRP loop and the GFRP sandwich; the results for the whole AFRP thermal break unit are similar. From this figure it is obvious that the internal superficial temperature remains at high levels and close to the ambient temperature, independently of the level of the insulation layer. This is the result of the high performance of the FRP thermal break. Moreover, there is no difference in the internal superficial temperature for the different thermal bridge widths, i.e. 15cm 30cm or 45cm. Comparing a.1. and a.2 in Figure F.4, the higher temperature exhibited at the cold side of the model, in the slab region in the case of a.1., is a result of the higher insulation level than in the case of a.2.

Furthermore, the temperature distribution through the thermal element, demonstrating the effectiveness of the joint, is shown in Fig. F.5 for all the thermal break configurations. Looking at this figure and for all the cases, the part of the FRP thermal break at the hot side is really close to the ambient temperature, a phenomenon which results from the effective combination of the aerogel and the high-performance FRPs at the temperature transition point. Figure F.6a shows the temperature distribution of the aerogel configuration, without the FRP thermal break. From this figure it is obvious that the integration of the FRP thermal break in the structure has no influence at all on the temperature distribution. Finally, Fig. F.6b presents the temperature distribution of the conventional thermal break.

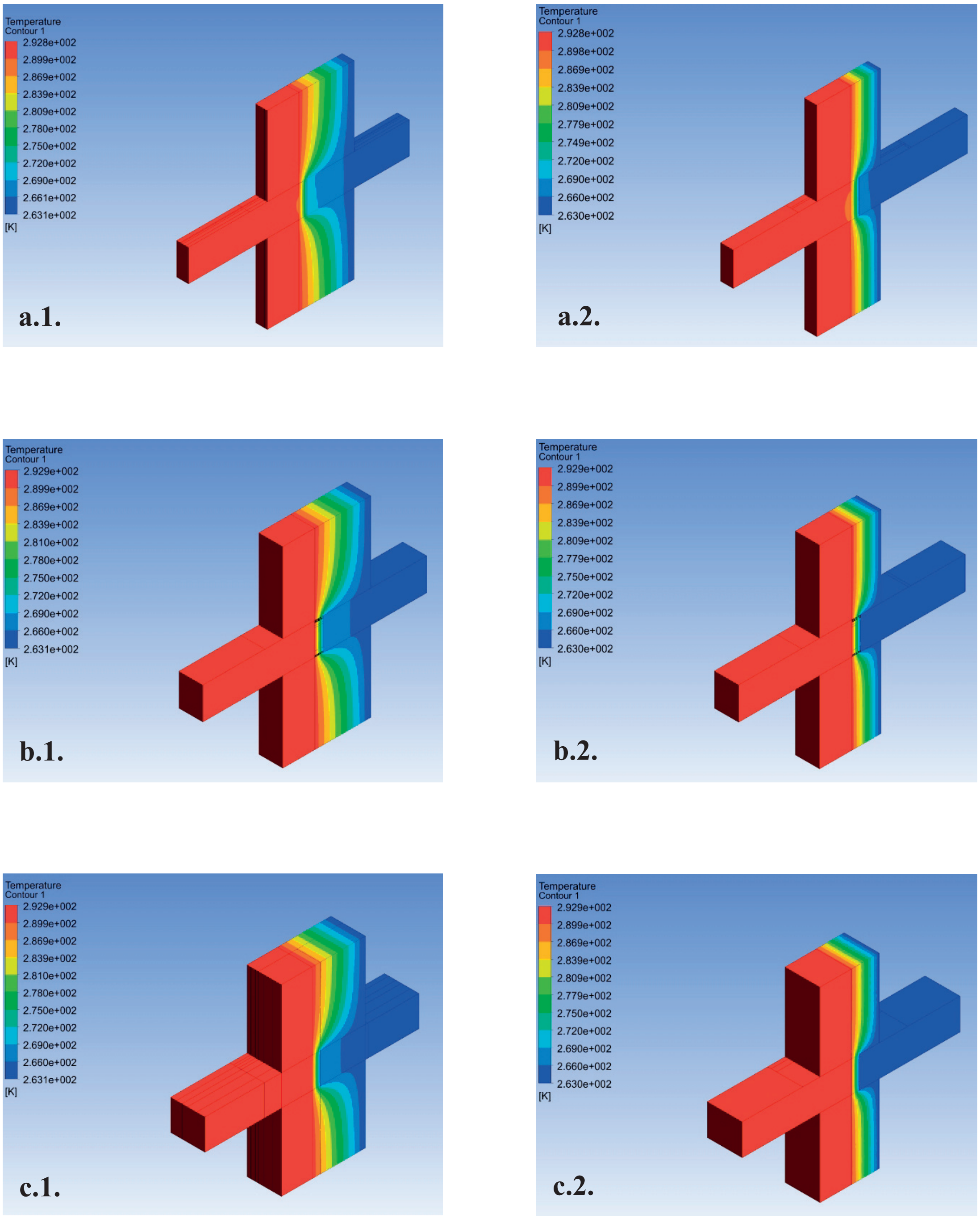
Temperature
Contour 1
2.928e+002
2.899e+002
2.869e+002
2.839e+002
2.809e+002
2.780e+002
2.750e+002
2.720e+002
2.690e+002
2.661e+002
2.631e+002
[K]
a.1.
Temperature
Contour 1
2.928e+002
2.898e+002
2.869e+002
2.839e+002
2.809e+002
2.779e+002
2.749e+002
2.720e+002
2.690e+002
2.660e+002
2.630e+002
[K]
a.2.
Temperature
Contour 1
2.929e+002
2.899e+002
2.869e+002
2.839e+002
2.810e+002
2.780e+002
2.750e+002
2.720e+002
2.690e+002
2.660e+002
2.631e+002
[K]
b.1.
Temperature
Contour 1
2.929e+002
2.899e+002
2.869e+002
2.839e+002
2.809e+002
2.779e+002
2.750e+002
2.720e+002
2.690e+002
2.660e+002
2.630e+002
[K]
b.2.
Temperature
Contour 1
2.929e+002
2.899e+002
2.869e+002
2.839e+002
2.810e+002
2.780e+002
2.750e+002
2.720e+002
2.690e+002
2.660e+002
2.631e+002
[K]
c.1.
Temperature
Contour 1
2.929e+002
2.899e+002
2.869e+002
2.839e+002
2.809e+002
2.779e+002
2.750e+002
2.720e+002
2.690e+002
2.660e+002
2.630e+002
[K]
c.2.

Figure F.4. Temperature distribution: a) balcony detail of 15cm thermal break; a.1) U=0.1W/m^{2}K and a.2.) U=0.2W/m^{2}K, b) balcony detail of 30cm thermal break; b.1) U=0.1W/m^{2}K and b.2.) U=0.2W/m^{2}K, c) balcony detail of 45cm thermal break; c.1) U=0.1W/m^{2}K and c.2.) U=0.2W/m^{2}K.

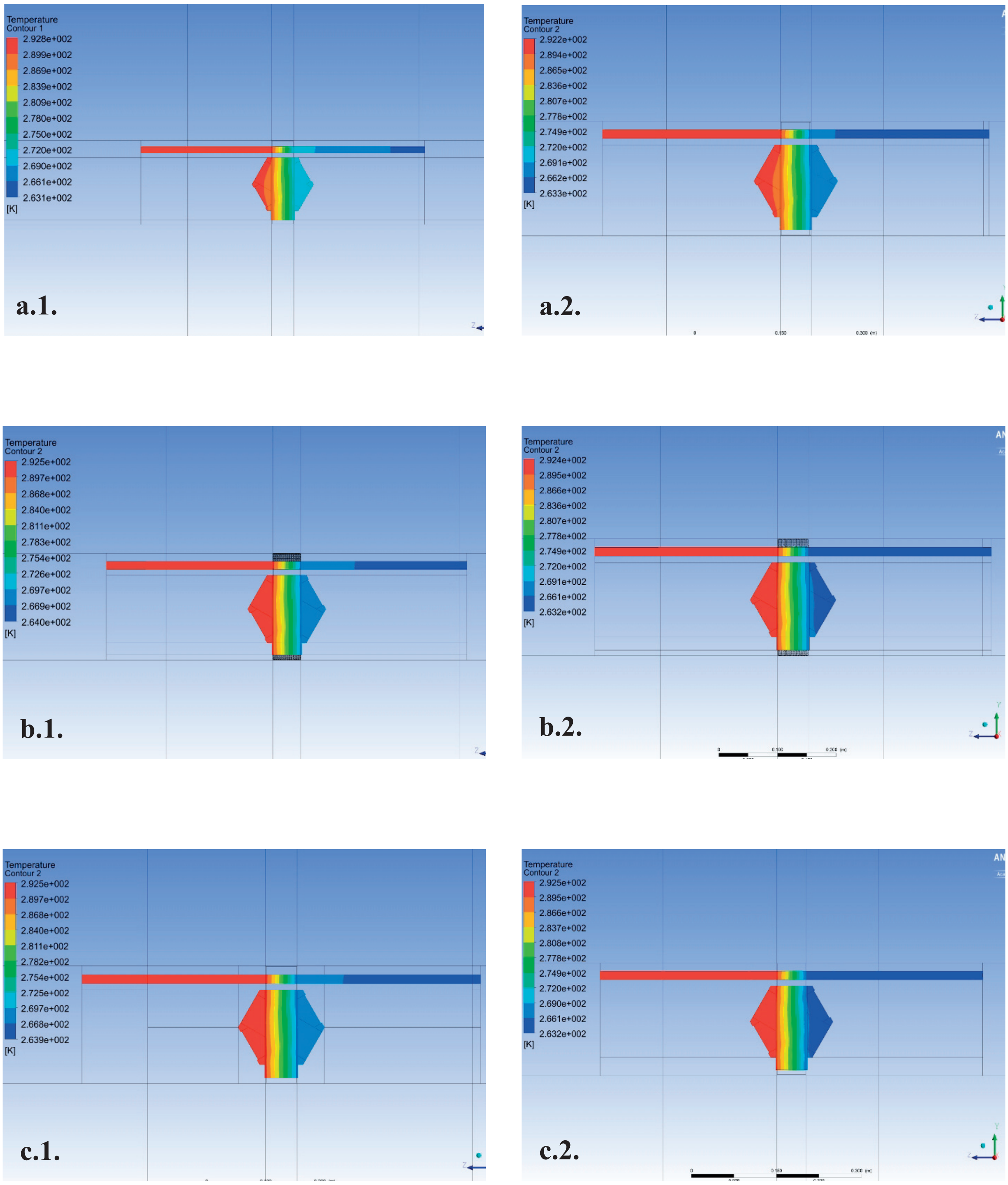

Figure F.5. Temperature distribution: a) 15cm thermal break; a.1) U=0.1W/m^{2}K and a.2.) U=0.2W/m^{2}K, b) 30cm thermal break; b.1) U=0.1W/m^{2}K and b.2.) U=0.2W/m^{2}K, c) 45cm thermal break; c.1) U=0.1W/m^{2}K and c.2.) U=0.2W/m^{2}K.

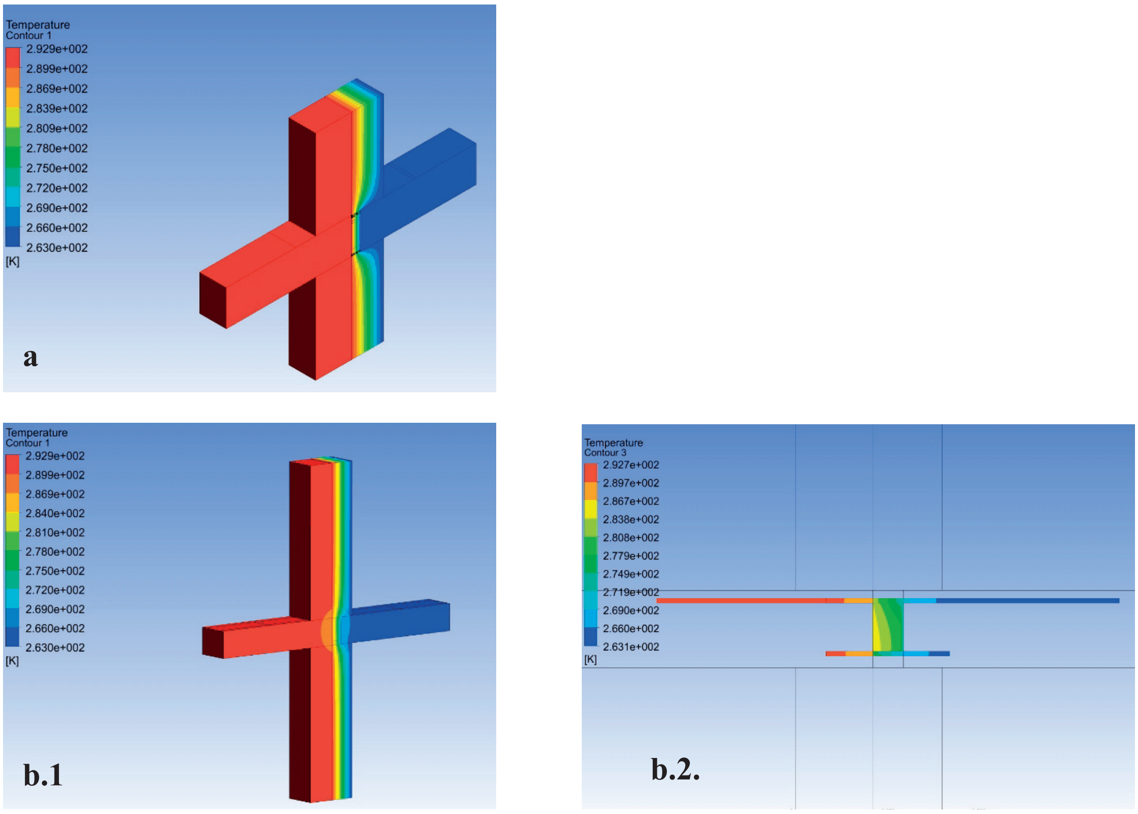
Temperature
Contour 1
2.929e+002
2.899e+002
2.869e+002
2.839e+002
2.809e+002
2.780e+002
2.750e+002
2.720e+002
2.690e+002
2.660e+002
2.630e+002
[K]
a
Temperature
Contour 1
2.929e+002
2.899e+002
2.869e+002
2.840e+002
2.810e+002
2.780e+002
2.750e+002
2.720e+002
2.690e+002
2.660e+002
2.630e+002
[K]
b.1
Temperature
Contour 3
2.927e+002
2.897e+002
2.867e+002
2.838e+002
2.808e+002
2.779e+002
2.749e+002
2.719e+002
2.690e+002
2.660e+002
2.631e+002
[K]
b.2.

Figure F.6. a) Temperature distribution of aerogel configuration, b) Temperature distribution of conventional thermal break: b.1.) balcony detail of 25cm thermal break, U=0.2W/m^{2}K, b.2.) 25cm thermal break.

The energy performance of the FRP thermal break can be evaluated by comparing the 30cm FRP thermal model of U=0.2W/m^{2}K with the conventional thermal break model. The linear thermal transmittance of this FRP thermal break configuration is ψ=0.142 W/mK, while for the conventional thermal break the heat losses are doubled, achieving a thermal transmittance of ψ =0.576 W/mK. It should be noted however that the inner superficial temperature, for both thermal breaks, is above the critical condensation temperature (T_{dew}=16°C for T_{int}=20°C); T_{surf}= 19°C (Fig. F.4.b.2) for the FRP thermal break and T_{surf}=18°C (Fig. F.6.a.1.) for the conventional one. Finally, Figs. F.5.b.2. and F.6.a.2 show the temperature distribution inside the two different thermal breaks. The enhanced thermal properties of the FRP materials are the reason for the sharp temperature gradient between the two environments, which leads to a high temperature on the inner surface of the thermal break. This behavior is more significant in the case of inadequate thermal insulation widths, since the thermal efficiency of the FRP thermal break maintains the inner superficial temperature at high levels, offering a uniform superficial inner temperature, unlike conventional thermal breaks, see Fig. F.7.

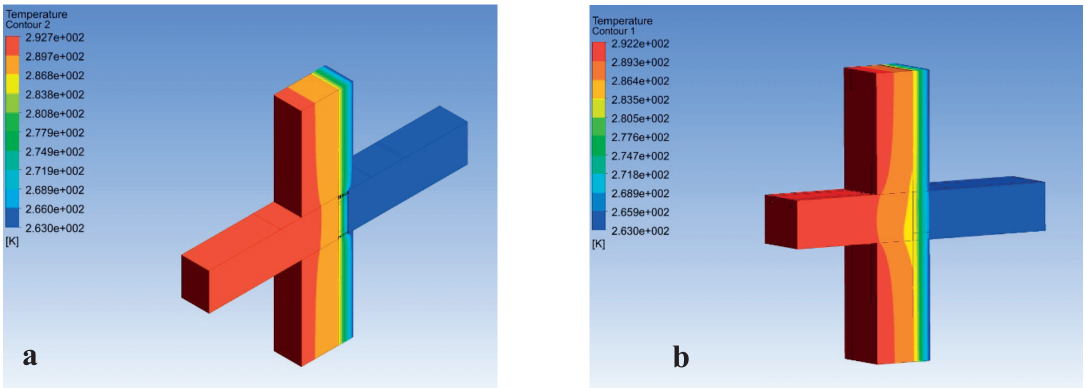
Temperature
Contour 2
2.927e+002
2.897e+002
2.868e+002
2.838e+002
2.808e+002
2.779e+002
2.749e+002
2.719e+002
2.689e+002
2.660e+002
2.630e+002
[K]
a
Temperature
Contour 1
2.922e+002
2.893e+002
2.864e+002
2.835e+002
2.805e+002
2.776e+002
2.747e+002
2.718e+002
2.689e+002
2.659e+002
2.630e+002
[K]
b

Figure F.7. a.1.) Temperature distribution of FRP thermal break, 30cm thermal break, U=0.37W/m^{2}K, ψ =0.08 W/mK b) Temperature distribution of conventional thermal break, 25cm thermal break, U=0.37W/m^{2}K, ψ =0.37 W/mK.

G Full scale beam experiments

G.1. Introduction

Appendix G includes additional photos and figures concerning the fabrication and the experiments of the six full-scale beams. These experiments constitute the last part of the structural validation of the FRP thermal break. They have organized in such a way in order to simulate the loading conditions in a real balcony cantilever. The beams were casted in the HES of Rapperswil, in Switzerland.

G.2. Fabrication

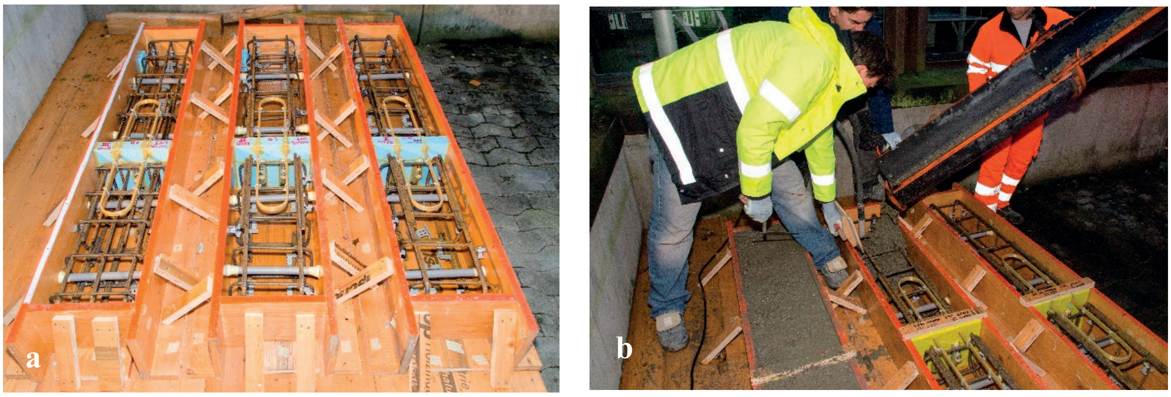

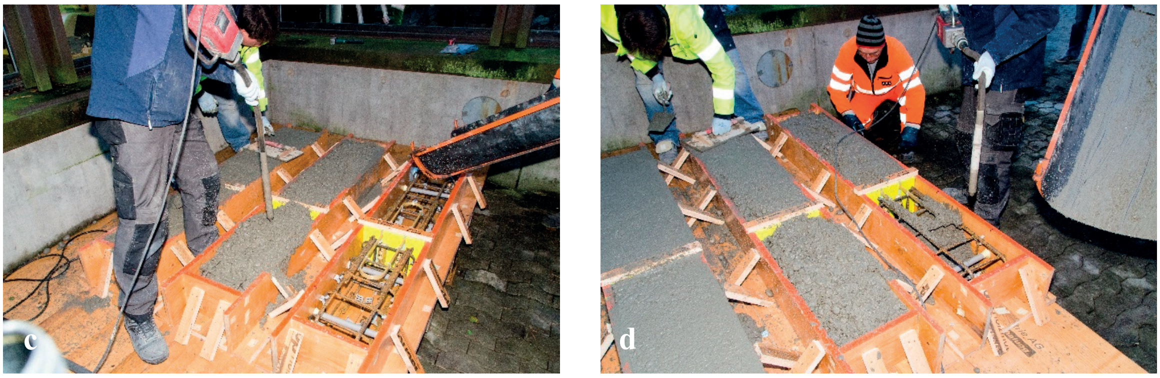

Figure G.1. Beam casting, 2nd series, a) Formwork and steel reinforcement of beams, b) pouring of concrete, c) concrete vibration, d) smoothing concrete surface.

G.3. Crack development

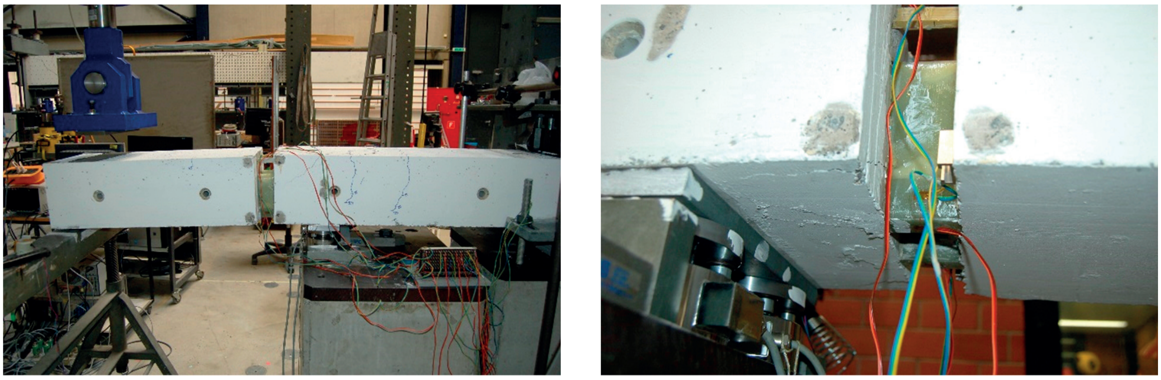

Figure G.2. Beam G600, F_u=26.4 kN.

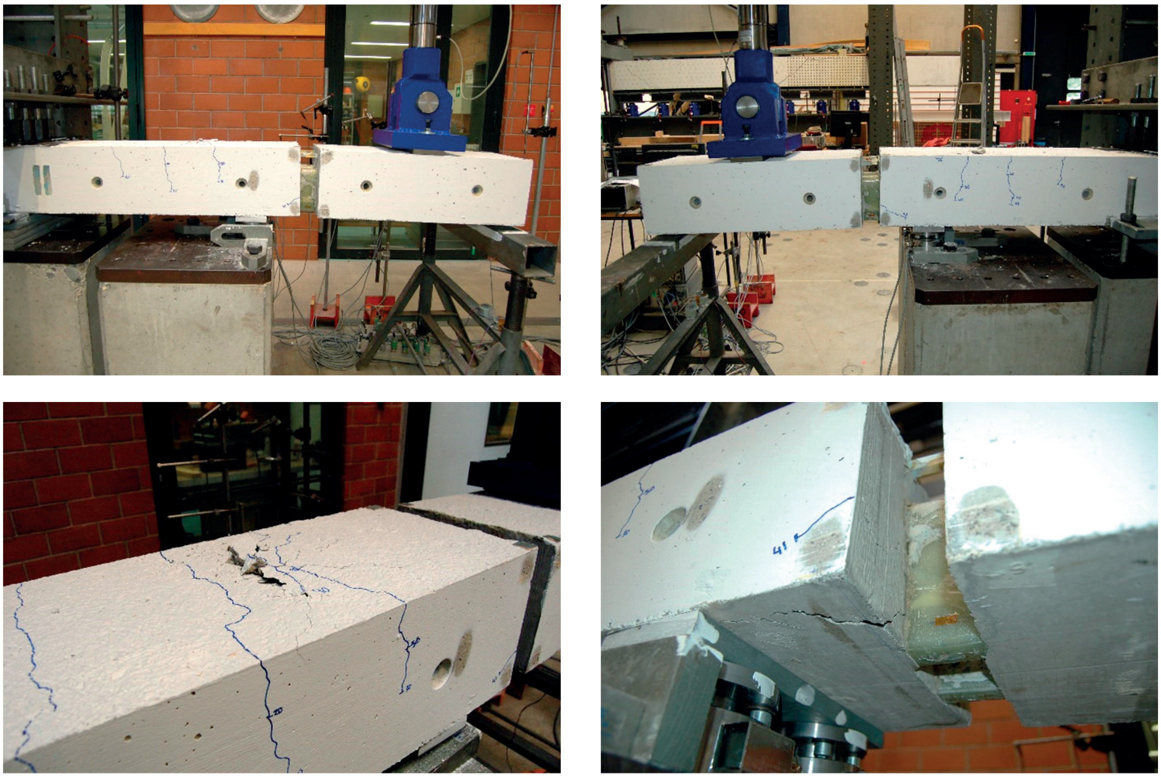

Figure G.3. Beam G400, F_u=40.7 kN.

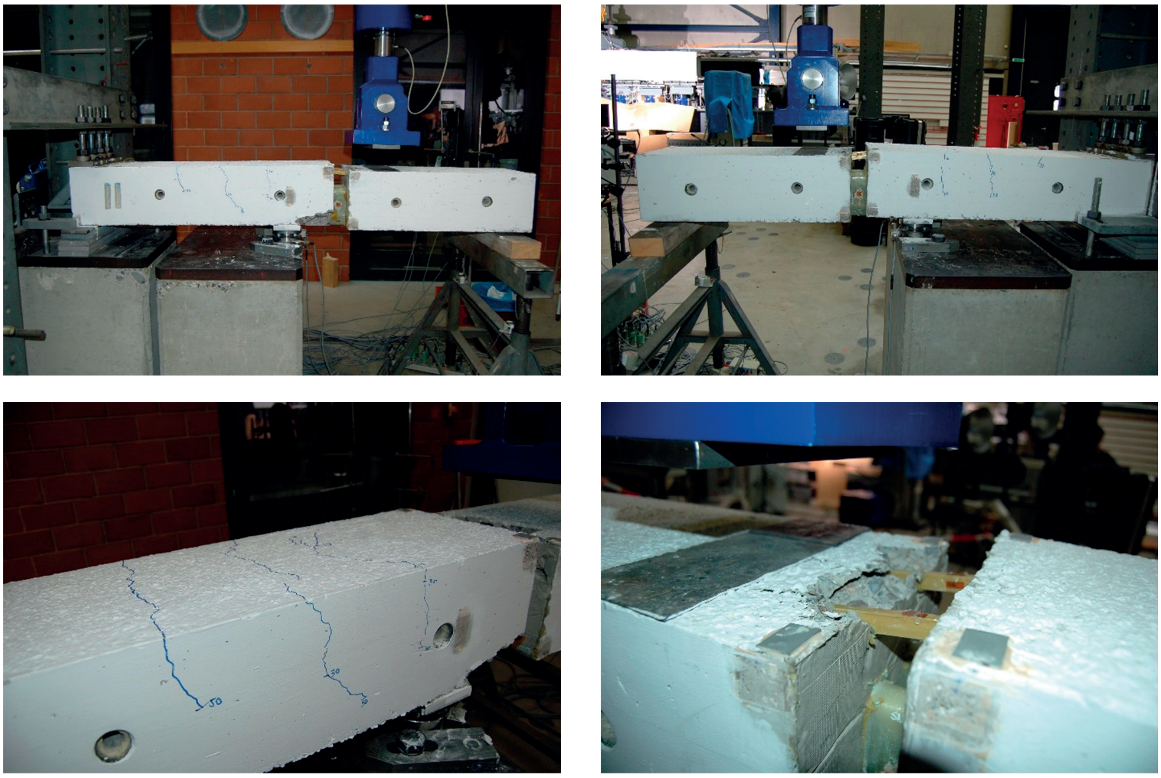

Figure G.4. Beam G200, F_u=48.1 kN.

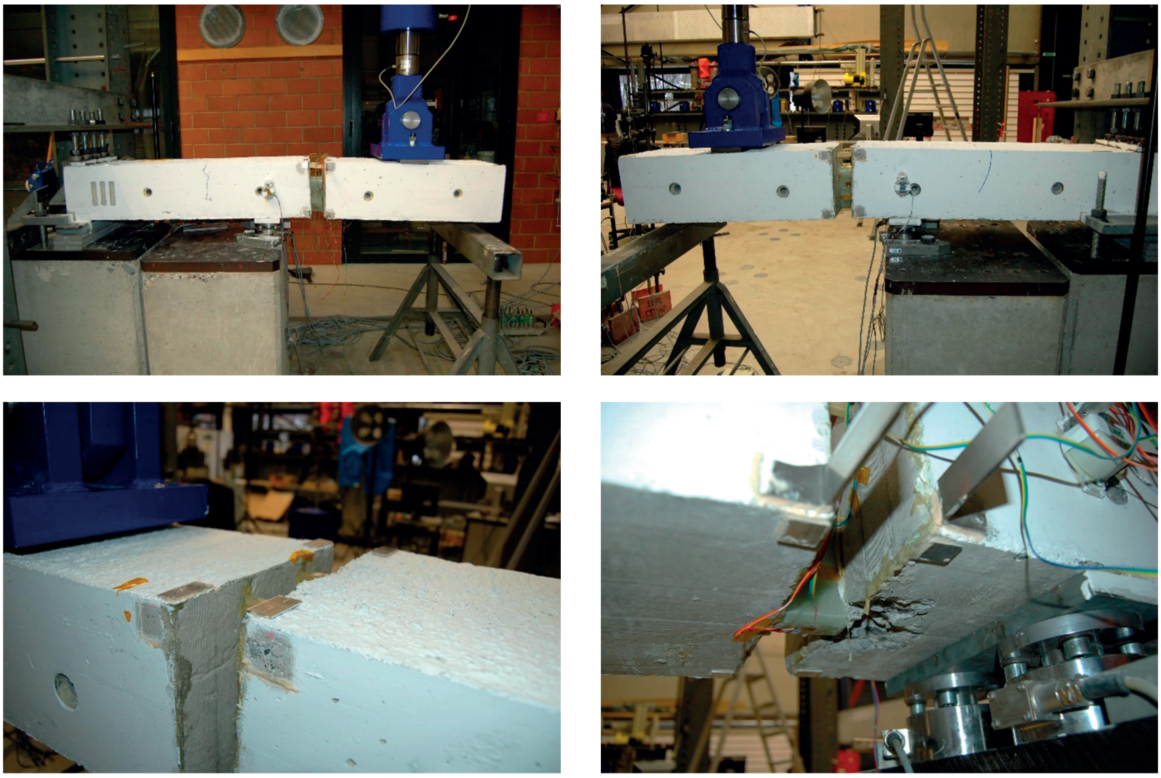

Figure G.5. Beam G400-1, F_u=25.8 kN.

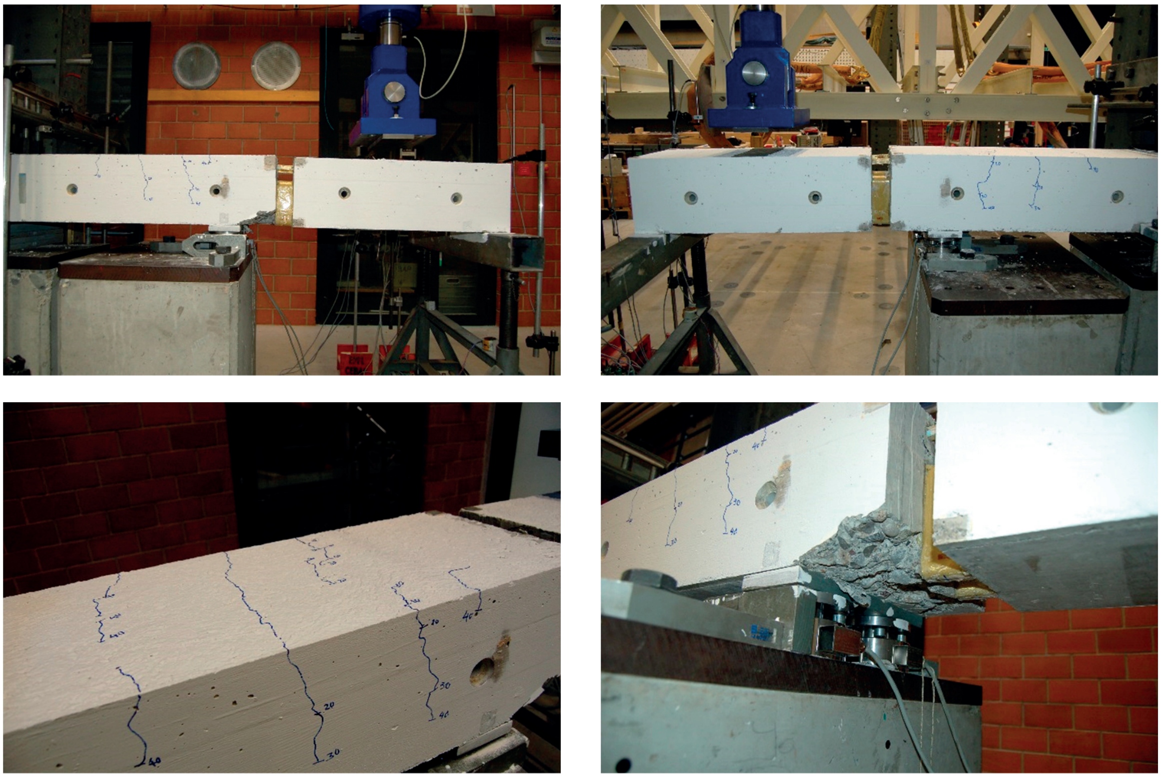

Figure G.6. Beam A400, F_u=39.2 kN.

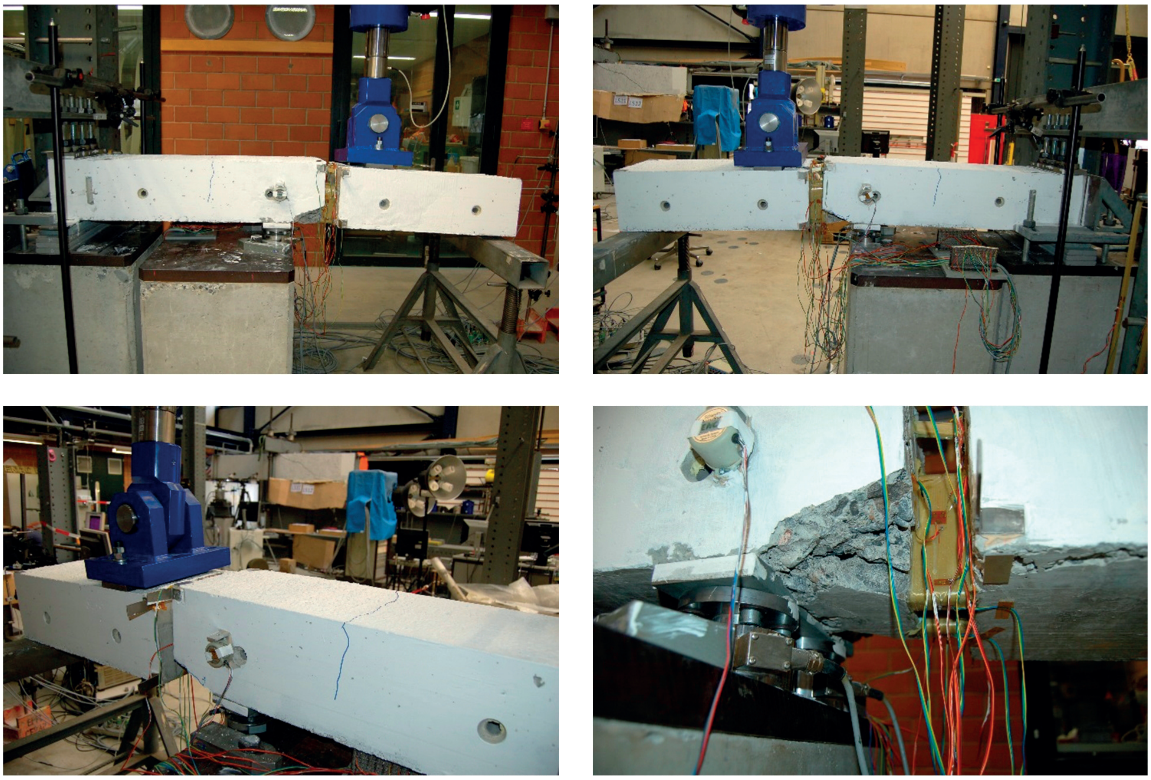

Figure G.7. Beam A200, F_u=43.2 kN.

G.4. Failure pattern

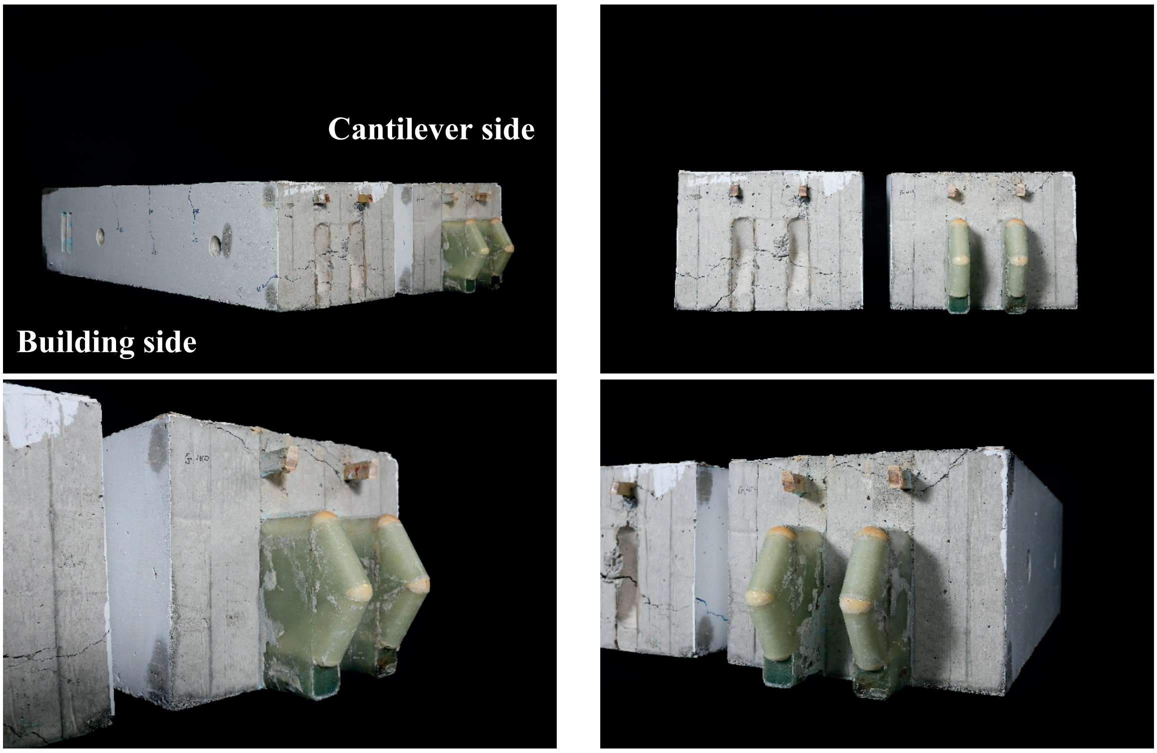
Cantilever side
Building side

Figure G.9. Beam G400, F_u=40.7 kN.

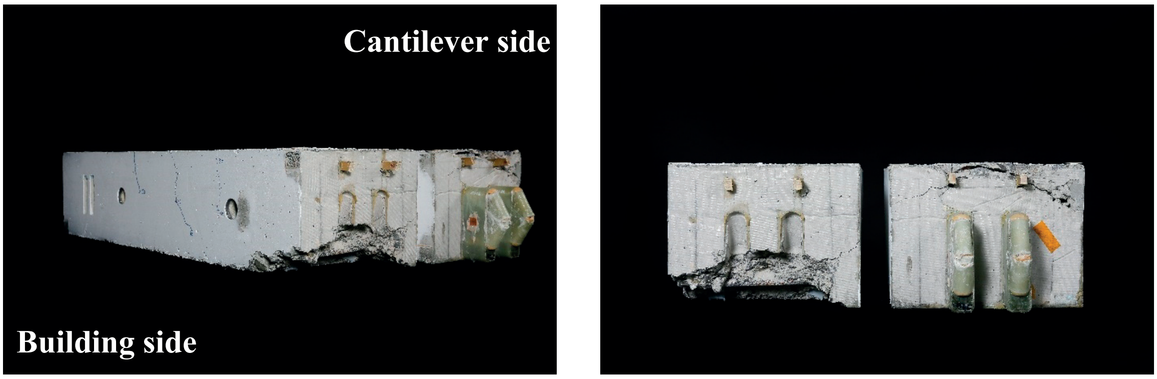
Cantilever side
Building side

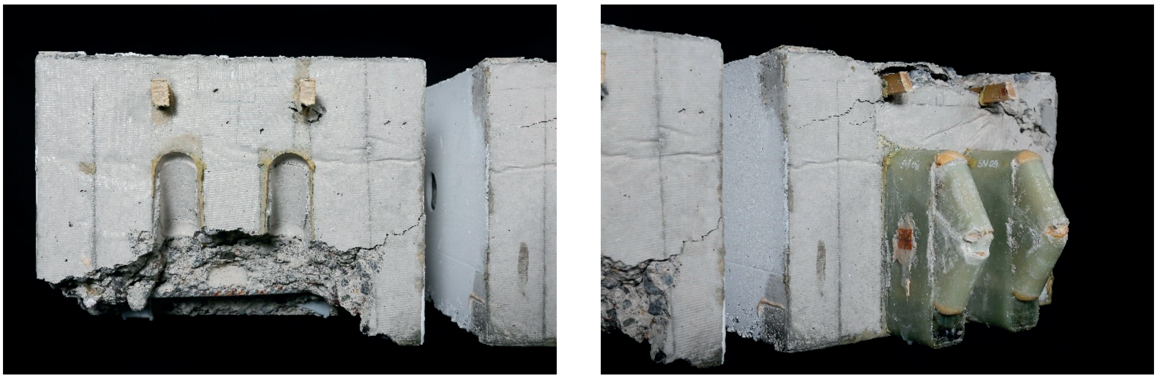

Figure G.10. Beam G200, F_u=48.1 kN.

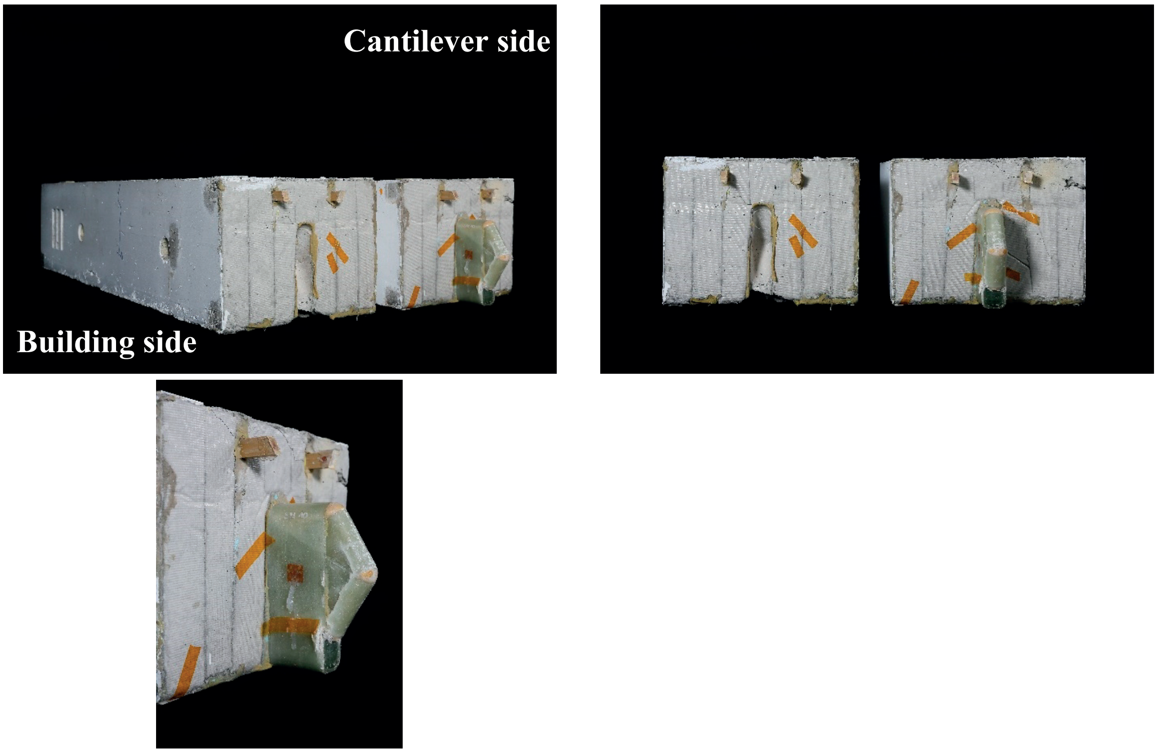
Cantilever side
Building side

Figure G.11. Beam G400-1, F_u=25.8 kN.

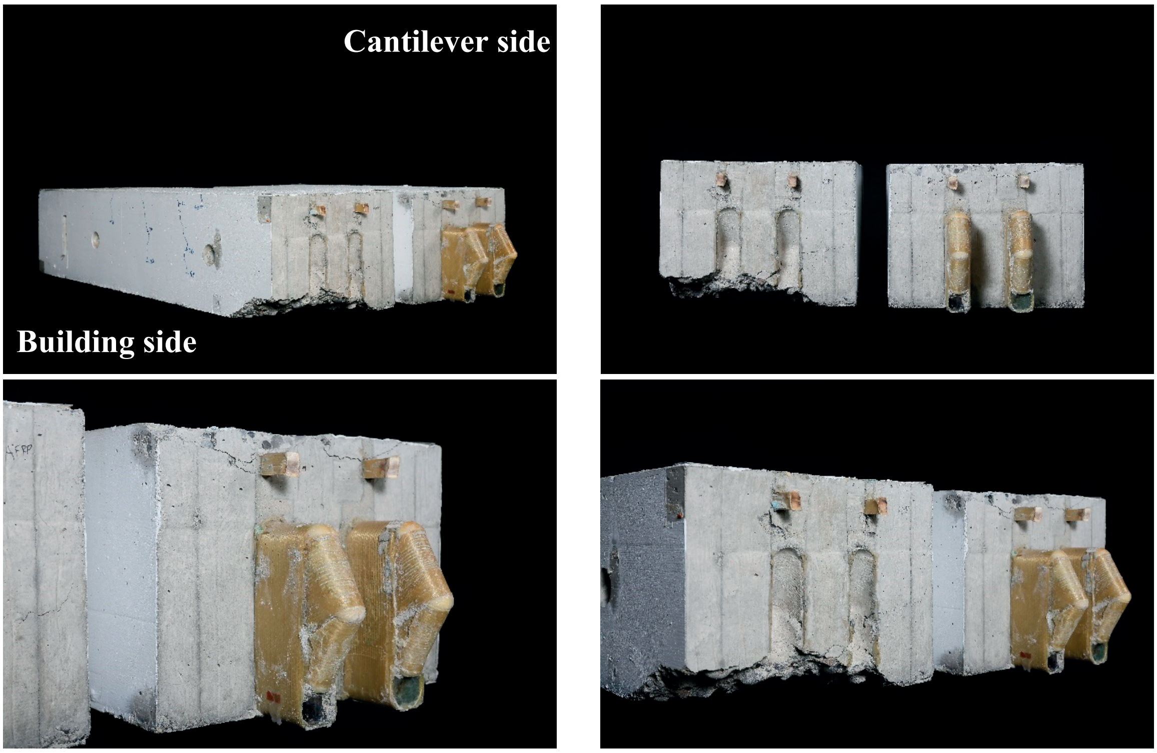
Cantilever side
Building side

Figure G.12. Beam A400, F_u=39.2 kN.

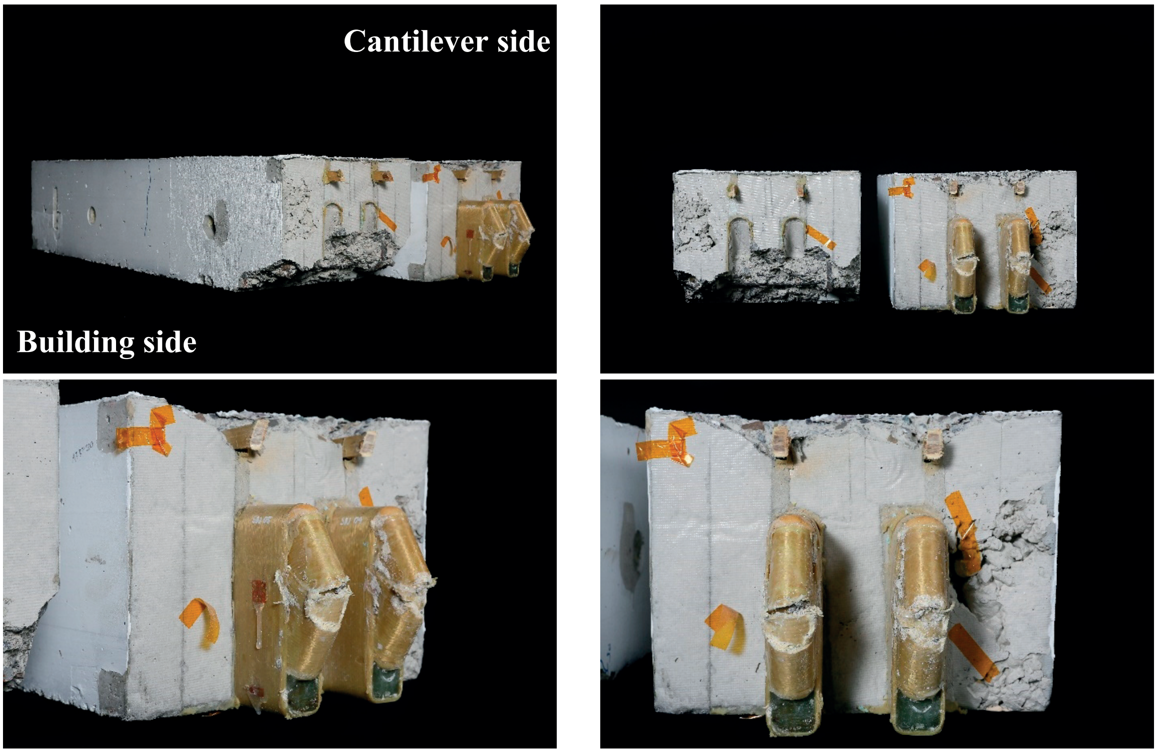
Cantilever side
Building side

Figure G.13. Beam A200, F_u=43.2 kN.

G.4. Load-displacement curves

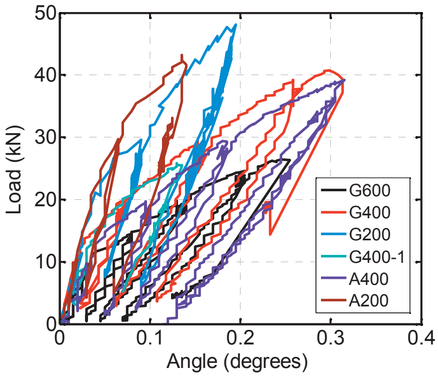

Figure G.14. Inclinometer measurements.

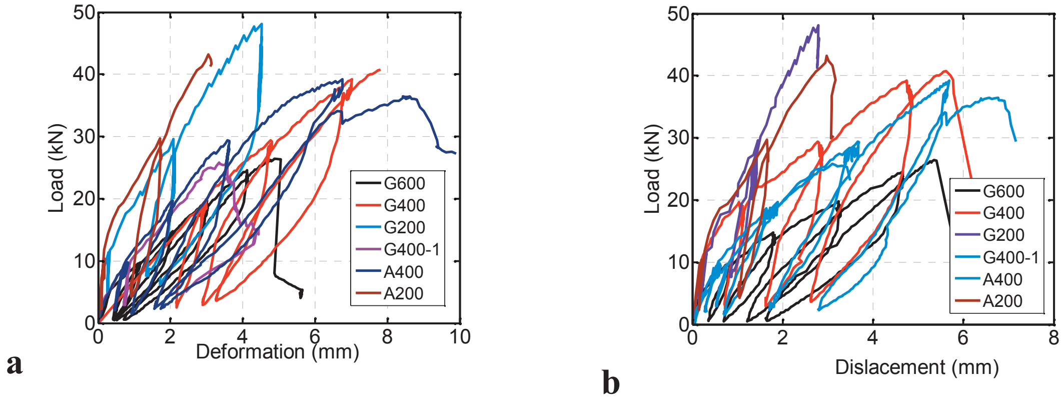

Figure G.15. a) LVDTs of AFRP loop elongation, b) Vertical displacement of the joint.

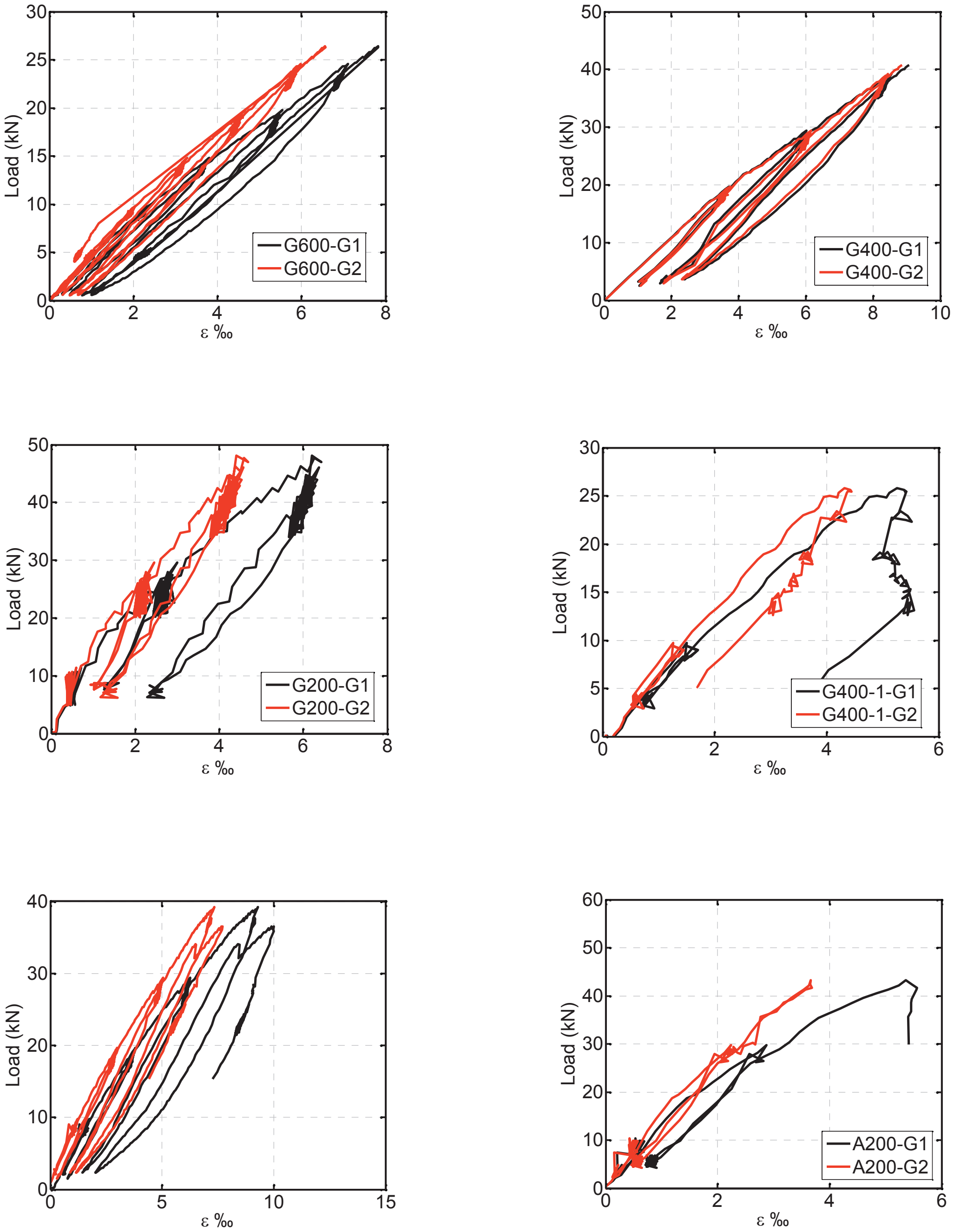

Figure G.16. Strain measurements of AFRP loop elongation, G1-average of top surface, G2-average of side surface.

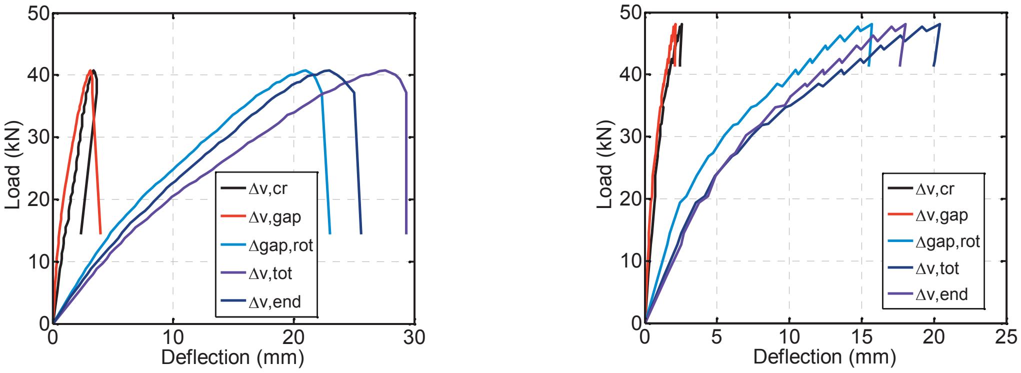

Figure G.17. Contributors to deflection at the cantilever end, G400 (left), G200 (right).

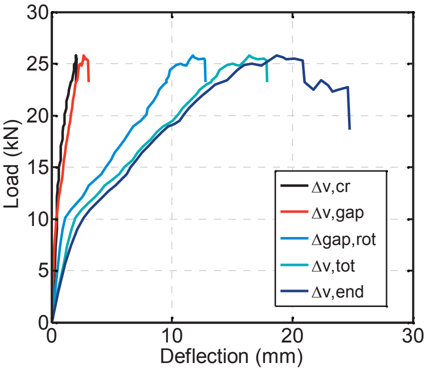

Figure G.18. Contributors to deflection at the cantilever end, G400-1.

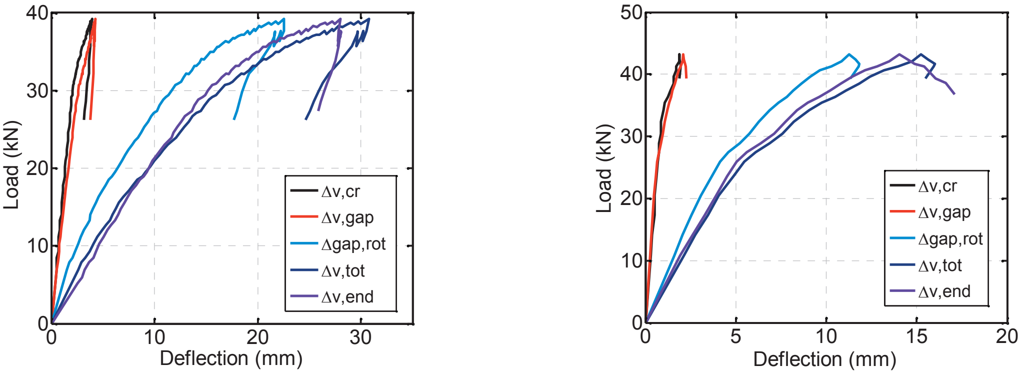

Figure G.19. Contributors to deflection at the cantilever end, A400 (left), A200 (right).

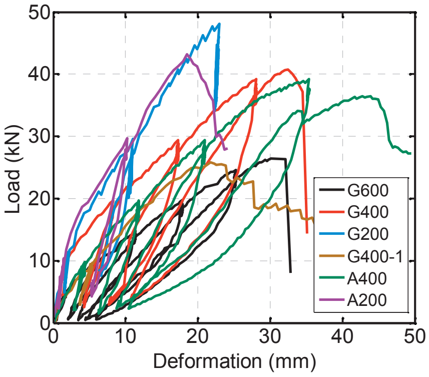

Figure G.20. End deflection for all cycles and beams.

H

Creep modeling and prediction

H.1. Introduction

The current annex includes additional information on the two proposed methodologies for creep prediction, which are presented in Chapter 5.

H.2. Power law models

The regression power law function had the form

$$\delta_c = at^b + c \quad (1)$$

The coefficients according to the different training lengths and the long – term prediction are presented in Tables H.1 – H.4 for the different creep experiments (creep deformation in μm and time in sec).

Table H.1. Compression creep 20kN.

Training length	*a*	*b*	*c*
50%	21.19	0.33	-14.03
60%	18.55	0.35	-10.69
70%	17.48	0.36	-9.28
80%	16.53	0.36	-7.99
25 years	15.57	0.37	-6.65

Table H.2. Compression creep 25kN.

Training length	*a*	*b*	*c*
50%	630	0.087	-541.17
60%	481.53	0.11	-389.03
70%	404.79	0.121	-309.57
80%	387.21	0.12	-291.24
25 years	392.54	0.12	-296.81

Table H.3. Tension creep 20kN.

Training length	*a*	*b*	*c*
50%	12.03	0.26	45.35
60%	8.37	0.30	51.98
70%	9.83	0.28	49.10
80%	11.80	0.27	45.46
25 years	1.99	0.45	70.70

Table H.4. Bending creep 61kN.

Training length	*a*	*b*	*c*
40%	61.77	0.19	40.79
70%	71.98	0.18	27.96
80%	77.63	0.17	21.05

H.3. Gradient regression models

The regression functions used for the analysis is

$$g_2(\theta) = \frac{p_1 x + p_2}{x^2 + q_1 x + q_2}, \qquad (2)$$

The coefficients according to the different training lengths and the long – term prediction are presented in Tables H.5 – H.11 for the different creep experiments (creep deformation in μm and time in sec).

Table H.5. Compression creep 20kN

Training length	p_1	p_2	q_1	q_2
50%	47.89	1.00×10^3	73.26	295.19
60%	62.21	4.76×10^3	247.27	1.47×10^3
70%	193.11	3.38×10^4	1.51×10^3	1.07×10^3
80%	109.08	1.37×10^4	642.00	4.33×10^3
25 years	131.76	1.92×10^4	878.93	6.08×10^3

Table H.6. Compression creep 25kN

Training length	p_1	p_2	q_1	q_2
50%	91.54	183.41	8.39	3.62
60%	93.59	239.77	9.57	5.20
70%	93.52	237.85	9.53	5.15
80%	93.36	232.97	9.43	5.01
25 years	93.72	243.60	9.65	5.31

Table H.7. Tension creep 20kN

Training length	p_1	p_2	q_1	q_2
50%	264.27	2.33×10^5	2.22×10^4	8.64×10^4
60%	61.79	4.38×10^4	4.17×10^3	1.63×10^4
70%	20.55	3.50×10^3	353.53	1.28×10^3
80%	40.48	2.47×10^4	9.35×10^3	9.27×10^3
25 years	40.48	9.28×10^5	9.19×10^4	3.19×10^5

Table H.8. Bending creep 25kN

Training length	m_1	m_2	n_1	n_2
40%	73.37	2.554×10^4	1.25×10^3	1.25×10^3
70%	73.27	2.54×10^4	1.25×10^3	1.21×10^3
80%	73.83	2.58×10^4	1.27×10^3	1.14×10^3

H.4. Non homogeneous Poisson process – NHPP models

Table H.9. Compression creep 20kN

Training length	p_1	p_2	q_1	q_2
50%	53.42	3.45×10^3	197.05	1.03×10^3
60%	244.82	4.90×10^4	2.42×10^3	1.5×10^4
70%	156.87	2.79×10^4	1.39×10^3	8.56×10^3
80%	136.29	2.28×10^4	1.14×10^3	6.97×10^4
25 years	145.85	2.53×10^4	1.26×10^3	7.76×10^3

Table H.10. Compression creep 25kN

Training length	p_1	p_2	q_1	q_2
50%	77.6	290.94	8.39	8.05
60%	78.29	330.60	9.12	9.23
70%	78.55	346.20	9.41	9.69
80%	78.63	351.17	9.50	9.84
25 years	79.05	379.22	10.00	10.69

Table H.11. Tension creep 20kN

Training length	p_1	p_2	q_1	q_2
50%	-8.41	305.70	21.91	111.96
60%	-9.28	333.05	24.29	121.55
70%	-10.50	377.90	28.83	136.62
80%	-11.06	398.88	30.99	143.60
25 years	-10.86	391.21	30.18	141.06

H.5. Compression creep 20 kN – additional figures

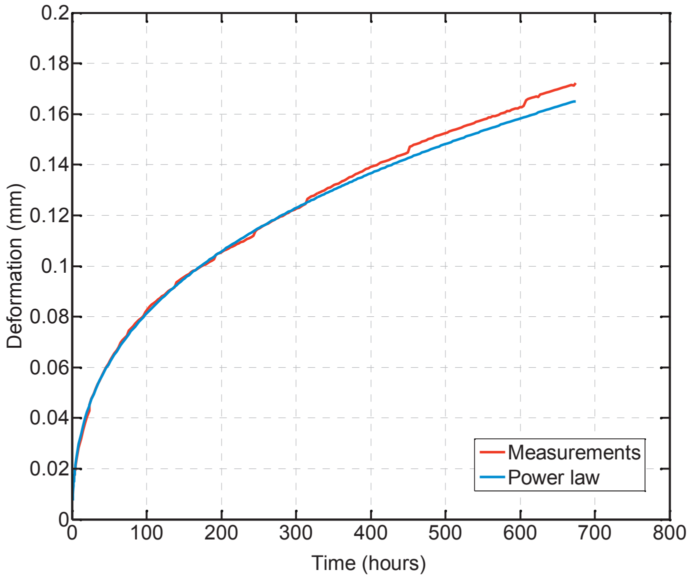

a

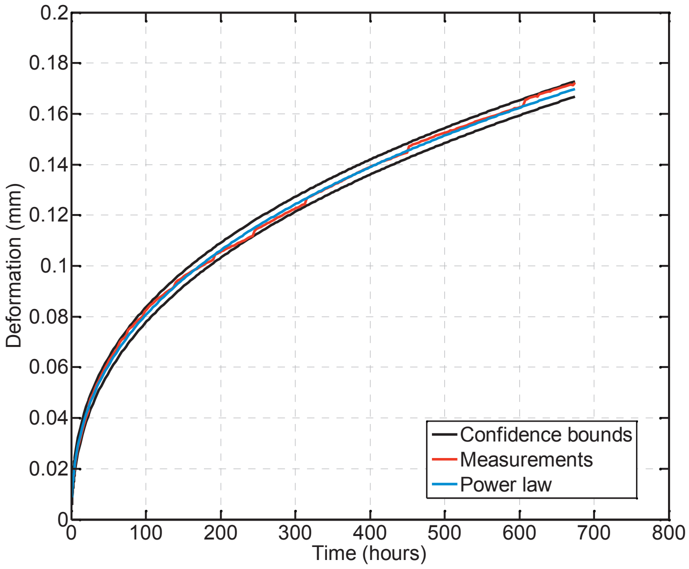

b

Figure H.1. Compression creep 20kN – Power law, a) 50% and b) 80%.

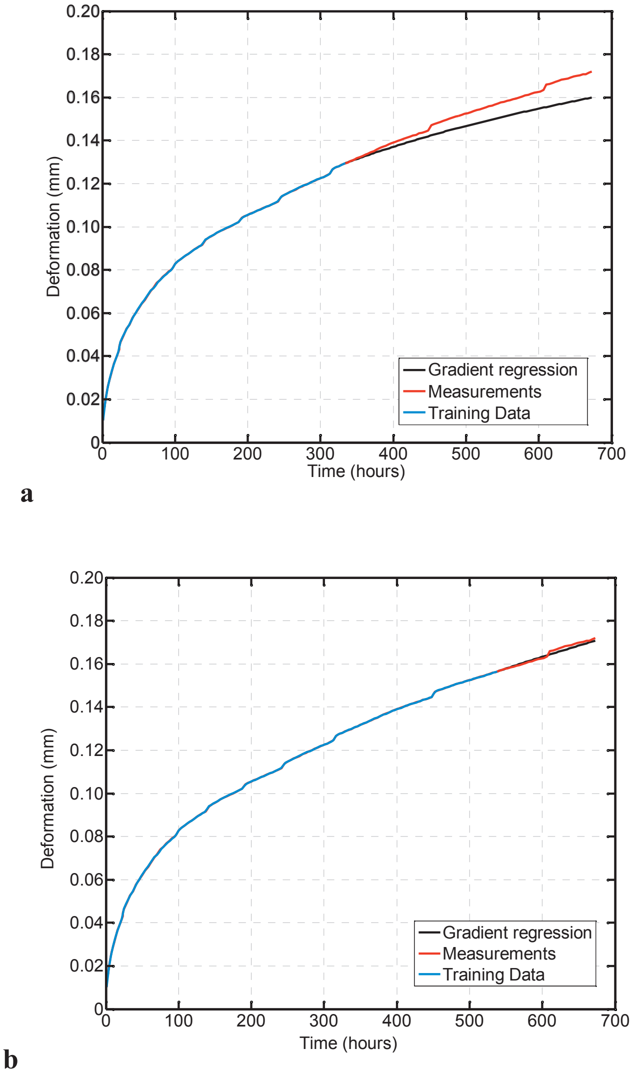

Figure H.2. Compression creep 20kN – Gradient regression, a) 50% and b) 80%.

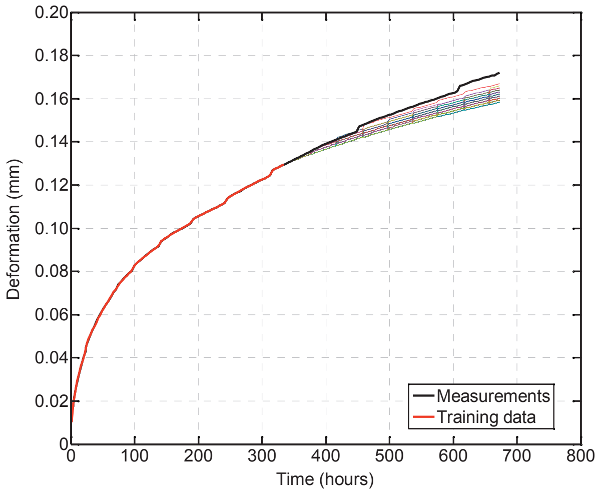

a

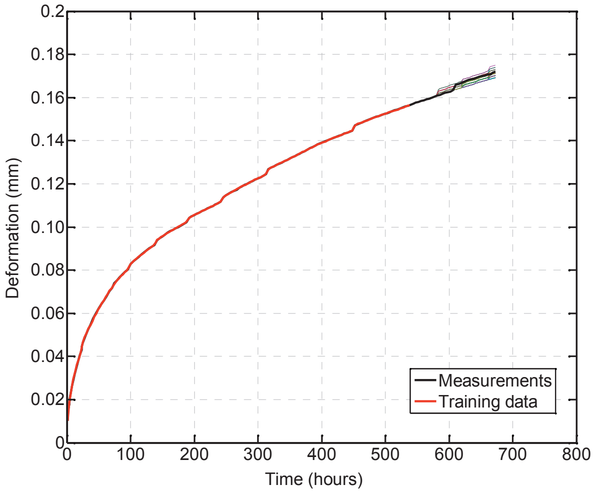

b

Figure H.3. Compression creep 20kN – NHPP, a) 50% and b) 80%.

Curriculum Vitae

Kyriaki GOULOUTI
Born :30.06.1986
Nationality : Hellenic
kgoulouti @yahoo.gr

EDUCATION

2013 – 2016: Ecole Polytechnique Fédérale de Lausanne, EPFL, Lausanne, Switzerland.
PhD student in Composite Construction Laboratory, CCLab.

2010 - 2011: Ecole Polytechnique Fédérale de Lausanne, EPFL, Lausanne, Switzerland.
Master thesis in Steel Structures Laboratory, ICOM (six months).

2005 – 2010: Aristotle Universtity of Thessaloniki, AUTH, Greece.
Msc in Civil Engineering.

WORKING EXPERIENCE

2012 – 2013: Ecole Polytechnique Fédérale de Lausanne, EPFL, Lausanne, Switzerland.
Scientific collaborator in Composite Construction Laboratory (CCLab).

2011 – 2012 : TBM Ingénieurs SA, Vevey, Switzerland.
Civil Engineer (six months).

PUBLICATIONS

Journal papers

1. Goulouti K, de Castro J, Vassilopoulos P A, Keller T, Thermal performance evaluation of fiber-reinforced polymer thermal breaks for balcony connections, Energy and Buildings, 70 (2014), 365-371.
2. Goulouti K, de Castro J, Keller T, Aramid/glass fiber-reinforced thermal break – thermal and structural performance, Composite Structures, 136 (2016), 113-123.

3. Goulouti K, de Castro J, Keller T, Aramid/glass fiber-reinforced thermal break – structural system performance, Composite Structures, 152 (2016), 455-463.
4. Goulouti K, Lymperopoulos I, Creep modeling and prediction for fiber-reinforced polymers with Gradient regression and Non-Homogeneous Poisson Process, (in progress).